Computational and Mathematical Methods in Medicine

Application and Decision-Making Implications of Novel Optimization Models in Public Health 2021

Lead Guest Editor: Plácido R. Pinheiro
Guest Editors: Miltiadis D. Lytras, Anna Visvizi, and Mirian C. D. Pinheiro

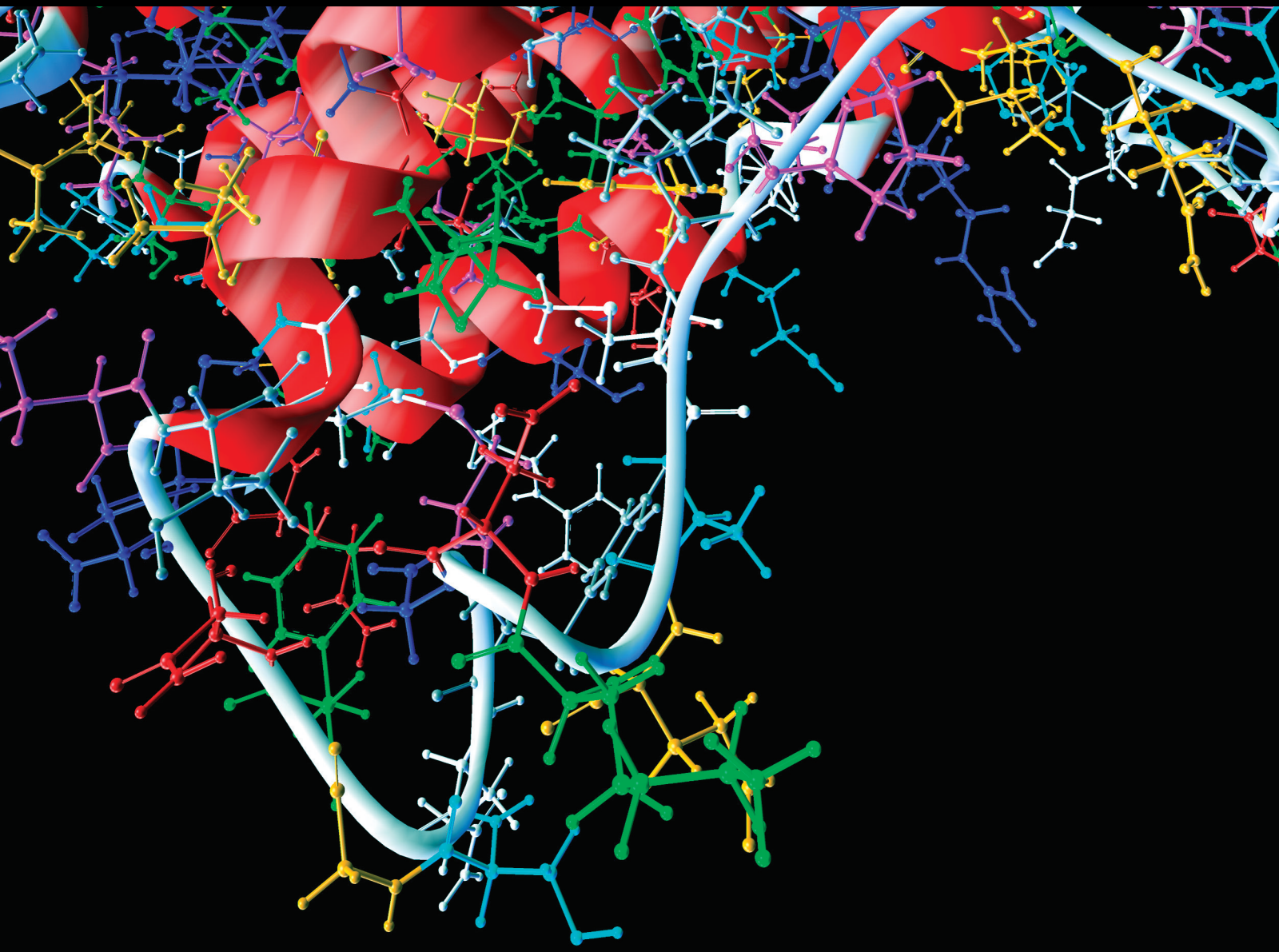

Application and Decision-Making Implications of Novel Optimization Models in Public Health 2021

Computational and Mathematical Methods in Medicine

Application and Decision-Making Implications of Novel Optimization Models in Public Health 2021

Lead Guest Editor: Plácido R. Pinheiro
Guest Editors: Miltiadis D. Lytras, Anna Visvizi, and Mirian C. D. Pinheiro

Contents

Retracted: A Three-Dimensional Cement Quantification Method for Decision Prediction of Vertebral Recompression after Vertebroplasty
Computational and Mathematical Methods in Medicine
Retraction (1 page), Article ID 9795242, Volume 2023 (2023)

Retracted: What Promotes Medical Overuse: Perspective on Evolutionary Game between Administration and Medical Institutions
Computational and Mathematical Methods in Medicine
Retraction (1 page), Article ID 9861647, Volume 2023 (2023)

[Retracted] Research Progress of B-Cell Lymphoma/Leukemia-2 Inhibitor Combined with Azacytidine in the Targeted Therapy of Acute Myeloid Leukemia
Yanyu Wang, Dan Huang, Lejia Liu, Aixin Wang, Yuan Gao, and Huan Lin
Research Article (8 pages), Article ID 3992224, Volume 2022 (2022)

[Retracted] Improving the Use of Blockchain Technology in Stroke Care Information Management Systems
Yuying Yang, Aixia Song, Qing Chang, Hongmei Zhao, Weidan Kong, Qian Xue, and Qianlong Xue
Research Article (9 pages), Article ID 2642841, Volume 2022 (2022)

[Retracted] Efficacy of *Ginkgo biloba* Extract Combined with Hormones in the Treatment of Sudden Deafness and Its Effect on the Reactivity of Peripheral Blood T Cell Subsets
Zhenhua Zhu, Qi Wu, Ge Hu, Xianwen Wang, Wei Chang, Ji Bin, and Weili Yang
Research Article (10 pages), Article ID 2903808, Volume 2022 (2022)

[Retracted] What Promotes Medical Overuse: Perspective on Evolutionary Game between Administration and Medical Institutions
Chenxi Xu, Li Luo, Siyu Zeng, Xiaozhou He, Jialing Li, and Guiju Zhu
Research Article (15 pages), Article ID 4351282, Volume 2022 (2022)

[Retracted] Screening of Differentially Expressed Iron Death-Related Genes and the Construction of Prognosis Model in Patients with Renal Clear Cell Carcinoma
Ding Wu, Zhenyu Xu, Zhan Shi, Ping Li, Huichen lv, Jie Huang, and Dian Fu
Research Article (10 pages), Article ID 4456987, Volume 2022 (2022)

[Retracted] Construction and Evaluation of Neural Network Correlation Model between Syndrome Elements and Physical and Chemical Indexes of Unstable Angina Pectoris Complicated with Anxiety
Xiaoyang Chen, Yifei Wang, Li Zhang, and Xuegong Xu
Research Article (11 pages), Article ID 6217186, Volume 2022 (2022)

Design and Analysis of Hospital Throughput Maximization Algorithm under COVID-19 Pandemic
Haochen Zou, Geer Jiang, Bowen Cheng, and Dejian Wang
Research Article (14 pages), Article ID 8127055, Volume 2022 (2022)

Contents

Hindawi
Computational and Mathematical Methods in Medicine
Volume 2023, Article ID 9872930, 1 page
https://doi.org/10.1155/2023/9872930

Retraction

Retracted: Improving the Use of Blockchain Technology in Stroke Care Information Management Systems

Computational and Mathematical Methods in Medicine

Received 17 October 2023; Accepted 17 October 2023; Published 18 October 2023

This article has been retracted by Hindawi following an investigation undertaken by the publisher [1]. This investigation has uncovered evidence of one or more of the following indicators of systematic manipulation of the publication process:

(1) Discrepancies in scope

(2) Discrepancies in the description of the research reported

(3) Discrepancies between the availability of data and the research described

(4) Inappropriate citations

(5) Incoherent, meaningless and/or irrelevant content included in the article

(6) Peer-review manipulation

The presence of these indicators undermines our confidence in the integrity of the article's content and we cannot, therefore, vouch for its reliability. Please note that this notice is intended solely to alert readers that the content of this article is unreliable. We have not investigated whether authors were aware of or involved in the systematic manipulation of the publication process.

Wiley and Hindawi regrets that the usual quality checks did not identify these issues before publication and have since put additional measures in place to safeguard research integrity.

We wish to credit our own Research Integrity and Research Publishing teams and anonymous and named external researchers and research integrity experts for contributing to this investigation.

The corresponding author, as the representative of all authors, has been given the opportunity to register their agreement or disagreement to this retraction. We have kept a record of any response received.

References

[1] Y. Yang, A. Song, Q. Chang et al., "Improving the Use of Blockchain Technology in Stroke Care Information Management Systems," *Computational and Mathematical Methods in Medicine*, vol. 2022, Article ID 2642841, 9 pages, 2022.

Hindawi
Computational and Mathematical Methods in Medicine
Volume 2023, Article ID 9828704, 1 page
https://doi.org/10.1155/2023/9828704

Retraction

Retracted: Retinal Vessel Automatic Segmentation Using SegNet

Computational and Mathematical Methods in Medicine

Received 17 October 2023; Accepted 17 October 2023; Published 18 October 2023

This article has been retracted by Hindawi following an investigation undertaken by the publisher [1]. This investigation has uncovered evidence of one or more of the following indicators of systematic manipulation of the publication process:

(1) Discrepancies in scope

(2) Discrepancies in the description of the research reported

(3) Discrepancies between the availability of data and the research described

(4) Inappropriate citations

(5) Incoherent, meaningless and/or irrelevant content included in the article

(6) Peer-review manipulation

The presence of these indicators undermines our confidence in the integrity of the article's content and we cannot, therefore, vouch for its reliability. Please note that this notice is intended solely to alert readers that the content of this article is unreliable. We have not investigated whether authors were aware of or involved in the systematic manipulation of the publication process.

Wiley and Hindawi regrets that the usual quality checks did not identify these issues before publication and have since put additional measures in place to safeguard research integrity.

We wish to credit our own Research Integrity and Research Publishing teams and anonymous and named external researchers and research integrity experts for contributing to this investigation.

The corresponding author, as the representative of all authors, has been given the opportunity to register their agreement or disagreement to this retraction. We have kept a record of any response received.

References

[1] X. Xu, Y. Wang, Y. Liang et al., "Retinal Vessel Automatic Segmentation Using SegNet," *Computational and Mathematical Methods in Medicine*, vol. 2022, Article ID 3117455, 11 pages, 2022.

Hindawi
Computational and Mathematical Methods in Medicine
Volume 2023, Article ID 9823636, 1 page
https://doi.org/10.1155/2023/9823636

Retraction

Retracted: Screening of Differentially Expressed Iron Death-Related Genes and the Construction of Prognosis Model in Patients with Renal Clear Cell Carcinoma

Computational and Mathematical Methods in Medicine

Received 17 October 2023; Accepted 17 October 2023; Published 18 October 2023

This article has been retracted by Hindawi following an investigation undertaken by the publisher [1]. This investigation has uncovered evidence of one or more of the following indicators of systematic manipulation of the publication process:

(1) Discrepancies in scope

(2) Discrepancies in the description of the research reported

(3) Discrepancies between the availability of data and the research described

(4) Inappropriate citations

(5) Incoherent, meaningless and/or irrelevant content included in the article

(6) Peer-review manipulation

The presence of these indicators undermines our confidence in the integrity of the article's content and we cannot, therefore, vouch for its reliability. Please note that this notice is intended solely to alert readers that the content of this article is unreliable. We have not investigated whether authors were aware of or involved in the systematic manipulation of the publication process.

In addition, our investigation has also shown that one or more of the following human-subject reporting requirements has not been met in this article: ethical approval by an Institutional Review Board (IRB) committee or equivalent, patient/participant consent to participate, and/or agreement to publish patient/participant details (where relevant).

Wiley and Hindawi regrets that the usual quality checks did not identify these issues before publication and have since put additional measures in place to safeguard research integrity.

We wish to credit our own Research Integrity and Research Publishing teams and anonymous and named external researchers and research integrity experts for contributing to this investigation.

The corresponding author, as the representative of all authors, has been given the opportunity to register their agreement or disagreement to this retraction. We have kept a record of any response received.

References

[1] D. Wu, Z. Xu, Z. Shi et al., "Screening of Differentially Expressed Iron Death-Related Genes and the Construction of Prognosis Model in Patients with Renal Clear Cell Carcinoma," *Computational and Mathematical Methods in Medicine*, vol. 2022, Article ID 4456987, 10 pages, 2022.

Hindawi
Computational and Mathematical Methods in Medicine
Volume 2023, Article ID 9797525, 1 page
https://doi.org/10.1155/2023/9797525

Retraction

Retracted: Serum TGF-β1 and VEGF Levels Reflect the Liver Hardness and Function in Children with Biliary Atresia

Computational and Mathematical Methods in Medicine

Received 17 October 2023; Accepted 17 October 2023; Published 18 October 2023

This article has been retracted by Hindawi following an investigation undertaken by the publisher [1]. This investigation has uncovered evidence of one or more of the following indicators of systematic manipulation of the publication process:

(1) Discrepancies in scope

(2) Discrepancies in the description of the research reported

(3) Discrepancies between the availability of data and the research described

(4) Inappropriate citations

(5) Incoherent, meaningless and/or irrelevant content included in the article

(6) Peer-review manipulation

The presence of these indicators undermines our confidence in the integrity of the article's content and we cannot, therefore, vouch for its reliability. Please note that this notice is intended solely to alert readers that the content of this article is unreliable. We have not investigated whether authors were aware of or involved in the systematic manipulation of the publication process.

Wiley and Hindawi regrets that the usual quality checks did not identify these issues before publication and have since put additional measures in place to safeguard research integrity.

We wish to credit our own Research Integrity and Research Publishing teams and anonymous and named external researchers and research integrity experts for contributing to this investigation.

The corresponding author, as the representative of all authors, has been given the opportunity to register their agreement or disagreement to this retraction. We have kept a record of any response received.

References

[1] D. Chang, X. Geng, L. Zhou, and G. Hou, "Serum TGF-β1 and VEGF Levels Reflect the Liver Hardness and Function in Children with Biliary Atresia," *Computational and Mathematical Methods in Medicine*, vol. 2022, Article ID 5802548, 5 pages, 2022.

Hindawi
Computational and Mathematical Methods in Medicine
Volume 2023, Article ID 9896832, 1 page
https://doi.org/10.1155/2023/9896832

Retraction

Retracted: Effects of Pelvic Floor Muscle Massage on the Pregnancy Outcome of Frozen Embryo Transfer in Patients with Thin Endometrium

Computational and Mathematical Methods in Medicine

Received 3 October 2023; Accepted 3 October 2023; Published 4 October 2023

This article has been retracted by Hindawi following an investigation undertaken by the publisher [1]. This investigation has uncovered evidence of one or more of the following indicators of systematic manipulation of the publication process:

(1) Discrepancies in scope

(2) Discrepancies in the description of the research reported

(3) Discrepancies between the availability of data and the research described

(4) Inappropriate citations

(5) Incoherent, meaningless and/or irrelevant content included in the article

(6) Peer-review manipulation

The presence of these indicators undermines our confidence in the integrity of the article's content and we cannot, therefore, vouch for its reliability. Please note that this notice is intended solely to alert readers that the content of this article is unreliable. We have not investigated whether authors were aware of or involved in the systematic manipulation of the publication process.

Wiley and Hindawi regrets that the usual quality checks did not identify these issues before publication and have since put additional measures in place to safeguard research integrity.

We wish to credit our own Research Integrity and Research Publishing teams and anonymous and named external researchers and research integrity experts for contributing to this investigation.

The corresponding author, as the representative of all authors, has been given the opportunity to register their agreement or disagreement to this retraction. We have kept a record of any response received.

References

[1] L. Shen, "Effects of Pelvic Floor Muscle Massage on the Pregnancy Outcome of Frozen Embryo Transfer in Patients with Thin Endometrium," *Computational and Mathematical Methods in Medicine*, vol. 2022, Article ID 2803363, 7 pages, 2022.

Hindawi
Computational and Mathematical Methods in Medicine
Volume 2023, Article ID 9839531, 1 page
https://doi.org/10.1155/2023/9839531

Retraction

Retracted: Efficacy of *Ginkgo biloba* Extract Combined with Hormones in the Treatment of Sudden Deafness and Its Effect on the Reactivity of Peripheral Blood T Cell Subsets

Computational and Mathematical Methods in Medicine

Received 3 October 2023; Accepted 3 October 2023; Published 4 October 2023

This article has been retracted by Hindawi following an investigation undertaken by the publisher [1]. This investigation has uncovered evidence of one or more of the following indicators of systematic manipulation of the publication process:

(1) Discrepancies in scope

(2) Discrepancies in the description of the research reported

(3) Discrepancies between the availability of data and the research described

(4) Inappropriate citations

(5) Incoherent, meaningless and/or irrelevant content included in the article

(6) Peer-review manipulation

The presence of these indicators undermines our confidence in the integrity of the article's content and we cannot, therefore, vouch for its reliability. Please note that this notice is intended solely to alert readers that the content of this article is unreliable. We have not investigated whether authors were aware of or involved in the systematic manipulation of the publication process.

Wiley and Hindawi regrets that the usual quality checks did not identify these issues before publication and have since put additional measures in place to safeguard research integrity.

We wish to credit our own Research Integrity and Research Publishing teams and anonymous and named external researchers and research integrity experts for contributing to this investigation.

The corresponding author, as the representative of all authors, has been given the opportunity to register their agreement or disagreement to this retraction. We have kept a record of any response received.

References

[1] Z. Zhu, Q. Wu, G. Hu et al., "Efficacy of *Ginkgo biloba* Extract Combined with Hormones in the Treatment of Sudden Deafness and Its Effect on the Reactivity of Peripheral Blood T Cell Subsets," *Computational and Mathematical Methods in Medicine*, vol. 2022, Article ID 2903808, 10 pages, 2022.

Hindawi
Computational and Mathematical Methods in Medicine
Volume 2023, Article ID 9837485, 1 page
https://doi.org/10.1155/2023/9837485

Retraction

Retracted: Research Progress of B-Cell Lymphoma/Leukemia-2 Inhibitor Combined with Azacytidine in the Targeted Therapy of Acute Myeloid Leukemia

Computational and Mathematical Methods in Medicine

Received 3 October 2023; Accepted 3 October 2023; Published 4 October 2023

This article has been retracted by Hindawi following an investigation undertaken by the publisher [1]. This investigation has uncovered evidence of one or more of the following indicators of systematic manipulation of the publication process:

(1) Discrepancies in scope

(2) Discrepancies in the description of the research reported

(3) Discrepancies between the availability of data and the research described

(4) Inappropriate citations

(5) Incoherent, meaningless and/or irrelevant content included in the article

(6) Peer-review manipulation

The presence of these indicators undermines our confidence in the integrity of the article's content and we cannot, therefore, vouch for its reliability. Please note that this notice is intended solely to alert readers that the content of this article is unreliable. We have not investigated whether authors were aware of or involved in the systematic manipulation of the publication process.

Wiley and Hindawi regrets that the usual quality checks did not identify these issues before publication and have since put additional measures in place to safeguard research integrity.

We wish to credit our own Research Integrity and Research Publishing teams and anonymous and named external researchers and research integrity experts for contributing to this investigation.

The corresponding author, as the representative of all authors, has been given the opportunity to register their agreement or disagreement to this retraction. We have kept a record of any response received.

References

[1] Y. Wang, D. Huang, L. Liu, A. Wang, Y. Gao, and H. Lin, "Research Progress of B-Cell Lymphoma/Leukemia-2 Inhibitor Combined with Azacytidine in the Targeted Therapy of Acute Myeloid Leukemia," *Computational and Mathematical Methods in Medicine*, vol. 2022, Article ID 3992224, 8 pages, 2022.

Hindawi
Computational and Mathematical Methods in Medicine
Volume 2023, Article ID 9827631, 1 page
https://doi.org/10.1155/2023/9827631

Retraction

Retracted: Lentinan Enhances the Function of Oxaliplatin on the Esophageal Tumors by Persuading Immunogenic Cell Death

Computational and Mathematical Methods in Medicine

Received 3 October 2023; Accepted 3 October 2023; Published 4 October 2023

This article has been retracted by Hindawi following an investigation undertaken by the publisher [1]. This investigation has uncovered evidence of one or more of the following indicators of systematic manipulation of the publication process:

(1) Discrepancies in scope

(2) Discrepancies in the description of the research reported

(3) Discrepancies between the availability of data and the research described

(4) Inappropriate citations

(5) Incoherent, meaningless and/or irrelevant content included in the article

(6) Peer-review manipulation

The presence of these indicators undermines our confidence in the integrity of the article's content and we cannot, therefore, vouch for its reliability. Please note that this notice is intended solely to alert readers that the content of this article is unreliable. We have not investigated whether authors were aware of or involved in the systematic manipulation of the publication process.

Wiley and Hindawi regrets that the usual quality checks did not identify these issues before publication and have since put additional measures in place to safeguard research integrity.

We wish to credit our own Research Integrity and Research Publishing teams and anonymous and named external researchers and research integrity experts for contributing to this investigation.

The corresponding author, as the representative of all authors, has been given the opportunity to register their agreement or disagreement to this retraction. We have kept a record of any response received.

References

[1] X. Huo, Z. Pei, W. Wang et al., "Lentinan Enhances the Function of Oxaliplatin on the Esophageal Tumors by Persuading Immunogenic Cell Death," *Computational and Mathematical Methods in Medicine*, vol. 2022, Article ID 2296574, 9 pages, 2022.

Hindawi
Computational and Mathematical Methods in Medicine
Volume 2023, Article ID 9807987, 1 page
https://doi.org/10.1155/2023/9807987

Retraction

Retracted: Construction and Evaluation of Neural Network Correlation Model between Syndrome Elements and Physical and Chemical Indexes of Unstable Angina Pectoris Complicated with Anxiety

Computational and Mathematical Methods in Medicine

Received 3 October 2023; Accepted 3 October 2023; Published 4 October 2023

This article has been retracted by Hindawi following an investigation undertaken by the publisher [1]. This investigation has uncovered evidence of one or more of the following indicators of systematic manipulation of the publication process:

(1) Discrepancies in scope

(2) Discrepancies in the description of the research reported

(3) Discrepancies between the availability of data and the research described

(4) Inappropriate citations

(5) Incoherent, meaningless and/or irrelevant content included in the article

(6) Peer-review manipulation

The presence of these indicators undermines our confidence in the integrity of the article's content and we cannot, therefore, vouch for its reliability. Please note that this notice is intended solely to alert readers that the content of this article is unreliable. We have not investigated whether authors were aware of or involved in the systematic manipulation of the publication process.

Wiley and Hindawi regrets that the usual quality checks did not identify these issues before publication and have since put additional measures in place to safeguard research integrity.

We wish to credit our own Research Integrity and Research Publishing teams and anonymous and named external researchers and research integrity experts for contributing to this investigation.

The corresponding author, as the representative of all authors, has been given the opportunity to register their agreement or disagreement to this retraction. We have kept a record of any response received.

References

[1] X. Chen, Y. Wang, L. Zhang, and X. Xu, "Construction and Evaluation of Neural Network Correlation Model between Syndrome Elements and Physical and Chemical Indexes of Unstable Angina Pectoris Complicated with Anxiety," *Computational and Mathematical Methods in Medicine*, vol. 2022, Article ID 6217186, 11 pages, 2022.

Hindawi
Computational and Mathematical Methods in Medicine
Volume 2023, Article ID 9795242, 1 page
https://doi.org/10.1155/2023/9795242

Retraction

Retracted: A Three-Dimensional Cement Quantification Method for Decision Prediction of Vertebral Recompression after Vertebroplasty

Computational and Mathematical Methods in Medicine

Received 3 October 2023; Accepted 3 October 2023; Published 4 October 2023

This article has been retracted by Hindawi following an investigation undertaken by the publisher [1]. This investigation has uncovered evidence of one or more of the following indicators of systematic manipulation of the publication process:

(1) Discrepancies in scope

(2) Discrepancies in the description of the research reported

(3) Discrepancies between the availability of data and the research described

(4) Inappropriate citations

(5) Incoherent, meaningless and/or irrelevant content included in the article

(6) Peer-review manipulation

The presence of these indicators undermines our confidence in the integrity of the article's content and we cannot, therefore, vouch for its reliability. Please note that this notice is intended solely to alert readers that the content of this article is unreliable. We have not investigated whether authors were aware of or involved in the systematic manipulation of the publication process.

Wiley and Hindawi regrets that the usual quality checks did not identify these issues before publication and have since put additional measures in place to safeguard research integrity.

We wish to credit our own Research Integrity and Research Publishing teams and anonymous and named external researchers and research integrity experts for contributing to this investigation.

The corresponding author, as the representative of all authors, has been given the opportunity to register their agreement or disagreement to this retraction. We have kept a record of any response received.

References

[1] Y. Zhang, T. Zhang, X. Ge et al., "A Three-Dimensional Cement Quantification Method for Decision Prediction of Vertebral Recompression after Vertebroplasty," *Computational and Mathematical Methods in Medicine*, vol. 2022, Article ID 2330472, 14 pages, 2022.

Hindawi
Computational and Mathematical Methods in Medicine
Volume 2023, Article ID 9861647, 1 page
https://doi.org/10.1155/2023/9861647

Retraction

Retracted: What Promotes Medical Overuse: Perspective on Evolutionary Game between Administration and Medical Institutions

Computational and Mathematical Methods in Medicine

Received 15 August 2023; Accepted 15 August 2023; Published 16 August 2023

This article has been retracted by Hindawi following an investigation undertaken by the publisher [1]. This investigation has uncovered evidence of one or more of the following indicators of systematic manipulation of the publication process:

(1) Discrepancies in scope

(2) Discrepancies in the description of the research reported

(3) Discrepancies between the availability of data and the research described

(4) Inappropriate citations

(5) Incoherent, meaningless and/or irrelevant content included in the article

(6) Peer-review manipulation

The presence of these indicators undermines our confidence in the integrity of the article's content and we cannot, therefore, vouch for its reliability. Please note that this notice is intended solely to alert readers that the content of this article is unreliable. We have not investigated whether authors were aware of or involved in the systematic manipulation of the publication process.

Wiley and Hindawi regrets that the usual quality checks did not identify these issues before publication and have since put additional measures in place to safeguard research integrity.

We wish to credit our own Research Integrity and Research Publishing teams and anonymous and named external researchers and research integrity experts for contributing to this investigation.

The corresponding author, as the representative of all authors, has been given the opportunity to register their agreement or disagreement to this retraction. We have kept a record of any response received.

References

[1] C. Xu, L. Luo, S. Zeng, X. He, J. Li, and G. Zhu, "What Promotes Medical Overuse: Perspective on Evolutionary Game between Administration and Medical Institutions," *Computational and Mathematical Methods in Medicine*, vol. 2022, Article ID 4351282, 15 pages, 2022.

Hindawi
Computational and Mathematical Methods in Medicine
Volume 2023, Article ID 9837485, 1 page
https://doi.org/10.1155/2023/9837485

Retraction

Retracted: Research Progress of B-Cell Lymphoma/Leukemia-2 Inhibitor Combined with Azacytidine in the Targeted Therapy of Acute Myeloid Leukemia

Computational and Mathematical Methods in Medicine

Received 3 October 2023; Accepted 3 October 2023; Published 4 October 2023

This article has been retracted by Hindawi following an investigation undertaken by the publisher [1]. This investigation has uncovered evidence of one or more of the following indicators of systematic manipulation of the publication process:

(1) Discrepancies in scope

(2) Discrepancies in the description of the research reported

(3) Discrepancies between the availability of data and the research described

(4) Inappropriate citations

(5) Incoherent, meaningless and/or irrelevant content included in the article

(6) Peer-review manipulation

The presence of these indicators undermines our confidence in the integrity of the article's content and we cannot, therefore, vouch for its reliability. Please note that this notice is intended solely to alert readers that the content of this article is unreliable. We have not investigated whether authors were aware of or involved in the systematic manipulation of the publication process.

Wiley and Hindawi regrets that the usual quality checks did not identify these issues before publication and have since put additional measures in place to safeguard research integrity.

We wish to credit our own Research Integrity and Research Publishing teams and anonymous and named external researchers and research integrity experts for contributing to this investigation.

The corresponding author, as the representative of all authors, has been given the opportunity to register their agreement or disagreement to this retraction. We have kept a record of any response received.

References

[1] Y. Wang, D. Huang, L. Liu, A. Wang, Y. Gao, and H. Lin, "Research Progress of B-Cell Lymphoma/Leukemia-2 Inhibitor Combined with Azacytidine in the Targeted Therapy of Acute Myeloid Leukemia," *Computational and Mathematical Methods in Medicine*, vol. 2022, Article ID 3992224, 8 pages, 2022.

Hindawi
Computational and Mathematical Methods in Medicine
Volume 2022, Article ID 3992224, 8 pages
https://doi.org/10.1155/2022/3992224

Research Article

Research Progress of B-Cell Lymphoma/Leukemia-2 Inhibitor Combined with Azacytidine in the Targeted Therapy of Acute Myeloid Leukemia

Yanyu Wang, Dan Huang, Lejia Liu, Aixin Wang, Yuan Gao, and Huan Lin

Department of Oncology and Hematology, People's Hospital of Leshan, Leshan 614000, Sichuan Province, China

Correspondence should be addressed to Yanyu Wang; yanyuwang123@sina.com

Received 8 July 2022; Revised 5 September 2022; Accepted 22 September 2022; Published 8 October 2022

Academic Editor: Plácido R. Pinheiro

Objective. To investigate the efficacy and safety of azacytidine and B-cell lymphoma/leukemia-2 inhibitors in the treatment of patients with acute myeloid leukemia (AML) and myelodysplastic syndrome (MDS). *Methods*. The clinical data of 31 patients with AML/MDS who were clearly diagnosed with AML/MDS were analyzed from 2018.10 to 2021.02, and the total amount of azacyclonol and B-cell lymphoma/leukemia-2 inhibitor was used for single or combined chemotherapy, with a total amount of 75 mg/m^{2}*7 d, divided into 7-10 days of continuous subcutaneous injection, every 28-30 days for a course of treatment. Overall response rate (ORR), median survival, poor response, and genetic mutations were observed. *Results*. A total of 104 courses of treatment were completed in 31 patients, the median course was 3 (1–12), and 6 patients who did not complete 2 courses of treatment were not counted in the statistics. After 2 courses, ORR was 72.0%, CRES was 2 (8.0%), mCR was 16 (64.0%), disease stable was 5 (20.0%), treatment failures were 2 (8.0%), mortality was 40.0%, and median survival time was >5 months. Single-agent and combined ORR was 64.3% and 81.8%, respectively, with median survival of 7.25 and 9 months; ORR for MDS and AML was 66.7% and 76.9%, respectively, median survival of 8 and 11 months was 66.7% and 80.0% of ORRs at 260 and V60 years, respectively, and median survival of 7 and 11.5 months; MDS-EB-1. The ORR of MDS-EB-2 was 75.0% and 62.5%, respectively, with median survival times of 11.5 and 6.5 months. During 2 courses and 4 courses, the rate of transfusion dependence was 64.0% and 55.5%, respectively. Fifteen cases were detected by second-generation sequencing, and the results were 14 cases of combined gene mutations. *Conclusion*. Azacytidine and B-cell lymphoma/leukemia-2 inhibitors have good efficacy and high safety in the treatment of AML and MDS, and the combined treatment is better than that of monotherapy, but the side effects of combination therapy are large.

1. Introduction

Acute myelogenous leukemia (AML) is a heterogeneous hematological malignancy characterized by clonal expansion of myeloid blast cells in peripheral blood, bone marrow, and/or other tissues [1, 2]. Clinical manifestations are mainly associated with inhibition of normal hematopoietic function and abnormal primitive and naïve cell infiltration of extramedullary tissues and organs, and the typical symptoms are fever, bleeding, anemia, hepatosplenomegaly, and lymphadenopathy. Myelodysplastic syndromes (MDS) are bone marrow stem cell diseases characterized by ineffective hematopoietic function, pancytopenia, and progressive bone marrow failure that have been discovered with the development of AML. According to statistics, the median age of patients diagnosed with AML is 68 years, while the median age of patients with confirmed MDS is more than 70 years [3].

Therefore, with the aging of the population, the incidence of the two is gradually increasing. Azacytidine and B-cell lymphoma/leukemia-2 inhibitors are demethylated drugs belonging to cytosine nucleotide analogues that kill tumor cells by inducing DNA demethylation and direct cytotoxic effects on bone marrow hematopoietic cells. Azacytidine is recommended for first-line treatment in elderly AML patients who are not suitable for intensive treatment regimens, and some studies have shown a combination of

azacytidine and B-cell lymphoma/leukemia-2 inhibitors. Compared with other approved therapies, azacytidine and B-cell lymphoma/leukemia-2 inhibitors can prolong the overall survival to a similar or greater extent and are less toxic [4]. There are reports of clinical experience and results of the use of azacytidine and B-cell lymphoma/leukemia-2 inhibitors similar to those seen in clinical trials. All in all, azacytidine and B-cell lymphoma/leukemia-2 inhibitors abroad have been used as first-line drugs for the treatment of AML and high-risk MDS, while the domestic is currently mainly used to treat high-risk intermediate-risk-2 MDS in the international prognostic scoring system of patients with AML and chronic myelogenous leukemia.

In recent years, some new drugs targeted therapy for AML have been listed [5, 6] as FMS-like tyrosine kinase 3 inhibitors, sorafenib, and platelet-derived growth factor receptor a/0 (PDGFRa/0) inhibitor. Crenolanib has yielded good results in clinical trials of AML. In a variety of AML-targeted therapies [7], direct stimulation of the mitochondrial apoptosis pathway of cancer cells is a new therapeutic strategy. This pathway is regulated by the Bcl-2 gene protein family, which overexpresses tumor cells to evade apoptosis and become resistant to a variety of antineoplastic drugs [8]. Inhibiting the expression of Bcl-2 family proteins inhibits the formation of tumor neovascularization, thereby inhibiting tumor metastasis. Therefore, targeting Bcl-2 family proteins can inhibit tumor occurrence, development, and drug resistance, and Bcl-2 inhibitors become novel drugs that induce apoptosis of tumor cells. This article has reviewed the research progress of Bcl-2 inhibitors in AML-targeted therapy.

2. Information and Methods

2.1. General Information. In 2018.10-2021.02, our hospital clearly diagnosed AML/MDS which applies azacytidine and B-cell lymphoma/leukemia-2 inhibitors. Of the 31 patients treated, the cell smear method was used to detect bone marrow cell morphology, flow cytology to detect immunophenotyping, cell culture to detect cytogenetics, and second-generation sequencing to detect molecules. PCR fusion genes are detected by the method: Patient-Based 2016 WHO-AML/WHO-MDS Diagnostic Criteria Guidelines [9]. The prognosis grouping is based on the revision of the International Prognosis Scoring System (IPSS-R).

The inclusion criteria were as follows: (1) patient age 218 years, (2) at least 2 courses of chemotherapy, and (3) confirmed diagnosis 2016 WHO Diagnostic criteria guidelines.

The median age of 31 patients was 63 (29-86) years, with AML 18 cases and MDS 13 cases: 13 males and 18 females, 21 cases over the age of 60 years (260), and 10 cases below 60 years of age (<60 years); 2016 WHO-AML/WHO-MDS Diagnostic Criteria for typing were as follows: M5b 11 cases, M2a 5 examples, M4a 1 case, mixed cell type 1 case, and MDS-EB-2 8 examples, MDS-EB-1 5 cases. MDS Reference IPSS-R Grouping were as follows: 1 case in the very low-risk group, 3 cases in the low-risk group, 4 cases in the medium-risk group, and 5 cases in the high-risk group. In addition, 15 cases were detected for genetic mutations by second-generation sequencing [10]. This study obtained the consent of the patient and his/her family and signed the Informed Information Form, which was also proved by the ethical committee of people's Hospital of Leshan.

2.2. Treatment. 31 patients with azacytidine and B-cell lymphoma/leukemia-2 inhibitor monotherapy or combination chemotherapy include 22 cases of Vidasa (Baxter Oncology GmbH, registration number H20170238, specification 100 mg/bottle) and 9 cases of Weishou (produced by Chia Tai Tianqing Pharmaceutical Group Co., Ltd., registration certificate number H20193278, specification 100 mg/bottle), which has the total dose of 75 mg/m^{2}*7 d, divided into 7-10 days of continuous subcutaneous injection, every 28-30 days for 1 course. There were 20 cases of monotherapy and 11 cases of combination therapy, including 4 cases of combined thalidomide and ubenemex, 2 cases of ubenmez, half of HAG cytidine, high spinel, and recombinant human granulocyte colony stimulator, and lenalidomide, venetok, cytarabine, dasatinib, and vermatinib mesylate of 1 case each [11]. During the treatment process, effective measures such as symptomatic stomach preservation, heart preservation, liver protection, alkalinization, and prevention of vomiting are also given to support and prevent; when hemoglobin V60 g/L, the infusion of filtered white red blood cell suspension is given as appropriate, and when the platelet count is V20*10^{9}/L, platelet transfusion and hemostatic sensitivity are appropriate to prevent bleeding; when infectious symptoms such as fever occur, routine improvement is routinely perfect CRP, procalcitonin, and blood bacteria cultures of both upper extremities, along with symptomatic antipyretics and antibiotic anti-inflammatory therapy [12].

2.3. Indicators and Efficacy and Safety Assessment. Adopted in fiscal 2006 MDS International Clinical Working Group (IWG 2006), efficacy evaluation criteria are judged, which mainly include complete remission (complete remission, CR), partial mitigation (partial remission, PR), bone marrow remission (marrow CR, mCR), hematology improved (hematological improve, HI) disease stabilization, and treatment failure: (1) CR: blast cells in the bone marrow < 5.0% simultaneously satisfy all cell lines with normal, peripheral blood neutrophil counts 21.0*10^{9}/L, hemoglobin 2110 g/L, platelet count 2100*10^{9}/L, and blast cells 0%; (2) mCR: the content of blast cells in the bone marrow < 5.0% decreases by 50.0% compared to before treatment, but if the peripheral blood reaches HIS, it could also be indicated; (3) PR: absolute peripheral blood values should be maintained for at least 2 months, with other requirements meeting the criteria for complete remission (in patients who are abnormal before treatment), but the total number of blast cells in the bone marrow is only 50.0% less than the overall number before treatment and still exceeds 5.0% regardless of the degree and morphology of cell proliferation; and (4) CR or PR recurrence after recurrence: at least one of the following should be included: (1) the proportion of bone marrow blast cells has returned to the proportion before chemotherapy; (2) the decrease in hemoglobin exceeds 15 g/L or rely entirely on blood transfusions; (3) 250.0% reduction in

platelet or granulocyte count compared to optimal efficacy; (5) disease stability does not meet the minimum criteria for partial remission, but there is no evidence of progression of the disease for at least 8 weeks; (6) treatment failure: the patient dies or progresses with disease while receiving treatment development includes exacerbation of decreased blood cells, an increase in the proportion of blast cells in the bone marrow or the development of more severe than before treatment FAB subtypes; (7) HI: patients are assessed for hematological improvement based on the results of blood cell analysis and a decrease in red blood cell transfusion; and (8) total remission rate (overall response rate, ORR) = (CR + PR + mCR)/total number of patients*100%. Adverse reactions occur during chemotherapy, see WHO evaluation criteria for indexes for the evaluation of adverse drug reactions during acute and subacute chemotherapy [13], which mainly include hematological toxicity and nonhematogenous, blood toxicity mainly such as decreased white blood cells, platelets, granulocytes, and decreased hemoglobin; nonhematogenous has gastrointestinal tract, liver function damage, kidneys, bladder, heart and nervous system abnormal symptoms, and positive signs, for the results of genetic mutations, the basis IWG 2006 efficacy evaluation criteria, and comprehensive analysis of gene polymorphisms for azacytidine treatment AML/MDS effects of efficacy and prognosis.

2.4. Statistical Analysis. Continuous normally distributed data are expressed as the means ± SDs. Statistical calculations were carried out using SPSS statistical software. Multiple comparisons were analyzed via analysis of variance (ANOVA) with the Tukey-Kramer multiple comparisons test. P values <0.05 were considered significant.

3. Result

3.1. Information of the Patients of This Study. A total of 104 courses of treatment were completed in the 31 patients of this study, the median course was 3 (1–12), and 6 patients who did not complete 2 courses of treatment were not counted in the statistics. The remaining 25 patients completed a total of 98 courses, with a median treatment course of 3 (2–12), 9 patients completed 4 courses, and 2 patients completed 6 courses. After 2 sessions, the ORR was 72.0% (18/25), with 2 CRES (8.0%), 16 mCR (64.0%), 5 patients with HI, 5 disease stable (20.0%), and 2 treatment failures (8.0%). The ORR of MDS was 66.7% (8/12), with CR 1 case (8.3%), mCR 7 cases (58.3%), and partner. In 1 case of HI, 4 cases (33.3%) were stable, the ORR of AML was 76.9% (10/13), and the CR1 case (7.7%) was mCR. There were 9 cases (69.2%), 4 cases with HI, 1 case (7.7%) with stable disease, and 2 cases (15.4%) who failed treatment. ORR over 60 years of age was 66.7% (10/15), with 10 mCR patients (66.7%), 3 patients with HI, and 5 patients (33.3%) that were treated stably; younger than 60 years of age, treatment failed treatment with 80.0% (8/10) ORR, 2 cases (20.0%), 6 cases (60.0%), 2 cases with HI, and example (20.0%) (see Table 1). For young and middle-aged patients, 2 patients did not undergo hematopoietic stem cell transplantation due to death in the later treatment process, and the remaining 8 patients refused due to economic problems. After 4 courses of treatment, the ORR was 77.8% (7/9), with 7 cases of mCR, 3 cases with HI, 1 case of recurrence after HI, and 2 cases of stable disease. After 6 courses of treatment, there were 2 cases of mCR and 1 case with HI. Followed up to 1 February 2021, the death toll was 10, the mortality rate was 40.0% (10/25), the median survival time was >5 (3–22) months, MDS and AML median survival was 8 (3–22) and 11 (3–19) months, respectively, and median survival times were 7 (3–22) and 11.5 (3–17) months at over and below 60 years. During 25 patients who received 2 courses of chemotherapy, 16 patients required blood transfusion products for support treatment, and the transfusion dependence rate reached 64%; during 9 patients receiving 4 courses of chemotherapy [14], only 5 patients needed blood transfusion products, and the transfusion dependence rate reached 55.5%.

Table 1: Information of patients of this study.

Courses of treatment	Patients	Median course	HI	Disease stable	Treatment failures
104	31	3 (1-12)	5	5	2

3.2. Prognosis of Azacytidine and B-Cell Lymphoma/Leukemia-2 Inhibitors in the Treatment of MDS/AML. Among the 25 patients counted in this study, 14 were treated with monotherapy, with ORR of 64.3% (9/14), CR was 2 (14.3%), mCR was 7 (50.0%), and HI was 2. In patients, 2 patients (14.3%) have stable disease (21.4%), median survival time was 7.25 (3–19) months, 11 patients have combined therapy, ORR was 81.8% (9/11), mCR9 (81.8%), with HI three patients, and 2 patients with stable disease (18.2%), and the median survival time was 9 (4.5-22) months. In 8 cases treated with AML monotherapy, the ORR was 62.5% (5/8), CR was 1 case, mCR was 4 cases, and the patient was accompanied by HI with 2 patients, 1 patient with stable disease, 2 patients with treatment failure, median survival time of 6.25 (3–17) months, and 5 patients with combined therapy, ORR was 100% (5/5), and mCR5 patients. In 2 cases of HI, the median survival time was 13 (8.5-19) months. MDS monotherapy was 6 patients, ORR was 66.7% (4/6), CR was 1 case, mCR was 3 cases, disease stabilization have 2 patients, and median survival is 7.75 (4.5-22) months; 6 patients were treated with a combination of 6 cases, ORR was 66.7% (4/6), mCR was 4 cases, and 1 case was accompanied by HI [15].

The disease was stable in 2 cases with a median survival time of 10 (3–19) months. Based on disease typing analysis, MDS-EB-1 was 4 cases, ORR was 75.0% (3/4), CR was 1 case, mCR was 2 cases, and accompaniment was HI1. In one case, the median survival time was 11.5 (6–22) months for 1 case with disease stabilization, the MDS-EB-2 was 8 cases, the ORR was 62.5% (5/8), and the mCR was 5. In 3 cases, the disease was stable, and the median survival time was 6.5 (3 to 19) months. AML-M2a was 3 patients, ORR was 66.7% (2/3), mCR was 2 patients, treatment failure was 1 patient, the median survival time was 3 (3–14) months

AML-M5b was 8 cases, ORR was 75.0% (6/8), CR was 1 case, and mCR was 5 cases, with HI 3 cases, one patient was stable, one patient was treated failed, and the median survival time was 12 (3–17) months, see Table 2.

3.3. Gene Mutations of Azacytidine and B-Cell Lymphoma/Leukemia-2 Inhibitors in the Treatment of MDS/AML. Fifteen patients were tested for gene mutations by second-generation sequencing, and the results were 14 combined mutations, including 11 TET2 mutations, 6 ASXL1 mutations (5 combined TET2 mutations), NPM1, and DNMT3A. There were 4 cases of mutations, there were 3 cases of U2AF1, NRAS, and IDH2 mutations, there were 2 cases of RUNX1, IDH1, and IDH1 CEBPA, FLT3-ITD and GATA mutations each in 2 cases: ETV6 and SF3B1, and there was 1 mutation each of KRAS, SETBP1, BCOR, PHF6, and MLL. TET2 mutation ORR was 54.5% (6/11), CR was 2 patients, mCR was 4 patients, with HI. In 2 cases, 4 patients were stable, and 1 patient failed treatment; ASXL1 mutation ORR was 66.7% (4/6), CR was 1 patient, and mCR was 3 cases. In 1 case, with 1 case of HI, 1 case of disease stabilization, and 1 case of treatment failure, TET2 with ASXL1 mutation ORR was 80.0% (4/5). 1 case of CR, 3 cases of mCR, 1 case with HI, and 1 case of stable disease were as follows. As of February 1, 2021, the above median survival times were 13 (3–22), 11 (8.5-22), and 13 (8.5-22) months, respectively. There were 9 cases of MDS comutation, ORR was 55.5% (5/9), CR was 1 case, mCR was 4 cases, with HI 1 patient, disease stable 4 patients, median survival time > AML comorbid mutation 5 patients, ORR of 60.0% (3/5), mCR 3 patients with 1 case of HI, and 2 cases of treatment failure, and the median survival time was 13 (3–14) months, see Table 3.

4. Discussion

AML is predominantly occurring in older adults and is mostly unsuitable for intensive therapy, due to a variety of poor prognostic factors, including a high proportion of poor cytogenetics, changes associated with myelodysplastic abnormalities, a high ECOG-PS score, and a combination of severe underlying disease [16]. The active ingredient of azacytidine and B-cell lymphoma/leukemia-2 inhibitors binds to RNA and DNA by interfering with RNA transcription and DNA of actively proliferating cells. Methyltransferase I is active and exerts its cytotoxic effect. Initially, it was thought that the main antitumor activity of azacytidine and B-cell lymphoma/leukemia-2 inhibitors was to interfere with nucleic acid metabolism and has a direct cytotoxic effect. Subsequently, however, azacytidine and B-cell lymphoma/leukemia-2 inhibitors have been shown to have preferential toxicity to proliferating malignant tumor cells but no toxic effect on normal cells. Subsequent studies have found that azacytidine and B-cell lymphoma/leukemia-2 inhibitors have other anticancer effects in addition to direct cytotoxicity, the most notable of which include targeting DNA hypermethylation, which is thought to help inhibit tumorigenesis and disrupt the maturation and differentiation of bone marrow cells [17]. In the pharmacokinetic study of azacytidine and B-cell lymphoma/leukemia-2 inhibitors, since the drug is only effective in proliferating cells and does not accumulate, a shorter treatment time per week is unlikely to cause azacytidine and B-cell lymphoma/leukemia-2 inhibitors to encounter at S Phase of all malignant cloned cells, which will demonstrate a higher efficacy with longer treatment per cycle [18].

The ORR of the two courses of this study was 72.0%, the median survival time was 8.5 months, the ORR of MDS and AML was 66.7% and 76.9%, respectively, and the median survival time was 8 and 11 months, respectively, suggesting that azacytidine improved the overall response rate of patients. It prolongs a certain amount of survival time. In a Canadian CCO study on the efficacy of azacytidine on AML/MDS, the ORR was 28.0%, and the median survival time was 11.6 months [19]. AZA-001 studies showed that azacytidine and B-cell lymphoma/leukemia-2 inhibitors had an ORR of 29.0% and a median survival of 24.5 for treatment of high-risk MDS months; AZA-AML-001 study [16] shows ORR in the treatment of AML patients with azacytidine and B-cell lymphoma/leukemia-2 inhibitors. At 27.8%, the median survival time was 10.8 months, which was an improvement in response rate compared with traditional supportive care, and azacytidine significantly improved patients' objective response rate, survival rate, and clinical outcome. The primary survival time in this study is relatively short, which is inconsistent with the above foreign studies, mainly because some patients are enrolled late and the follow-up time is too short, and the follow-up time of 6 patients is only about 3 months. The total response rate of this study is higher than that of foreign studies, and the reasons for the analysis may be related to the following factors; first of all, the number of samples studied in this paper is too small; secondly, the selection of enrollment objects is different, the CCO study enrollment objects are IPSS score medium-risk-2 and high-risk MDS and bone marrow blastocyst ratio 20-30% of patients with AML, and the patients enrolled in this article only need to meet the WHO 2016 diagnostic criteria, including patients with bone marrow blast cells > 30% and IPSS-R scores for each risk stratification; then, the length of treatment cycles varies, and this article only covers 2 courses, and 4 efficacy was evaluated after each session, with a median of 3 sessions compared with 6 and 9 for the CCO study and AZA-001, respectively. Again, the median age in the CCO study may be 74 years (19-99 years), possibly due to the difference in median age. AZA-001 is 69 years (42-83 years old) compared to the median age of 63 years (29-86 years) in this study; there may also be differences in treatment regimens, with 11 cases of combination therapy in this article resulting in a high overall response rate, compared with CCO and AZA-001. All patients enrolled in the group were monotherapy, but it did not exclude the difference in sensitivity to drugs and the difference in drug metabolism in domestic and foreign patients. The Rowe study [17] showed an ORR of 48.0% and a median survival time of 9.6 months, concluding that azacytidine appeared to be right WHO-AML has a good efficacy; although, IWG 2006 is not currently considered the standard form of AML efficacy assessment, but disease stabilization and HI are considered to continue to be used criteria

Table 2: Baseline features of 25 patients with AML/MDS.

Serial number	Gender	Age	FAB classification	IPSS-R	Score ECOG score	Transfusion dependence	Previous treatment
1	Man	71	M4a	—	1	Not	Not
2	Man	75	M5b	—	4	Not	Not
3	Woman	59	Hybrid	—	3	Be	Not
4	Woman	55	M5b	—	1	Be	Not
5	Woman	29	M2a	—	0	Be	Not
6	Woman	50	M5b	—	2	Be	Not
7	Woman	68	M5b	—	2	Be	Not
8	Woman	68	M5b	—	1	Not	Not
9	Man	45	M5b	—	1	Not	Not
10	Woman	62	M5b	—	1	Be	Not
11	Woman	58	M5b	—	0	Not	Not
12	Woman	63	M2a	—	1	Be	Not
13	Woman	80	M2a	—	2	Not	Not
14	Woman	64	MDS-EB-2	Risk	4	Be	Not
15	Woman	66	MDS-EB-2	Very low risk	2	Be	Not
16	Man	67	MDS-EB-1	Low risk	1	Not	Not
17	Man	68	MDS-EB-2	Medium-risk	1	Be	Not
18	Man	73	MDS-EB-2	Low risk	1	Be	Not
19	Man	53	MDS-EB-1	Medium-risk	2	Not	Not
20	Woman	57	MDS-EB-2	Risk	4	Be	Not
21	Woman	71	MDS-EB-1	Risk	3	Be	Not
22	Woman	60	MDS-EB-2	Medium-risk	3	Not	Not
23	Man	51	MDS-EB-1	Risk	2	Be	Not
24	Woman	65	MDS-EB-2	Low risk	1	Be	Not
25	Man	48	MDS-EB-2	Risk	3	Be	Not

Table 3: Comparison of reported results of azacytidine and B-cell lymphoma/leukemia-2 inhibitors in the treatment of MDS/AML.

Test code name	Number	Of patients of median age pa /years	/people	Total response rate/%	Median survival time/month
This article investigates	AML/MDS	63	31	72.0	8.5
AZA-001	High-risk MDS	70	179	29.0	24.5
AZA-AML-001	265 years old AML	75	241	27.8	10.8
CCO	High-risk MDS/AML	74	1101	28.0	11.6
Pleyer	High-risk MDS/AML	73	302	48.0	9.6

for efficacy of azacytidine and B-cell lymphoma/leukemia-2 inhibitor therapy. In this paper, the ORR was 72.0% after 2 courses and 77.8% after 4 courses, indicating that the effective rate of patients increased with the prolongation of the treatment cycle, which is consistent with foreign related studies [18]. Azacytidine and B-cell lymphoma/leukemia-2 inhibitors' long-term chemotherapy can significantly improve patient survival outcomes. And patients with CR and PR should be appropriately extended chemotherapy, and treatment should be continued as long as the patient continues to benefit. In this article, the ORR for MDS is 66.7%, the ORR for AML is 76.9%, and the results show AML. The overall response rate was higher than that of MDS, indicating that the efficacy of azacytidine in the treatment of AML may be better than that of MDS, but the results of this study are inconsistent with the above domestic and foreign studies. The main reason may be that the sample size in this article is too small to cause the results to be different. Finally, the ORR of MDS-EB-1 in this paper was 75.0%, with a median survival time of 11.5 months and ORR of MDS-EB-2. It was 62.5% with a median survival time of 6.5 (3–19) months, suggesting that azacytidine and B-cell lymphoma/leukemia-2 inhibitors may be more effective than MDS-EB-2 in the treatment of MDS-EB-2. This seems to be consistent with the

results of the study of Pichler et al. abroad. Therefore, azacytidine and B-cell lymphoma/leukemia-2 inhibitors are more effective in the treatment of AML/MDS [20].

In this study, the ORR of azacytidine and B-cell lymphoma/leukemia-2 inhibitor was 64.3%, the median survival time was 7.25 months, the ORR of the combination was 81.8%, and the median survival time was 9 months. Among them, AML single-agent ORR was 62.5%, median survival time was 6.25 months, combined ORR was 100%, and median survival time was 13 months. The ORR was 66.7%, the median survival was 7.75 months, the combined ORR was 66.7%, and the median survival time was 10 months. For adverse reactions, the incidence of hematoxicity of grades III-IV was 90.9% during combination therapy, and there were 3 cases of lung infection, 5 cases of liver function impairment, 2 cases of renal function impairment, 7 cases of hypoalbuminemia, and 2 cases of hyperuricemia; during monotherapy, the incidence of grade III-IV hematoxicity was 85.7%, and there were 3 cases of lung infection, 2 cases of liver function impairment, 1 case of renal function damage, and 3 examples of hypoalbuminemia. As can be seen above, the combined treatment of azacytidine and B-cell lymphoma/leukemia-2 inhibitors may be more effective than monotherapy, but the side effects of combination therapy are large, and others have found the receiving azacytidine and B-cell lymphoma. Patients treated with leukemia-2 inhibitors in combination with venetoclax had a longer overall survival and a higher incidence of remission than patients treated with azacytidine and B-cell lymphoma/leukemia-2 inhibitors alone. The incidence of febrile neutropenia was higher in the group than in the control group [21]. There is one azacytidine and B-cell lymphoma/leukemia-2 inhibitor combined with thalidomide for the treatment of clinically advanced MDS, CMML, and AML. The results of the phase II study [21–23] ORR was 63.0%, the overall survival was 28.1 months, and the nonhematotoxicity was grade III or higher 85.0%, indicating that combination therapy is good and that treatment is tolerated. This paper is consistent with the conclusions of relevant foreign studies, and all reflect the combination of azacytidine and B-cell lymphoma/leukemia-2 inhibitors with good efficacy, but the drug toxicity is greater.

The TET2 gene is located on chromosome 4q24, and the ASXL1 gene is located in chromosome 20qll, both of which are involved in the epigenetic and regulation of DNA. ASXL1 encodes an internal nuclear protein of 1541 amino acids and has transcriptional functions, which typically causes the C-terminus of the protein upstream of pPhD to be truncated, resulting in loss of gene function. TET2, on the other hand, is involved in the epigenetic regulation of DNA through the conversion of 5-methylcytosine to 5-hydroxycytosine. Multiple studies have shown that mutations in genes such as TET2 and ASXL1 are factors of poor prognosis, significantly shortening progression-free survival (PFS) and overall survival. In an evaluation study on TET2 gene mutation prediction of responses of MDS patients to demethylated drugs, the results showed Bejar et al. and Itzykson. The findings of the two authors were consistent, with ORRs of 55.0% and 52.0%, respectively, and it was concluded that TET2 deletion appeared to make tumor cells more sensitive in vivo to azacytidine and B-cell lymphoma/leukemia-2 inhibitors. TET2 mutations are more likely to identify patients who respond to the demethylated drug cocozacyanin. In this study, the TET2 mutation ORR was 54.5%, the median survival time was 13 months, the ASXL1 mutation ORR was 66.7%, the median survival time was 11 months, and the results were more consistent with foreign countries, indicating that although prognosis is poor in patients with AML/MDS mutations in TET2 and ASXL1 genes, treatment with azacytidine and B-cell lymphoma/leukemia-2 inhibitors may improve overall response rates and median survival, patient outcomes, and quality of life. Thus, azacytidine and B-cell lymphoma/leukemia-2 inhibitors may improve efficacy in patients with AML/MDS with genetic mutations [22].

In this study, 25 patients had different degrees of bone marrow suppression during chemotherapy, the incidence of grade III-IV hematogenous toxicity was 88.0%, the incidence of grade II hematogenousness was 12.0%, and most of them significantly improved after symptomatic support therapy. All patients experienced nausea and vomiting, with 1 case developed constipation and 2 cases developed diarrhea, supplemented by symptomatic antiemetic, laxative, and antidiarrheal treatment, symptoms were relieved, and no further gastrointestinal symptoms were developed. Foreign studies by Pleyer et al. showed that the incidence of grade III-IV hematoxicity was 48.0%, and III-IV grade neutrophilia, thrombocytopenia, and hemoglobin decreases were 35.0%, 30.0%, and 28.0%, respectively; the most common nonhemotoxicity was fatigue, gastrointestinal manifestations, unexplained pain, and erythema at the injection site. In this paper, 13 patients had fever, including 6 cases of fever with lung infection, the infection rate was 24.0%, the symptoms were basically alleviated after antibiotic treatment, and the chest CT showed that the inflammation was significantly reduced compared with before. The infection rate of the foreign AGMT research group was 33.0%, which was mainly manifested by pulmonary infection, sepsis, and other fever with unclear etiology, which was significantly higher than the results of this study. A systematic review and meta-analysis showed that the use of azacytidine and B-cell lymphoma/leukemia-2 inhibitors was associated with an increased risk of decreased neutrophil counts and platelet counts in patients with MDS/AML, and that azacytidine and B-cell lymphoma/leukemia-2 inhibitors did not significantly increase high anemia, leukopenia, or febrile neutrality compared with traditional supportive care risk of agranulocytosis [22]. In this study, 3 cases of renal function impairment and 7 cases of liver function damage appeared, and foreign studies found that adverse reactions such as elevated serum creatinine occurred during the application of azacytidine and B-cell lymphoma/leukemia-2 inhibitors; so, biochemical indicators such as liver and kidney function should be closely monitored during the chemotherapy process [23]. Nonhematogenousness is found to cause patients to develop symptoms of the heart system, mainly manifested as left ventricular failure, arrhythmias, hypertension, myocardial infarction, and angina. However, the above adverse reactions

in the heart did not occur in this paper; therefore, in the treatment process, it is also necessary to improve the ECG and cardiac color ultrasound and monitor the cardiac enzyme profile and brain natriuretic peptides and other cardiac indicators. The transfusion dependence rate in 2 sessions of this study was 64.0%, and the transfusion dependence rate in 4 sessions was 55.5%. The results of the CCO study showed that the transfusion dependence rate of 354 patients receiving less than 4 cycles of treatment was 73.2%, the transfusion dependence rate of 692 patients receiving more than 4 cycles of treatment was 60.0%, and it was concluded that with the prolonged chemotherapy cycle time, the transfusion dependence rate of patients decreased and the safety increased. Therefore, azacytidine and B-cell lymphoma/leukemia-2 inhibitors are better off in the treatment of AML/MDS [24, 25].

5. Conclusion

In summary, the treatment of azacytidine and B-cell lymphoma/leukemia-2 inhibitors in AML/MDS can improve certain efficacy and has good safety, and the combination treatment is better than that of single drugs, but the side effects of combination drugs are large. However, the number of cases studied in this paper is small, and the sample size needs to be increased to further investigate the efficacy and safety of azacytidine and B-cell lymphoma/leukemia-2 inhibitors.

Data Availability

The data used to support this study is available from the corresponding author upon request.

Conflicts of Interest

The authors declare that they have no conflicts of interest.

Authors' Contributions

Yanyu Wang and Dan Huang contributed equally to this work.

References

[1] E. K. Abdalhabib, D. E. Jackson, B. Alzahrani et al., "Combined GSTT1 null, GSTM1 null and XPD Lys/Lys genetic polymorphisms and their association with increased risk of chronic myeloid leukemia," *Pharmacogenomics and Personalized Medicine*, vol. 14, pp. 1661–1667, 2021.

[2] E. Andretta, C. Costa, C. Longobardi et al., "Potential approaches versus approved or developing chronic myeloid leukemia therapy," *Frontiers in Oncology*, vol. 11, article 801779, 2021.

[3] R. Ciftciler and I. C. Haznedaroglu, "Tailored tyrosine kinase inhibitor (TKI) treatment of chronic myeloid leukemia (CML) based on current evidence," *European Review for Medical and Pharmacological Sciences*, vol. 25, no. 24, pp. 7787–7798, 2021.

[4] S. El Hussein, C. D. DiNardo, K. Takahashi et al., "Acquired WT1 mutations contribute to relapse of NPM1-mutated acute myeloid leukemia following allogeneic hematopoietic stem cell transplant," *Bone Marrow Transplantation*, vol. 57, no. 3, pp. 370–376, 2022.

[5] A. H. Elsayed, X. Cao, A. K. Mitra et al., "Polygenic Ara-C response score identifies pediatric patients with acute myeloid leukemia in need of chemotherapy augmentation," *Journal of Clinical Oncology*, vol. 40, no. 7, article JCO2101422, 2022.

[6] A. Grenier, L. Poulain, J. Mondesir et al., "AMPK-PERK axis represses oxidative metabolism and enhances apoptotic priming of mitochondria in acute myeloid leukemia," *Cell Reports*, vol. 38, no. 1, article 110197, 2022.

[7] K. Harada, S. Mizuno, S. Yano et al., "Donor lymphocyte infusion after haploidentical hematopoietic stem cell transplantation for acute myeloid leukemia," *Annals of Hematology*, vol. 101, no. 3, pp. 643–653, 2022.

[8] G. Jia, X. Jiang, Z. Li et al., "Decoding the mechanism of Shen Qi Sha Bai Decoction in treating acute myeloid leukemia based on network pharmacology and molecular docking," *Frontiers in Cell and Development Biology*, vol. 9, article 796757, 2021.

[9] Y. Kaito, M. Hirano, M. Futami et al., "CD155 and CD112 as possible therapeutic targets of FLT3 inhibitors for acute myeloid leukemia," *Oncology Letters*, vol. 23, p. 51, 2021.

[10] N. Keren-Froim, G. Heering, G. Sharvit et al., "ELN 2017 classification significantly impacts the risk of early death in acute myeloid leukemia patients receiving intensive induction chemotherapy," *Annals of Hematology*, vol. 101, no. 2, pp. 309–316, 2022.

[11] L. Largeaud, S. Bertoli, E. Bérard et al., "Genomic landscape of hyperleukocytic acute myeloid leukemia," *Blood Cancer Journal*, vol. 12, no. 1, p. 4, 2022.

[12] M. Y. Li, C. Zhao, L. Chen et al., "Quantitative proteomic analysis of plasma exosomes to identify the candidate biomarker of imatinib resistance in chronic myeloid leukemia patients," *Frontiers in Oncology*, vol. 11, article 779567, 2021.

[13] W. Y. Lin, S. E. Fordham, E. Hungate et al., "Author correction: genome-wide association study identifies susceptibility loci for acute myeloid leukemia," *Nature Communications*, vol. 13, no. 1, p. 2, 2022.

[14] J. A. Moore, J. J. Mistry, C. Hellmich et al., "LC3-associated phagocytosis in bone marrow macrophages suppresses acute myeloid leukemia progression through STING activation," *The Journal of Clinical Investigation*, vol. 132, no. 5, 2022.

[15] Y. Numan, Z. Abdel Rahman, J. Grenet et al., "Gilteritinib clinical activity in relapsed/refractory FLT3 mutated acute myeloid leukemia previously treated with FLT3 inhibitors," *American Journal of Hematology*, vol. 97, no. 3, pp. 322–328, 2022.

[16] P. K. Reville, K. Sasaki, H. M. Kantarjian et al., "Improved outcomes among newly diagnosed patients with FMS-like tyrosine kinase 3 internal tandem duplication mutated acute myeloid leukemia treated with contemporary therapy: revisiting the European LeukemiaNet adverse risk classification," *American Journal of Hematology*, vol. 97, no. 3, pp. 329–337, 2022.

[17] J. M. Rowe, "The "7+3" regimen in acute myeloid leukemia," *Haematologica*, vol. 107, no. 1, p. 3, 2022.

[18] M. Salek, N. Oak, M. R. Hines et al., "Development of BRAFV600E-positive acute myeloid leukemia in a patient on long-term dabrafenib for multisystem LCH," *Blood Advances*, vol. 6, no. 8, pp. 2681–2684, 2022.

[19] J. Schetelig, H. Baldauf, L. Koster et al., "Corrigendum: haplotype motif-based models for KIR-genotype informed selection

Hindawi
Computational and Mathematical Methods in Medicine
Volume 2023, Article ID 9872930, 1 page
https://doi.org/10.1155/2023/9872930

Retraction

Retracted: Improving the Use of Blockchain Technology in Stroke Care Information Management Systems

Computational and Mathematical Methods in Medicine

Received 17 October 2023; Accepted 17 October 2023; Published 18 October 2023

This article has been retracted by Hindawi following an investigation undertaken by the publisher [1]. This investigation has uncovered evidence of one or more of the following indicators of systematic manipulation of the publication process:

(1) Discrepancies in scope

(2) Discrepancies in the description of the research reported

(3) Discrepancies between the availability of data and the research described

(4) Inappropriate citations

(5) Incoherent, meaningless and/or irrelevant content included in the article

(6) Peer-review manipulation

The presence of these indicators undermines our confidence in the integrity of the article's content and we cannot, therefore, vouch for its reliability. Please note that this notice is intended solely to alert readers that the content of this article is unreliable. We have not investigated whether authors were aware of or involved in the systematic manipulation of the publication process.

Wiley and Hindawi regrets that the usual quality checks did not identify these issues before publication and have since put additional measures in place to safeguard research integrity.

We wish to credit our own Research Integrity and Research Publishing teams and anonymous and named external researchers and research integrity experts for contributing to this investigation.

The corresponding author, as the representative of all authors, has been given the opportunity to register their agreement or disagreement to this retraction. We have kept a record of any response received.

References

[1] Y. Yang, A. Song, Q. Chang et al., "Improving the Use of Blockchain Technology in Stroke Care Information Management Systems," *Computational and Mathematical Methods in Medicine*, vol. 2022, Article ID 2642841, 9 pages, 2022.

Hindawi
Computational and Mathematical Methods in Medicine
Volume 2022, Article ID 2642841, 9 pages
https://doi.org/10.1155/2022/2642841

Research Article

Improving the Use of Blockchain Technology in Stroke Care Information Management Systems

Yuying Yang,[1] Aixia Song,[2] Qing Chang,[2] Hongmei Zhao,[1] Weidan Kong,[2] Qian Xue,[2] and Qianlong Xue[3]

[1]*Stroke Office, The First Affiliated Hospital of Hebei North University, Zhangjiakou, Hebei 075000, China*
[2]*Department of Neurology, The First Affiliated Hospital of Hebei North University, Zhangjiakou, Hebei 075000, China*
[3]*Emergency Department, The First Affiliated Hospital of Hebei North University, Zhangjiakou, Hebei 075000, China*

Correspondence should be addressed to Aixia Song; 202006000333@hceb.edu.cn

Received 24 June 2022; Revised 14 July 2022; Accepted 22 July 2022; Published 26 September 2022

Academic Editor: Plácido R. Pinheiro

Blockchain is a new and popular technology in the digital age. Blockchain technology is referred to as decentralised and distributed digital ledgers, which are called blocks. These blocks are linked together with the cryptographic hashes and are used to record transactions between many computers. No single block can be altered without altering the related blocks. Modification of individual block data is impossible because each block contains information from the previous block. This is the unique strength of blockchain. Timestamps and hashes are some of the important terms when blockchains are considered. Data security is guaranteed with this advanced technology. Blockchain technology finds its application in the healthcare industry with many advantages in a queue. Medical data can be transferred safely and securely for fool-proof management of the medicine supply chain, which helps in healthcare research. Blockchains are used to securely encrypt a patient's information in the event of an outbreak of a pandemic disease. A stroke is referred to as a brain attack, also called cerebral infarction. A cerebral infarction is a sudden stoppage of blood flow in the blood vessels connected to the brain. This study focused on evaluating the application of blockchain technology in Stroke Nursing Information Management Systems. This emerging technology is already in use in the healthcare industry. The patient's data is kept decentralized, transparent, and mainly incorruptible, thus keeping it secured and sharing of data is quick.

1. Introduction

Validation and storage are performed using the blockchain data structure. Consensus methods and distributed nodes are typically used together to generate and update data. Both data transit and access are protected by encryption. Smart contracts, which are automated script codes, are being used to build and modify the blockchain [1]. It fosters trust in an untrustworthy competitive atmosphere while costing very little, and blockchain technology is seen as a breakthrough development in computing. As a result of the rapid advancement of new technology, industries all around the world have been reorganised [2]. The blockchain, which is increasingly being used by other firms, is built on encrypted digital currency. It is becoming increasingly clear that blockchain technology has the potential to revolutionise several industries, including medicine and healthcare. Because of blockchain technology, people could witness a major shift in how medical records are processed. Among the many benefits of storing data in a decentralised manner are increased trust, information security, and individual privacy [3]. When it comes to this new technology, there are so many ways in which it may be applied.

One of the hottest blockchain study areas right now is electronic medical data processing. A blockchain can be used to store electronic medical records. If all medical data were kept on the blockchain, it would place a greater load on the network's compute and storage resources [4]. These concerns can be avoided by using a hybrid storage architecture that keeps medical data in a database, and only the index of that data on a distributed ledger like blockchain, which can then be used to locate the data. To help diagnose e-

health systems, they came up with the notion of using two different types of distributed ledgers: a private and a consortium blockchain [5]. Custom data structures and consensus methods are required for both types of blockchain. The Electronic Health Record (EHR) sharing protocol was built on two types of blockchains: a private blockchain to store EHRs and a consortium blockchain to store safe indices of EHRs [6]. The privacy and security of patients' medical records must be safeguarded if blockchain technology is to be used. Authorized users can securely exchange data thanks to the blockchain's encryption capabilities. They established a blockchain-based system that enables patients, healthcare professionals, and third parties to securely, interoperatively, and quickly access medical data [7]. The use of smart contracts and cutting-edge encryption methods on an Ethereum-based blockchain has improved data security [8].

Because there is no trusted central authority on the blockchain network, consensus is extremely difficult to achieve. [9]. Prior to encrypting the material, the researchers were able to verify Proof of Word and interoperability for blockchain-based data discovery and access [10]. According to the researchers, the PBFT algorithm was used to construct a blockchain-based solution for patient-to-researcher transfers that maintains privacy [11]. As long as a distributed consensus is in place, medical data can be transmitted safely. A smart contract could be created by utilising the framework. Using hospitals and clinics as miners and verifiers, the Proof of Authenticity consensus method is used [12]. The Hyper Ledger Fabric open-source project uses an open-source framework to implement a permissioned blockchain and provides scalable applications, such as identity verification, peer-to-peer protocol, access control, consensus algorithm, and smart contracts, to support blockchain use cases in electronic medical records sharing [13]. Hyperledger Fabric-based Blockchains can be utilised to govern the use of a mobile health application [14].

There are a few studies on this topic, but blockchain technology has sparked the interest of researchers interested in managing electronic medical data [15]. Despite the importance of technical inquiry into the difficulties of blockchain technology, nothing has been said about the concept, connotation, and management approaches for the expansion of electronic medical records in the contemporary technological environment. For blockchain solutions, the present literature lacks an integrated research framework that focuses on a specific technological difficulty, such as protecting privacy in electronic medical records or improving consensus algorithms [16]. For the most part, blockchain systems are built only on the basis of computer simulations, with no thought given to how they would be used in the real world. According to the findings of the researchers, while considering legal and regulatory limits, very little thought was given to how the answer might be applied in real industrial settings [17, 18]. Although there are numerous ways in which blockchain technology might improve the integrity and efficiency of electronic medical records, the technology itself is not the most significant component of the process.

According to the findings provided here, ERMR data may be shared securely across a distributed network using blockchain technology [19]. This is the first study of its kind. The study's blockchain-based medical data sharing system also has two other features: system controllability and data security levels. With blockchain technology, ERMR administration may be made easier and more cost-effective by addressing the question of how ERMR can be safely shared and gathered while addressing practical issues. There has been a positive impact on healthcare technology and efficiency because of the conclusions of this study [20]. Additionally, this article uses advanced computer technology to provide an industry reference path and to design and develop a path that would help lead to specific blockchain applications in the healthcare and medical industries. Blockchain is more than simply a piece of information technology; it is a unique blend of existing data storage and transmission technologies, like decentralised databases and point-to-point links, with novel algorithms for consensus and encryption [21]. As an alternative to traditional methods of distributing ERMRs, it offers the advantages of open source and programmability, as well as distributed storage and partial decentralisation [22]. Using a peer-to-peer network architecture, the nodes of the blockchain network are connected together. Since the distributed storage system does not have a central node, each of the distributed storage nodes has a copy of all the data [23]. Since all nodes in the system have access to the block data, the blockchain is a distributed and decentralised database. In the blockchain, a data structure organises and stores data. Two new blocks are created when a block's header and body are separated. The block timestamp and difficulty are two pieces of information included in the block header that are necessary when constructing a Merkle tree. A Merkle tree structure is used to store the block's data transactions. Perform hash operations in pairs on all of the leaf nodes to get to the Merkle tree's root [24]. The hash algorithm is a key component of the blockchain. Block transaction data can be obscured by generating a series of hash values with a defined length using the hash function, which is a general term for various different hashing methods (akin to garbled codes). Many algorithms, such as SHA-256, can convert any transaction data string into a 64-character string. People will never be able to figure out what the initial hashing algorithm was [25]. This means that it can be used to protect both personal information and sensitive data by encrypting them, so it can do this. Multifactor Authentication (MFA) including Elliptical Curve Cryptography is compared to the standard technique of conducting online transactions in the suggested framework (ECC). The performance evaluation demonstrates that the proposed framework is both secure and efficient, requiring less time and money to execute encryption and decryption. The reduced computational time is evaluated with a sample dataset to validate the suggested work [26].

2. Materials and Methods

In Stroke Nursing, the management of medical information is an important task represented in Figure 1. Safety and security are considered to be important points to be taken care of. The medical data of the patient like treatment taken,

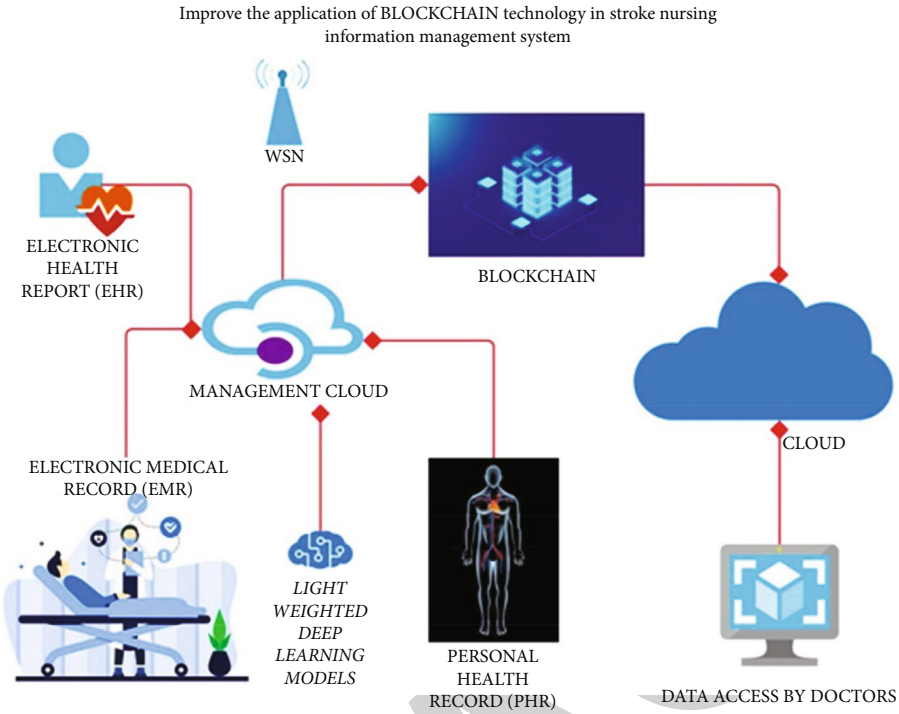

Figure 1: Architecture diagram of the proposed system.

medical reports like Electronic Medical Record (EMR), Personal Health Reports (PHR), Electronic Health Report (EHR) are fed into the management cloud. These information are formed into blocks in the blockchain phase. The hospitals are well equipped with wireless sensor networks (WSN). The wireless networking technology helps in sharing the data to the cloud. Light-weighted Deep Learning Models are deployed in transferring the written and typed medical information to the blockchain. The Natural Language Processing (NLP) algorithm is used along with Deep Learning Models for this purpose.

The patient's data are securely encrypted with the help of blockchain. The blockchain data can be accessed from the cloud by the users (patients, doctors, healthcare staff, nurses). Blockchain technology provides an improved way of sharing medical data in a secured manner. The digital health records are securely stored and accessed by authorized users. The identity of the patient is protected in this case. The administration process is well automated by establishing secured contracts between the patients and hospitals with the help of blockchain. The safe arrival of drug shipment and prevention of counterfeit medicines. The blockchains monitor diseases and reports in the case of an outbreak of a pandemic.

Light-Weighted Deep Learning Models are used to predict stroke in patients. Tests like EEG, ECG, and EMG use the sensor technologies to diagnose the patients in treating stroke. The patient's brain activity is monitored with an electroencephalogram (EEG). It is a test that detects electrical activity of the brain using small electrodes attached to the scalp. Electromyography (EMG) is referred to as a process used to measure the activity of the muscle in response to nervous stimulations. An electrocardiogram (ECG) uses sensors that were taped to the chest, arms and legs. The sensors measure the heartbeat. The signals are depicted in a wave pattern that can be monitored on a computer screen. The data from these sensor technology devices are collected and sent through the WSN network to the cloud. The data in the cloud is analysed and stroke prediction is done with the help of AI. These data are sent to the medical practitioners who in turn act quickly and treat the patient immediately. Thus blockchain technology improves the Stroke Nursing Information Management system.

2.1. Proposed Work. A neural system identifies the $g[k, k+1]$ operation as part of the confidence earned via stroke prediction neural network interpretation. Using the period of time given by k and also the framework conditions $k+1$, this should provide $g(k+1)$. A stochastic modification module not only increases the authority of the stroke prediction neural network function and g is the anticipated possibility of judgments with $g(k)$ but it also provides a finished result. These definitions are given as.

$$m'(k) = \sum_{k+1}^{d} d\left(m(k) + \sum_{g=1}^{k} g[k, k+1]\right). \tag{1}$$

The stroke prediction neural network rule unit n_i is organized for evaluate the stroke prediction neural network guideline. The data $m(k)$ device is a standard predecessor that receives a unit. Unit $g=1$ communicates with the behaviour control. The process is completed with a neutralized combination.

Signs and weightlifting are actual values with input nodes. These indicators are unaffected by the data. The result is substantially equal to the data. The signal n_i may collaborate with truck full to s_i to create such objects as.

$$g = \sum s_i n_i + \sum_{g=1}^{k} g[k, k+1] \quad i = 1, 2. \tag{2}$$

In order to implement the data, necessary data input FL is gathered as.

$$\mathrm{FL} = \sum_{g \longrightarrow n}^{s} g_1 + g_2 = \sum_{k=1}^{s=1} s_1 k_1 + s_2 k_2. \tag{3}$$

The neuron uses its transfer work $f(y)$ to calculate the FL is neural network production, which could be a sigmoid function result $f(y) = (1 + e^{-y})^{-1}$ is calculated as.

$$f(y) = \sum f(\mathrm{FL}) = \int f(s_1 k_1 + s_2 k_2) + \sum_{g \longrightarrow n}^{s} g_1 + g_2. \tag{4}$$

An ordinary deep network is a simple neural net that makes use of redundancy, inclusion, and the sigmoid function $f(\mathrm{FL})$.

A set of stroke prediction neural networks was defined for the decision support system employed during DL-based digital stroke nursing information management and system records. These are based on both factual data and stroke prediction neural network information. The following are some neural network examples.

Because, when $G = 1$ completing activities, this mode command technology not only uses the point of entry and the available spectrum and data transfer but it also transmits $h_{(i)}$ web access.

$$s_i^g = \sum_{G=1}^{Y} \alpha_i R \log\left(1 + \frac{\left|g_{i,n}\right|^2 Y_{i,n} g^{-n}}{\sigma^2}\right) + \sum f(\mathrm{FL}). \tag{5}$$

In the Equation (5), i denotes its percentage of internet connectivity bandwidth inhabited by terminal update specific assignments, $g_{i,n}$ denotes the connection downturn transformation function between access point and terminal; and $Y_{i,n}$ denotes terminal products, g^{-n} denotes node facility distance, b denotes news team loss, and σ^2 denotes interaction noise level. Similarly, the efficiency of g_i downlink data transfer is defined as.

$$d_i^k = \sum_{g=1}^{X} \beta_i B \log\left(1 + \frac{\left|g_{n,i}\right|^2 X_n g^{-b}}{\sigma^2}\right) + \sum_{i=1}^{s} s_i^g + \sum_{i=1}^{n} \left|g_{n,i}\right|^2 X_n g^{-b}, \tag{6}$$

which, the β_i represents the proportion of the throughput frequency range occupied by a terminal capable of receiving tasks, $g_{n,i}$ represents the link economic downturn correlation between entry point and terminal, and X_n represents the foundation network's connection speed.

The fundamental goal of optimizing an online healthcare system based on edge devices is to achieve the task information technology offload framework with the shortest time delay, which is constituted of two bits: digital technology time delay solely on local and frame clients.

If task n_i also is not offloaded to a network edge, it is approximated on the gateway as well. The time difference between doing the jobs geographically is denoted as.

$$X_i^n = \sum_{k=1}^{n} \frac{g_i}{g_i^k} + \left|g_{n,i}\right|^2 X_n g^{-b} + \sum_{i=1}^{n=1} \frac{\left|g_{n,i}\right|^2 X_n g^{-b}}{\sigma^2}. \tag{7}$$

In where g_i^k signifies the terminal g_i communication processing's ability to organise tasks regionally. As a result, the entire time delay identified by g_i researchers at the local scale is depicted as.

$$g_i^m = \sum_{m \in g} (1 - \alpha_i) g_i^m + \sum_{k=1}^{n} \frac{g_i}{g_i^k} + \left|g_{n,i}\right|^2 X_n g^{-b}. \tag{8}$$

Therefore in situation, we connect the approaching information to a neuron using various activities including a t-norm or even a n_i-conorm; these results are calculated using Equation (9) which can be termed as a hybrid artificial neuron.

$$g_i^n = \sum_{i=1}^{n=1} \frac{m_i}{g_i^n} + \sum_{k=1}^{n} \frac{g_i}{g_i^k} + \left|g_{n,i}\right|^2 X_n g^{-b}. \tag{9}$$

As a result of these modifications, stroke prediction neural network neural planning is dependent on stroke prediction neural network increasing computational. As shown in the graph, the frequency band delay time is proportional to the amount of data obtained and also the network capacity for data transfer function.

$$g_i^n = \sum_{i=1}^{k} \frac{g_i}{b_i^k} + \sum_{m \in g} (1 - \alpha_i) g_i^m. \tag{10}$$

A set of neural networks was described for stroke nursing information management with health system of care employed in deep learning based stroke nursing information management with health system care. These have been backed not only by facts but also by stroke prediction neural network data, and the server's calculation time is comparable to a magnitude of a clear stands and the server's computing capabilities:

$$b_i^f = \sum_{i=1}^{X} \frac{f_i}{X_i} + \sum_{i=1}^{n} \left(1 + \frac{\left|g_{i,n}\right|^2 Y_{i,n} g^{-n}}{\sigma^2}\right). \tag{11}$$

A temperature sensor is a small chip that measures the body's temperature in degrees Celsius. The temperature is

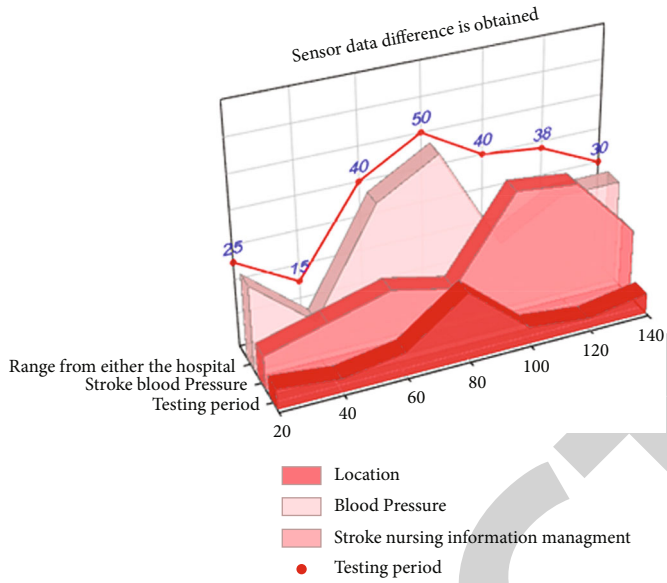

Figure 2: Performance analysis for sensor data difference is obtained in stroke nursing identification for the blood pressure.

displayed in this framework of body temperature controller which is expected to function far better than a linear temperature controller. As a result, the time spent offloading assignment s_i to the edge devices is sent as.

$$s_i^n = \sum_{i=1}^{s=1} s_i^c + s_i^h + s_i^f + \sum_{G=1}^{Y} \alpha_i R \log\left(1 + \frac{\left|g_{i,n}\right|^2 Y_{i,n} g^{-n}}{\sigma^2}\right). \tag{12}$$

Respiratory arrest, cardiac condition, vagal convulsion, and the pressure gauge are all monitored urgent requirements. As a consequence, the time duration associated with the task of discharging s_i to the edge device is communicated as.

$$X_i^n = \sum_{i=1}^{n=1} \alpha_i s_i^n + \sum_{i=1}^{s=1} s_i^c + s_i^h + s_i^f. \tag{13}$$

The pulse rate appears to be the most important sign of vital medical behaviour with stroke nursing data management for health-care system fitness. A pulse-rate sensor is the most commonly explored sensor in the field of patient outcomes and management:

$$\min\ g = \sum_{i=1}^{n} (g_i^n + d_i^n) + \sum_{i=1}^{n=1} X_i^n. \tag{14}$$

It is being used to assess pulse rate including more complex disorders such as a heart attack. The sensor activates whenever an object $f1$ places its finger directly on the information display. The outcome is displayed on the input panel:

$$s.t.f1 : \sum_{h_i \in d} m_i \le m_y + m(k) + \sum_{g=1}^{k} g[k, k+1]. \tag{15}$$

Table 1: Result analysis for information on experimental investigation as well as data analysis.

No	Location ID	Stroke nursing information management	Blood pressure selective sample	Stroke testing period
1	Loc-4	19	5	Oct 2021
2	Loc-1	25	3	Nov 2021
3	Loc-7	37	2	Jan-20201
4	Loc-3	48	4	July – 2021
5	Loc-5	33	5	Sep-2021
6	Loc-2	16	3	Aug-2021
7	Loc-6	65	2	Feb – 2021

The deep learning smart stroke nursing information management scheme is necessary for health system care client administration and monitoring. The proposed $f2$ technique (Equation (16)) benefited from a neural network architecture that is simple to use and enforce for decision making.

$$f2 : \sum_{g_i \in d} \alpha_i \le 1 + \sum_{h_i \in d} m_i \le m_y + m(k). \tag{16}$$

The organization of the $f3$, proposed system as in Equation (17), is unusual in that it uses not just sensory data but also a stroke prediction neural network decision-making process.

$$f3 : \sum_{g_i \in d} \beta_i \le 1 + \sum_{h_i \in d} m_i \le m_y + g[k, k+1]. \tag{17}$$

Table 2: Report from the patient information.

Patient data		Sensor information	
Name of the patient	ABC	The body's temperature	99.96°F
CNIC patient	33165674548246	The rate of pulse	87BPM
Address of the patient A	XYZ	High blood pressure	97/140

Since the $f4$ in Equation (18) is to reduce an energy economy's delay time, attractiveness is characterised in terms of the time delay, and reduced time latency corresponds to higher athletic.

$$f4 : \sum_{i=1}^{n=1} m_i^n \geq 0, \forall i \in d + \sum_{i=1}^{d=1} d_i = \frac{1}{g_i}. \quad (18)$$

The Equation (18) is used to compute the d_i strength and endurance value.

3. Result and Discussion

Figure 2 depicts the variance in data acquired by the temperature sensor, pulse rate sensor, and blood pressure sensor. The data distances are also calibrated using Table 1 and Table 2. The input data is captured and calibrated before stroke prediction neural network is utilised to make decisions about the patient's status in the second step. Table 1 displays the scaled output values for the user-entered data.

Cardiac arrest, blood clot, vagal convulsion, and the pulse sensor are all monitored emergency situations. The key determinant for critical health issues as well as skin fitness is heart rate. The pulse rate receiver is the most extensively used and research detector in patient monitoring and safety.

Sensors for temperature, pulse rate as well as blood pressure are used in this technique to assess the patient's condition under analysis (Figure 3). The scheme used a body of knowledge and stroke prediction neural network system for decision support for patient care, supervising as well as management to determine possible circumstances and cures. The stroke prediction neural network technique also tried to improve the performance of this system for patient monitoring and treatment in terms of the time, cost, and workforce consumption.

Within a week of receiving information collected using sensors and transferred via smart device, the patient document measure is generated solely on the server. The data is separated into three sections: patient data, geographical information, and the patient's ailments. Table 2 only contains information about the places where we choose to test the model. Testing will be done in approximately eight different locations. The location of the chosen establishments and the testing time frame range.

The technique incorporates patient monitoring to sensors and offers great precision and efficiency benefits over current systems (Figure 4). The investigation was conducted on a small sample population and proven to be efficient, exact, and purposeful. So far, the technique has been generalized, and it is conceivable to tailor it to more serious conditions such as operating room patients, intensive care patients, newborns, and patients with considerably more complex medical histories.

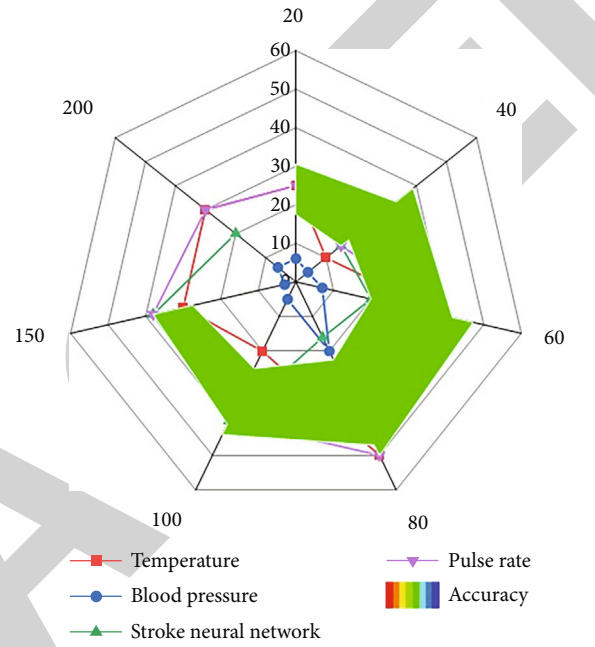

Figure 3: Accuracy of results of stroke prediction with neural networks algorithm based decision making.

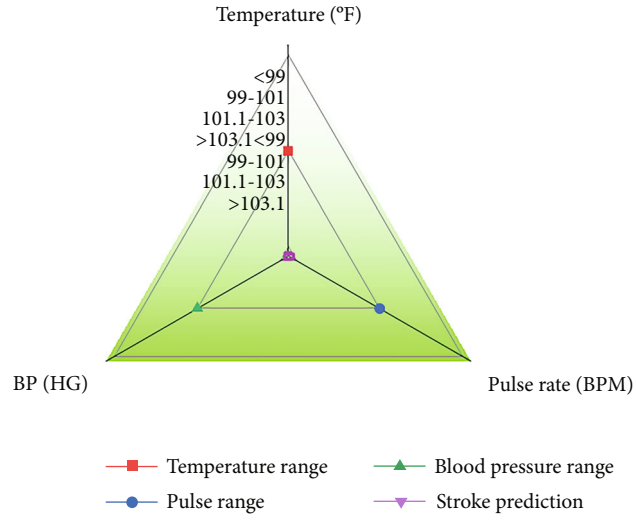

Figure 4: The dependability of the outcomes of neural network-based stroke prediction decisions.

Table 3: Temperature ranges.

Parameters	Temperature ranges	Classes of pulse rate	Classes of blood pressure	Class
Temperature (°F)	<99 99–101 101.1–103 >103.1			There is no fever. Fever A fever is prevalent. Extremely high fever
Pulse rate (NN)		>100 61 to 100 <60		Increased Normal Reduced
BP (HG)			<110/<70 120–110/80–70 120/80 130–139/80–89 >140/>90	Incredibly low Low Ordinary High Extremely high

Temperature ranges ranging from 100°F to 105°F have been used to identify four categories of temperature measurements (there is no fever, fever, a fever is prevalent, and exceptionally high fever). It has three pulse rate classes for a typical human being: low, normal, and high. Low pulse rate is defined as less than 60 beats per minute. Normal pulse rate is described as a pulse rate between 60 and 100. A pulse rate more than 100 is considered to be a high pulse rate. The difference in blood pressure from normal to abnormal is depicted in Table 3. A blood pressure reading of 120/80 mmHg is considered normal. High blood pressure is defined as a pulse rate of 129–140/81–89 BP. Extremely high blood pressure.

A first patient results monitoring and control system that uses a stroke prediction neural network method to identify patients' symptoms as well as prospective therapies (Figure 5). The results in Tables 4 show that when sensors and recommender systems were used, this technique performed well. The neural network system's judgment process increases the method system's efficacy and practicality. This system is distinct in that it makes suitable decisions using sensors and a DL-based architecture.

Table 4 illustrates a patient's information gathered on that website after receiving data collected via sensors and transferred via smart device. The report is broken into three sections: patient data, sensor information, and also the patient's ailments.

The choice is made by the neural network system, and indeed the stroke prediction decision accuracy is measured (Figure 6). The accuracy of the suggested service ranges from 97 percent to 100 percent, according to Table 5. It shown that the proposed system follows the rules defined for patient safety along with managed services decision making.

Also to time it took the general practitioner to respond to the inquiries. The proposed technique is a low-cost and efficient option for those living in rural places; it may be used to detect if they have a major health problem and treat them appropriately by contacting neighboring hospitals. Using detectors and decision support tools in healthcare is a novel approach, and Table 5 demonstrates how it decreases time limitations when compared to typical telemedicine methods. Using blockchain technology in the healthcare sector has many advantages, including decreasing wait times. Medical data can

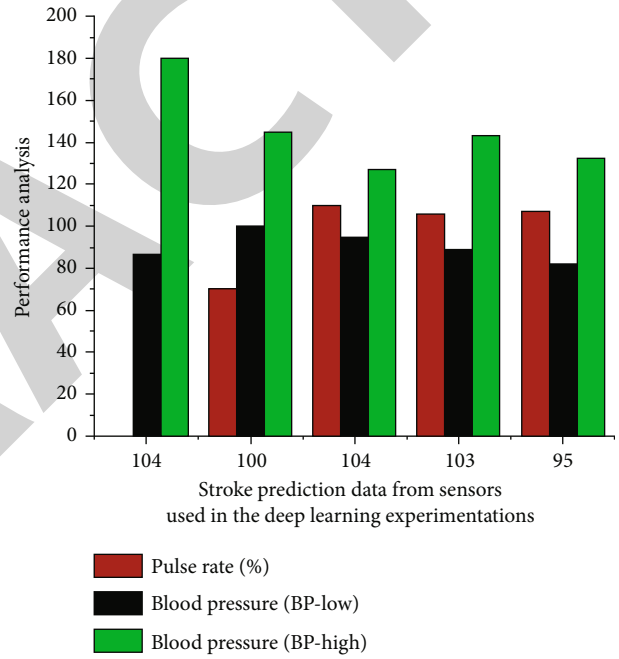

Figure 5: Performance analysis for stroke prediction data from sensors will be used in the deep learning experimentations.

Table 4: Result analysis for stroke prediction data from sensors will be used in the deep learning experimentations.

No	Temperature (°F)	Pulse rate (%)	Blood pressure (BP-low)	Blood pressure (BP-high)
1	104	61-100	87	180
2	100	70	100	145
3	104	110	95	127
4	103	106	89	143
5	95	107	82	132

be transmitted safely and reliably in healthcare research to guarantee an error-free medication supply chain. Blockchain can be used to securely encrypt patient data in the event of a pandemic disease outbreak. A stroke is a type of brain attack,

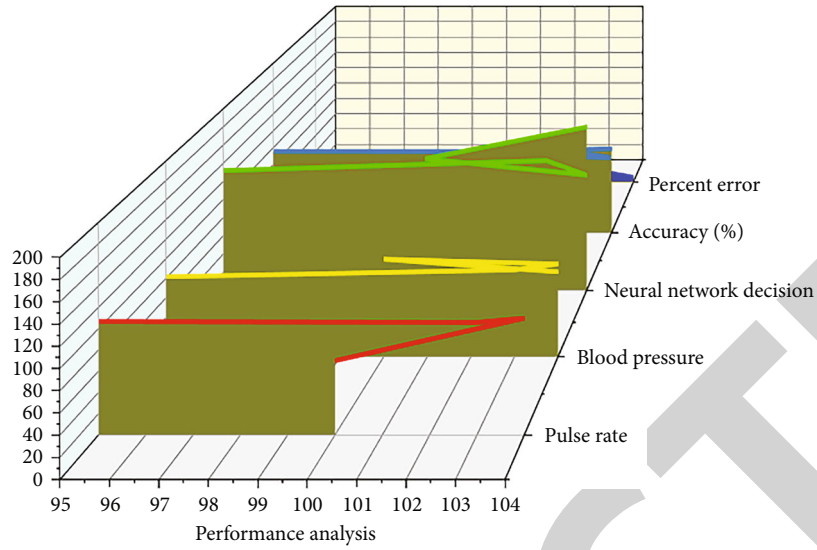

Figure 6: The outcomes of decision-making based on stroke prediction neural network.

Table 5: Stroke prediction sensor data measurement using a neural network technique.

No	Temperature	Pulse rate	Blood pressure	Neural network decision	Accuracy (%)	Percent error (%)
1	Normal	High	Low	High	99.43	4.6
2	High	Normal	High	Medium	94.32	6.6
3	Normal	High	Medium	Low	88.64	6.5
4	Low	Low	Low	Low	95.88	14.64
5	High	High	High	High	96.42	12.99
6	Normal	Medium	Medium	High	98.98	8.4
7	Medium	Low	Low	Medium	94.66	9.5
8	Very high	High	High	Low	93.97	8.65
9	Medium	High	Low	High	88.65	9.65
10	Very high	Medium	Low	Low	87.98	9.35

often known as an infarction. A cerebral infarction is an abrupt stoppage of blood flow in the brain's arteries. The inquiry into the application of blockchain technology in this article focuses on stroke nursing information management systems.

4. Conclusions

The digital age has given rise to a new and popular technology is called blockchain. Decentralized digital ledgers, or blocks are used to describe blockchain technology. The cryptographic hashes link these blocks together, allowing them to serve as a record of transactions involving multiple machines. When discussing blockchain, concepts like timestamps and hashes are critical. With this cutting-edge technology, you can rest assured that your data is safe. There are numerous benefits to using blockchain technology in the healthcare industry, such as reducing wait times. In healthcare research, medical data can be sent securely and reliably to ensure a flawless supply chain for medicines. In the case of a pandemic illness breakout, patient data can be encrypted securely using blockchains. A brain assault or infarction is referred to as a stroke. A sudden halt in blood flow in the brain's arteries is known as a cerebral infarction. Stroke nursing information management systems are the focus of this article's investigation into the use of blockchain technology. This study helps in analysing the security aspects of storing patient information in stroke nursing. The results shown that the proposed system follows the rules defined for patient safety along with managed services decision making.

Data Availability

The data used to support the findings of this study are available from the corresponding author upon request.

Conflicts of Interest

The authors declare that there are no conflicts of interest.

Acknowledgments

This work was supported by Study on the value of stroke management model in the early treatment of ischaemic stroke (Project No. 1921065D).

Hindawi
Computational and Mathematical Methods in Medicine
Volume 2023, Article ID 9839531, 1 page
https://doi.org/10.1155/2023/9839531

Retraction

Retracted: Efficacy of *Ginkgo biloba* Extract Combined with Hormones in the Treatment of Sudden Deafness and Its Effect on the Reactivity of Peripheral Blood T Cell Subsets

Computational and Mathematical Methods in Medicine

Received 3 October 2023; Accepted 3 October 2023; Published 4 October 2023

This article has been retracted by Hindawi following an investigation undertaken by the publisher [1]. This investigation has uncovered evidence of one or more of the following indicators of systematic manipulation of the publication process:

(1) Discrepancies in scope

(2) Discrepancies in the description of the research reported

(3) Discrepancies between the availability of data and the research described

(4) Inappropriate citations

(5) Incoherent, meaningless and/or irrelevant content included in the article

(6) Peer-review manipulation

The presence of these indicators undermines our confidence in the integrity of the article's content and we cannot, therefore, vouch for its reliability. Please note that this notice is intended solely to alert readers that the content of this article is unreliable. We have not investigated whether authors were aware of or involved in the systematic manipulation of the publication process.

Wiley and Hindawi regrets that the usual quality checks did not identify these issues before publication and have since put additional measures in place to safeguard research integrity.

We wish to credit our own Research Integrity and Research Publishing teams and anonymous and named external researchers and research integrity experts for contributing to this investigation.

The corresponding author, as the representative of all authors, has been given the opportunity to register their agreement or disagreement to this retraction. We have kept a record of any response received.

References

[1] Z. Zhu, Q. Wu, G. Hu et al., "Efficacy of *Ginkgo biloba* Extract Combined with Hormones in the Treatment of Sudden Deafness and Its Effect on the Reactivity of Peripheral Blood T Cell Subsets," *Computational and Mathematical Methods in Medicine*, vol. 2022, Article ID 2903808, 10 pages, 2022.

Hindawi
Computational and Mathematical Methods in Medicine
Volume 2022, Article ID 2903808, 10 pages
https://doi.org/10.1155/2022/2903808

Research Article

Efficacy of *Ginkgo biloba* Extract Combined with Hormones in the Treatment of Sudden Deafness and Its Effect on the Reactivity of Peripheral Blood T Cell Subsets

Zhenhua Zhu, Qi Wu, Ge Hu, Xianwen Wang, Wei Chang, Ji Bin, and Weili Yang

Otolaryngology-Wide Head and Neck Surgery Department, The First Affiliated Hospital of Hunan University of Traditional Chinese Medicine, Changsha, 410007 Hunan, China

Correspondence should be addressed to Zhenhua Zhu; 202013000604@hceb.edu.cn

Received 24 June 2022; Revised 15 July 2022; Accepted 20 July 2022; Published 26 September 2022

Academic Editor: Plácido R. Pinheiro

This work was aimed at exploring the efficacy of *Ginkgo biloba* extract combined with hormones in the treatment of sudden deafness and the influence on the reactivity of peripheral blood T cell subsets (PBTCSs). In this work, 64 patients with sudden deafness who were treated in The First Affiliated Hospital of Hunan University of Traditional Chinese Medicine from August 2019 to August 2022 were selected as the research objects. The patients were randomly divided into a hormone group (treatment with prednisone acetate, $n = 34$) and a combination group (treatment with Ginkgo-Damole combined with prednisone acetate, $n = 30$). After the two groups of patients were treated in different ways, their efficacy, symptom improvement, changes in blood rheology, and PBTCSs were compared. The total effective rates (TERs) of the hormone group and the combination group were 76.32% and 95.73%, respectively ($P < 0.05$). The fibrinogen contents of the patients in the combination group were obviously lower than those in the hormone group after 5 d, 7 d, and 10 d of treatment ($P < 0.05$). The high blood viscosity (HBV) values of patients in the combination group at 5 d, 7 d, and 10 d after treatment were greatly lower than those in the hormone group ($P < 0.05$). The low blood viscosity (LBV) values after 3 d, 7 d, and 10 d of treatment in the combined group were much lower in contrast to those in the hormone group ($P < 0.05$). The CD3+, CD4+, and CD4+/CD8+ in peripheral blood in the combination group were sharply higher while the CD8+ in the combined group was lower in contrast to the hormone group ($P < 0.05$). There was no visible difference in the incidence of adverse reactions between the two groups of patients after treatment ($P > 0.05$). In conclusion, the combined application of *Ginkgo biloba* extract and hormones could effectively improve the abnormal hemorheological indexes of patients with sudden deafness and effectively relieve the imbalance of PBTCSs, which was safe.

1. Introduction

Sudden deafness, also known as idiopathic deafness, refers to the sudden onset of unexplained sensorineural hearing loss within 72 hours [1]. In the process of diagnosis and treatment, it can be divided into low-frequency descending type, high-frequency descending type, flat descending type, and total deafness type. Different types of patients have different hearing loss and healing conditions [2]. Among them, the recovery rate of patients with low-frequency descending type can reach more than 75% after treatment, and the outcome is good; while the recovery rate of patients with total deafness is less than 20%, the outcome is poor and easy to relapse [3, 4]. At present, the research on the etiology and pathogenesis of sudden deafness has not yet reached a clear conclusion, and it is generally believed that it has a certain correlation with the blood supply disorder of the inner ear and the membranous labyrinth [5]. Studies have found that sudden deafness can be caused by viral or bacterial infections, or by certain obstacles in the human circulatory system [6]. In addition, it may be caused by immune system problems, some foreign pathogens invade the body, causing the body's balance to be disrupted and resulting in the occurrence of sudden deafness [7, 8]. Some patients may

be accompanied by cold symptoms before the onset of sudden deafness, when the virus enters the inner ear, causing infection and inflammation, which may lead to hearing loss [6, 9]. Factors such as high mental stress, mood swings, irregular daily routines, and sleep disturbances may be the triggers for sudden deafness. The onset of the disease is acute, the overall treatment efficiency is low, and the efficacy is highly correlated with the onset time, so it is recommended to diagnose and treat within 1 week of onset [10, 11].

Sudden deafness is generally treated with drugs, including glucocorticoids (methylprednisolone or dexamethasone, etc.), *Ginkgo biloba* extract, nutritive nerve drugs and antioxidants, and fibrinogen-lowering drugs (lowering fibrinogen improves inner ear circulation) [12–14]. Glucocorticoids are more suitable for patients with various types of sudden deafness, exerting anti-inflammatory and antitumor effects, while *Ginkgo biloba* extract is suitable for improving blood circulation in the inner ear and reducing blood viscosity [15]. Studies have found that *Ginkgo biloba* extract has free radical scavenging effects, regulating effects on the circulatory system, and improving hemodynamics and tissue protection. Therefore, it plays a key role in the treatment of sudden deafness [16]. In addition, hyperbaric oxygen can be used as a rescue therapy for patients who have no obvious effect on conventional drug therapy [17].

However, the long-term use of glucocorticoids will affect the metabolism of sugar and fat in the body, causing problems such as hyperglycemia and hyperlipidemia, so it is necessary to strictly follow the doctor's guidance for medication [18]. In addition, patients with underlying diseases such as diabetes and hypertension need regular monitoring during medication and should choose a reasonable and safe medication strategy under the guidance of doctors [19, 20]. At present, a large number of studies have found that both glucocorticoids and *Ginkgo biloba* extracts have obvious curative effects on sudden deafness, but few studies have combined the two drugs, and the safety and efficacy of the combined use are still unclear. Some studies suggest that the occurrence of sudden deafness may be related to the immune status of the body [21]. However, whether it is possible to predict the efficacy of hormone combined with *Ginkgo biloba* extract in the treatment of patients with sudden deafness and the correlation between the two can be determined by detecting the level of T cell subsets in patients' peripheral blood. Therefore, this work selected patients with sudden deafness as the research object for analysis and discussion.

2. Materials and Methods

2.1. Research Objects and Their Grouping. 64 patients with sudden deafness (sudden deafness within 72 hours, unexplained sensorineural hearing loss, and hearing loss in at least two adjacent frequencies ≥20 dBHL) who visited The First Affiliated Hospital of Hunan University of Traditional Chinese Medicine from August 2019 to August 2022 as the research objects. Among them, there were 27 male patients and 37 female patients, aged 20 to 85 years old, with an average age of 34.72 ± 12.15 years old. Patients were randomized into a hormone group (treated with prednisone acetate, $n = 34$) and a combination group (treated with Ginkgo-Damole combined with prednisone acetate, $n = 30$). The experiment was approved by the Medical Ethics Committee of The First Affiliated Hospital of Hunan University of Traditional Chinese Medicine, and the patients and their families understood the research content and methods and agreed to sign the corresponding informed consents.

Patients included had to satisfy the following items: (1) the initial visit time was 1 to 5 days after the onset of the disease; (2) the age was 20 to 85 years old; (3) the patients with normal blood pressure, liver and kidney function, blood sugar, blood lipids, and normal blood routine; and (4) patients who were willing to actively cooperate with treatment.

If any of the following conditions was satisfied, the patient had to be excluded: (1) poor general condition and unable to tolerate hormone therapy; (2) pregnant or breastfeeding women or allergic to treatment drugs; (3) cognitive impairment and unable to complete the hearing test; (4) allergic rhinitis and autoimmune diseases; and (5) hepatitis B and hepatitis C virus carriers and those with a history of immune diseases.

2.2. Research Methods. The included patients were divided into a hormone group and a combination group. The patients in the hormone group were treated with prednisone acetate. After getting up in the morning, the patient was required to take 60 mg of prednisone acetate (Guoyao Zhunzi H62020285, Gansu Fuzheng Pharmaceutical, 5 mg/tablet) orally 1 time/day. After 3 days of administration, it should reduce the drug dose, with prednisone acetate 30 mg/time and 1 time/day. The patients in the combination group were treated with Ginkgo-Damole combined with prednisone acetate. Ginkgo-Damole (Guoyao Zhunzi H52020032, Guizhou Yibai Pharmaceutical Co., Ltd., 10 mL added to 500 mL of 0.9% sodium chloride injection) was taken intravenously once a day. For combined treatment with prednisone acetate, the patients should take 60 mg of prednisone acetate (Guoyao Zhunzi H62020285, Gansu Fuzheng Pharmaceutical Co., 5 mg/tablet) orally after getting up in the morning once a day. After 3 days of administration, the dose was adjusted to 30 mg/time once/day. The two groups were treated continuously for 7 days as a course of treatment, and the curative effect was observed. Figure 1 shows the structural formula of prednisone acetate.

2.3. Evaluation Standards. Symptoms improved: after the two groups of patients were treated in different ways, their symptoms (ear fullness, tinnitus, and vertigo) were scored for syndrome. The occurrence of the three symptoms was graded into 0 points (no symptoms), 2 points (mild ear fullness, tinnitus, and dizziness), 4 points (moderate ear fullness, tinnitus, and dizziness), and 6 points (severe ear fullness, tinnitus, and dizziness), respectively. It can calculate the degree of improvement of the patient's symptoms, the

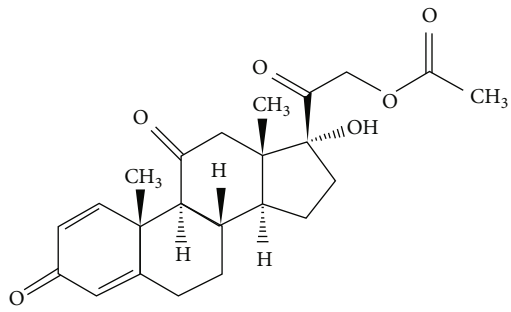

Figure 1: The structural formula of prednisone acetate.

calculation method was

$$I = \text{Score}_{T_0} - \text{Score}_{T_1}. \quad (1)$$

In the above equation, I denoted the symptom improvement degree; Score_{T_0} refers to the syndrome score before treatment; and Score_{T_1} represents the syndrome score after treatment.

The therapeutic effect was assessed into cured, markedly effective, effective, and ineffective. Recovery: tinnitus and vertigo disappeared completely, and hearing returned to normal; markedly effective: tinnitus and vertigo disappeared, and hearing improved by more than 30 dB; effective: tinnitus and vertigo were relieved, and hearing was improved by 15-30 dB; and ineffective: tinnitus and vertigo were unchanged, and hearing was improved by less than 10 dB or even more serious. The calculation method of total effective rate (TER) was

$$\text{Total effective rate} = A + B + C. \quad (2)$$

In the equation above, A represented the cure rate; B represented the markedly effective rate; and C represented the effective rate.

It should monitor and record the changes of hemorheology indexes and endothelial function indicators before treatment, 3 d, 5 d, 7 d, and 10 d after treatment. These indicators included fibrinogen, high blood viscosity (HBV), low blood viscosity (LBV), soluble vascular cell adhesion molecule-1 (sVCM-1), endothelin-1 (ET-1), and PBTCS indicators (CD3+, CD4+, CD8+, and CD4+/CD8+). The levels of sVCM-1 and ET-1 were detected by enzyme-linked immunosorbent assay (ELISA), and the detection kits were purchased from Shanghai Keaibo Biotechnology Co., Ltd. Detection of T cell subset levels: the whole blood samples were detected by EPICSX flow cytometer (Beckman-Coulter, USA). Fibrinogen, whole blood HBV, and LBV were detected by LG-R-80 type hemorheometer (Beijing Zhongqin Shidi Company).

2.4. Statistical Methods. Data processing in this work was performed using SPSS 24.0. Measurement data were expressed as the mean ± standard deviation ($\bar{x} \pm s$), the comparison within the group before and after treatment was performed by the Paired t-test, and the comparison between the two groups was performed by the Independent t-test. The enumeration data were expressed as percentage (%), and the pairwise comparison was made by variance analysis. To evaluate the correlation of PBTCSs with the pathogenesis of sudden deafness and its impact on the recovery of prognosis and the correlation was expressed by OR value (95% CI). The difference was statistically significant at $P < 0.05$.

3. Results

3.1. Basic Data of Patients. All patients included were divided into two groups and then treated with hormones (prednisone acetate) and Ginkgo-Damole combined with prednisone acetate. In order to analyze the curative effect of the two groups of patients after treatment in different ways, the basic information such as age and gender of the patients were first compared, and the results are shown in Table 1. It can be seen that the proportion of male patients in the hormone group and the combination group was 19.05% and 17.46%, respectively, and there was no visible difference ($P > 0.05$). The mean age and disease course of patients between the hormone group and the combination group showed no obvious difference ($P > 0.05$). In addition, the proportions of patients with different degrees of deafness, different tinnitus conditions, and symptoms in the two groups were compared, and the results are shown in Figure 2. The proportions of patients with moderate deafness, severe deafness, and total deafness in the hormone group were 21.23%, 49.56%, and 29.21%, respectively; while those in the combination group were 20.62%, 51.05%, and 28.33%, respectively. The proportions of patients with low-key tinnitus, high-profile tinnitus, and no tinnitus in the hormone group were 28.31%, 47.33%, and 24.36%, respectively; while those in the combination group were 28.06%, 49.08%, and 22.86%, respectively. The proportion of patients with ear fullness symptoms in the two groups were 52.33% and 50.47%, respectively; the proportions of patients with facial discomfort symptoms were 48.65% and 46.12%, respectively; and the proportions of patients with vertigo symptoms were 10.18% and 12.33%, respectively. The proportion of patients with different degrees of deafness, tinnitus, and accompanying symptoms showed no visible difference between two groups ($P > 0.05$).

3.2. Patient Efficacy and Symptom Improvement. The improvement of ear fullness, tinnitus, and dizziness was evaluated in the two groups of patients after treatment in different ways. The curative effect of patients was judged by four grades as cured, markedly effective, effective, and ineffective, and TER was calculated. The results are shown in Figure 3. In the hormone group, the patients with curative effect as cured, markedly effective, effective, and ineffective were 8 cases, 7 cases, 11 cases, and 8 cases, respectively. In the combination group, 11, 13, 3, and 3 patients were cured, markedly effective, effective, and ineffective, respectively. The number of cured and markedly effective patients was significantly higher in the combination group. The TER of the hormone group and the combination group were 76.32% and 95.73%, respectively, showing statistically great difference ($P < 0.05$). The improvement degrees of ear

Table 1: Basic data of patients.

Item	Type	Proportion (%) Hormone group ($n = 34$)	Combination group ($n = 30$)
Gender	Males	12 (19.05%)	11 (17.46%)
	Females	9 (14.29%)	10 (15.87%)
Age (years old)		33.68 ± 10.98	35.08 ± 12.24
Disease course (h)		8.09 ± 2.55	8.21 ± 1.08

fullness, tinnitus, and dizziness in the hormone group patients were 1.52, 1.65, and 1.8, respectively; while those in the combination group were 2.31, 2.53, and 2.66, respectively, showing great difference statistically ($P < 0.05$).

3.3. Changes in Hemorheological Indexes of Patients. The two groups of patients were treated in different ways, and the changes of hemorheology indexes were monitored and recorded before treatment and after 3 d, 5 d, 7 d, and 10 d after treatment. The differences between the two groups at different times were compared; the results are shown in Figure 4. Figure 4(a) showed the changes of fibrinogen. With the prolongation of treatment time, the fibrinogen content of the two groups of patients gradually decreased, and the fibrinogen content of the combination group decreased more obviously. No obvious difference in fibrinogen content was found before treatment and 3 days after treatment ($P > 0.05$). The fibrinogen contents of patients in the combination group at 5 d, 7 d, and 10 d after treatment were 3.19 ± 0.87 g/L, 2.89 ± 0.61 g/L, and 2.51 ± 0.83 g/L, respectively, which were lower than those in the hormone group (3.9 ± 0.64 g/L, 3.89 ± 0.54 g/L, and 3.55 ± 0.78 g/L, respectively); in addition, the fibrinogen contents of both groups were obviously lower than the contents before treatment ($P < 0.05$). Figure 4(b) shows the changes of HBV. It suggested that with the prolongation of treatment time, HBV in both groups gradually decreased, and the decrease in HBV in the combination group was more obvious. HBV before treatment and 3 days after treatment showed no obvious difference ($P > 0.05$). The HBV levels of patients in the combination group at 5 d, 7 d, and 10 d after treatment (4.02 ± 0.6 mPa∗s, 3.98 ± 0.66 mPa∗s, and 3.66 ± 0.6 mPa∗s) were significantly lower than those in the hormone group (6.43 ± 0.55 mPa∗s, 5.89 ± 0.69 mPa∗s, and 5.72 ± 0.48 mPa∗s), and all were much lower than the levels before treatment ($P < 0.05$). Figure 4(c) shows the changes of LBV. It indicated that with the prolongation of treatment time, the LBV of the two groups of patients decreased gradually, and the LBV of the combination group decreased more obviously, but the difference in between the two groups before treatment was not obvious ($P > 0.05$). The LBV of patients in the combination group at 3 d, 7 d, and 10 d after treatment (10.06 ± 0.49 mPa∗s, 7.35 ± 0.62 mPa∗s, and 6.48 ± 0.72 mPa∗s) were sharply lower compared to those in the hormone group (11.54 ± 0.65 mPa∗s, 9.37 ± 0.73 mPa∗s, and 8.79 ± 0.49 mPa∗s), and all were lower than the levels before treatment ($P < 0.05$).

3.4. Changes of Endothelial Function Indexes in Patients. The two groups of patients were treated in different ways, and the changes of endothelial function indexes were monitored and recorded before treatment and after 3 d, 5 d, 7 d, and 10 d after treatment. The differences between the two groups at different times were compared; the results are illustrated in Figure 5. Among them, Figure 5(a) revealed the changes of sVCM-1. With the prolongation of treatment time, the levels of sVCM-1 in the two groups were gradually decreased, and the levels of sVCM-1 in the combination group decreased more obviously. The sVCM-1 showed no great difference between the two groups before treatment and 3 days after treatment ($P > 0.05$). The levels of sVCM-1 in patients in the combination group were 203.54 ± 19.38 g/L, 185.43 ± 15.01 g/L, and 170.52 ± 19.02 g/L after treatment for 5 d, 7 d, and 10 d, respectively, which were notably lower than those in the hormone group (240.44 ± 19.92 g/L, 238.91 ± 20.45 g/L, and 236.88 ± 18.3 g/L), and all decreased than those before treatment ($P < 0.05$). Figure 5(b) suggests the changes of Endothelin-1 (ET-1). As it illustrates the prolongation of treatment time, the levels of ET-1 in the two groups gradually decreased, and the levels of ET-1 in the combination group decreased more obviously. There was no obvious difference before treatment and 3 days after treatment ($P > 0.05$). The levels of ET-1 in the combination group at 5 d, 7 d, and 10 d after treatment (125.36 ± 17.81 g/L, 100.03 ± 19.4 g/L, and 85.93 ± 18.82 g/L) were notably lower than those in the hormone group (139.81 ± 18.15 g/L, 125.44 ± 20.59 g/L, and 118.92 ± 19.7 g/L), and all were effectively lower than those before treatment ($P < 0.05$).

3.5. Comparison of PBTCSs of Patients. Figure 6 demonstrates the comparison results of PBTCSs indicators of patients. No visible difference was found in CD3+, CD4+, CD8+, and CD4+/CD8+ between the hormone group and the combination group before treatment ($P > 0.05$). After different treatments, the CD3+, CD4+, and CD4+/CD8+ in the combination group were much higher in contrast to those in the hormone group ($P < 0.05$). The CD8+ in peripheral blood in the combination group was observably lower than that in the hormone group ($P < 0.05$).

3.6. The Incidence of Adverse Reactions. Figure 7 reveales the occurrence of adverse reactions (nausea, dizziness, skin allergy, and other adverse reactions) in the hormone group and the combination group patients after prednisone acetate and Ginkgo-Damole combined with prednisone acetate treatment, respectively. The proportions of patients with nausea, dizziness, skin allergy, and other adverse reactions in the hormone group were 8.21%, 11.37%, 5.34%, and 6.31%, respectively; while those in the combination group were 8.66%, 10.96%, 5.45% and 6.54%, respectively ($P > 0.05$).

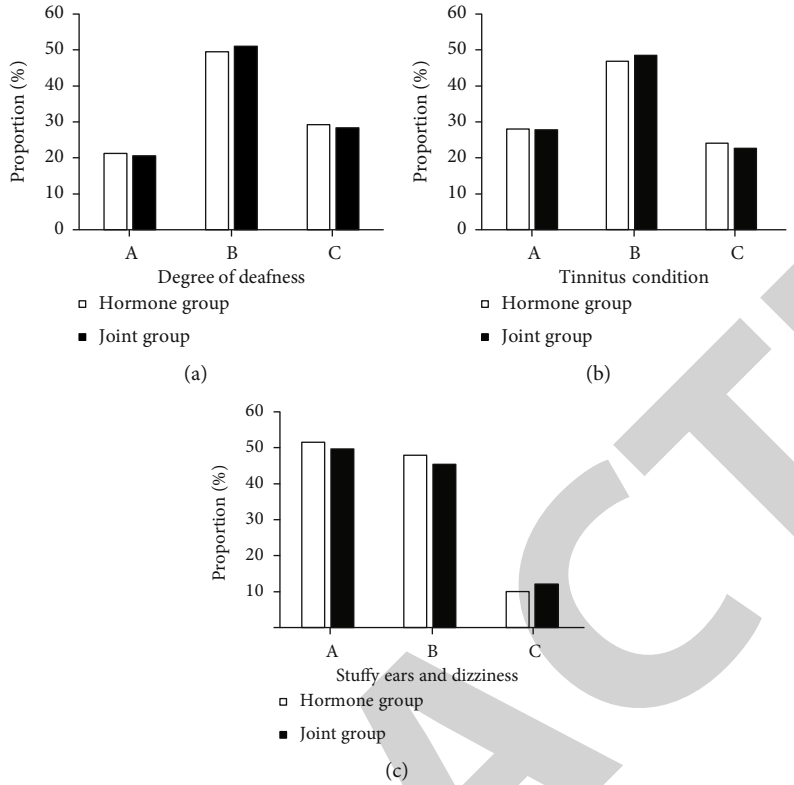

Figure 2: The degree and symptoms of deafness in patients. Note: (a) showed the degree of deafness of the two groups of patients, where (A)–(C) represented moderate deafness, severe deafness, and total deafness, respectively; (b) showed the patient's tinnitus status, where (A)–(C) represented low-key tinnitus, high-key tinnitus, and no tinnitus, respectively; (c) represented other symptoms of the patient, where (A)–(C) represented ear fullness, facial discomfort, and dizziness, respectively.

4. Discussion

Sudden deafness is a sudden onset of sensorineural hearing loss manifested as unilateral hearing loss, which can be accompanied by tinnitus, ear blockage, dizziness, nausea, and vomiting. It usually occurs suddenly within 72 hours, and the hearing loss of two adjacent frequencies can be found to be greater than or equal to 20 dBHL during pure tone audiometry [22]. The causes of sudden deafness are more complicated and may be related to factors such as inner ear blood supply disorder and viral infection [23]. At present, the widely recognized virus infection theory, circulatory disorder theory, autoimmunity theory, and membrane labyrinth rupture theory are the main ones. The disease is more common in people with high blood pressure, arteriosclerosis, hypothyroidism, and low blood pressure [24]. According to the frequency and degree of hearing loss, it can be divided into: high-frequency descending type, low-frequency descending type, flat descending type, and total deafness type (including profound deafness). Low-frequency descending type: hearing loss at frequencies below 1,000 Hz (inclusive), at least 250 Hz and 500 Hz hearing loss ≥20 dBHL; high-frequency descending type: hearing loss at frequencies above 2,000 Hz (inclusive), at least 4,000 Hz and 8,000 Hz hearing loss ≥20 dBHL; flat descending type: hearing loss at all frequencies, 250-8,000 Hz average hearing threshold ≤80 dBHL; and totally deafness type: hearing loss at all frequencies, with an average hearing threshold of 250-8,000 Hz ≥81 dBHL [25]. Different types have different treatment options. Sudden deafness should be treated with glucocorticoid drugs and neurotrophic drugs in accordance with the doctor's order. Common drugs include prednisone and methylcobalamin. Treatment options include microcirculation-improving drugs (such as *Ginkgo biloba* extract) combined with glucocorticoids; ion channel blockers (such as lidocaine) are better for reducing high-profile tinnitus; and neurotrophic drugs (such as methylcobalamin). The research of Singh et al. [26] showed that if the drug treatment was not effective, hyperbaric oxygen therapy and stellate ganglion block therapy can also be given. With appropriate treatment, the patient's hearing can be gradually restored.

Currently, *Ginkgo biloba* extract is the most commonly used drug for the treatment of sudden deafness clinically. *Ginkgo biloba* extract is made from *Ginkgo biloba* leaves and extracted with appropriate solvents. The main component is *Ginkgo biloba* flavonoid glycosides. Its main function is that of ginkgo flavone glycosides, and the main functions include: (1) scavenging of free radicals: *Ginkgo biloba* extract removes excess free radicals in the body and inhibits lipid peroxidation in cell membranes; thereby, protecting cell membranes and preventing a series of damage to the cochlea caused by free radicals. (2) Adjustment to the circulatory system: arterial relaxation is produced by stimulating the

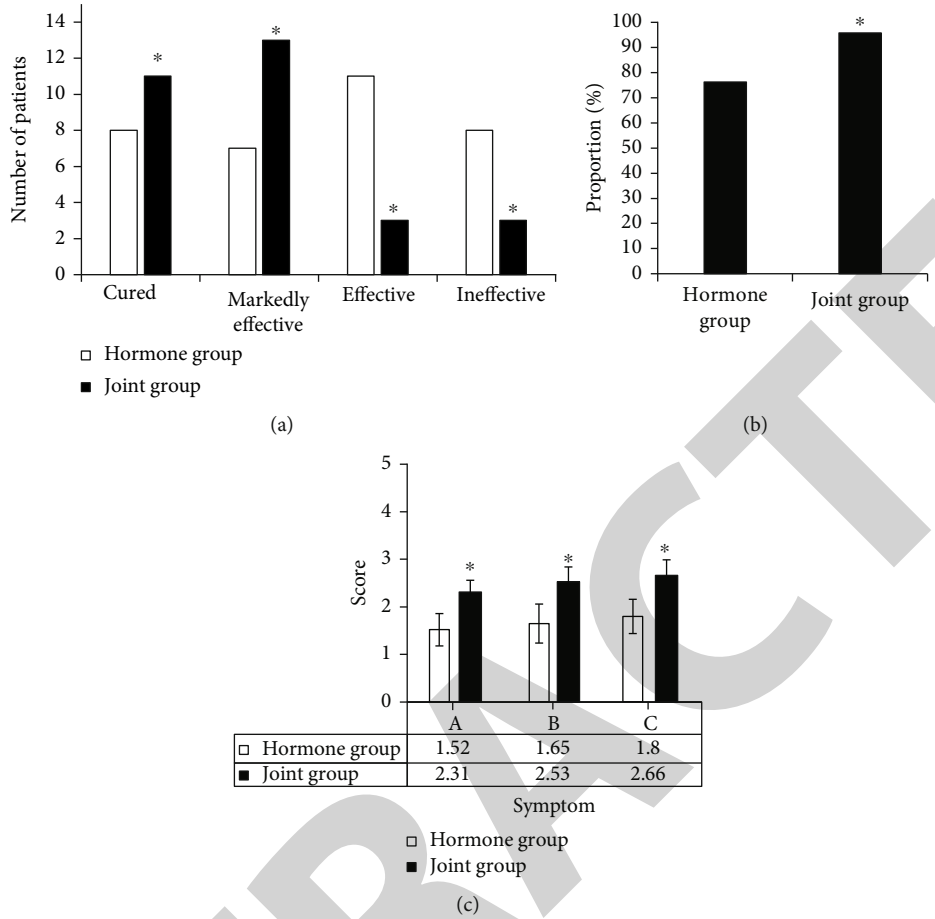

Figure 3: Curative effect and symptom improvement. Note: (a) showed the comparison of the two groups of patients whose curative effects were, respectively, cured, markedly effective, effective, and ineffective; (b) showed the TER; and (c) showed the degree of improvement of the patient's symptoms, where (A)–(C) indicated ear fullness, tinnitus, and dizziness, respectively; ∗ indicated $P < 0.05$ compared with the hormone group.

release of catecholamines and inhibiting degradation, stimulating the production of prostacyclin and endothelial relaxation factor, and jointly maintaining the tension of arterial and venous blood vessels. (3) Hemodynamic improvement effect: the onset of sudden deafness is generally considered to be related to thrombosis, especially the blood vessels of the cochlea are slender peripheral blood vessels. Research by Suzuki et al. [27] found that *Ginkgo biloba* extract can reduce the viscosity of whole blood, increase the plasticity of red blood cells and white blood cells, and improve the blood circulation of the cochlea. (4) Tissue protection: *Ginkgo biloba* extract has a protective effect on body tissues, which can increase the supply of oxygen and glucose to ischemic tissues (including the cochlea).

In this work, patients with sudden deafness were selected as the research objects, and their therapeutic effects were investigated after prednisone acetate and Ginkgo-Damole combined with prednisone acetate, respectively. The results showed that with the prolongation of treatment time, the blood rheology indexes of fibrinogen content, HBV, and LBV in the two groups were gradually decreased, and the content of the combination group decreased more obviously. The fibrinogen content, whole blood HBV, and LBV of patients in the combined group were significantly lower than those in the hormone group at 5 d, 7 d, and 10 d after treatment, and were significantly lower than those before treatment ($P < 0.05$). This result is similar to the research result of Övet et al. [28], which may be due to the flavonoid glycosides in *Ginkgo biloba* extract exerting the effect of scavenging free radicals and protecting brain tissue. Ginkgolide can balance lipid peroxidation, increase the tolerance of cells to hypoxia, change blood rheology, and increase the plasticity of whole blood. After different treatments, the peripheral blood CD3+, CD4+, CD4+/CD8+ in the combined group were significantly higher than those in the hormone group, and the differences were statistically significant ($P < 0.05$). In addition, the peripheral blood CD8+ in the combined group was significantly lower than that in the hormone group, and the difference was statistically significant ($P < 0.05$). Such results are similar to the research results of Suzuki et al. [29]. It indicates that T cell subsets may have a certain correlation with the prognosis and efficacy of patients with sudden deafness. Patients with sudden deafness may have an imbalance of peripheral blood T cell subsets, and the combined treatment of *Ginkgo biloba* extract and hormones has a certain improvement effect on the

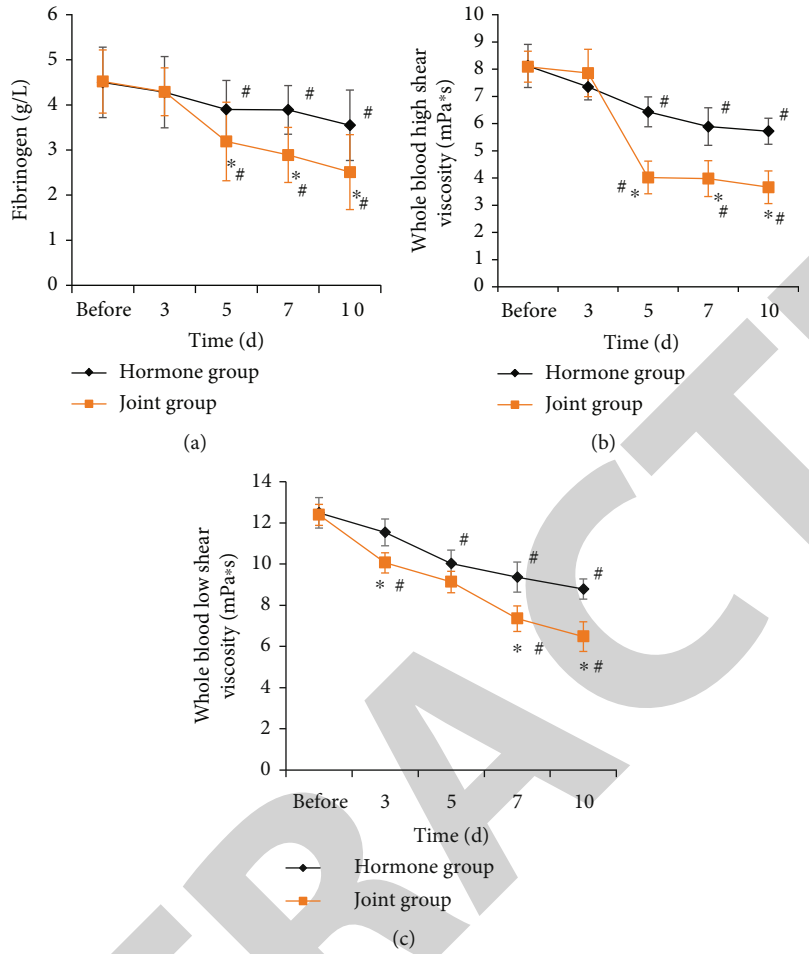

Figure 4: Changes of hemorheological indexes in patients. Note: (a)–(c) showed the fibrinogen content, HBV level, and LBV level, respectively; ∗ indicated $P < 0.05$ to the hormone group; # indicated $P < 0.05$ compared with before treatment.

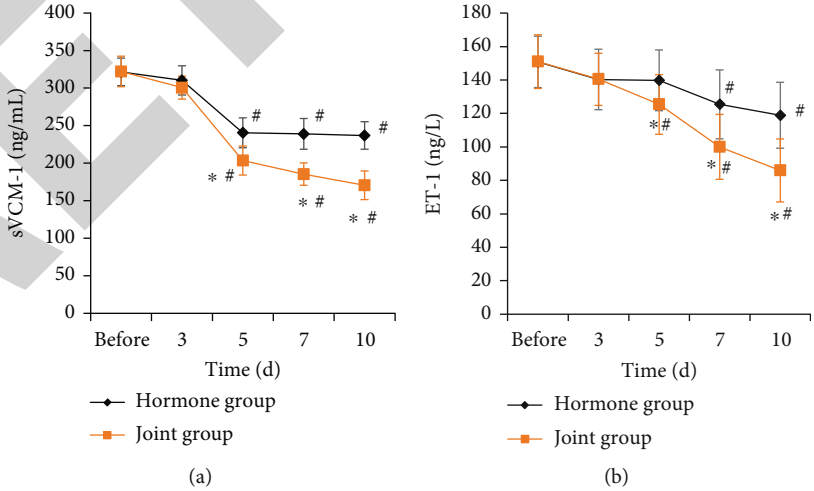

Figure 5: Changes of endothelial function indexes in patients. Note: (a) and (b) compared the sVCM-1 and ET-1, respectively; ∗ and # indicated $P < 0.05$ to the hormone group and the combination group before treatment, respectively.

imbalance of PBTCSs. No great difference was found in nausea, dizziness, skin allergy, and other incidence of adverse reactions between the hormone group and the combination group after different treatments ($P > 0.05$). It indicates that the treatment method of this study has certain safety for sudden deafness treatment.

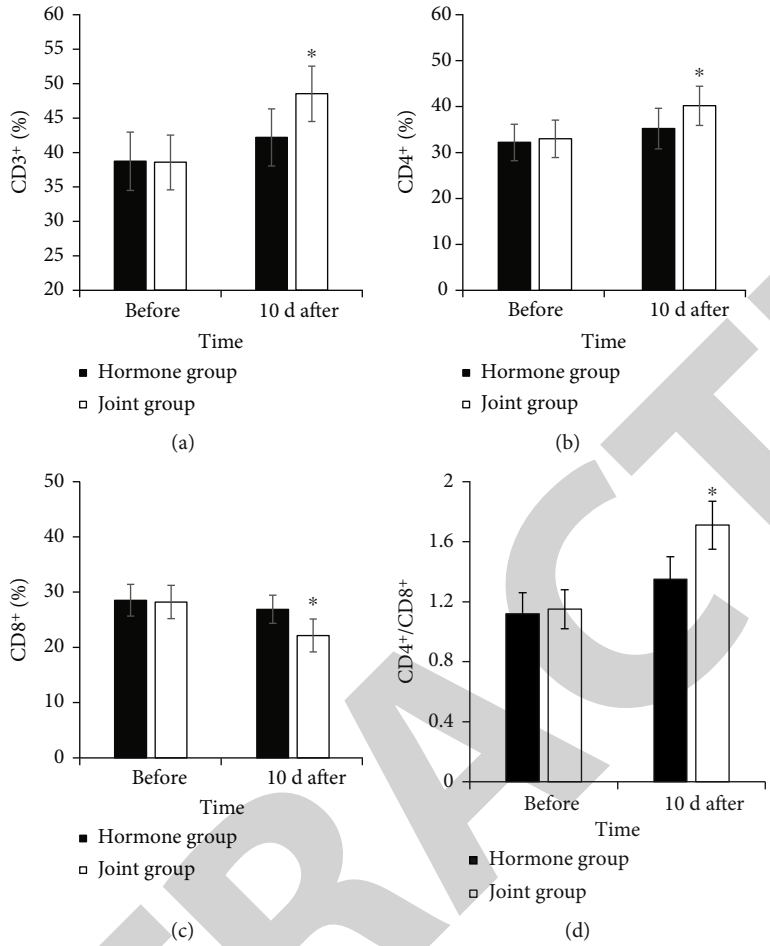

Figure 6: Comparison of PBTCSs of patients. Note: (a): CD3+; (b): CD4+; and (c): CD8+; D: CD4+/CD8+; ∗ indicated $P < 0.05$ to the hormone group.

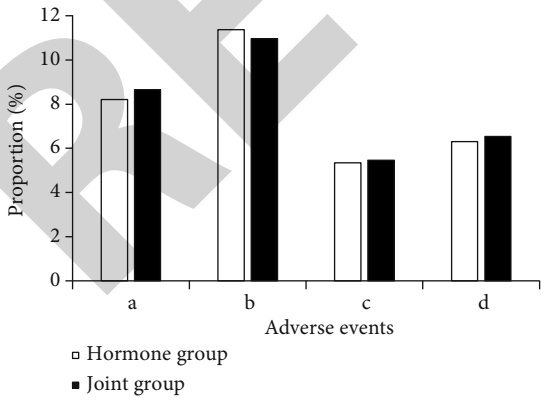

Figure 7: The incidence of adverse reactions. Note: (a)–(d) represented nausea, dizziness, skin allergy, and other adverse reactions, respectively.

5. Conclusions

In this work, patients with sudden deafness were included, two methods of prednisone acetate and Ginkgo-Damole combined with prednisone acetate were used to intervene, and the comprehensive efficacy of the two groups of patients was compared. The results showed that the combined application of *Ginkgo biloba* extract and hormones can effectively improve the abnormal hemorheological indexes of patients with sudden deafness and effectively relieve the imbalance of PBTCSs, showing high safety. However, the sample size included in this work was small and the sources were concentrated, so it may have a certain impact on the reliability of the research results. In addition, according to the results of this work, *Ginkgo biloba* extract combined with hormones had a good therapeutic effect on sudden deafness, but the mechanism of its effect was still unclear. Therefore, the above aspects needed to be improved and optimized in the follow-up research, so as to make the research more perfect.

Data Availability

The data used to support the findings of this study are available from the corresponding author upon request.

Conflicts of Interest

The authors declare that they have no conflicts of interest.

Acknowledgments

This work was supported by the Hunan University of Traditional Chinese Medicine university-level project "Prediction and Correlation of Peripheral Blood T-Cell Subsets in the Treatment of Sudden Deafness with Hormone Combined with Murine Nerve Growth Factor" (Project No. 2019XJJJ056) and supported by the Hunan Provincial Administration of Traditional Chinese Medicine subject project general project "Clinical Observation and Mechanism Study on the Treatment of Tinnitus Caused by Kidney Essence Deficiency with *Cistanche cistanica* Total Glycosides" (Project NoE2022031).

References

[1] J. J. Han, J. Y. Jung, K. H. Park et al., "Nimodipine and steroid combination therapy for idiopathic sudden sensorineural hearing loss," *Otology & Neurotology*, vol. 41, no. 7, pp. e783–e789, 2020.

[2] M. Y. Kwak, C. J. Yang, H. J. Shim et al., "Intratympanic steroid injection for sudden sensorineural hearing loss: impact of injection interval on therapeutic efficacy," *Auris, Nasus, Larynx*, vol. 47, no. 6, pp. 982–989, 2020.

[3] H. Suzuki, T. Ohbuchi, B. H. Do et al., "Frequency-specific efficacy of intratympanic steroid on idiopathic sudden sensorineural hearing loss," *Acta Oto-Laryngologica*, vol. 140, no. 9, pp. 756–760, 2020.

[4] M. Amizadeh, K. Mozafarnia, J. Moslemikia, and A. Naghibzadeh-Tahami, "Combination of pulse steroid with intratympanic injections in sudden sensorineural hearing loss," *Iranian Journal of Otorhinolaryngology*, vol. 33, no. 114, pp. 9–13, 2021.

[5] S. M. Han, H. S. Lee, H. S. Chae, and Y. J. Seo, "Usefulness of vertebrobasilar artery radiological finding as a predictive and prognostic factor for sudden sensorineural hearing loss," *Auris, Nasus, Larynx*, vol. 48, no. 5, pp. 823–829, 2021.

[6] S. X. Zhong, W. Q. Zuo, B. Y. Zhang, Y. Qian, and Y. Lei, "A prospective controlled study on the proper time of intratympanic steroid for profound sudden sensorineural hearing loss of total frequency type," *Zhonghua er bi yan hou tou Jing wai ke za zhi= Chinese Journal of Otorhinolaryngology Head and Neck Surgery*, vol. 53, no. 11, pp. 806–810, 2018.

[7] J. Hou, W. She, X. Du, Y. Dai, L. Xie, and Q. Zhou, "Histone deacetylase 2 in sudden sensorineural hearing loss patients in response to intratympanic methylprednisolone perfusion," *Otolaryngology and Head and Neck Surgery*, vol. 154, no. 1, pp. 164–170, 2016.

[8] X. Si, Z. Yu, X. Ren, L. Huang, and Y. Feng, "Efficacy and safety of standardized Ginkgo biloba L. leaves extract as an adjuvant therapy for sudden sensorineural hearing loss: a systematic review and meta-analysis," *Journal of Ethnopharmacology*, vol. 282, p. 14587, 2022.

[9] Z. W. Bear and A. A. Mikulec, "Intratympanic steroid therapy for treatment of idiopathic sudden sensorineural hearing loss," *Missouri Medicine*, vol. 111, no. 4, pp. 352–356, 2014.

[10] J. W. Koo, M. Y. Chang, S. C. Yun et al., "The efficacy and safety of systemic injection of Ginkgo biloba extract, EGb761, in idiopathic sudden sensorineural hearing loss: a randomized placebo-controlled clinical trial," *European Archives of Oto-Rhino-Laryngology*, vol. 273, no. 9, pp. 2433–2441, 2016.

[11] G. B. Sheng, H. Su, H. L. Li et al., "Effect of electro-nape-acupuncture on hearing in patients with refractory flat descending idiopathic sudden sensorineural hearing loss," *Zhongguo Zhen jiu= Chinese Acupuncture & Moxibustion*, vol. 40, no. 7, pp. 726–730, 2020.

[12] D. Lai, Y. L. Huang, J. M. Pu, and L. Liu, "Intratympanic steroid intervention as initial therapy for sudden sensorineural hearing loss: a systematic review of reviews," *Lin Chuang er bi yan hou tou Jing wai ke za zhi= Journal of Clinical Otorhinolaryngology, Head, and Neck Surgery*, vol. 31, no. 16, pp. 1258–1264, 2017.

[13] S. C. Chew and M. K. Md Daud, "The efficacy of intratympanic steroid injection for the treatment of idiopathic sudden sensorineural hearing loss," *The Medical Journal of Malaysia*, vol. 75, no. 1, pp. 74–77, 2020.

[14] M. Lechner, L. Sutton, M. Ferguson, Y. Abbas, J. Sandhu, and A. Shaida, "Intratympanic steroid use for sudden sensorineural hearing loss: current otolaryngology practice," *The Annals of Otology, Rhinology, and Laryngology*, vol. 128, no. 6, pp. 490–502, 2019.

[15] Y. Wang, G. Gao, L. Wang, X. Ma, L. Yu, and F. Ye, "Association between the number of intratympanic steroid injections and hearing recovery in sudden sensorineural hearing loss," *Frontiers in Neurology*, vol. 12, article 798569, 2021.

[16] A. Yücel and Y. Özbuğday, "Comparison of steroid treatment with and without hyperbaric oxygen therapy for idiopathic sudden sensorineural hearing loss," *Journal of Audiology & Otology*, vol. 24, no. 3, pp. 127–132, 2020.

[17] H. Suzuki, R. Kawaguchi, T. Wakasugi, B. H. Do, T. Kitamura, and T. Ohbuchi, "Efficacy of intratympanic steroid on idiopathic sudden sensorineural hearing loss: an analysis of cases with negative prognostic factors," *American Journal of Audiology*, vol. 28, no. 2, pp. 308–314, 2019.

[18] H. J. Hu, W. Zhang, and D. F. Fan, "Letter: HBO2 combined with steroid therapy for sudden sensorineural hearing loss within two weeks," *Undersea & Hyperbaric Medicine*, vol. 48, no. 1, pp. 103-104, 2021.

[19] F. Vanwijck, F. Rogister, S. Pierre Barriat, S. Camby, and P. Lefebvre, "Intratympanic steroid therapy for refractory sudden sensory hearing loss: a 12-year experience with the Silverstein catheter," *Acta Oto-Laryngologica*, vol. 139, no. 2, pp. 111–116, 2019.

[20] J. Ajduk, A. Košec, I. Kelava, M. Ries, T. Gregurić, and L. Kalogjera, "Recovery from sudden sensorineural hearing loss may be linked to chronic stress levels and steroid treatment resistance," *American Journal of Audiology*, vol. 28, no. 2, pp. 315–321, 2019.

[21] M. H. Song, S. Y. Jung, J. W. Gu, and D. B. Shim, "Therapeutic efficacy of super-high-dose steroid therapy in patients with profound sudden sensorineural hearing loss: a comparison with conventional steroid therapy," *Acta Oto-Laryngologica*, vol. 141, no. 2, pp. 152–157, 2021.

[22] W. C. Lan, C. Y. Wang, and C. D. Lin, "Pentoxifylline versus steroid therapy for idiopathic sudden sensorineural hearing loss with diabetes," *The Journal of International Advanced Otology*, vol. 14, no. 2, pp. 176–180, 2018.

Hindawi
Computational and Mathematical Methods in Medicine
Volume 2023, Article ID 9861647, 1 page
https://doi.org/10.1155/2023/9861647

Retraction

Retracted: What Promotes Medical Overuse: Perspective on Evolutionary Game between Administration and Medical Institutions

Computational and Mathematical Methods in Medicine

Received 15 August 2023; Accepted 15 August 2023; Published 16 August 2023

This article has been retracted by Hindawi following an investigation undertaken by the publisher [1]. This investigation has uncovered evidence of one or more of the following indicators of systematic manipulation of the publication process:

(1) Discrepancies in scope

(2) Discrepancies in the description of the research reported

(3) Discrepancies between the availability of data and the research described

(4) Inappropriate citations

(5) Incoherent, meaningless and/or irrelevant content included in the article

(6) Peer-review manipulation

The presence of these indicators undermines our confidence in the integrity of the article's content and we cannot, therefore, vouch for its reliability. Please note that this notice is intended solely to alert readers that the content of this article is unreliable. We have not investigated whether authors were aware of or involved in the systematic manipulation of the publication process.

Wiley and Hindawi regrets that the usual quality checks did not identify these issues before publication and have since put additional measures in place to safeguard research integrity.

We wish to credit our own Research Integrity and Research Publishing teams and anonymous and named external researchers and research integrity experts for contributing to this investigation.

The corresponding author, as the representative of all authors, has been given the opportunity to register their agreement or disagreement to this retraction. We have kept a record of any response received.

References

[1] C. Xu, L. Luo, S. Zeng, X. He, J. Li, and G. Zhu, "What Promotes Medical Overuse: Perspective on Evolutionary Game between Administration and Medical Institutions," *Computational and Mathematical Methods in Medicine*, vol. 2022, Article ID 4351282, 15 pages, 2022.

Hindawi
Computational and Mathematical Methods in Medicine
Volume 2022, Article ID 4351282, 15 pages
https://doi.org/10.1155/2022/4351282

Research Article

What Promotes Medical Overuse: Perspective on Evolutionary Game between Administration and Medical Institutions

Chenxi Xu,[1] **Li Luo**,[1] **Siyu Zeng**,[2] **Xiaozhou He**,[1] **Jialing Li**,[3] **and Guiju Zhu**[3]

[1]*Business School, Sichuan University, No. 24 South Section 1, Yihuan Road, Chengdu, China*
[2]*School of Logistics, Chengdu University of Information Technology, No. 10, Xingfu Road, Chengdu, China*
[3]*School of Management, Hunan University of Technology and Business, No. 569 Yuelu Avenue, Changsha, China*

Correspondence should be addressed to Xiaozhou He; xiaozhouhe126@qq.com

Received 17 April 2022; Accepted 28 August 2022; Published 14 September 2022

Academic Editor: Plácido R. Pinheiro

Medical overuse is the leading cause of high expenditure among healthcare systems worldwide, with the degree varying from region to region. There is increasing evidence to indicate that in China, National Healthcare Security Administration (NHSA) supervision plays the most crucial role in decreasing medical overuse. For medical overuse, traditional studies focus on empirical researches and qualitative analysis, most of which ignore how the two important participants, i.e., medical institutions and NHSA, affect the strategy of each other. To reduce the losses incurred by insufficient supervision, this study starts from bounded rationality, builds an evolutionary game model to study the relations between the NHSA and medical institutions, and reveals the dynamic evolution process of the supervision of NHSA and overuse of medical institutions. Through stable evolutionary strategy analysis, numerical simulation results, and sensitive experiments under diverse scenarios, we found that when profit gap of medical overuse is high or low, medical institution will adopt fixed strategy, which is medical overuse or appropriate medical use. Only when the profit gap is at a medium level will NHSA's choice affects medical institutions' strategy. Furthermore, NHSA's strategy is affected by the profit gap between medical use and supervision cost. Our work enriches the understanding of supervision for medical overuse and provides theoretical support for the NHSA to make decisions to reach an ideal condition, i.e., to supervise without exertion.

1. Introduction

Medical overuse is defined as the provision of superfluous healthcare services. It involves the unnecessary expenditure of resources beyond the actual needs of a medical condition, which might even result in possible harm [1–3].

Medical overuse is the leading cause of high expenditure among healthcare systems worldwide [4, 5]. Previous studies have estimated that approximately 30% of healthcare spending might be considered wasted expenditure [6]. In the United States, waste from overuse costs more than $210 billion a year [7], and this figure is even higher in low- and middle-income countries [3]. Elimination of medical overuse could substantially improve healthcare efficiency. The reasons that lead to medical overuse are complex, such as insufficient investment by the government, the pharmaceutical industry's incentives to doctors, hospitals' pursuit of increased profits, and patients' demand for additional medical services to promote faster recovery [8]. Furthermore, the information asymmetry between doctors, patients, and insurance companies leads to considerable risks and uncertainty in the purchase of medical services, which leads to excessive medical treatment [9]. The Chinese medical care system has experienced noteworthy changes after three decades of reform, which improved medical insurance coverage [10]. Most medical expenditure is paid for by the National Healthcare Security Administration (NHSA) in China, but the NHSA is facing a serious imbalance of income and expenditure and continuous growth of medical expenses [11]. In China, the current medical insurance payment is mostly based on fee-for-service; that is, the insurer compensates according to the quantity and price of medical services provided in a certain proportion. This payment method makes hospitals hardly bear the risk of rising

medical costs and obtain higher income by increasing the number of medical services. Therefore, hospitals not only lack initiative to control medical costs but also induce demand and provide unnecessary medical services, which is medical overuse [12]. China is at a loss as to how to transform its new money into efficient and effective healthcare. Many papers argue that unless China tackles the root causes of wasteful healthcare delivery, the healthcare system will be severely threatened [13]. Thus, reducing medical overuse is an urgent concern for the Chinese government.

As a result, many studies focused on understanding how to mitigate medical overuse [1]. Previous studies mainly focused on retrospective analysis of data [14, 15] or on the analysis of treatment for a specific disease or the overuse of a single service [16] and the influence factors of medical overuse [17, 18]; some findings sought to determine if there was variance among medical specialties [19]. To reduce medical overuse, it is found that intervention's impact on media coverage of medicine can help patients to stay away from medical overuse [20]. It is found that NHSA's supervising and punishment of doctors' behaviour, establishing reputation mechanism, and protecting patient's right are important factors to restrain medical overuse behaviour [21]. Most of them suggested that strengthening NHSA's supervision could decrease the overuse of medical service [22] but did not make detailed suggestions regarding ways to regulate it. Previous studies tend to start from a single perspective, but there is still a lack of research on the evolutionary game in which NHSA and medical institutions are fully integrated under the background of FFS (fee-for-service).

In this study, however, we aim at figuring out the interest coordination of the main stakeholders in medical overuse based on evolutionary game theory whose formation and evolution is an interactive and game process between the two organisations, that is, NHSA and medical institutions. And we construct a dynamic evolutionary game model to investigate the supervisory mechanism for reducing medical overuse in government and hospitals, based on the premise of limited rationality. With the constructed model, we first analyse evolutionary stable strategies and then make further analysis on equilibrium stable strategy. And via numerical simulation on MATLAB with the model and stable strategies, we explore what factors influence the strategy making of medical institutions and NHSA.

To build the evolutionary game model, we first need to make clear the game mechanism. So, what is the NHSA's regulatory mechanism for medical institutions on medical overuse? NHSA and medical institutions are two participants in the decision-making of reducing medical overuse. For NHSA, the strategies are composed of strict supervision and loose supervision. And for medical institutions, the strategies are composed of medical overuse and appropriate medical overuse. For the two participants, different strategies will lead to different profit and cost, which will also affect the decision-making of both sides. The hardcore is to dig out how the variation of cost and profit is related to the strategy adoption of NHSA and medical institutions.

This paper discusses the influence of the profit gap between medical overuse and appropriate use and supervision costs on the decision-making of NHSA and medical institutions by analysing six scenarios. There are two main contributions:

(1) A model based on game theory is proposed to design mechanism and solve issues on overuse medical costs via analysing the strategies between medical institutions and NHSA with the consideration of patient supervision

(2) The proposed model and the numerical experiments under different scenarios show the factors influencing decision-making of NHSA and medical institutions and suggest that to reduce the occurrence of medical overuse, this paper finds that minimizing the high profits of medical overuse from the source forward is more effective than to strengthen supervision

This paper is organised as follows: Section 2 is the literature review; Section 3 describes the construction of an evolutionary game model and discussion of the equilibrium of the model; Section 4 explains the simulation analysis of the game model; and Section 5 presents the results and conclusions.

2. Literature Review

2.1. Effect of Medical Overuse. Scholars conducted extensive studies to explore the reason of the continuous increase of medical cost. Worldwide, the growth in healthcare expenditure from the rising volume of medical services has been identified as the biggest threat to government finances. Population growth and ageing are believed to be the leading causes of medical cost increase over last century [23]. Recently, Berwick and Andrew [24] and Daley and Savage [25] suggested another root cause: medical overuse. Wennberg et al. indicated that the proportion of Medicare spending owing to overuse is almost 29% [26]. Korenstein et al. claimed that overuse can be as high as 89% in certain populations worldwide [27]. A study published in Lancet in 2007 pointed out that overuse is harmful to patients and healthcare systems, and thus, physicians, politicians, and policy-makers must understand overuse and act to reduce it [3]. These studies suggested that medical overuse is the main reason of high medical expenditure.

Medical overuse will not only increase medical costs but also do harm to patients' health. The risk of harm from overuse varies depending on the disease [28]. Bansal et al. discussed end-of-life medication for cancer patients, half of whom received ineffective radiotherapy [16]. Ming et al. reviewed the situation, reasons, and countermeasures of overuse of cardiovascular services in America and explored its implications to China [22]. Researchers are also concerned about the overuse of certain medical services. The use of antibiotics, which is a global overuse problem, has drawn considerable attention [14]. André et al. [15], Gulliford et al. [29], and Panasiuk et al. [30] proved that 50% of patients receive unnecessary antibiotics. Currie et al. tested antibiotics abuse in China [31]. Xiang and Yan analysed the overuse of injections in China [32]. Taasan and Winchester

used patients' hospitalisation data between 2012 and 2015 to identify the overuse of cardiac troponin [33]. Romano et al. [34] evaluated continuity using the Bice–Boxerman continuity of care index and discovered that higher continuity of care could reduce medical overuse. All of these studies point out the harm of medical overuse and the need to decrease it.

2.2. Reasons of Medical Overuse. Lots of studies focus on how to reduce medical overuse. A few papers suggested strategies to mitigate overuse, and monitoring is seen to be one of the most effective measures [22, 35]. Supervision of medical overuse generally considers three aspects: internal supervision of hospitals [22], patients [36], and government departments [22]. McCulloch et al. pointed out that interventions targeting healthcare systems using financial, regulatory, or incentivisation strategies may reduce overuse of surgery [35]. Arab-Zozani et al. [36] and McCulloch et al. [35] suggested that patient engagement, such as shared decision-making, may reduce medical overuse. Ming et al. suggested that strengthening government supervision could decrease the overuse of medical services [22]. A few studies considered the supervision of medical institutions by both patients and NHSA. However, none of these studies analysed how NHSA regulations to supervise medical costs can affect the strategy selection of hospitals, which in turn affects the use of insurance funds. Furthermore, few studies have considered the impact of patient complaints. We aim to address these lacunae in our research.

2.3. Applications of Evolutionary Game Theory. Scholars' applications of evolutionary game theory among stakeholders bring inspirations to this study. Evolutionary game theory is a successful mathematical framework geared towards understanding the selections that affect the evolution of the strategies of agents engaged in interactions with potential conflicts [37], fully take into account the behaviours of multiple participants, and analyse the interaction of behavioural changes of participants dynamically. It considers the bounded rationality of the decision-maker and is widely used in many fields [38]. Chen et al. built an evolutionary game model to consider green retrofitting from the perspective of green credit [39]. Yang used an evolutionary game to analyse the cooperative construction of international transport corridors [40]. Wu et al. built a complex model of an evolutionary game between the government and enterprises in a low-carbon network environment and studied the effect of government incentives for enterprises [41]. Luo and Zhao used an evolutionary game to find ways to reduce food waste [42]. It is a good tool to fulfill the expectation of maximizing stakeholder interests by predicting the behaviour of others to determine the most advantageous strategy [43].

2.4. Summary. In sum, an evolutionary game is an effective way to explore the regulatory mechanism of NHSA to reduce medical overuse, but the existing research focuses on using historical data to analyse the medical overuse from doctors or opinions from the perspective of NHSA's supervision. Therefore, we proposed an evolutionary game theory to construct a dynamic evolutionary game model between hospitals' medical overuse and NHSA supervision. We also considered patients' complaints as third-party supervision to investigate the supervisory mechanism for reducing medical overuse in the NHSA and hospitals. From the perspective of NHSA supervision, we explore the punishment-and-reward mechanism to ensure the stability of both sides. We also summarise countermeasures and suggestions conducive to reducing excessive medical treatment, to enable the medical insurance fund to play a better role.

3. Evolutionary Game Model

3.1. Problem Description. Medical overuse has increasingly attracted the attentions and discussions in the academic field. On the one hand, the NHSA's lack of professionalism makes it difficult to review the reasonableness of diagnosis and treatment, and hence, its supervision is insufficient [44]. In order to maximize the income, the hospital will increase the income of nondrug medical services through too many examinations and tests. On the other hand, the total revenue of the hospital can be expanded by allowing patients to make multiple visits [45]. The patient had less health-related knowledge, and misconception of medical overuse, doctor-patient communication, and information asymmetry will affect patients' medical overuse cognition, eventually leading to their overtreatment behavioural choices [46]. In summary, policy-makers are faced with the challenge of how to urge medical overuse. Thus, in order to comprehensively explore the relationship between NHSA and medical institutions, an evolutionary game model is developed.

3.1.1. Basic Assumption. Medical insurance departments and medical institutions face a very complex decision-making environment in attempting to reduce medical overuse. Therefore, for the convenience of analysis, some basic assumptions are set in advance as follows.

(1) Only Two Parties in the Game. NHSA and medical institutions are the two participants in the game model, and they are all bounded rational.

In this study, we assumed the relationship between doctors and medical institutions is a traditional principal-agent relationship; i.e., the behaviour of doctors is consistent with that of medical institutions [47].

(2) Behaviour Strategies. There are two kinds of supervision strategies that NHSA can offer, i.e., strict and loose. Strict supervision generally means that the NHSA will expend considerable money, time, and human resources to regulate doctors' behaviour, by means such as increasing the frequency of spot checks and appointing inspectors. Loose supervision implies that the NHSA will not take additional restrictive measures but conduct some routine inspections and so on. Medical institutions also have two kinds of strategies, i.e., medical overuse and appropriate medical use. Appropriate medical use means that the doctor will make a diagnosis and treatment plan that is most suitable

Table 1: Parameter symbol descriptions in the evolutionary game.

Stakeholders	Parameters	Descriptions
Medical institutions	R_1	Revenue of appropriate medical use
	R_2	Revenue of medical overuse
	R_3	Revenue of reputation given by NHSA because of appropriate medical use
	F	Penalty from NHSA because of medical overuse behaviour discovered
	M	Reputation loss because of medical overuse behaviour discovered such as decreased credibility and reduced number of patients
	θ	Probability of patients questioning and complaining about medical institutions' medical overuse
	q	Probability of medical institutions adopting appropriate medical use
NHSA	C_1	All the costs of NHSA offering strict supervision
	C_2	Cost and loss to NHSA's verification behaviour because of medical overuse behaviour complained by patients, mainly including: verification cost, credibility decline, and reputation loss
	p	Probability of NHSA offering strict supervision

for the patient according to the patient's condition. Conversely, medical overuse refers to doctors tending to provide excessive medical treatment to get extra benefits, such as some unnecessary drug prescriptions and medical examination.

3.1.2. Parameter Assumption

(1) Assumption 1. Assume that NHSA offers "strict supervision" at a rate of p and "loose supervision" at a rate of $1 - p$; assume that medical institutions choose "appropriate medical use" at a rate of q and choose "medical overuse" at a rate of $1 - q$, where $p, q \in [0, 1]$.

(2) Assumption 2. The cost of NHSA is C_1 when it offers strict supervision and 0 when it offers loose supervision. Under strict supervision, the administration can detect medical overuse behaviour before patients.

(3) Assumption 3. If and when the medical institution's excessive diagnosis and treatment behaviour is discovered, the NHSA will impose a penalty of F upon the medical institution, which will cause the hospital to incur a reputation loss of M.

(4) Assumption 4. The marginal revenue of appropriate medical use in medical institutions is R_1, and the marginal revenue of medical overuse is R_2, with $R_1 < R_2$. The profit gap is then denoted as $\Delta R = R_2 - R_1$. Appropriate medical use behaviours of medical institutions can also improve an institution's reputation, attracting more patients, and the revenue associated with reputation is R_3.

(5) Assumption 5. Under loose supervision, patients will question the medical overuse behaviour of medical institutions and have a probability of θ $(0 < \theta < 1)$ of reporting it to the NHSA.

(6) Assumption 6. After the patients' reporting to NHSA, the administration needs to conduct further verification, which would cause reputation loss, and the cost of verification and loss are recorded as C_2. The model parameters are summarised in Table 1, and the payoff matrix of the evolutionary game is displayed in Table 2.

3.2. Analysis of Evolutionary Stable Strategies. Variable G_1 represents the expected payoff of NHSA when choosing the "strict supervision" strategy, while G_2 represents the expected payoff of NHSA when choosing the "loose supervision" strategy, and $\bar{G}$ represents the average expected payoff. According to the assumptions and Tables 1 and 2, G_1, G_2, and $\bar{G}$ are as follows:

$$G_1 = (-C_1 + F) - qF, \tag{1}$$

$$G_2 = \theta(1 - q)(F - C_2), \tag{2}$$

$$\bar{G} = pG_1 + (1 - p)G_2. \tag{3}$$

Similarly, variable E_1 represents the expected payoff of medical institutions when choosing the "appropriate medical use" strategy, E_2 represents the expected payoff of medical institutions when choosing the "medical overuse" strategy, and $\bar{E}$ represents the average expected payoff. According to the assumptions and Tables 1 and 2, E_1, E_2, and $\bar{E}$ are as follows:

$$E_1 = pR_3 + R_1, \tag{4}$$

$$E_2 = -p(1 - \theta)(F + M) + [R_2 - \theta(F + M)], \tag{5}$$

$$\bar{E} = qE_1 + (1 - q)E_2. \tag{6}$$

Table 2: The payoff matrix of the model.

		Medical institutions	
		Appropriate medical use (q)	Medical overuse ($1-q$)
NHSA	Strict supervision (p)	$-C_1, R_1+R_3$	$-C_1+F, R_2-F-M$
	Loose supervision ($1-p$)	$0, R_1$	$\theta(F-C_2), R_2-\theta(F+M)$

Table 3: The det J and trac J at each LEP.

LEP	det J	trac J
(0,0)	$[(1-\theta)F+\theta C_2-C_1][R_1-R_2+\theta(F+M)]$	$F-\theta C_2-C_1+R_1-R_2+\theta M$
(0,1)	$C_1[R_1-R_2+\theta(F+M)]$	$-[R_1-R_2+\theta(F+M)+C_1]$
(1,0)	$-[(1-\theta)F+\theta C_2-C_1](R_1-R_2+R_3+F+M)$	$R_1-R_2+R_3+M-\theta F-\theta C_2$
(1,1)	$-(R_1-R_2+R_3+F+M)C_1$	$C_1-(R_1-R_2+R_3+F+M)$
(p^*,q^*)	-AB	0

Note: AB denotes $((R_1-R_2+R_3+F+M)*[R_1-R_2+\theta(F+M)])/(R_3+(1-\theta)(F+M))*(C_1[(1-\theta)F+\theta C_2-C_1])/((1-\theta)F+\theta C_2)$.

Based on the principles of evolutionary games, the game dynamic replication equations between medical institutions and NHSA are as follows [48]:

$$\begin{cases} F(p)=\dfrac{dp}{dt}=p\left(G_1-\bar{G}\right)=p(1-p)\{(1-q)[(1-\theta)F+\theta C_2]-C_1\}, \\ F(q)=\dfrac{dq}{dt}=q\left(E_1-\bar{E}\right)=q(1-q)\{p[R_3+(1-\theta)(F+M)]+[R_1-R_2+\theta(F+M)]\}. \end{cases} \tag{7}$$

The derivatives with respect to $F(p)$ and $F(q)$ are as follows:

$$\begin{cases} \dfrac{dF(p)}{dp}=(1-2p)\{(1-q)[(1-\theta)F+\theta C_2]-C_1\}, \\ \dfrac{dF(q)}{dq}=(1-2q)\{p[R_3+(1-\theta)(F+M)]+[R_1-R_2+\theta(F+M)]\}. \end{cases} \tag{8}$$

According to the stability theorem of differential equations, the equilibrium points of the replicator dynamic equations presented by (7) should satisfy $F(p)=F(q)=0$, and $\{(p,q)|0\le p,q\le 1\}$. Apparently, (0,0), (0,1), (1,0), and (1,1) are the four fixed equilibrium points. For convenience, let $p*=(R_2-R_1-\theta(F+M))/(R_3+(1-\theta)(F+M))$ and $q*=((1-\theta)F+\theta C_2-C_1)/((1-\theta)F+\theta C_2)$; then, (p^*,q^*) is also an equilibrium point when meeting the following conditions: $0\le(R_2-R_1-\theta(F+M))/(R_3+(1-\theta)(F+M))\le 1$ and $0\le((1-\theta)F+\theta C_2-C_1)/((1-\theta)F+\theta C_2)\le 1$.

According to the method proposed by Friedman [49], the stability at the equilibrium point of the evolution system can be judged by the local stability of the Jacobian matrix of the entire system. The Jacobian matrix of this system made of (7) is as follows:

$$J=\begin{bmatrix} \dfrac{\partial F(p)}{\partial p} & \dfrac{\partial F(p)}{\partial q} \\ \dfrac{\partial F(q)}{\partial p} & \dfrac{\partial F(q)}{\partial q} \end{bmatrix}=\begin{bmatrix} (1-2p)\{(1-q)[(1-\theta)F+\theta C_2]-C_1\} & -p(1-p)[(1-\theta)F+\theta C_2] \\ q(1-q)[R_3+(1-\theta)(F+M)] & (1-2q)\{p[R_3+(1-\theta)(F+M)]+[R_1-R_2+\theta(F+M)]\} \end{bmatrix}. \tag{9}$$

Table 4: The evolutionary stability of each LEP.

Scenarios	LEP	det J	trac J	State
Scenario 1: $R_1 - R_2 < \theta(F+M)$ $C_1 > (1+\theta)F + \theta C_2$	(0,0)	—	Uncertain	Saddle point
	(0,1)	+	—	ESS
	(1,0)	+	+	Unstable
	(1,1)	—	Uncertain	Saddle point
Scenario 2: $\theta(F+M) < R_2 - R_1 < R_3 + F + M$ $C_1 > (1+\theta)F + \theta C_2$	(0,0)	+	—	ESS
	(0,1)	—	Uncertain	Saddle point
	(1,0)	+	+	Unstable
	(1,1)	—	Uncertain	Saddle point
Scenario 3: $R_2 - R_1 > R_3 + F + M$, $C_1 > (1+\theta)F + \theta C_2$	(0,0)	+	—	ESS
	(0,1)	—	Uncertain	Saddle point
	(1,0)	—	Uncertain	Saddle point
	(1,1)	+	+	Unstable
Scenario 4: $R_2 - R_1 < \theta(F+M)$, $C_1 < (1+\theta)F + \theta C_2$	(0,0)	+	+	Unstable
	(0,1)	+	—	ESS
	(1,0)	—	Uncertain	Saddle point
	(1,1)	—	Uncertain	Saddle point
Scenario 5: $\theta(F+M) < R_2 - R_1 < R_3 + F + M$ $C_1 < (1+\theta)F + \theta C_2$	(0,0)	—	Uncertain	Saddle point
	(0,1)	—	Uncertain	Saddle point
	(1,0)	—	Uncertain	Saddle point
	(1,1)	—	Uncertain	Saddle point
	(p^*,q^*)	+	0	Central point
Scenario 6: $R_2 - R_1 > R_3 + F + M$ $C_1 < (1+\theta)F + \theta C_2$	(0,0)	—	Uncertain	Saddle point
	(0,1)	—	Uncertain	Saddle point
	(1,0)	+	—	ESS
	(1,1)	+	+	Unstable

Table 5: Relationship between ESS and levels of profit gap and supervision cost.

Level of profit gap	Level of supervision cost	Equilibrium stable strategies	
		NHSA	Medical institutions
High	High	Loose supervision	Medical overuse
	Low	Strict supervision	Medical overuse
Medium	High	Loose supervision	Medical overuse
	Low	—	—
Low	High	Loose supervision	Appropriate medical use
	Low	Loose supervision	Appropriate medical use

The local equilibrium points (LEP) of the replicated dynamic system are judged as an evolutionarily stable strategy (ESS) if it satisfies the following conditions: det $J > 0$ and trac $J < 0$, where det J and trac J denote the determinant and trace of J, respectively. Meanwhile, to resist disturbance in the stable state, the ESS must satisfy the conditions $(dF(p))/dp < 0$ and $(dF(q))/dq < 0$. det J and trac J for each LEP are presented in Table 3.

3.3. Stability Analysis of Equilibrium Point. Furthermore, the stability of equilibrium points in the government–enterprise evolutionary game system will be analysed according to various value ranges of parameters. The det J and trac J of every point's Jacobi matrix point are calculated, and its state is discussed.

Scenario 1: $R_2 - R_1 < \theta(F + M_1)$, $C_1 > (1-\theta)F + \theta C_2$

At this point, there are four fixed equilibrium points of the evolutionary game dynamic replication equations, i.e., (0,0), (0,1), (1,0), and (1,1).

For the hospital, the gap between the excess profit obtained through medical overuse and the profit obtained by appropriate medical use is less than the expected fines and reputation loss caused by patient complaints reporting medical overuse. Therefore, hospitals are more likely to

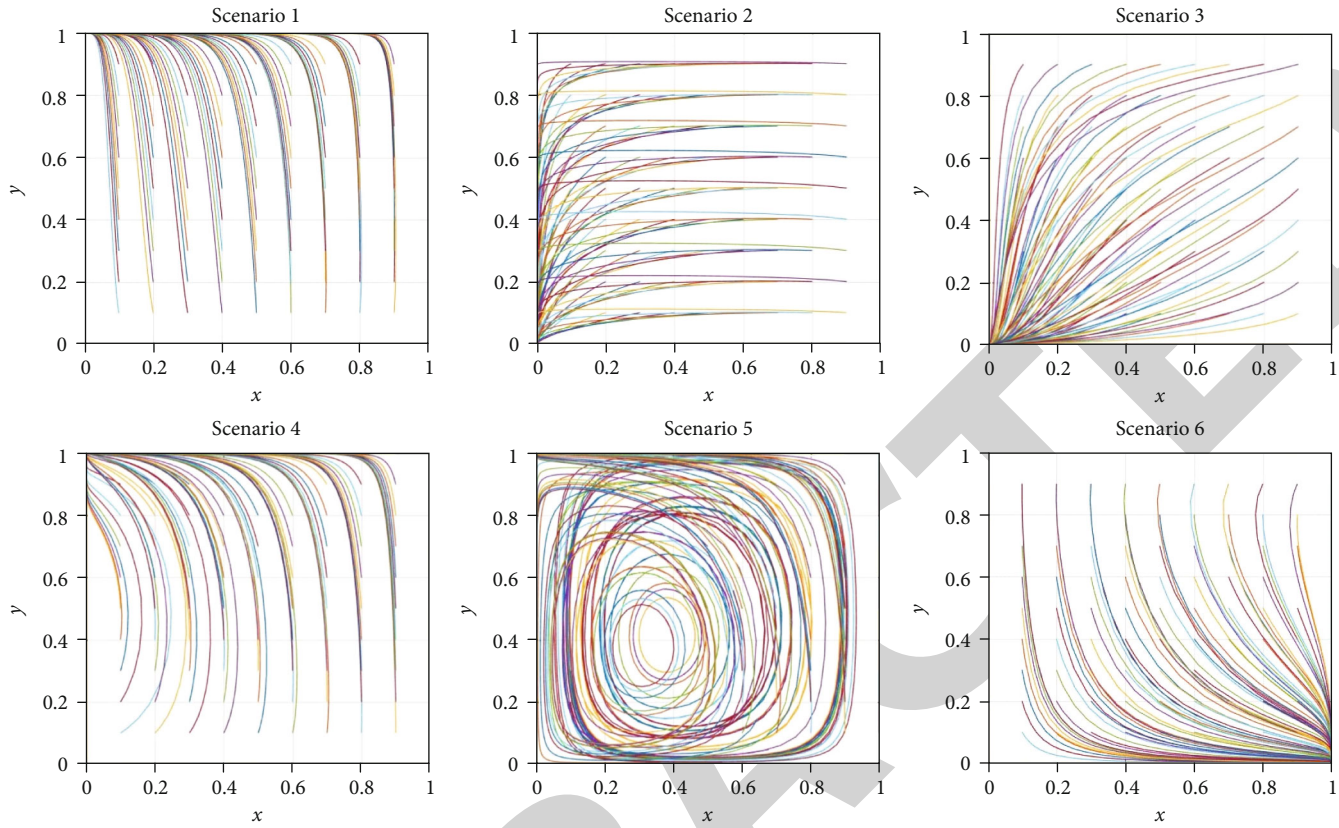

Figure 1: The evolutionary processes of six scenarios.

Table 6: Initial parameters setting in Scenario 5.

Parameters	R_1	R_2	R_3	F	M	C_2	θ	C_1
Scenario 5	90	140	20	40	35	20	0.6	20

Table 7: Initial parameter setting in Scenario 6.

Parameters	R_1	R_2	R_3	F	M	C_2	θ	C_1
Scenario 6	80	150	10	40	15	20	0.6	5

choose appropriate medical use, while NHSA has a probability of $1-\theta$ of being fined and incurring reputation loss from loose supervision, which is the cost of less-than-strict supervision. Therefore, NHSA tends to choose loose supervision. For Scenario 1, as presented in Table 4, point (0,1) is the ESS of the system, namely, {loose supervision, appropriate medical use}.

Scenario 2: $\theta(F+M) < R_2 - R_1 < R_3 + F + M,\ C_1 > (1-\theta)F + \theta C_2$

At this point, there are four fixed equilibrium points of the evolutionary game dynamic replication equations, which are (0,0), (0,1), (1,0), and (1,1).

For the hospital, the difference between the profit obtained by medical overuse and the profit obtained by appropriate medical use is less than the revenue caused by reputation, but higher than the fines and reputation loss caused by medical overuse reported via patient complaints. Under circumstances where the medical overuse strategy is more profitable, hospitals are more likely to use medical resources excessively. For NHSA, the cost caused by fines and reputation loss is less than strict supervision. NHSA is more likely to choose loose supervision. For Scenario 2, as presented in Table 4, point (0,0) is the ESS of the system, namely, {loose supervision, medical overuse}.

Scenario 3: $R_2 - R_1 > R_3 + F + M,\ C_1 > (1-\theta)F + \theta C_2$

At this point, there are four fixed equilibrium points of the evolutionary game dynamic replication equations, which are (0,0), (0,1), (1,0), and (1,1).

For the hospital, the difference between the profit obtained through medical overuse and the profit obtained by appropriate medical use is higher than the sum of reputation earnings by appropriate medical use and the fines and reputation loss caused by medical overuse. Under such circumstances, where the medical overuse strategy is more profitable, hospitals are more likely to choose excessive treatments. However, there is probability of $1-\theta$ that NHSA will fine them and they will suffer a loss of reputation under loose supervision. The high cost of strict supervision enforces the administration to choose the loose strategy. For Scenario 3, as presented in Table 4, point (0,0) is the

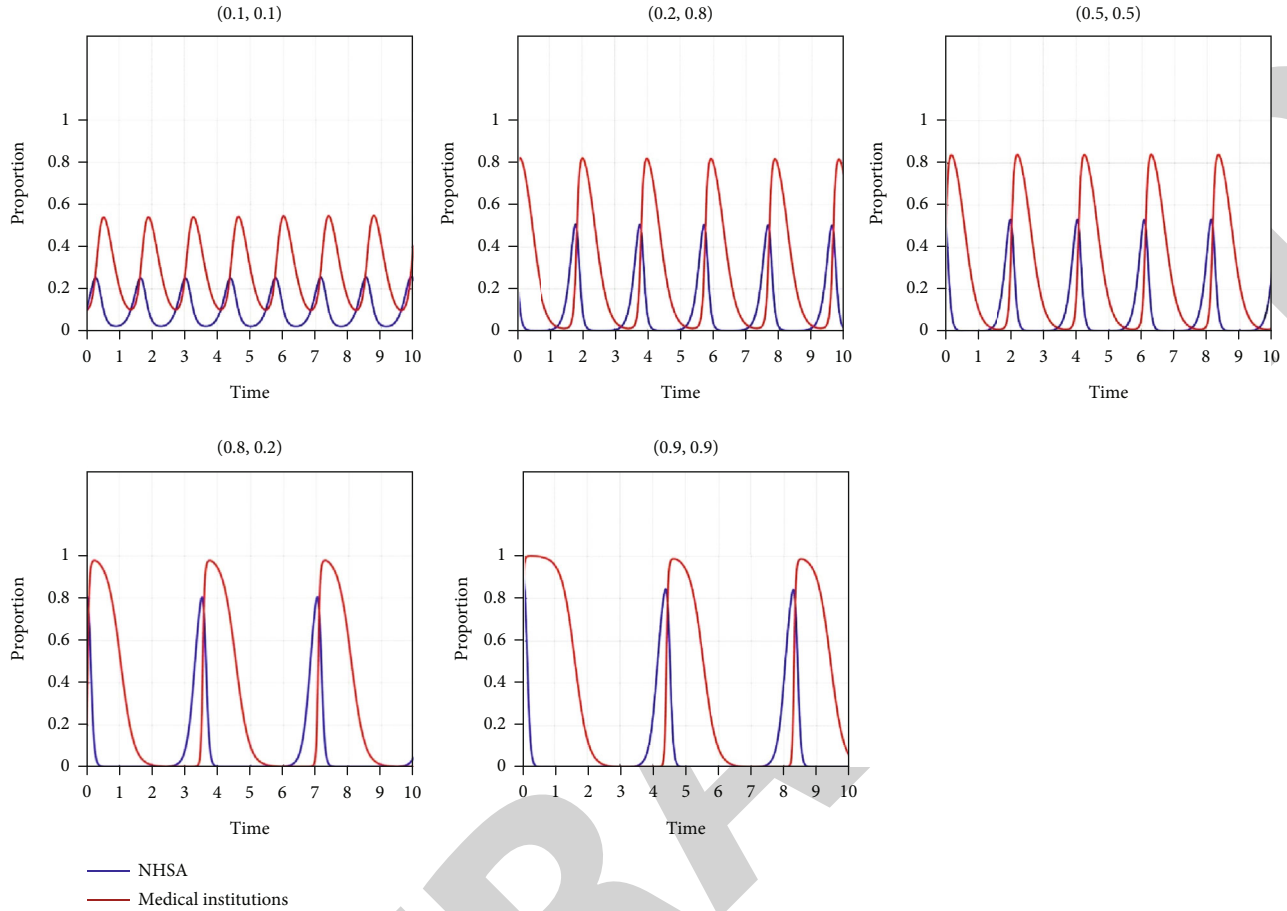

Figure 2: Evolution results of Scenario 5 under different behaviour ratios.

ESS of the system, namely, {loose supervision, medical overuse}.

Scenario 4: $R_2 - R_1 < \theta(F + M)$, $C_1 < (1 - \theta)F + \theta C_2$

At this point, there are four fixed equilibrium points of the evolutionary game dynamic replication equations, i.e., (0,0), (0,1), (1,0), and (1,1).

For the hospital, the difference between the profit obtained by medical overuse and the profit obtained by moderate treatment is less than the sum of reputation earnings by appropriate medical use and the fines and reputation loss caused by medical overuse. Without profits to earn, hospitals tend to adopt appropriate medical use. With fines and reputation loss at a probability of $1 - \theta$ from loose supervision, NHSA tends to adopt strict supervision with a lower cost. For Scenario 4, as presented in Table 4, point (0,1) is the ESS of the system, namely, {loose supervision, appropriate medical use}.

Scenario 5: $\theta(F + M) < R_2 - R_1 < R_3 + F + M$, $C_1 < (1 - \theta)F + \theta C_2$

At this point, there are five fixed equilibrium points of the evolutionary game dynamic replication equations, i.e., (0,0), (0,1), (1,0), (1,1), and (p^*, q^*).

For the hospital, the gap between the profit obtained by medical overuse and the profit obtained by appropriate medical use is less than the revenue associated with reputation, but higher than the fines and reputation loss caused by medical overuse. Under the circumstances, hospitals are more likely to use medical resources overly. However, for NHSA, the strict supervision is less than the cost caused by fines and reputation loss. NHSA is more likely to choose strict supervision. The strategy choices between the two sides are contradictory. For Scenario 5, as presented in Table 4, there is no ESS in the system; i.e., NHSA and medical institutions both choose a mixed strategy.

Scenario 6: $R_2 - R_1 > R_3 + F + M$, $C_1 < (1 - \theta)F + \theta C_2$

At this point, there are four fixed equilibrium points of the evolutionary game dynamic replication equations, i.e., (0,0), (0,1), (1,0), and (1,1).

For the hospital, the difference between the profit obtained by medical overuse and the profit obtained by appropriate medical use is not only higher than the revenue caused by reputation but also higher than the fines and reputation loss caused by medical overuse reported through patient complaints. With profits to earn, hospitals are more likely to choose overuse. The cost of fines and reputation loss from loose supervision is higher than that of strict supervision. Therefore, the administration tends to regulate strictly. For Scenario 6, as presented in Table 4, point (1,0)

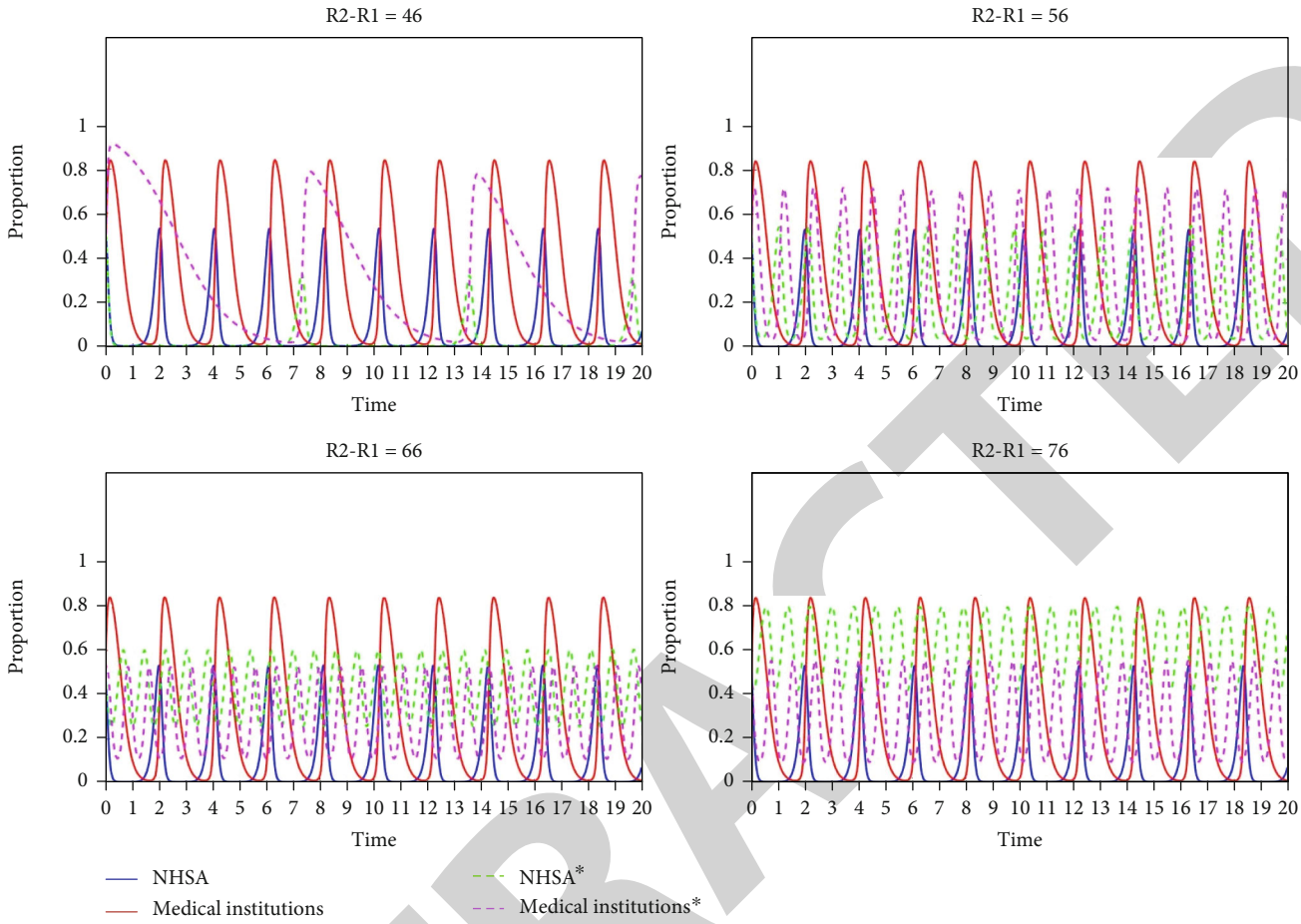

Figure 3: Evolution process of Scenario 5 under different ΔR values.

is the ESS of the system, namely, {strict supervision, medical overuse}.

In the study, we divide the profit gap into three levels, high, medium, and low, and divide the supervision cost into two levels, high and low, thus proposing six scenarios. Through the analysis above, the results corresponding to each scenario are listed in Table 5.

(1) High profit gap

When the profits of medical overuse are high enough, medical institutions will choose medical overuse regardless of whether NHSA takes regulatory measures. For hospitals, the promotion of profit is far higher than the inhibition of supervision of NHSA. NHSA's choice of strategy totally depends on the cost of supervision: the higher the cost, the lower the level of supervision.

(2) Medium profit gap

When the profit of medical overuse is at a medium level and the supervision cost is at a low level, NHSA naturally tends to supervise loosely and medical institutions tend to gain profit in such a low-risk regulatory environment, whereas when the supervision cost is low, the strategy is mixed.

(3) Low profit gap

When the profits of medical overuse are low enough, medical institutions will choose appropriate medical use regardless of NHSA's loose supervision. This indicates that without the motivation of profit, medical institutions will naturally promote appropriate medical use. Meanwhile, the medical institutions' strategy also affects NHSA's decisions. In such a scenario, regulatory measures are unnecessary. Therefore, even when the supervision cost changes, NHSA will still choose loose supervision. Under this condition, the strategic choice of both sides reaches the ideal state of medical supervision, i.e., to supervise without exertion.

4. Simulation Analysis

4.1. Evolutionary Simulation of the Game System. Based on the analysis above, we can obtain the evolutionary game results between NHSA and medical institutions under various scenarios, but the analysis does not explain how to achieve these results. We will use MATLAB as an analysis tool to simulate the dynamic evolution of the strategies of NHSA and medical institutions.

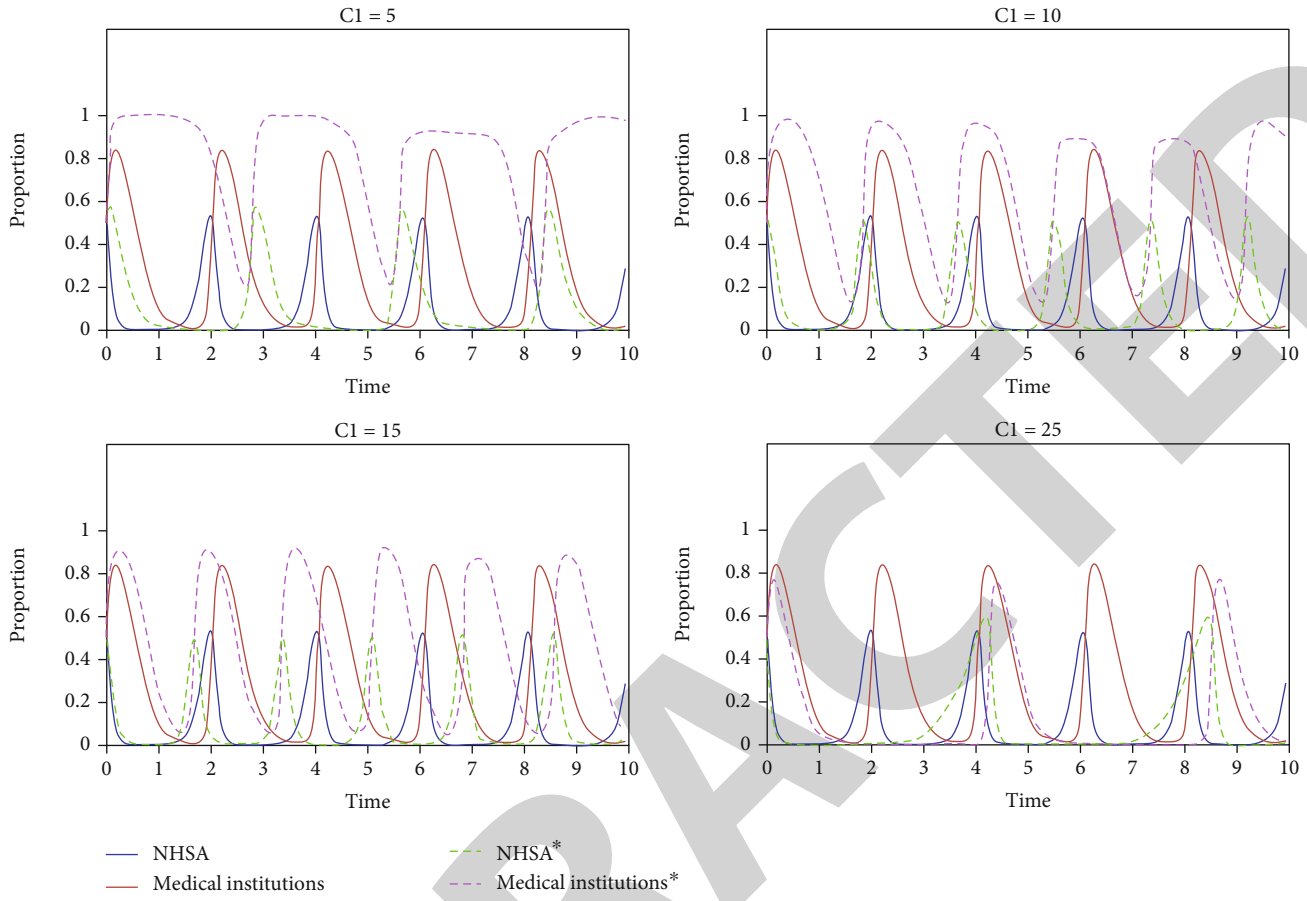

Figure 4: Evolution process of Scenario 5 under different C_1 values.

Our research is mainly based on the background of China's medical insurance payment method, fee-for-service. We have conducted surveys in medical insurance bureaus in many cities in southwest China and summarised four kinds of scenarios as below. These situations can represent the reality of the regulation of NHSA in China. Through simulation with parameters under different scenarios, we can provide reference opinions for policy-makers.

In this section, six simulation experiments are conducted to explore the dynamic evolution of the strategies, as shown in Figure 1. According to the results, we can divide all scenarios into four kinds.

(1) Profit gap at low level and supervision cost at any level

For Scenario 1 and Scenario 4, the unique ESS under the two situations is the same (0,1). As the profit gap between medical overuse and appropriate medical use is not large enough, hospitals will always choose the "appropriate medical use" strategy. At this time, no matter how high the cost that NHSA needs to pay, it will choose the "loose supervision" policy.

(2) Profit gap at medium and high level and supervision cost at high level

For Scenario 2 and Scenario 3, (0,0) is the ESS. In both cases, NHSA will pay a high cost for governing strictly so that "loose supervision" is the behaviour strategy. Naturally, with no limitation on regulation and considerable profits brought by medical overuse, these medical institutions will engage in medical overuse.

(3) Profit gap at high level and supervision cost at low level

Under Scenario 6, the ESS is (1,0). The low cost of strict supervision drives NHSA to supervise strictly, while the high profits brought by medical overuse make the hospitals choose to treat excessively.

(4) Profit gap at medium level and supervision cost at low level

Specifically, there is no ESS for Scenario 5. At this time, increasing the profit gap will drive the system to evolve to (1,0). Decreasing the profit gap will drive the system to

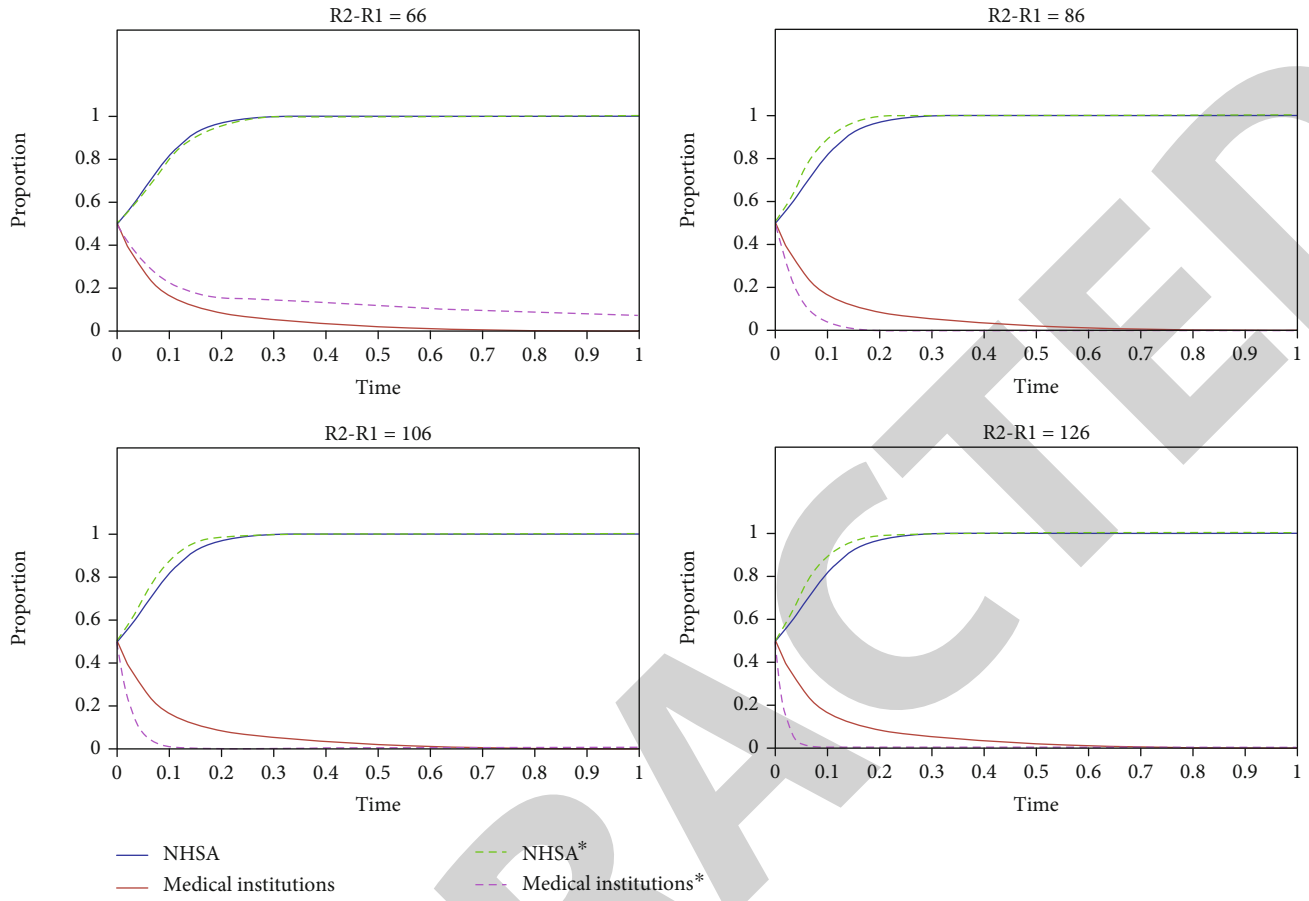

Figure 5: Evolution process of Scenario 6 under different ΔR values.

evolve to (0,1). Increasing the supervision cost will drive the system to evolve to (0,0).

4.2. Numerical Simulation of Stability Influencing Factors. In the real world, hospitals are always driven to engage in medical overuse by the high profit gap, and with the limitations of high supervision costs, administration's supervision is mainly cursory and infrequent. Comparatively, the hypothesis of Scenario 6 is more consistent with the real world. Second, specifically, there is no ESS in Scenario 5. Therefore, we will conduct some numerical experiments for further analysis. The following simulation analysis background is used to set the relevant parameters to meet the conditions corresponding to Scenario 5 and Scenario 6. The data of the parameters setting, as shown in Tables 6 and 7, is first collected from field survey on medical institutions and local Healthcare Security Administration in southwestern China. The data is private and not allowed to be released to public. Via expert interviews method, we get a rough ratio of several costs and profits involved in the research and then we processed the rough data collected according to the model.

4.2.1. Impact of Initial Intentions on Evolution in Scenario 5. We will analyse the evolution trend of Scenario 5 for further understanding. Based on the actual situation, the initial parameters are set in Table 6.

First, it is not difficult to realise that the behaviour of the participants is cyclical and there is no stable strategy. As can be seen from Figure 2, the preferences of NHSA and the medical institutions are not clear. No matter what the initial status is, the proportion of strategic choice between the two sides fluctuates a little, and the medical institutions always tend to adopt appropriate medical use at the beginning.

When the likelihood of NHSA choosing "strict supervision" as the initial strategy is higher, the fluctuation cycle of medical institutions' strategy choice is longer. Similarly, the larger the proportion of medical institutions choosing the initial strategy of "medical overuse," the longer the fluctuation cycle of NHSA's strategy choice.

4.2.2. Impact of Profit and Cost on Evolution in Scenario 5. Next, we conduct several numerical experiments to derive the impacts of parameters on the evolutionary results. We fix other parameters and conduct experiments when $\Delta R =$ 46, 56, 66, and 76 and $C_1 = 5$, 10, 15, and 25. All initial probabilities $p = q = 0.5$. The dashed line represents the evolution process when the parameters change, and the solid line represents the original evolution process of both sides.

The increase of the profit gap ΔR will shorten the evolutionary cycle, as shown in Figure 3. With the increase of

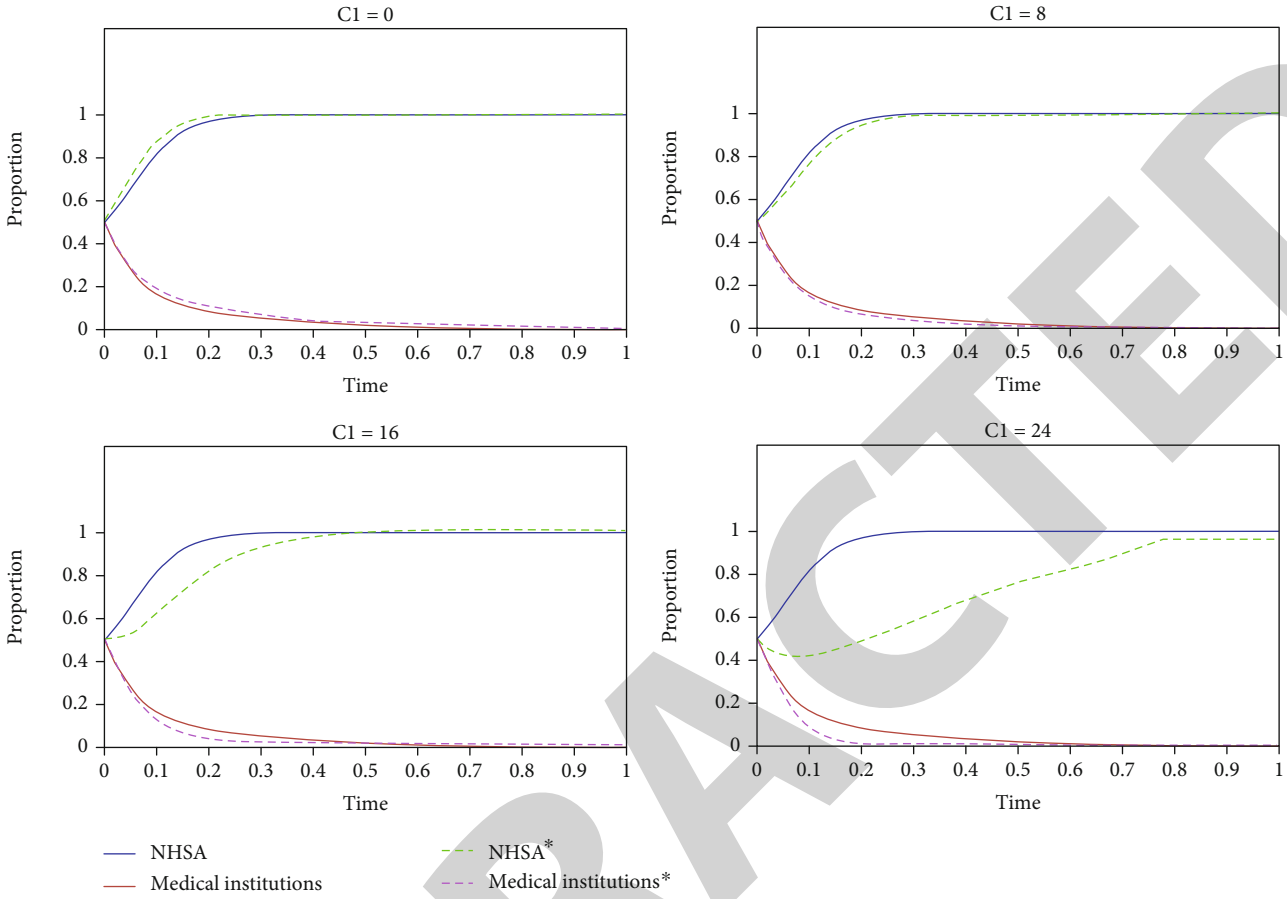

Figure 6: Evolution process of Scenario 6 under different C_1 values.

supervision cost C_1, the evolutionary cycle of the game gets longer, and then, it gets shorter after reaching a particular value, as shown in Figure 4.

Specifically, when ΔR reaches a certain value, the strategy of NHSA will change from "loose" to "strict," and the strategy of medical institutions will change from "appropriate medical use" to "medical overuse." It is worth noting that the increase of C_1 will ultimately make medical institutions adopt "medical overuse" as their policy.

4.2.3. Impact of Profit, Cost, and Probability of Complaint on Evolution in Scenario 6. To better understand the evolution of Scenario 6, we analyse the impacts of three parameters on the evolutionary results separately, including the supervision cost C_1, the profit gap ΔR, and the probability of patients' complaints, θ.

Based on the actual situation, the initial parameters are set in Table 7.

The first experiments are conducted when $\Delta R = 66$, 86, 106, and 126. The second experiment is conducted when $C_1 = 0$, 8, 16, and 24. The third experiment is conducted when $\theta = 0.1$, 0.3, 0.5, and 0.7. For all experiments, the initial probabilities $p = q = 0.5$.

Similar to the analysis above, the dashed line represents the evolution process when the parameters change, and the solid line represents the original evolution process of both sides. As is shown in Figure 5, with the increase of the profit gap, the convergence speed of NHSA becomes slightly slow. Conversely, the convergence speed of medical institutions becomes fast clearly with the profit gap increasing. The result shows that the excessive profit gap brought by medical overuse is a main contributor for hospitals to engage in medical overuse, but not a key impact factor of NHSA's strategy choice.

As shown in Figure 6, the convergence rate of the medical institution's strategy increases with the increase of supervision cost. However, the change of supervision cost has little effect on the strategy choice of the medical institution. By contrast, the convergence rate of NHSA's strategy decreases heavily with the increase of supervision cost. When $C_1 = 24$, the tendency of NHSA's strategy drops to a certain degree but then rises and converges to the ESS. The result shows that the higher the supervision cost, the lower the willingness of NHSA to supervise strictly, and when the cost reaches a particular value, NHSA will finally choose "loose supervision."

As shown in Figure 7, the convergence rate of both sides' strategies decreases with the increase of the probability of patients questioning and complaining. The more likely patients are to report, the more cautious medical institutions are, so that the less likely they are to adopt medical overuse. However, the more likely patients are to report, the more

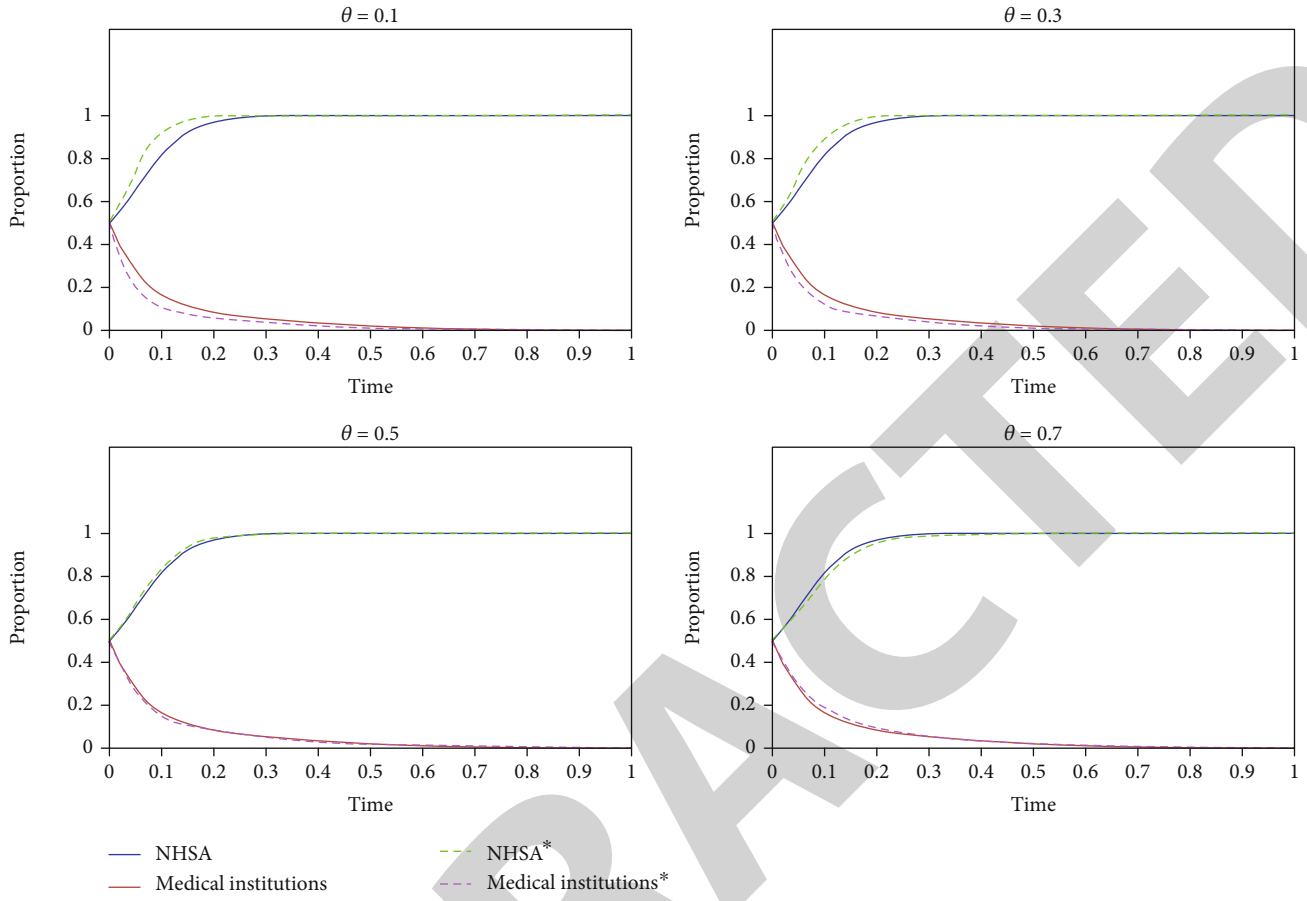

Figure 7: Evolution process of Scenario 6 under different θ values.

likely NHSA is to rely on patients' supervision, and the less it is involved in supervision.

5. Conclusions

This study starts from bounded rationality, builds an evolutionary game model to study the relations between the NHSA and medical institutions, and reveals the dynamic evolution process between the supervision of NHSA and medical overuse of medical institutions. By analysing the evolutionary stable strategies, numerical studies are conducted and show good results. Through the numerical simulation and sensitive experiments under various scenarios, we obtain the following results:

(1) In the most common situation that the profit gap is at a medium level, the regulatory measures of NHSA work well. Medical institutions' strategies change as the supervision cost changes. When the supervision cost is high, medical institutions tend to choose medical overuse, otherwise choose appropriate medical use

(2) In the other two scenarios, regulatory measures of NHSA cannot work: if the profit gap is too high, the medical institution will definitely choose medical overuse. While if the profit gap is lower than the fines and reputation loss caused by medical overuse, the medical institution will choose appropriate medical use no matter a punishment mechanism is set or not

(3) Patient involvement in supervision exerted a significant impact on the strategies of medical institutions and NHSA. The more likely patients are to report, the less possibility NHSA is involved in supervision, and the less likely medical institutions are to adopt medical overuse

From the results of the study, we know that NHSA should strengthen supervision and issue relevant policies to curb behaviours such as prescribing excess drugs and medical tests. And NHSA should also improve the public's participation in health regulation. Multiple participation and supervision are key to preventing excessive diagnosis and treatment. To decrease medical overuse and rationalise hospital costs, supervision of hospitals by NHSA is essential. More research in this area is urgently needed. Specifically, we obtain some management insights as follows:

(1) It is necessary to establish a comprehensive medical insurance payment system to curb excessive medical

use and promote reasonable medical examination and treatment

(2) The authorities should consider how to reduce the cost of supervision by optimising the process systematically. In this manner, NHSA would supervise frequently so that the probability of medical overuse can be reduced

(3) Some activities on education of medical knowledge for the public should be carried out to enhance the awareness of the patients' cognitive status on excessive medical examination and treatment. NHSA should try its best to facilitate the supervision of the public through multiple channels

There are two potential directions that could be investigated in the future. First, since the supervision of the medical overuse involves patients, also considering patients as stakeholders and modelling as tripartite game can be studied. Second, as there are many different hospitals and institutions, competition and cooperation among medical institutions can be included.

Data Availability

No data were used to support this study.

Ethical Approval

The study does not involve human subjects and adheres to all current laws of China.

Conflicts of Interest

The authors report no conflict of interest concerning the materials or methods used in this study or the findings presented in this paper.

Acknowledgments

This project was sponsored by the National Natural Science Foundation of China (No. 72001153, No. 72104076, and No. 71902058) and the Excellent Youth Scientific Research Foundation of Hunan Education Department (No. 20B155).

References

[1] M. L. Parchman, L. Palazzo, B. T. Austin, P. Blasi, and E. Ganos, "Taking action to address medical overuse: common challenges and facilitators," *The American Journal of Medicine*, vol. 133, no. 5, pp. 567–572, 2020.

[2] S. Schleicher, P. Bach, K. Matsoukas, and D. Korenstein, "Medication overuse in oncology: current trends and future implications for patients and society," *The Lancet Oncology*, vol. 19, no. 4, pp. e200–e208, 2018.

[3] S. Brownlee, K. Chalkidou, J. Doust et al., "Evidence for overuse of medical services around the world," *The Lancet (British Edition)*, vol. 390, no. 10090, pp. 156–168, 2017.

[4] A. H. Oakes, A. P. Sen, and J. B. Segal, "the impact of global budget payment reform on systemic overuse in Maryland," *Healthcare: The Journal of Delivery Science and Innovation*, vol. 8, no. 4, article 100475, 2020.

[5] Y. Zhang, Z. Zhou, and Y. Si, "When more is less: what explains the overuse of health care services in China?," *Social Science & Medicine (1982)*, vol. 232, pp. 17–24, 2019.

[6] W. H. Shrank, T. L. Rogstad, and N. Parekh, "Waste in the US health care system: estimated costs and potential for savings," *JAMA: The Journal of the American Medical Association*, vol. 322, no. 15, pp. 1501–1509, 2019.

[7] S. C. Chimonas, K. L. Diaz-Macinnis, A. N. Lipitz-Snyderman, B. A. Brooke, and D. R. Korenstein, "Why not? Persuading clinicians to reduce overuse," *Mayo Clinic Proceedings: Innovations, Quality & Outcomes*, vol. 4, no. 3, pp. 266–275, 2020.

[8] P. A. Samuelson and W. D. Nordhausen, *Economics*, Posts and Telecommunications Presssss, Beijing, 2004.

[9] Y. Z. Han, K. Wang, and K. Zheng, "Analysis on the root causes and countermeasures of excessive medical treatment in public hospitals," *Chinese Hospital Management*, vol. 9, pp. 16-17, 2010.

[10] Z. Chen, C. P. Barros, and X. Hou, "Has the medical reform improved the cost efficiency of Chinese hospitals?," *The Social Science Journal*, vol. 53, no. 4, pp. 510–520, 2016.

[11] Z. X. Zhu, Y. S. Yang, and T. Y. Wang, "Study on the balance of income and expenditure of medical insurance fund for urban workers: empirical analysis based on the data of C city," *China Public Administration Review*, vol. 14, no. 1, pp. 20–37, 2013.

[12] Y. C. Yang and J. Q. Chao, "The summary of single disease paying and DRGs prepay model," *Chinese Health Economics*, vol. 27, no. 6, pp. 66–70, 2008.

[13] M. L. Wang, "China's health care system at a crossroads in the World Trade Organization framework," in *WTO, Globalization and China's Health Care System*, pp. 1–39, Palgrave Macmillan, London, 2007.

[14] P. Davey, C. A. Marwick, C. L. Scott et al., "Interventions to improve antibiotic prescribing practices for hospital inpatients," *Cochrane Database of Systematic Reviews*, vol. 2017, no. 2, article CD003543, 2017.

[15] M. André, Å. Schwan, and I. Odenholt, "Upper respiratory tract infections in general practice: diagnosis, antibiotic prescribing, duration of symptoms and use of diagnostic tests," *Scandinavian Journal of Infectious Diseases*, vol. 34, no. 12, pp. 880–886, 2002.

[16] M. Bansal, F. D. Patel, B. K. Mohanti, and S. C. Sharma, "Setting up a palliative care clinic within a radiotherapy department: a model for developing countries," *Supportive Care in Cancer*, vol. 11, no. 6, pp. 343–347, 2003.

[17] V. M. Vaughn, D. L. Giesler, D. Mashrah et al., "Pharmacist gender and physician acceptance of antibiotic stewardship recommendations: an analysis of the reducing overuse of antibiotics at discharge home intervention," *Infection Control and Hospital Epidemiology*, pp. 1–8, 2022.

[18] M. O'Keeffe, A. Barratt, C. Maher et al., "Media coverage of the benefits and harms of testing the healthy: a protocol for a descriptive study," *BMJ Open*, vol. 9, no. 8, article e029532, 2019.

[19] A. Haslam, K. Powell, and V. Prasad, "How often do medical specialties question the practices that they perform? An empirical, cross-sectional analysis of the published literature," *Inquiry (Chicago)*, vol. 58, article 469580211061034, 2021.

[20] T. Copp, T. Dakin, B. Nickel et al., "Interventions to improve media coverage of medical research: a codesigned feasibility

Hindawi
Computational and Mathematical Methods in Medicine
Volume 2023, Article ID 9823636, 1 page
https://doi.org/10.1155/2023/9823636

Retraction

Retracted: Screening of Differentially Expressed Iron Death-Related Genes and the Construction of Prognosis Model in Patients with Renal Clear Cell Carcinoma

Computational and Mathematical Methods in Medicine

Received 17 October 2023; Accepted 17 October 2023; Published 18 October 2023

This article has been retracted by Hindawi following an investigation undertaken by the publisher [1]. This investigation has uncovered evidence of one or more of the following indicators of systematic manipulation of the publication process:

(1) Discrepancies in scope

(2) Discrepancies in the description of the research reported

(3) Discrepancies between the availability of data and the research described

(4) Inappropriate citations

(5) Incoherent, meaningless and/or irrelevant content included in the article

(6) Peer-review manipulation

The presence of these indicators undermines our confidence in the integrity of the article's content and we cannot, therefore, vouch for its reliability. Please note that this notice is intended solely to alert readers that the content of this article is unreliable. We have not investigated whether authors were aware of or involved in the systematic manipulation of the publication process.

In addition, our investigation has also shown that one or more of the following human-subject reporting requirements has not been met in this article: ethical approval by an Institutional Review Board (IRB) committee or equivalent, patient/participant consent to participate, and/or agreement to publish patient/participant details (where relevant).

Wiley and Hindawi regrets that the usual quality checks did not identify these issues before publication and have since put additional measures in place to safeguard research integrity.

We wish to credit our own Research Integrity and Research Publishing teams and anonymous and named external researchers and research integrity experts for contributing to this investigation.

The corresponding author, as the representative of all authors, has been given the opportunity to register their agreement or disagreement to this retraction. We have kept a record of any response received.

References

[1] D. Wu, Z. Xu, Z. Shi et al., "Screening of Differentially Expressed Iron Death-Related Genes and the Construction of Prognosis Model in Patients with Renal Clear Cell Carcinoma," *Computational and Mathematical Methods in Medicine*, vol. 2022, Article ID 4456987, 10 pages, 2022.

Hindawi
Computational and Mathematical Methods in Medicine
Volume 2022, Article ID 4456987, 10 pages
https://doi.org/10.1155/2022/4456987

Research Article

Screening of Differentially Expressed Iron Death-Related Genes and the Construction of Prognosis Model in Patients with Renal Clear Cell Carcinoma

Ding Wu,[1] Zhenyu Xu,[1] Zhan Shi,[2] Ping Li,[1] Huichen lv,[1] Jie Huang,[1] and Dian Fu[1]

[1]*Department of Urology, Jinling Hospital, Medical School of Nanjing University, Nanjing 210002, China*
[2]*The Comprehensive Cancer Centre of Drum Tower Hospital, Medical School of Nanjing University & Clinical Cancer Institute of Nanjing University, Nanjing 210008, China*

Correspondence should be addressed to Zhenyu Xu; zhenyuxu2022@163.com and Dian Fu; fudian1986@hotmail.com

Received 10 June 2022; Revised 13 July 2022; Accepted 9 August 2022; Published 30 August 2022

Academic Editor: Plácido R. Pinheiro

Objective. In this study, we used the TCGA database and ICGC database to establish a prognostic model of iron death associated with renal cell carcinoma, which can provide predictive value for the identification of iron death-related genes and clinical treatment of renal clear cell carcinoma. *Methods*. The gene expression profiles and clinical data of renal clear cell carcinoma and normal tissues were obtained in the TCGA database and ICGC database, and the differential genes related to iron death were screened out. The differential genes were screened out by single and multifactor Cox risk regression model. *R* software, "edge" package (version 4.0), was used to identify the DELs of 551 transcriptional gene samples and 522 clinical samples. The risk prediction model with genes was established to analyze the correlation between the genes in the established model and clinical characteristics, Through the final screening of iron death related genes, it can be used to predict the prognosis of renal clear cell carcinoma and provide advice for clinical targeted therapy. *Results*. Seven iron death differential genes (CLS2, FANCD2, PHKG2, ACSL3, ATP5MC3, CISD1, PEBP1) associated with renal clear cell carcinoma were finally screened and were refer to previous relevant studies. These genes are closely related to iron death and have great value for the prognosis of renal clear cell carcinoma. *Conclusion*. Seven iron death genes can accurately predict the survival of patients with renal clear cell carcinoma.

1. Background

According to the latest statistical data obtained by GLOBALCAN in 2020, renal cancer is still the main cause of death among cancer affected people [1]. There are about 2.2 million more cases of renal cancer in the world, of which 1.8 million cases of cancer patients die due to renal cancer, which is one of the malignant tumors with high incidence rate and mortality in the world. In recent years, the incidence rate and mortality of renal cancer have shown an obvious upward trend. Early renal cancer basically has no obvious symptoms. Clinically, most patients are diagnosed as advanced when symptoms appear, and the 5-year survival rate of patients with advanced renal cell carcinoma is not high. Renal clear cell carcinoma is a common renal cell carcinoma, which is the most common subtype of renal cell carcinoma in the world [2–4].

Although with the development of medical technology, the diagnosis, surgical treatment, radiotherapy, and molecular therapy of renal clear cell carcinoma are gradually progressing, which can enable patients with renal clear cell carcinoma to have a relatively long survival time [5]. However, the 5-year survival rate of patients with renal clear cell carcinoma is still at a low level. In recent years, tumor immunotherapy can kill tumor cells by regulating the immune defense system of the human body. Because of its advantages of small adverse reactions and strong specificity, it has been widely concerned by many scholars [5].

With the in-depth progress of research, new targets and technologies for immunotherapy continue to appear. The

discovery of iron death makes people have a new understanding of the formation and progress of tumor diseases. Iron death is a nonapoptotic cell death process with iron-dependent nature and characterized by the increase of intracellular reactive oxygen species discovered by Dixon in 2012 [6]. It is different from the conventional cell death mode of apoptosis and necrosis. It is an oxidation and antioxidant mechanism that converges in the mechanism of cell degradation, thus forming an iron death mechanism. The mechanism of iron death will change with the change of the effect of stressors [7]. Iron death is considered to be a cell death mode driven by the imbalance between the oxidative stress system and the antioxidant system. Iron death may have two main pathways, namely, exogenous and endogenous regulatory pathways. For example, the most common endogenous pathway is to induce lipid peroxidation process or mitochondrial dysfunction by regulating glutathione peroxidase 4 (GPX4). However, the occurrence and development of exogenous or endogenous pathways are closely related to various metabolic pathways and subcellular organelles (such as endoplasmic reticulum, mitochondria, golgi apparatus, lysosome, nucleus, and peroxisome). In the current research on drugs for the treatment of tumors through the iron death pathway, iron chelators antioxidants and other drugs can induce the iron death process of tumor cells to inhibit the proliferation and metastasis of tumor cells. Therefore, the discovery of iron death-related genes may become a new target for the treatment of related tumors in the future [8–10].

In this study, based on the gene expression profile of renal clear cell carcinoma in the TCGA public database and clinical-related data, the differentially expressed genes related to iron death were screened by *R* language software, and the prognostic risk prediction model was constructed by single factor and multifactor Cox analysis. The relationship between the relevant genes in the model and clinical pathological features was further evaluated, and the model was applied to the prognosis prediction of renal clear cell carcinoma.

2. Data and Methods

2.1. Data Source. In this study, samples of renal clear cell carcinoma (CCRC) were obtained from the Cancer Genome Atlas (TCGA) (https://cancergenome.nih.gov) database. 522 iron death gene transcripts and clinical data of patients with renal clear cell carcinoma (CCRC) were downloaded, and the known iron death-related genes were listed from 2018 to 2022. The intersection genes were extracted and verified by data downloaded from the ICGC database (http://icgc.org/).Take $p > 0.05$ as the statistical standard and divide the samples into high-risk and low-risk groups according to the model. According to the experiment and expression data analysis, the primary tumor samples were selected to extract the relevant expression volume. We performed survival analysis, risk analysis, and independent prognostic analysis to validate the prognostic model of renal clear cell carcinoma (CCRC). Finally, we performed univariate and multivariate Cox regression analysis to determine the correlation between iron death-related differential genes and independent risk factors. The feasibility of the prediction model was evaluated by subject operating characteristic analysis.

2.2. Data Acquisition and Processing. In this study, samples of renal clear cell carcinoma (CCRC) were obtained from the TCGA database. These data include 551 iron death-related transcriptional gene samples and the expression data of renal clear cell carcinoma and normal renal tissue. The iron death sequencing data and relevant clinical information of patients with renal clear cell carcinoma were obtained from TCGA. In addition, we screened the clinical data of 522 patients with renal clear cell carcinoma from TCGA. Extract relevant clinical information, including survival time, survival status, age, gender, clinical stage, and TNM stage, using the list of known iron death-related genes, the generic domain name format. According to the corresponding gene sequence numbers, the two sets of data were combined to screen 49 overlapping iron death-related mRNA for further analysis. Among the 49 mRNA genes, 42 iron death genes related to the prognosis of renal clear cell carcinoma were identified.

2.3. Differential Expression Analysis. The known iron death-related genes and clinical data were used to analyze the related data, and the expression of iron death-related genes was obtained. Finally, 49 iron death-related genes related to renal clear cell carcinoma were obtained. According to the screening criteria of$|\log FC| > 0$ and $p < 0.05$, 42 differentially expressed genes between renal clear cell carcinoma and normal renal tissue were obtained by Wilcox test analysis. According to the relevant literature, the differential genes of iron death were further determined. In *R* software, "edge" package (version 4.0, URL: http://bioinf.wehi.edu.au/edgeRhttps://bioconductor.Org/packages/edge) was used to identify the DELs of 551 transcriptional gene samples and 522 clinical samples. These samples were adjusted according to $|\log FC| > 2$ and $p < 0.01$. In the analysis of survival time, it was found that there were significant differences in 7 mRNA-related to prognosis.

2.4. Clinical Pathological Correlation Analysis. By using the "survival" package in *R* software and combining the clinical and pathological characteristics (age, TNM stage, and survival time) of the patients, the expression of related genes, survival time, and survival status in the model was further analyzed. By performing univariate Cox regression analysis on the expression genes related to iron death ($p < 0.05$), the iron death prognosis genes related to renal clear cell carcinoma were obtained. Analyze the correlation between the genes in the model and the clinicopathological features.

2.5. Establishment of Prognostic Risk Survival Analysis Model. By analyzing the intersection of prognosis-related genes and differential genes, the iron death differential genes related to the prognosis of renal clear cell carcinoma were finally obtained. The $p < 0.05$ standard was considered as the difference was statistically significant and included in the multifactor Cox regression, which was used to establish

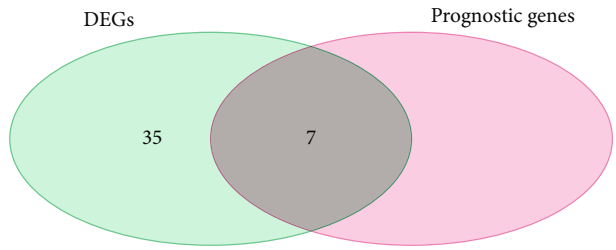

Figure 1: Venn illustrates the intersection of differential genes and iron death-related genes in renal clear cell carcinoma.

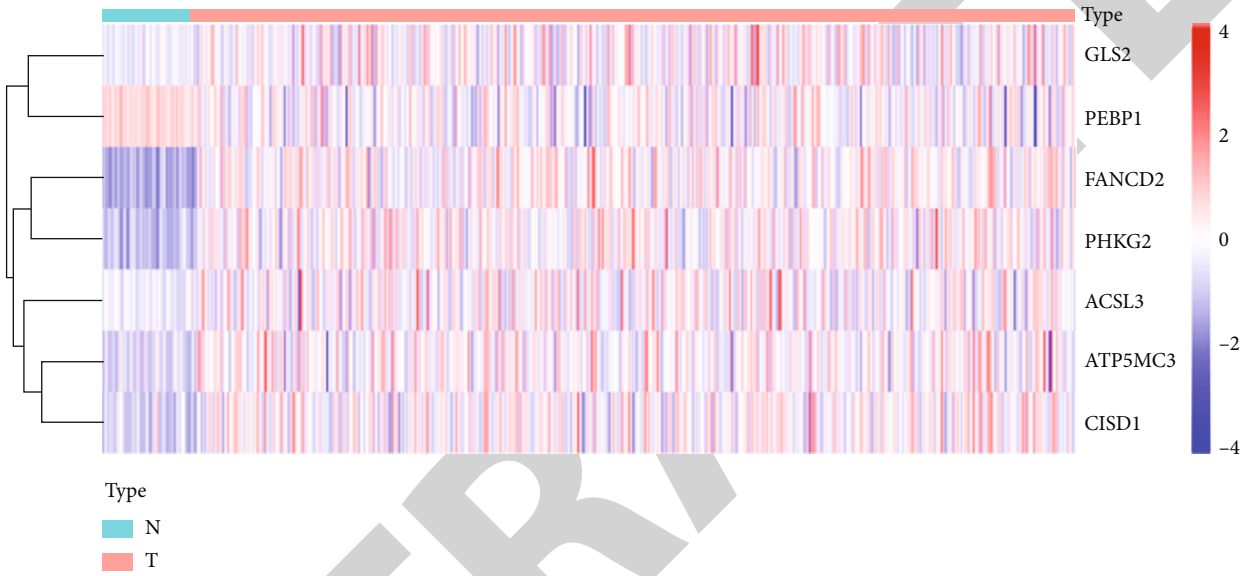

Figure 2: Heat map shows the expression of 7 iron death-related genes between high-risk and low-risk patients.

the prognostic risk prediction model and calculate the risk scores of patients with different renal clear cell carcinoma. Divide the patients into high-risk and low-risk groups according to the different scores and carry out relevant tests.

2.6. Statistical Analysis. Continuous normally distributed data are expressed as the means ± SDs. All statistical calculations were carried out using SPSS statistical software (SPSS Inc., USA). The $p < 0.05$ standard was considered as the difference.

3. Results

3.1. Acquisition of Iron Death-Related Differentially Expressed Genes. By analyzing the gene expression information and clinical expression data of 522 transcriptional samples downloaded from the TGCA database, 49 differentially expressed genes were obtained, including 28 upregulated genes and 14 downregulated genes. Seven iron death-related genes were differentially expressed between tumor and normal tissues. Finally, seven prognostic genes related to iron death in renal clear cell carcinoma were identified (Figure 1).

3.2. Screening of Differential Genes and Iron Death-Related Genes in Renal Clear Cell Carcinoma. After obtaining seven iron death prognosis differential genes associated with renal clear cell carcinoma, we used *R* package "pheatmap" to map differential genes based on the intersection differential genes and differential gene expression. The abscissa represents the sample, and the ordinate represents the genes related to prognosis. It can be seen that CLS2, FANCD2, PHKG2, ACSL3, ATP5MC3, and CISD1 genes are upregulated, and PEBP1 gene is downregulated in the tumor group (Figure 2). In previous studies, scholars have found that iron inhibin-1 can combine with 15LOX/PEBP1 complex, inhibit the production of peroxidized ETE-PE, and prevent iron death.

3.3. Prognosis Evaluation of Intersection Genes. In this study, we further used the intersection genes, single factor analysis result files, and "survival" package to construct the forest map. The first column is the name of the prognosis difference gene. $p < 0.05$ represents that the gene is related to prognosis; HR > 1 indicates that the gene is a high-risk gene; HR < 1 indicates that the gene is a low-risk gene. We visualized the gene to obtain the forest map. Through the forest map, we can see that ATP5MC3, CISD1, FANCD, and ACSL3 are a high-risk gene in renal clear cell carcinoma, and the rest are low-risk genes (Figure 3).

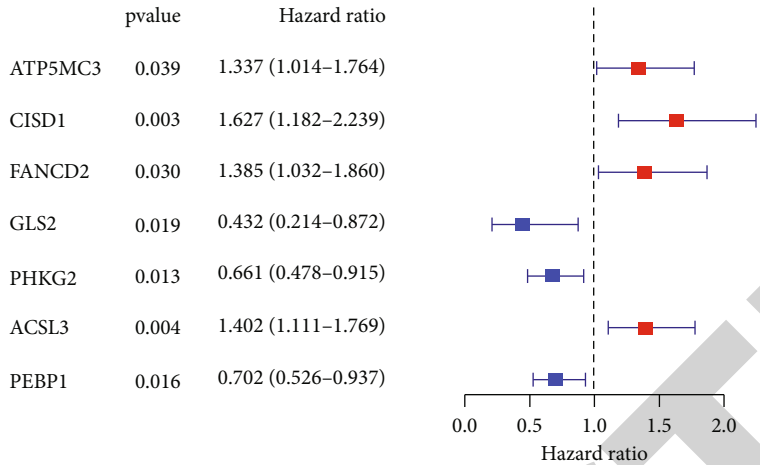

Figure 3: Single factor Cox regression analysis.

3.4. ICGC Database Validation Analysis. Taking the data of Japanese samples as an example, the samples were classified into high-risk and low-risk groups according to the model with $p > 0.05$ as the statistical standard. According to the experiment and expression data analysis, the primary tumor samples were selected, and the relevant expression quantities were extracted,

3.5. Survival Analysis. Using the primary tumor data samples extracted by ICGC, according to the survival time and survival status of the patient samples, the blank ones are deleted to obtain the text related to the single factor significant gene expression in the tumor data samples and the samples of iron death difference genes related to the prognosis extracted from the TCGA database. The *R* language "limma" package is used to read the files and delete the normal samples. Extract survival data.

3.6. Construction of Prognosis Model. According to the obtained prognosis-related differential genes, a single factor Cox regression analysis was performed to construct a prognosis model. According to the formula of the prognosis model, the risk value of each patient in the TCGA database was calculated. According to the median value of risk value, the patients were divided into high-risk and low-risk groups. According to the obtained single factor significant gene expression files, ICGC expression and survival data, and iron death prognosis-related differential genes, the model was constructed by using the "glmnet" package and "survival" package in *R* language. If the *s* value (the minimum value of crossvalidation error) coefficient was 0, it was deleted to obtain the relevant gene coefficient. Get the model formula, get the risk value of the train group, extract the gene expression amount whose gene coefficient is not 0 in the train group model, the location function: add the gene expression amount * coefficient, use the obtained formula to get the risk value of each patient, and divide the patients into high-risk and low-risk groups according to the median value of the risk value. According to the survival analysis of the ICGC database, the survival time is /365, the gene expression amount is treated with log2, the gene expression amount is extracted, and the risk score is obtained according to the formula.

3.7. Survival Curve. Based on the obtained risk file, using the "survival" and "survivminer" packages in *R* language, and using the survival function, the significance *p* value of the difference between high and low risk values is obtained, which is displayed in the form of scientific counting method. The survival curves of TCGA and ICGC were drawn. The Kaplan–Meier curve showed that high-risk patients had significantly worse OS; so, they were more likely to die early than low-risk patients ($p < 0.001$) (Figure 4).

3.8. ROC Curve. A good survival model can predict the patient's survival gene and verify the accuracy of the survival gene. It can be realized through the ROC curve, and the ROC curve can be obtained by using the *R* language "timeROC" package. TCGA time-related ROC curve and area under curve (AUC) show that the score is 0.695 in 1 year, 0.678 in 2 years, and 0.674 in 3 years. Time-related ROC curve and area under curve (AUC) of TCGA and ICGC show that the score is 0.695 in one year, 0.678 in two years, and 0.674 in three years (Figure 5).

3.9. Risk Curve. The relationship between risk value and survival status is observed through the risk curves of the two databases. The patients are sorted by risk score. The patients are divided into high- and low-risk groups according to the median value of risk value. It can be seen that the risk value is related to the patients. With the increase of risk value, the number of dead patients increases (Figure 6).

3.10. PCA Analysis and T-SNE Analysis. By reducing the dimension of gene expression data and visualizing the selected 7 genes, it can be seen that high-risk and low-risk patients are separated. It can be seen that high-risk and low-risk patients can be distinguished by the model gene expression. Some low-risk patients are in the high-risk group. It can be seen that this kind of patients cannot be distinguished by the model gene expression. It can be seen that our model can divide patients into high- and low-risk groups (Figure 7).

3.11. Independent Prognostic Analysis of TCGA and ICGC. To evaluate whether the model can be used as an

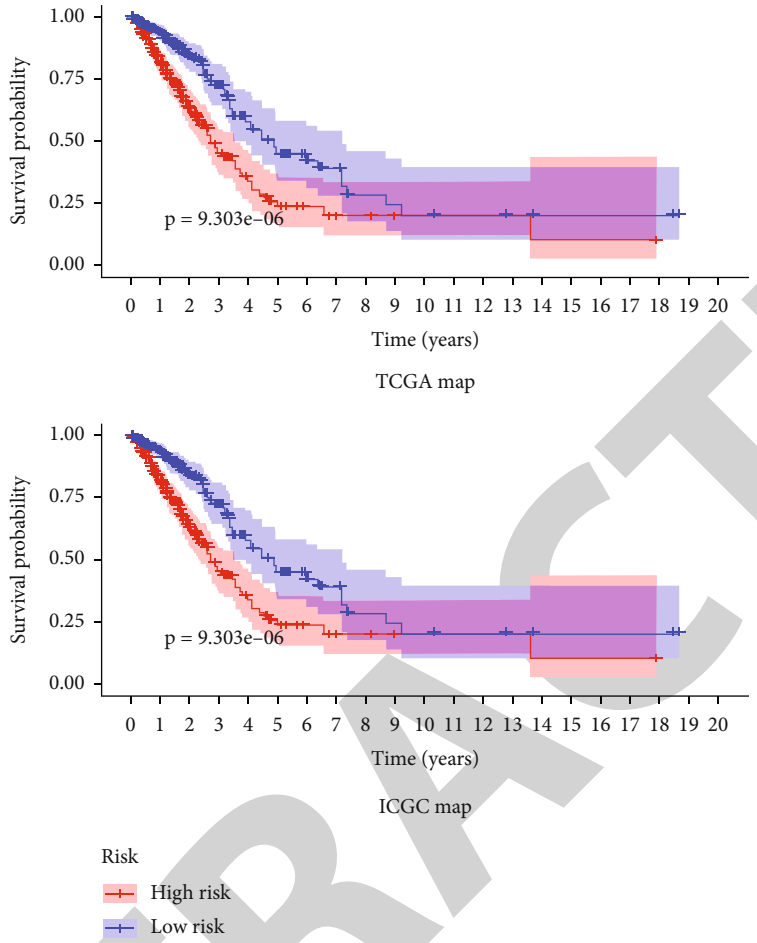

Figure 4: Kaplan–Meier survival curve.

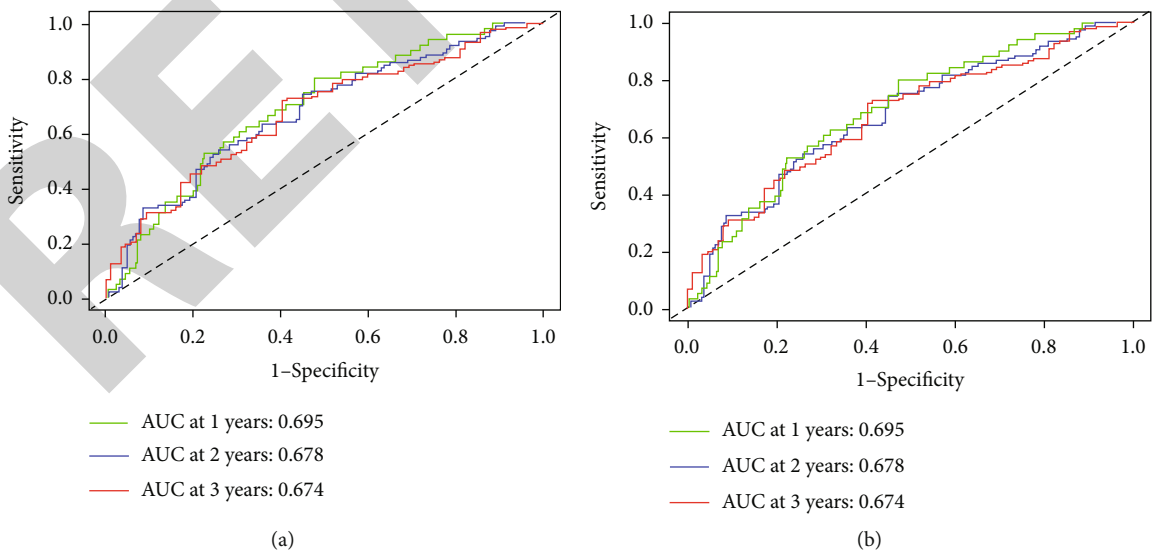

Figure 5: ROC curve analysis of risk score and prognosis of clinicopathological parameters.

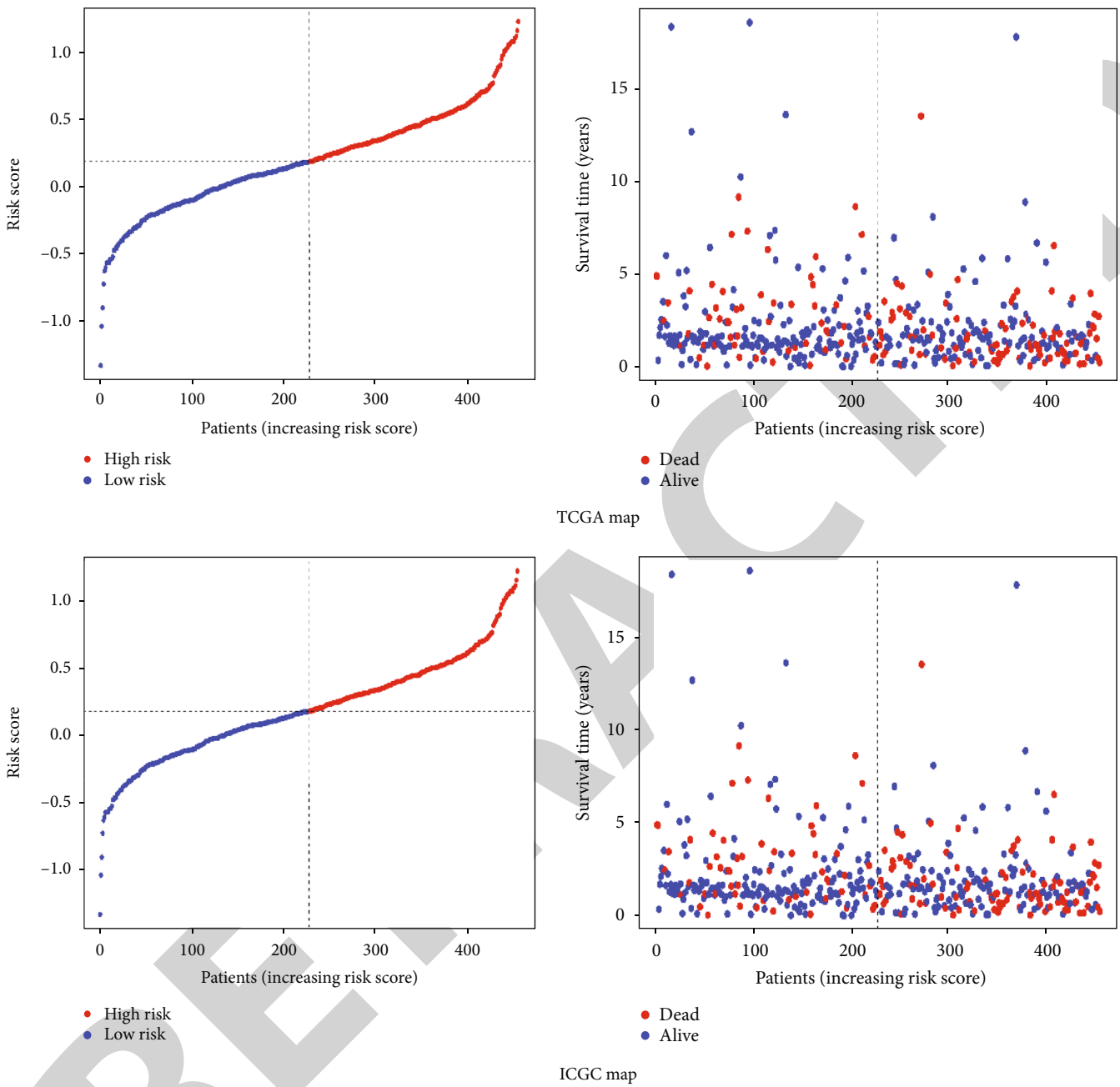

Figure 6: Distribution of risk scores of high-risk and low-risk renal clear cell carcinoma patients with prognostic characteristics of iron death related genes.

independent prognostic factor independent of other clinical characteristics, univariate independent prognostic risk analysis. By comparing univariate with survival time and survival status, if $p < 0.05$, it indicates that univariate is related to survival prognosis. In the model, only stage and risk value p are less than 0.05, indicating that these two factors are related to prognosis. If HR value is greater than 1, it indicates that this factor is a high-risk factor. That is to say, the greater the value, the higher the risk of the patient. It can be seen from the model that it is a high-risk factor. The greater the risk, the higher the patient risk. Gender is a low-risk factor, male is 1, and female is 0, indicating that the lower the value, the greater the patient risk, because male is 1 and female is 0, indicating that the risk of female is higher than that of male. The risk of stages III and IV is greater than that of stages I and II. The higher the risk value, the greater the patient risk. The independent prognostic risk of multiple factors is to conduct an independent prognostic analysis of multiple factors for single factor significant clinical traits and compare the multiple factors with survival time and survival status, If $p < 0.05$, it means that this factor can be used as an independent prognostic factor independent of other factors. From the model, it can be seen that stage and risk score $p < 0.05$ indicate that risk score can be used as an independent prognostic factor independent of stage. If the results are <0.05 in univariate and multivariate analysis, it indicates

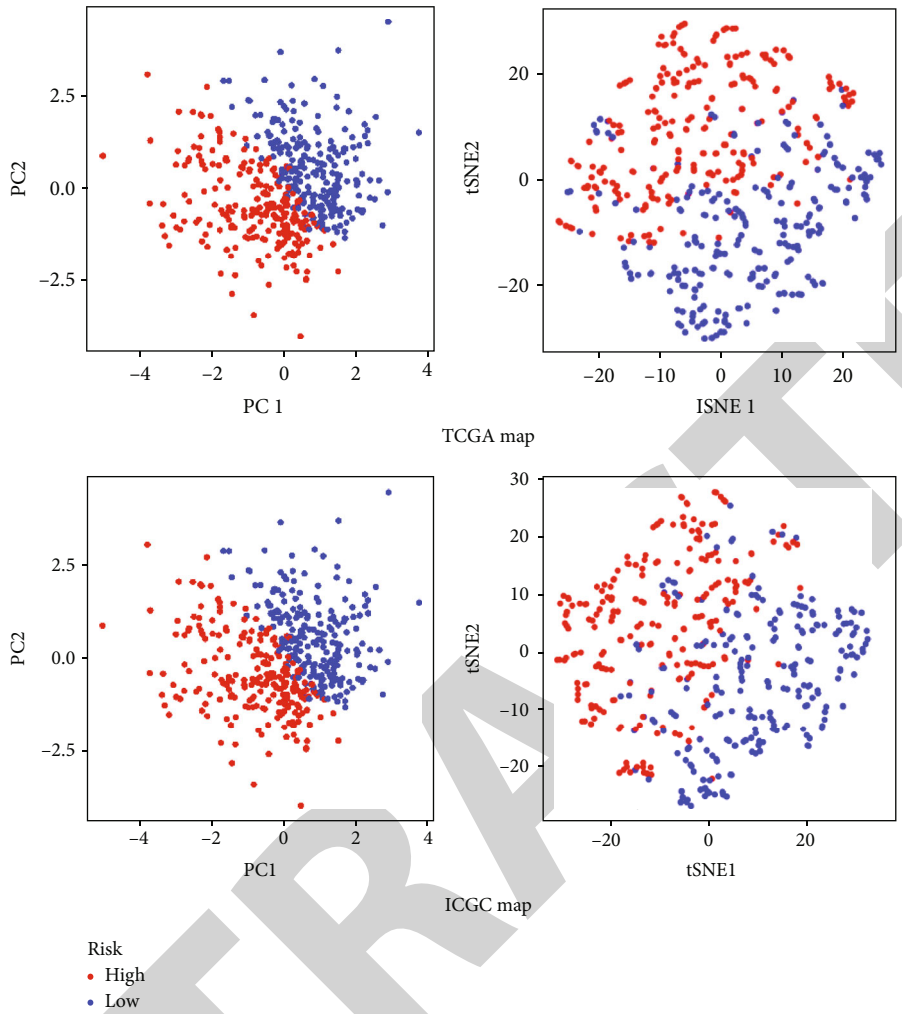

Figure 7: Analysis of gene differences between PCA and T-SNE and iron death.

that our model can be used as an independent prognostic factor independent of other clinical traits. Methods were as follows: by analyzing the survival time, survival status, risk value of the risk file, and the age, sex, and stage of the patient's clinical information, to verify whether our model can be independent of these clinical traits as an independent factor, find the intersection sample. Then, merge to get the p value, HR value, and fluctuation range of HR value of each factor. Univariate independent prognostic analysis was obtained, and the univariate results were filtered. The univariate information with $p < 0.05$ was extracted, and the multivariate prognostic risk was compared with survival time and survival status. Forest map is obtained by forest map function.

3.12. Univariate and Multivariate Cox Regression Analysis. To determine whether the risk score is an independent prognostic factor for OS, we realized that in the univariate Cox regression analysis of TCGA, risk score (HR = 3.861; 95% CI = 2.338 – 6.376; $p < 0.001$), stage (HR = 2.884; 95%CI = 1.972 – 4.216; $p < 0.001$), T (HR = 1.597; 95%CI = 1.283 – 1.986; $p < 0.001$), and N (HR = 1.769; 95%CI = 1.440 – 2.174; $p < 0.001$) were significantly correlated with OS, and other confounding factors were corrected in the multivariate Cox regression analysis. Then, the risk score proved to be an independent predictor of OS (HR = 2.904; 95%CI = 1.713 – 4.922; $p < 0.001$) (Figure 8).

In the univariate Cox regression analysis of ICGC, the risk score was significantly correlated with OS (HR = 4.401; 95%CI = 2.072 – 9.384; $p < 0.001$). Other confounding factors were corrected in multivariate Cox regression analysis, and the risk score proved to be an independent predictor of OS (HR = 2.904; 95%CI = 1.713 – 4.922; $p < 0.001$) (Figure 9).

4. Discussion

Renal clear cell carcinoma is one of the most common malignant tumors in human beings, and it is also the main cause of cancer death (accounting for 18.4% of the total cancer deaths) [11]. Iron death is a special regulatory cell death process (RCD) regulated by genes, which is closely related to excessive iron load. It is the abnormal lipid oxidation metabolism of cells catalyzed by iron ions or iron-containing enzymes. Recent studies have found that iron death is related to a variety of diseases. The research field is basically

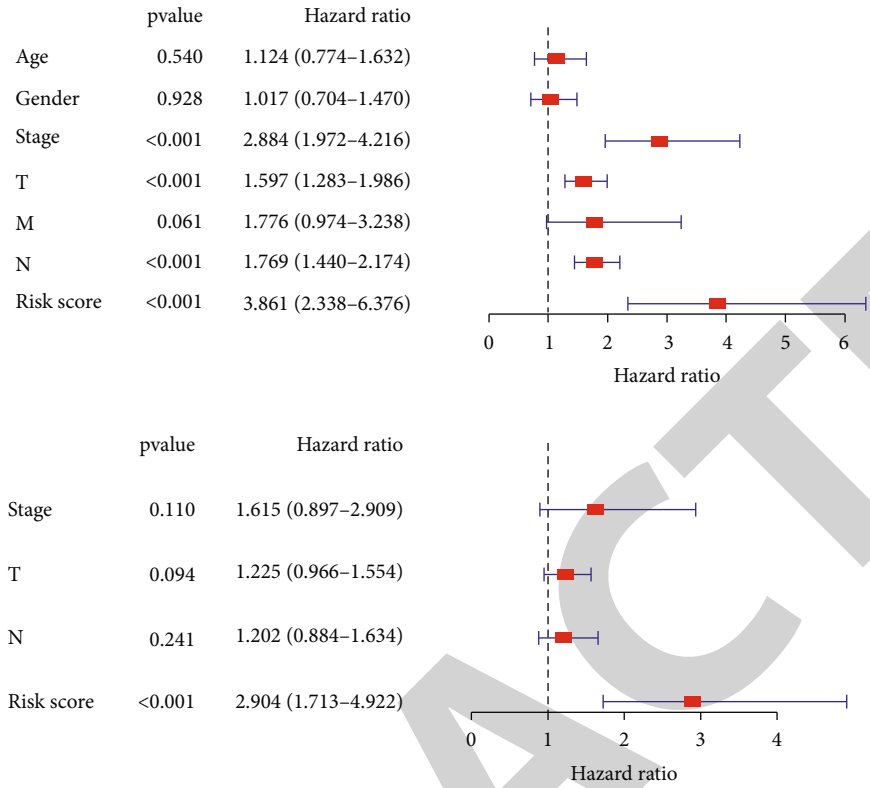

Figure 8: Univariate independent prognostic analysis and multivariate prognostic analysis of TCGA.

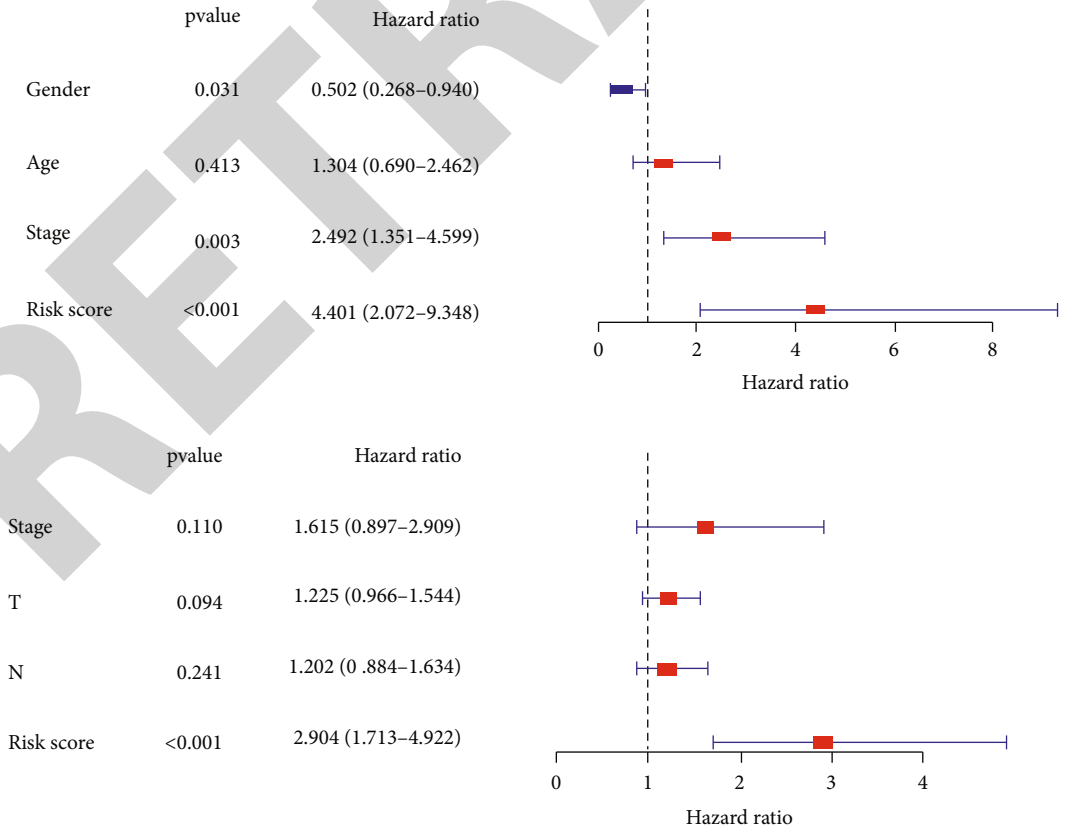

Figure 9: Univariate independent prognostic analysis and multivariate prognostic analysis of ICGC.

neurodegenerative diseases and many cancers [12]. It may play a very important role in antitumor immune mechanism and tumor inhibition. Therefore, biomarkers related to iron death may be potential diagnostic biomarkers and therapeutic targets for patients with renal cancer [13]. As a common subtype of renal cell carcinoma, in recent years, many medical researchers have devoted themselves to studying the occurrence, development, and treatment of renal clear cell carcinoma [14–18]. Many studies have shown that different subtypes of renal cell carcinoma have different clinical characteristics and results. Iron death is closely related to the occurrence and development of cancer cells [19–22]. Therefore, more and more studies have focused on the genetic characteristics related to the occurrence of iron death to predict the survival rate and immune response of patients with renal clear cell carcinoma [23]. Most epidemiological and experimental studies show that there is a close relationship between iron and renal cell carcinoma [24].

In our study, bioinformatics and statistical tools were used to systematically analyze the prediction accuracy of iron death-related genes in renal clear cell carcinoma. We used the sample data of renal clear cell carcinoma patients in TCGA and ICGC databases to obtain the expression level of iron death-related genes and established a Cox regression model composed of seven genes. The risk score of each renal clear cell carcinoma patient was calculated according to the expression of these seven genes in the prognostic markers, and the patients were divided into the high-risk group and low-risk group according to the median risk score. The Kaplan-Meier survival curve shows that the survival rates of patients in the high-risk group and low-risk group are different. ROC curve verifies the accuracy of the model, and then principal component analysis (PCA) proves that the high-risk group and low-risk group are two different components. Then, we analyzed the correlation between prognosis and clinical pathological features and found that the prognostic features we constructed can be widely applied to different populations with different clinical features [25]. The calibration curve showed that the actual 1-, 3-, and 5-year survival rates were highly consistent with the predictions. It is suggested that the prognostic characteristics of iron death-related genes can correctly predict the prognosis of patients with renal clear cell carcinoma, which has great clinical application potential, and can provide reference value for clinical workers to make clinical decisions in time. This established a new prognostic model of seven genes associated with iron death. Among the iron death-related genes that have been studied, some genes have been proved to regulate the occurrence and development of various related cancers through the iron death pathway. For example, FANCD2 inhibited the accumulation of Fe 2 and lipid peroxidation process of iron death induced by erastin, while the deletion of FANCD2 significantly inhibited the mRNA expression of FTH11 (which can bind Fe 2) and steam3 (a metal reductase that can convert iron from Fe 3 to Fe 2) induced by erastin [26]. In the existing studies, it was found that the reason why PHKG2 inhibits the lethality of erastin may be the unknown function of PHKG2. There is a certain hypothetical association between PHKG2 and iron metabolism related to p53. Because studies have shown that the reduction of iron level will inhibit cell death, this iron regulatory function of PHKG2 may be the reason for regulating iron sensitivity [27]. Therefore, the silencing of PHKG2 may be an important factor leading to iron consumption. However, how PHKG2 affects the specific pathway of iron death has not been confirmed by relevant studies. Among the iron death differential genes we screened, CISD1 is highly expressed in tumor tissues. According to previous studies, CISD1 can regulate mitochondrial iron uptake and respiratory capacity. The loss of CISD1 can lead to iron accumulation and peroxidation damage in mitochondria. Mitochondria participate in lipid and glucose metabolism. CISD1 can limit iron uptake in mitochondria, thus inhibiting iron death. Therefore, CISD1 can inhibit iron death by protecting mitochondrial lipid peroxidation [28]. ATP5MC3 and ACSL3 have also been associated with iron death. The above studies show the importance of these iron death related differential genes in their prognostic characteristics [29]. Kaplan-Meier survival curve shows that these seven iron death-related genes are significantly related to OS in patients with renal clear cell carcinoma, reflecting great prognostic value. Our research also has some limitations. These results are best to help us understand the biological functions of iron death related genes in its further biochemical experiments [30]. As mentioned above, we constructed a risk model for the prognostic characteristics of iron death. In this model, we identified 7 differential genes related to iron death among 42 differential genes related to renal clear cell carcinoma. These genes can accurately predict the survival outcome of patients with renal clear cell carcinoma.

The advantage of this study was to show that seven iron death genes can accurately predict the survival of patients with renal clear cell carcinoma. However, there are also limits of this study. The mechanism was not clarified, and future studies are needed to verify this.

5. Conclusion

Therefore, these seven iron death-related genes are promising biomarkers for prognosis, diagnosis, and targeted therapy in patients with renal clear cell carcinoma. However, the way in which these genes affect the occurrence and development of renal clear cell carcinoma needs further research to find and confirm.

Data Availability

The data used to support this study is available from the corresponding authors upon request.

Conflicts of Interest

The authors declare that they have no conflicts of interest.

Authors' Contributions

Ding Wu and Zhenyu Xu wrote the manuscript. Zhan Shi and Ping Li analyzed the data. Huichen lv and Jie Huang searched the database. Dian Fu provided the financial support and final approval of manuscript. Ding Wu and Zhenyu Xu contributed equally to this work.

Hindawi
Computational and Mathematical Methods in Medicine
Volume 2023, Article ID 9807987, 1 page
https://doi.org/10.1155/2023/9807987

Retraction

Retracted: Construction and Evaluation of Neural Network Correlation Model between Syndrome Elements and Physical and Chemical Indexes of Unstable Angina Pectoris Complicated with Anxiety

Computational and Mathematical Methods in Medicine

Received 3 October 2023; Accepted 3 October 2023; Published 4 October 2023

This article has been retracted by Hindawi following an investigation undertaken by the publisher [1]. This investigation has uncovered evidence of one or more of the following indicators of systematic manipulation of the publication process:

(1) Discrepancies in scope

(2) Discrepancies in the description of the research reported

(3) Discrepancies between the availability of data and the research described

(4) Inappropriate citations

(5) Incoherent, meaningless and/or irrelevant content included in the article

(6) Peer-review manipulation

The presence of these indicators undermines our confidence in the integrity of the article's content and we cannot, therefore, vouch for its reliability. Please note that this notice is intended solely to alert readers that the content of this article is unreliable. We have not investigated whether authors were aware of or involved in the systematic manipulation of the publication process.

Wiley and Hindawi regrets that the usual quality checks did not identify these issues before publication and have since put additional measures in place to safeguard research integrity.

We wish to credit our own Research Integrity and Research Publishing teams and anonymous and named external researchers and research integrity experts for contributing to this investigation.

The corresponding author, as the representative of all authors, has been given the opportunity to register their agreement or disagreement to this retraction. We have kept a record of any response received.

References

[1] X. Chen, Y. Wang, L. Zhang, and X. Xu, "Construction and Evaluation of Neural Network Correlation Model between Syndrome Elements and Physical and Chemical Indexes of Unstable Angina Pectoris Complicated with Anxiety," *Computational and Mathematical Methods in Medicine*, vol. 2022, Article ID 6217186, 11 pages, 2022.

Hindawi
Computational and Mathematical Methods in Medicine
Volume 2022, Article ID 6217186, 11 pages
https://doi.org/10.1155/2022/6217186

Research Article

Construction and Evaluation of Neural Network Correlation Model between Syndrome Elements and Physical and Chemical Indexes of Unstable Angina Pectoris Complicated with Anxiety

Xiaoyang Chen,[1,2] **Yifei Wang**,[3] **Li Zhang**,[3] **and Xuegong Xu**[3,4,5]

[1]*Guangzhou University of Chinese Medicine, Guangzhou 510016, China*
[2]*Henan University of Chinese Medicine, Zhengzhou 450046, China*
[3]*Cardiovascular department, Zhengzhou Hospital of Chinese Medicine, Zhengzhou 450007, China*
[4]*Laboratory of Zhengzhou Hospital of Traditional Chinese Medicine, Zhengzhou 450007, China*
[5]*Key Laboratory of traditional Chinese medicine for cardiovascular diseases of Henan Province, Zhengzhou 450007, China*

Correspondence should be addressed to Li Zhang; 532825609@qq.com and Xuegong Xu; xuxg1115@126.com

Received 8 June 2022; Revised 20 June 2022; Accepted 15 July 2022; Published 21 August 2022

Academic Editor: Plácido R. Pinheiro

Objective. Syndrome elements are regarded as the smallest unit of syndrome differentiation, which is characterized by indivisibility and random combination. Therefore, it can well fit the goal of syndrome differentiation and unity. *Methods*. Clinical physicochemical indicators are important references for disease diagnosis, but they are often not used too much in the process of TCM syndrome differentiation. In the era of intelligence, communicating TCM syndrome differentiation at the macro level with physiological and pathological processes at the micro level (i.e., these clinical physicochemical indicators) is an effective tool to realize intelligent medicine. Taking the collected relevant clinical physical and chemical indexes as the research object, on the basis of routine *t*-test and nonparametric test, logistic regression model is used to mine the main syndrome elements, and neural network multilayer perceptron is used to predict the feature model. *Results*. Compared with non-blood stasis patients, there were significant differences in HGB, PLT, Pt, PTA, Na^+, TG, LDL, BNP, LVEDd, and EF in blood stasis patients. Taking blood stasis as the dependent variable and the above physical and chemical indexes with statistical significance ($P < 0.05$) as independent variables. Compared with non-qi depression patients, there were significant differences in atpp, TG, TC, LDL, LVESD, and FS in qi depression patients ($P < 0.05$). Taking Yin deficiency as dependent variable and the above physical and chemical indexes (Hgb, APTT, CKMB, LVEDd, and LVPW) with statistical significance ($P < 0.05$) as independent variables, binary logistic regression analysis was carried out. *Conclusion*. The combination pattern of physical and chemical indexes obtained from the neural network model provides a clinical reference basis for identifying the syndrome elements of unstable angina pectoris complicated with anxiety, such as blood stasis, qi depression, Qi deficiency, yin deficiency, phlegm turbidity, and qi stagnation.

1. Background

Chinese medicine has remarkable curative effect in the treatment of patients with heart disease. Traditional Chinese medicine (TCM) has apparent advantages in stabilizing the heart disease, improving heart function, and improving the quality of life. In recent years, inspired by modern medicine, many doctors try to explain the mechanism of syndrome with a single experimental index in order to solve the problem of syndrome inconsistency. Because syndrome is the overall response of multiple system levels [1], the results often have certain limitations. Although it can show its relevance, it is difficult to justify it in the process of interpretation.

Syndrome elements are regarded as the smallest unit of syndrome differentiation, which is characterized by indivisibility and random combination [2]. It is the key to realize the

Table 1: Factors of physical and chemical indexes related to blood stasis.

	Blood stasis ($n = 169$)	Non-blood stasis ($n = 31$)	P
HGB(g/L)	120.07 ± 22.18	128.55 ± 20.89	0.034∗
PLT(10^9/L)	245.63 ± 73.59	216.48 ± 58.40	0.038∗
PT (s)	10.62 ± 2.83	10.72 ± 2.10	0.032∗
PTA (%)	117.20 ± 20.92	108.96 ± 18.64	0.042∗
Na^+ (mmol/L)	140.01 ± 3.65	141.30 ± 1.70	0.020∗
TG (mmol/L)	1.56 ± 0.94	1.34 ± 0.97	0.026∗
LDL (mmol/L)	2.66 ± 0.89	2.32 ± 0.77	0.048∗
BNP (pg/ml)	187.67 ± 164.89	149.24 ± 154.06	0.047∗
LVEDD (mm)	41.47 ± 9.70	45.48 ± 7.79	0.045∗
EF (%)	65.31 ± 8.16	68.10 ± 6.66	0.037∗

Note: Compared with the two groups, $*P < 0.05$. The same below.

Table 2: Binary logistic regression analysis of blood stasis and physical and chemical indexes.

Independent variable	Coefficient value	Standard error	Wald X^2	P	OR	95% confidence interval Upper limit	Lower limit
HGB	− 0.040	0.019	4.581	0.032∗	0.961	0.926	0.997
PT	0.433	0.201	4.625	0.032∗	1.542	1.039	2.288
PTA	0.056	0.024	5.621	0.018∗	1.058	1.010	1.108
EF	− 0.181	0.081	4.131	0.042∗	0.835	0.701	0.994

Table 3: Factors of physical and chemical indexes related to qi depression.

	Qi depression ($n = 137$)	Non-qi depression ($n = 63$)	P
APTT(s)	26.89 ± 7.53	29.25 ± 9.16	0.022∗
TG (mmol/L)	1.49 ± 1.04	1.60 ± 0.70	0.048∗
TC (mmol/L)	4.55 ± 1.27	4.92 ± 1.13	0.048∗
LDL (mmol/L)	2.52 ± 0.88	2.80 ± 0.85	0.041∗
LDL (mmol/L)	2.52 ± 0.88	2.80 ± 0.85	0.041∗
LVESD (mm)	27.75 ± 3.81	28.81 ± 3.67	0.026∗
FS (%)	38.82 ± 5.20	36.91 ± 4.59	0.005∗

objectification of syndrome [3], so it can well fit the goal of syndrome differentiation and unity. Clinical physicochemical indicators are important references for disease diagnosis, but they are often not used too much in the process of TCM syndrome differentiation [4]. In today's intelligent era, communicating TCM syndrome differentiation at the macro level with physiological and pathological processes at the micro level (i.e., these clinical physicochemical indicators) is an effective tool to realize intelligent medicine [5]. In the face of the regularity of TCM syndromes and the multilevel problems of pathophysiology, data mining technology shows great advantages. Through literature search, no research on the combination of macro and micro was found.

Therefore, based on the syndrome related data collected in the process of clinical epidemiological investigation, this study explored the distribution and combination characteristics of TCM syndrome elements in unstable angina pectoris complicated with anxiety and provides reference for the unity of syndrome differentiation of the disease. Then, taking the collected relevant clinical physical and chemical indexes as the research object, on the basis of routine t-test and nonparametric test, logistic regression model is used to mine the main syndrome elements, neural network multilayer perceptron is used to predict the characteristic model, and the correlation between the main syndrome elements and physical and chemical indexes of unstable angina pectoris complicated with anxiety is analyzed to explore the role and significance of the combination mode of clinical physical and chemical indexes in the diagnosis of syndrome elements.

2. Materials and Methods

2.1. Observation Object. The cases came from patients hospitalized in the Department of Cardiology of Zhengzhou

Table 4: Regression analysis results of qi depression and physical and chemical indexes.

Independent variable	Coefficient value	Standard error	Wald X^2	P	OR	95% confidence interval upper limit	lower limit
APTT	-0.45	0.021	4.620	0.032∗	0.956	0.917	0.996
TC	− 0.304	0.133	5.193	0.023∗	0.738	0.568	0.958
FS	0.097	0.034	8.392	0.004∗	1.102	1.032	1.177

Table 5: Factors of physical and chemical indexes related to Qi deficiency.

	Qi deficiency ($n = 94$)	Non-Qi deficiency ($n = 106$)	P
HGB (g/L)	106.66 ± 18.99	134.43 ± 15.64	0.000∗
APTT (s)	28.90 ± 7.59	26.51 ± 8.46	0.022∗
K^+ (mmol/L)	4.01 ± 0.42	4.12 ± 0.37	0.048∗
BNP (pg/ml)	206.12 ± 180.64	160.08 ± 144.04	0.043∗
LVEDD (mm)	34.89 ± 8.08	48.48 ± 5.16	0.000∗∗
LAD (mm)	36.20 ± 4.55	34.32 ± 5.97	0.012∗

Table 6: Regression analysis results of qi deficiency and physical and chemical indexes.

Independent variable	Coefficient value	Standard error	Wald X^2	P	OR	95% confidence interval upper limit	lower limit
HGB	− 0.095	0.020	23.660	0.000∗	0.909	0.875	0.945
LVEDD	− 0.389	0.078	24.965	0.000∗	0.678	0.582	0.790
LAD	0.147	0.054	7.302	0.007∗	1.159	1.041	1.289

hospital of traditional Chinese medicine from January 2017 to January 2019. Our study was approved by the institutional review board of the hospital, and written informed consent was obtained from each participant.

2.2. Diagnostic Criteria of Western Medicine. Diagnostic criteria of unstable angina pectoris: refer to the 2016 guidelines for the diagnosis and treatment of unstable angina pectoris and non-ST segment elevation myocardial infarction. Diagnostic criteria of anxiety state: Under the guidance of psychiatrists, all patients were scored and investigated with HAMA anxiety scale. Specific criteria: ≥29 points are classified as severe anxiety state; ≥21 points, obvious anxiety; ≥14 points, there must be anxiety; ≥7 points, may have anxiety; and <7 points, no anxiety.

2.3. Diagnostic Criteria of TCM Syndrome Elements. Referring to the relevant parts in terms of clinical diagnosis and treatment of traditional Chinese medicine syndrome [6] in 1997 and the guiding principles for clinical research of new traditional Chinese medicine, diagnostics of traditional Chinese medicine, and internal medicine of traditional Chinese medicine in 2002, it is divided into blood stasis, phlegm turbidity, cold coagulation, yin deficiency, Qi deficiency, Yang deficiency, qi stagnation, excess dampness, fire heat, and qi depression. Within 24 hours of admission, three deputy directors or above, clinicians with relevant clinical experience of 5 years or above and trained will judge the syndrome elements on the basis of disease diagnosis. The criteria for determining the patient's syndrome elements are as follows: ① when the opinions of 3 clinicians are consistent; ② if the opinions of two clinicians are consistent with that of another clinician, the first two opinions shall be adopted; ③ if the opinions of the three clinicians are inconsistent, the doctors with the qualification of deputy director and above shall re-collect the information of the four diagnoses and re-judge the syndrome elements until they meet the conditions of ① and ②.

2.4. Inclusion Criteria. The inclusion criteria are as follows: (1) 18-79 years old; (2) unstable angina pectoris; (3) HAMA anxiety was between 14 and 29 points; (4) normal cognitive function and no reading and writing impairment; and (5) after informed consent, they can voluntarily cooperate and participate in the investigation and research.

2.5. Exclusion criteria. The exclusion criteria are as follows: (1) severe valvular disease, cardiomyopathy, pericardial disease, congenital heart disease, cardiogenic shock, acute myocarditis, infective endocarditis, and severe arrhythmia with hemodynamic changes; (2) other congenital diseases such as rheumatic aortic stenosis and syphilis; (3) liver dysfunction (liver function index value >2 times the normal value) and renal insufficiency (renal insufficiency decompensated period, CCR <50 ml/min, SCR >2 mg/dL, or >177 μMol/L), serious electrolyte disorders, blood system and other primary diseases, malignant tumors, pulmonary embolism, diabetes combined with severe complications, hypertension, hyperthyroidism, hypothyroidism, and

Table 7: Factors of physical and chemical indexes related to yin deficiency.

	Yin deficiency ($n = 85$)	Non-Yin deficiency ($n = 115$)	P
HGB (g/L)	113.14 ± 21.38	127.47 ± 20.78	0.000∗
APTT (s)	29.47 ± 7.76	26.28 ± 8.16	0.001∗
CKMB (u/L)	12.19 ± 6.37	16.10 ± 14.76	0.048∗
LVEDD (mm)	37.62 ± 9.98	45.40 ± 7.68	0.000∗
LVPW (mm)	9.79 ± 1.07	9.37 ± 0.96	0.021∗

Table 8: Regression analysis results of yin deficiency and physical and chemical indexes.

Independent variable	Coefficient value	Standard error	Wald X^2	P	OR	95% confidence interval upper limit	lower limit
APTT	0.060	0.022	7.277	0.007∗	1.062	1.017	1.109
CKMB	− 0.065	0.026	6.323	0.012∗	0.937	0.890	0.986
LVEDD	− 0.089	0.023	15.596	0.000∗	0.915	0.875	0.956
LVPW	0.673	0.186	13.096	0.000∗	1.961	1.362	2.824

Table 9: Factors of physical and chemical indexes related to phlegm turbidity.

	Phlegm turbidity ($n = 54$)	Non-phlegm turbidity ($n = 146$)	P
HGB (g/L)	127.50 ± 20.46	119.12 ± 22.39	0.018∗
PLT (10^9/L)	223.72 ± 68.89	247.54 ± 72.42	0.038∗
APTT (s)	24.55 ± 9.74	28.78 ± 7.15	0.021∗
ALT (u/L)	19.68 ± 11.61	23.83 ± 13.56	0.023∗
AST (u/L)	18.83 ± 7.77	21.98 ± 8.33	0.034∗
Cl^- (mmol/L)	105.21 ± 3.31	103.98 ± 8.86	0.030∗
LVEDD (mm)	45.65 ± 7.98	40.78 ± 9.74	0.001∗
FS (%)	36.02 ± 6.43	39.03 ± 4.23	0.002∗

other serious endocrine diseases or other uncontrollable systemic diseases; and (4) pregnant or lactating women.

2.6. Removal, Falling Off, and Suspension Standards. These are enumerated as follows: (1) patients who were wrongly included, (2) patients whose data were incomplete for various reasons after inclusion and could not be counted; and (3) patients who were unable to complete the study due to mental or physical disorders.

2.7. Collection of Clinical Routine Indexes. All selected patients completed white blood cell (WBC), red blood cell (RBC), hemoglobin concentration (HGB), platelet (PLT), thyroglobulin (TG), total cholesterol (TC), high density lipoprotein cholesterol (HDL), low density lipoprotein cholesterol (LDL), cardiac troponin (cTnI), myoglobin, CKMB, alt, AST, bun within 1-3 days after admission creatinine (CR), N-terminal pro-B-type natriuretic peptide (NT proBNP), potassium (K+), sodium (Na+), chloride (Cl-), calcium (Ca2+), prothrombin time (PT), prothrombin activity (PTA), partial prothrombin time (APTT), fibrinogen concentration (FIB), D-dimer (D-D), left ventricular end diastolic diameter (LVEDd), left ventricular end systolic diameter (LVESD), left ventricular posterior wall thickness (LVPW), ventricular septal thickness (IVS), left ventricular stroke output (SV), output per minute (CO), left ventricular end diastolic volume (EDV), left ventricular end systolic volume (ESV), ejection fraction (EF), left ventricular short axis shortening rate (FS), left atrial inner diameter (LAD), right ventricular inner diameter (RIV), and other examinations. Fill in the results in the clinical information collection form and attach relevant copies.

2.8. Neural Network Model Construction Method. The dependent variable is a binary variable. Binary logistic regression square analysis is used to assign values to the dependent variable, in which "yes =1" and "no =0." The method is forward: Wald (forward stepwise method). The test level of the variable entering the model is less than 0.05. Taking the physical and chemical indexes ($P < 0.05$) entered into logistic in each syndrome element as the covariate and each syndrome element as the dependent variable; a neural network model was established and tested.

2.9. Statistical Methods. SPSS21.0 for statistical analysis of data was used. The measurement data of normal distribution is described by (± s), and the counting index is described by frequency and composition ratio. For the hypothesis

Table 10: Regression analysis results of phlegm turbidity and physical and chemical indexes.

Independent variable	Coefficient value	Standard error	Wald X^2	P	OR	95% confidence interval upper limit	lower limit
ALT	−0.034	0.017	4.186	0.041∗	0.966	0.935	0.999
APTT	−0.056	0.025	4.997	0.025∗	0.946	0.901	0.993
LVEDD	0.062	0.021	9.029	0.003∗	1.064	1.022	1.108
FS	−0.105	0.037	8.323	0.004∗	0.900	0.838	0.967

Table 11: Factors of physical and chemical indexes related to qi stagnation.

	Qi stagnation ($n = 52$)	Non-Qi stagnation ($n = 148$)	P
WBC (10^9/L)	6.38 ± 1.66	5.78 ± 1.65	0.005∗
HGB (g/L)	131.73 ± 19.73	117.74 ± 21.86	0.000∗
PT (s)	12.23 ± 4.67	10.08 ± 1.11	0.041∗
FIB (g/L)	2.54 ± 0.62	2.89 ± 1.06	0.049∗
HDL (mmol/L)	1.30 ± 0.34	1.75 ± 3.33	0.010∗
BNP (pg/ml)	129.16 ± 122.40	200.19 ± 172.23	0.006∗
LVEDD (mm)	46.42 ± 7.25	40.57 ± 9.78	0.000∗
LAD (mm)	33.48 ± 6.63	35.81 ± 4.80	0.023∗

Table 12: Regression analysis results of qi stagnation and physical and chemical indexes.

Independent variable	Coefficient value	Standard error	Wald X^2	P	OR	95% confidence interval upper limit	lower limit
WBC	0.288	0.119	5.877	0.015∗	1.333	1.057	1.682
PT	0.335	0.093	12.923	0.000∗	1.398	1.165	1.678
BNP	−0.004	0.002	6.728	0.009∗	0.996	0.993	0.999
FIB	−0.705	0.258	7.467	0.006∗	0.494	0.298	0.819
LVEDD	0.074	0.023	10.206	0.001∗	1.077	1.029	1.126
LAD	−0.102	0.037	7.526	0.006∗	0.903	0.840	0.971

test of comparison between the two groups, the measurement data of normal distribution adopts t-test, the counting data adopts C2 test, and the measurement data of non-normal distribution adopts rank sum test. According to international standards, there was significant difference ($P < 0.05$).

3. Result

3.1. General Information. From January 2017 to January 2019, 238 eligible cases were collected in the inpatient department of Cardiology of Zhengzhou hospital of traditional Chinese medicine, of which 13 cases were excluded because the score of HAMA anxiety scale was between 7 and 14; 6 cases were excluded due to lack of blood lipid index test results; 11 cases were excluded due to lack of cardiac color Doppler ultrasound results; and 8 cases were excluded due to lack of liver and kidney function test results. There were 137 more women, with a constituent ratio of 68.5%. The average age of the patients was 59.77 ± 10.79, the minimum age was 33 years old, and the maximum age was 79 years old. Most of the patients were between 51 and 70 years old, accounting for 59.0%. The majority of patients were retired, followed by workers and intellectuals. The most common syndrome elements are blood stasis, accounting for 84.5%, followed by qi depression, a total of 137 cases, accounting for 68.5%, followed by qi deficiency and yin deficiency, accounting for 47.0% and 42.5%, respectively, followed by phlegm turbidity and qi stagnation, accounting for 27.0% and 26.0%, with less heat accumulation, Yang deficiency, dampness, and cold coagulation.

3.2. Factor Screening of Physical and Chemical Indexes Related to Syndrome Elements

3.2.1. Blood Stasis. Due to the small number of cases of heat accumulation, excessive dampness, Yang deficiency, and cold coagulation, it will not be discussed in the correlation analysis. By nonparametric test or t-test, compared with nonblood stasis patients, there were significant differences in HGB, PLT, Pt, PTA, Na^+, TG, LDL, BNP, LVEDd, and EF in blood stasis patients ($P < 0.05$), as shown in Table 1.

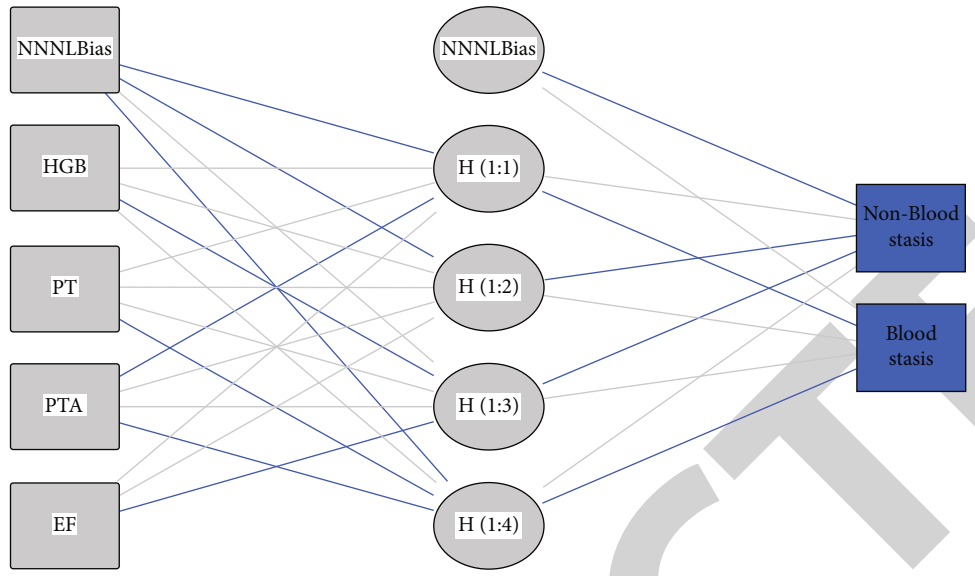

Figure 1: Neural network model for distinguishing blood stasis by characteristic indexes.

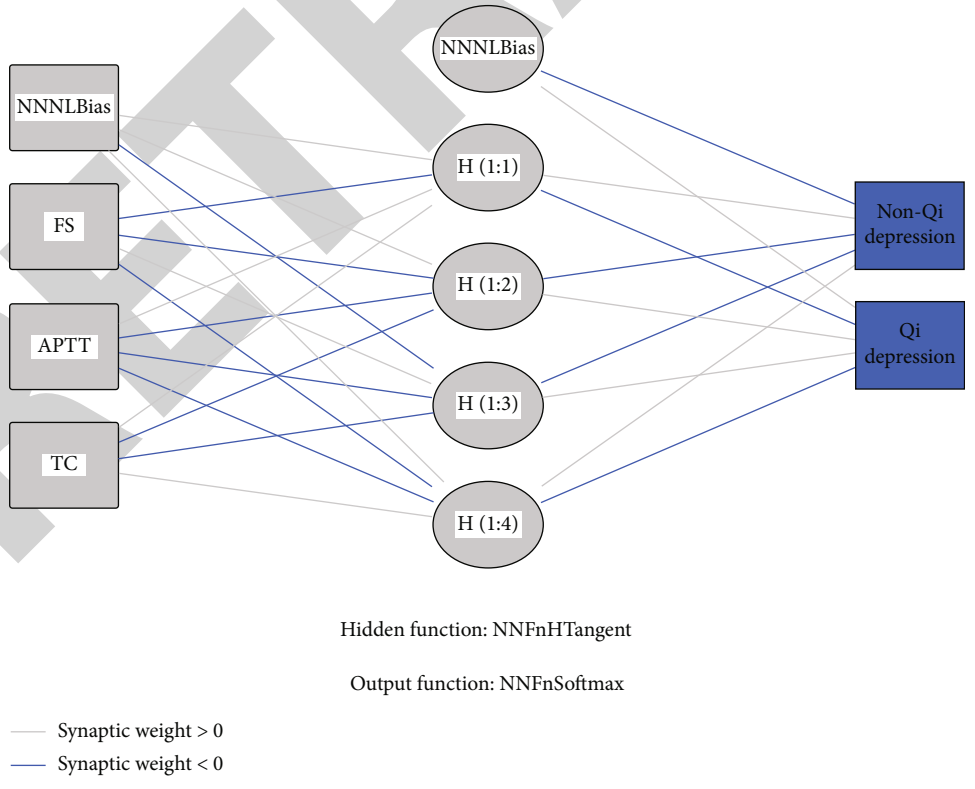

Figure 2: Neural network model for distinguishing qi depression by characteristic indexes.

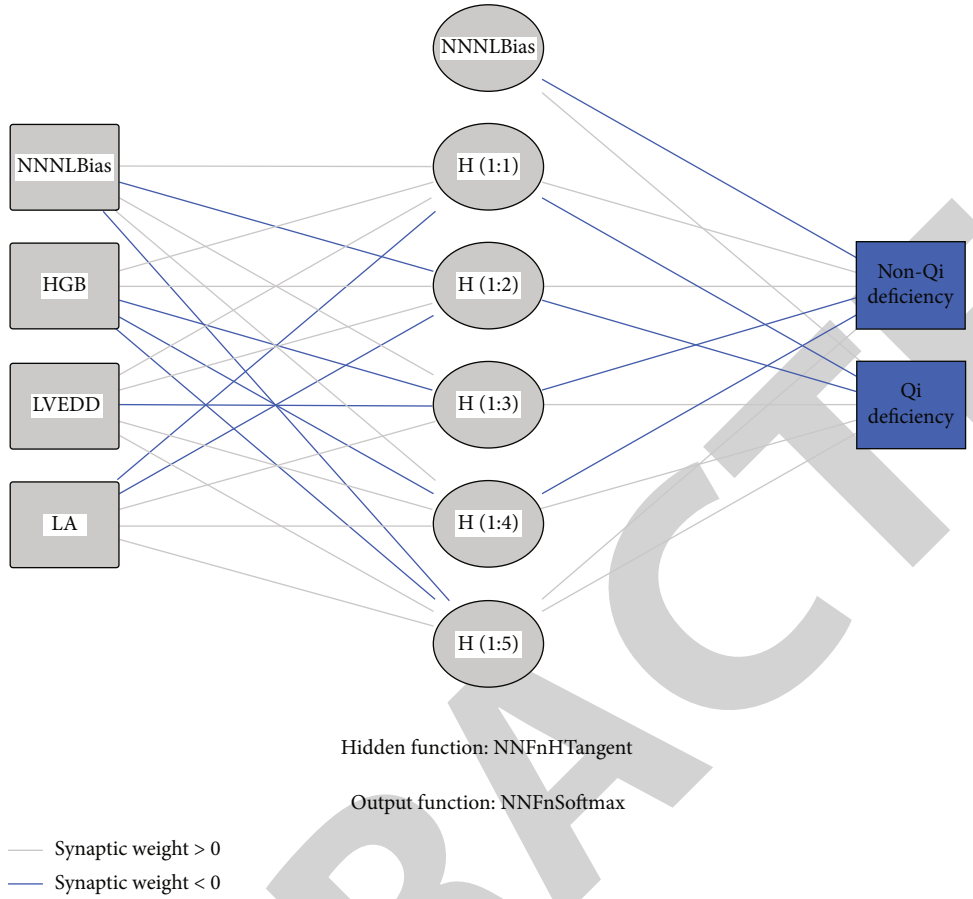

Figure 3: Neural network model for distinguishing Qi deficiency by characteristic indexes.

Taking blood stasis as the dependent variable and the above physical and chemical indexes (Hgb, PLT, Pt, PTA, Na^+, TG, LDL, BNP, LVEDd, and EF) with statistical significance ($P < 0.05$) as independent variables, binary logistic regression analysis is carried out. The results are shown in Table 2. Four indexes enter the regression equation, namely, HGB, Pt, PTA, and ef ($P < 0.05$), as shown in Table 2.

3.2.2. Qi Depression. Compared with non-qi depression patients, there were significant differences in atpp, TG, TC, LDL, LVESD, and FS in qi depression patients ($P < 0.05$), as shown in Table 3.

Taking qi depression as the dependent variable and the above physical and chemical indexes (atpp, TG, TC, LDL, LVESD, and FS) with statistical significance ($P < 0.05$) as independent variables, binary logistic regression analysis was carried out. As shown in Table 4, the three indexes entered the regression equation, namely, APTT, TC, and FS ($P < 0.05$), as shown in Table 4.

3.2.3. Qi Deficiency. Compared with non-Qi deficiency patients, the differences of HGB, APTT, K +, BNP, LVEDd, and LAD in Qi deficiency patients were statistically significant ($P < 0.05$), as shown in Table 5.

Taking Qi deficiency as the dependent variable and the above physical and chemical indexes with statistical significance ($P < 0.05$) (Hgb, APTT, K +, BNP, LVEDd, and LAD) as independent variables, binary logistic regression analysis was carried out. As shown in Table 6, the three indexes entered the regression equation, namely, HGB, LVEDd, and LAD ($P < 0.05$), as shown in Table 6.

3.2.4. Yin Deficiency. Compared with non-Yin deficiency, HGB, APTT, CKMB, LVEDd, and LVPW in patients with Yin deficiency were statistically significant ($P < 0.05$), as shown in Table 7.

Taking Yin deficiency as dependent variable and the above physical and chemical indexes (Hgb, APTT, CKMB, LVEDd, and LVPW) with statistical significance ($P < 0.05$) as independent variables, binary logistic regression analysis was carried out. As shown in Table 8, four indexes entered the regression equation, namely, APTT, CKMB, LVEDd, and LVPW ($P < 0.05$), as shown in Table 8.

3.2.5. Phlegm Turbidity. Compared with non-phlegm turbidity, the differences of HGB, PLT, APTT, alt, AST, Cl-, LVEDd, and FS in patients with phlegm turbidity were statistically significant ($P < 0.05$), as shown in Table 9.

Taking phlegm turbidity as dependent variable and the above physical and chemical indexes (Hgb, PLT, APTT, alt, AST, Cl-, LVEDd, and FS) with statistical significance ($P < 0.05$) as independent variables, binary logistic regression analysis was carried out. As shown in Table 10, four

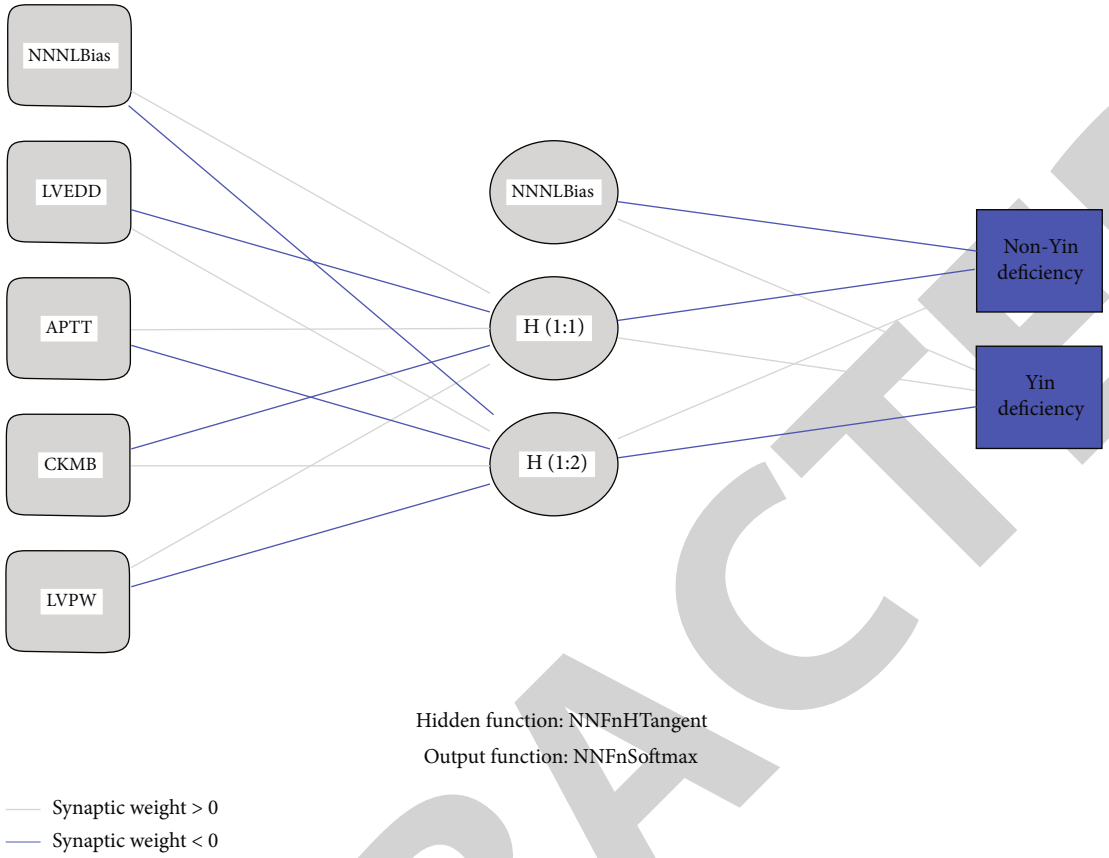

Figure 4: Neural network model for distinguishing Yin deficiency by characteristic indexes.

indexes entered the regression equation, alt, APTT, LVEDd, and FS ($P < 0.05$), as shown in Table 10.

3.2.6. Qi Stagnation. Compared with non-qi stagnation, the differences of WBC, HGB, Pt, FIB, HDL, BNP, LVEDd, and LAD in Qi stagnation patients were statistically significant ($P < 0.05$), as shown in Table 11.

The above physical and chemical indexes (WBC, HGB, Pt, FIB, HDL, BNP, LVEDd, and LAD) with statistical significance ($P < 0.05$) were taken as independent variables for binary logistic regression analysis. As shown in Table 12, six indexes entered the regression equation, namely, WBC, Pt, BNP, FIB, LVEDd, and lad, as shown in Table 12.

3.3. Construction and Evaluation of Neural Network Model. Taking blood stasis as dependent variable and HGB, Pt, PTA, and EF as covariates, build a neural network model and test the model. The results are shown in Figure 1. The accuracy of the model is 85.4% in the training set and 87.1% in the test set.

Taking qi depression as the dependent variable and APTT, TC, and FS as the covariates, the neural network model is established and tested. The results are shown in Figure 2. The accuracy of the model is 71.1% in the training set and 69.0% in the test set.

Taking Qi deficiency as the dependent variable and HGB, LVEDd, and lad as covariates, the neural network model is established and tested. The results are shown in Figure 3. The accuracy of the model is 88.8% in the training set and 91.2% in the test set.

Taking Yin deficiency as dependent variable and APTT, CKMB, LVEDd, and LVPW as covariates, a neural network model is built and tested. The results are shown in Figure 4. The accuracy of the model is 75.0% in the training set and 75.0% in the test set.

Taking phlegm turbidity as dependent variable and alt, APTT, LVEDdm and FS as covariates, build a neural network model and test the model. The results are shown in Figure 5. The accuracy of the model is 79.8% in the training set and 73.2% in the test set.

Taking qi stagnation as the dependent variable and WBC, Pt, BNP, FIB, LVEDd, and lad as the covariates, the neural network mode is established, and the model is tested. The results are shown in Figure 6. The accuracy of the model is 82.6% in the training set and 79.0% in the test set.

4. Discussion

Unstable angina pectoris complicated with anxiety has the common characteristics of unstable angina pectoris and anxiety. Literature studies have found that the most common syndrome elements of coronary heart disease complicated with anxiety are qi stagnation, blood stasis, phlegm, and heat accumulation. In this study, blood stasis, qi depression, Qi deficiency, yin deficiency, phlegm turbidity, and qi

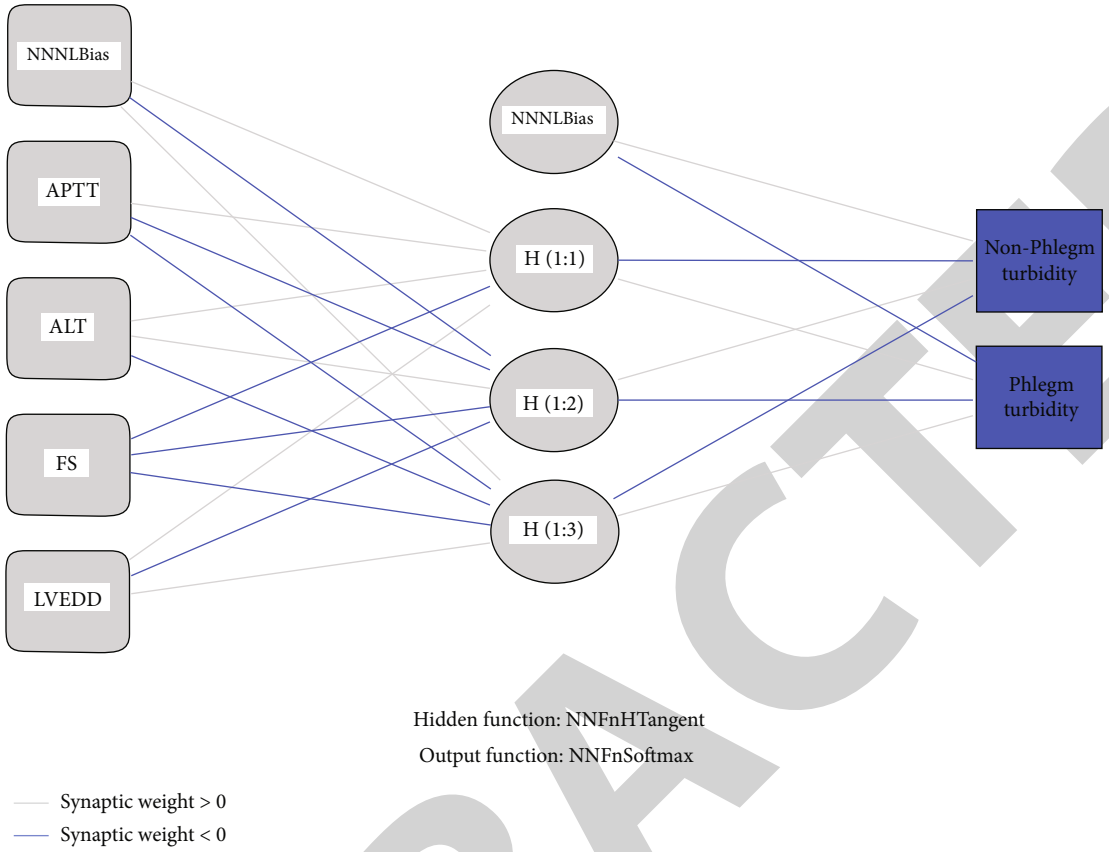

Figure 5: Neural network model for distinguishing phlegm turbidity by characteristic indexes.

stagnation are the most common syndrome elements, which is generally consistent with the results of literature research.

From the perspective of syndrome combination, the syndrome types of three factor combination and four factor combination appear more in this study, and the syndrome performance tends to be complex. In the combination of syndromes, other syndromes are mainly superimposed on the basis of qi depression and blood stasis, suggesting that qi depression and blood stasis are the key pathogenesis of the disease and the main pathological link. However, blood stasis syndrome accounts for 84.5% of the total cases, indicating that blood stasis is the initiating factor of the occurrence of the disease. As the "syndrome sanctions" says: "the depression within the seven emotions starts with Qi injury, and the blood will follow."

HGB is a protein, whose main function is to transport oxygen. It combines with oxygen in the lungs, then transports it to various tissues and organs of the whole body, and transports the waste away at the same time [7]. After anemia, the myocardium is in a state of hypoxia. If the body itself suffers from coronary heart disease, it will increase the burden of the heart, resulting in myocardial ischemia and hypoxia. The patient will show an increase in the number of angina pectoris attacks [8], the aggravation of the degree of angina pectoris, and then develop into heart failure and blood stasis [9]. In this study, HGB in patients was lower than that in non-deficiency and blood stasis group. It is considered that patients in blood stasis group may have anemia.

FS is an index parameter of left ventricular systolic function. It is a sensitive index reflecting myocardial contractility. Its calculation is the ratio of the shortening value of left ventricular diameter at each contraction to the ventricular diameter at each end of diastole. Studies have shown that there is an obvious linear correlation between FS and EF and FS is more accurate and repeatable than EF in evaluating cardiac systolic function [10]. In this study, the level of FS is high, suggesting that compared with patients with non-qi depression syndrome, the myocardial contractility of patients with qi depression syndrome may be relatively better.

Studies have shown that lad can accurately predict the mortality of patients with coronary heart disease and heart failure [11]. The enlargement of LAD reflects a certain degree of myocardial remodeling. When the left ventricular systolic function is not changed, the increase of LAD reflects the impairment of left ventricular diastolic function [12]. Studies have shown that the increase of lad is comparable to the decrease of LVEF [13]. In this study, lad in patients with Qi deficiency syndrome is relatively high, suggesting that patients with Qi deficiency syndrome may have certain myocardial remodeling and reduced systolic function.

ALT is an important raw material for the synthesis of a variety of non-essential amino acids. It is involved in the diagnosis of many diseases. The liver is the most common site of alt, followed by the kidney, heart, and skeletal muscle. ALT includes the following: two isozymes, alts, and ALTM, exist in cytoplasm and mitochondria, respectively, and the activity of

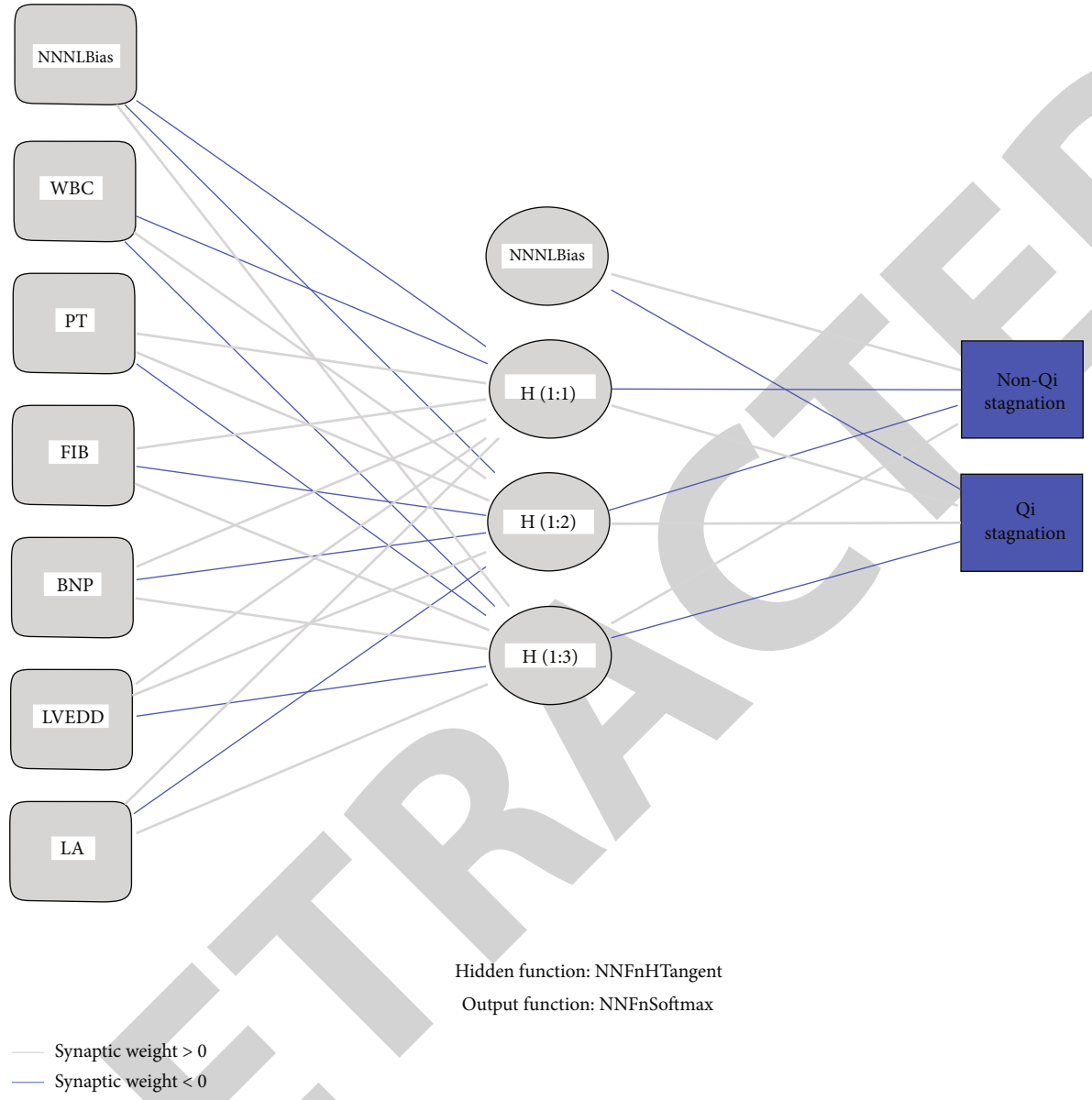

Figure 6: Neural network model for distinguishing qi stagnation by characteristic indexes.

the latter is greater than that of the former. The increase of serum ALT generally indicates liver injury, and the damaged hepatocytes are mainly ALTM [14], while the serum ALT is low, and the disease is generally not considered. In this study, the ALT level of phlegm turbidity syndrome is lower than that of non-phlegm turbidity syndrome, and there are few studies on this aspect. Therefore, the relationship between phlegm turbidity syndrome and ALT still needs to be discussed.

FIB is a "protagonist" protein synthesized by the liver and playing a role in the coagulation system. It is a class II glycosylated protein synthesized by the liver and free in plasma. Its half-life is 3-6 days, and its molecular metabolic rate is 31-46 mg/kg. It accounts for about 3% of the total plasma protein [15]. When coagulation occurs, FIB is hydrolyzed into fibrin monomer under the action of thrombin and then cross-linked to fibrin. In addition, FIB can specifically bind to platelet membrane glycoprotein II B/III a receptor to promote platelet aggregation[1, 2] [16, 17]. In this study, FIB in patients with qi stagnation syndrome was significantly lower than that in patients with non-qi stagnation syndrome, suggesting that the blood coagulation function of patients with qi stagnation syndrome was reduced. However, this study also has some shortcomings, such as not including the number of cases in a wider range and not using external validation set validation. Besides, the mechanism is not verified. Further studies are needed to study this.

5. Conclusion

To sum up, the combination pattern of physical and chemical indexes obtained from the neural network model provides a clinical reference basis for identifying the syndrome elements of unstable angina pectoris complicated with

Hindawi
Computational and Mathematical Methods in Medicine
Volume 2022, Article ID 8127055, 14 pages
https://doi.org/10.1155/2022/8127055

Research Article

Design and Analysis of Hospital Throughput Maximization Algorithm under COVID-19 Pandemic

Haochen Zou, Geer Jiang, Bowen Cheng, and Dejian Wang

Department of Computer Science and Software Engineering, Concordia University, Montreal, QC, Canada H3G 1M8

Correspondence should be addressed to Haochen Zou; haochen.zou@mail.concordia.ca

Received 27 May 2022; Accepted 18 July 2022; Published 11 August 2022

Academic Editor: Plácido R. Pinheiro

Under the global pandemic of COVID-19, public health facilities, such as hospitals, are required to readjust, design, and plan a safe movement flow of people to meet the social distance rules and quarantine COVID-19 and the non-COVID-19 patients to prevent cross-infection. However, readjustments to separate patients have significantly reduced the maximum throughput of public health facilities, worsening already scarce public health resources. Therefore, this paper proposes throughput maximization algorithms based on the one-way street problem which meets the requirements of social distance rules. First, the floor plan of a hospital is transformed into a graph, each node is traversed by breadth-first search. Then, this paper considers patients' node pair sets as different set unions, the direction of edges, and the color of links based on DFS-XOR algorithm are designed to distinguish the paths of COVID-19 and non-COVID-19 patients. Finally, this paper utilizes minimum shared link algorithms to determine the minimized sharing links between paths linking different set unions and components. The throughput is maximized by reducing the number of shared links and alternating links. The results indicate that compared with the brute force algorithms, the algorithms proposed in this paper significantly improve the maximum throughput.

1. Introduction

The COVID-19 pandemic broke out in December 2019 and quickly swept the world, with the virus affecting the global economy and everyone's daily lives. The COVID-19 pandemic has introduced unprecedented challenges in the world. Due to the emergence and prevalence of COVID-19 and variant strains of COVID-19 such as Omicron, hospitals and other public health facilities are required to readjust, design, and plan a safe movement flow of people to meet social distancing requirements [1]. The goal is to isolate COVID-19 patients from non-COVID-19 populations to avoid crossinfection and thereby reduce the number of COVID-19 cases [2]. However, although the redesigned flow of movement meets the requirements of social distance, the ability of public health facilities to accommodate patients is significantly reduced due to the need for extra spaces. This worsens the already strained public medical resources. At the same time, doctors and nurses may also be infected with COVID-19 during work and leave their posts, which exacerbates the shortage of hospital staff and further reduces hospitals' patient intake levels [3]. Therefore, this paper intends to solve the problem of how to redesign and plan the movement routes of people in hospitals and other public health facilities under the premise of meeting the requirements of social distancing in order to maximize throughput.

The arrival of infectious variants of COVID-19, such as Omicron, has led to an exponential and dramatic increase in confirmed COVID-19 cases in a relatively short period, and the number of patients needing to visit public health facilities grows as well [4]. Much of the disaster planning in hospitals around the country addresses overcrowded emergency departments and decompressing these locations. However, in the case of COVID-19 pandemic, intensive care units, emergency departments, and medical wards ran the risk of being overwhelmed by a large influx of patients needing high-level medical care [5]. Sarier et al. contradistinguished the number of patients attending the hospital urology clinic during the first year of the COVID-19 pandemic compared to 2018 and 2019 [6]. Previous works have been conducted to modify and deploy existing hospital consultation plans to quickly care for large numbers of

medically complex patients. These studies are designed to maximize the throughput of patients that hospitals can accommodate. Bowden et al. described a scale-up approach to managing residents' clinical practices during the COVID-19 pandemic. Their study provides a framework for maximizing patient admission while also leveraging a broad clinician workforce, minimizing exposure, and maximizing the pool of clinicians who may not be involved in inpatient care [5]. However, their study is aimed at describing a scale-up approach to managing residents' clinical practices during the COVID-19 pandemic, targeting physicians rather than hospitals, since the situation of physicians varies greatly from hospital to hospital. Therefore, although the plan has been successful in their institutions, it needs to be significantly modified for other public health facilities. Meanwhile, their plan does not consider the social distance rules. Shahverdi et al. proposed models for assessing strategies for improving hospital capacity for handling patients during the pandemic [7]. It enables hospitals to repurpose space, modify operations, implement crisis standards of care, collaborate with other health care facilities, or request external support, thereby increasing hospital capacity. However, the strategy evaluation model they designed is mainly focusing on the routine emergency and emergency care under the pandemic, which is difficult to apply to the overall situation of hospitals and other public health facilities. Meanwhile, only a fraction of all COVID-19 cases requires emergency care, meaning that the majority of COVID-19 patients will not benefit from the above strategic assessment model [8]. Olanipekun focuses on preventing delays in transferring patients to long-term lower acuity level nursing facilities, reducing length of hospital stay, improving patient flow, and ultimately freeing up hospital beds for incoming COVID-19 patients [9]. The above-described approach maximizes the throughput of patients. However, the process involves transferring patients to nursing facilities to shorten the length of stay, rather than improving hospitals' own situations.

Therefore, in addition to the approaches discussed above, this paper is aimed at designing hospital throughput maximization algorithms which meet the requirements of social distance and can be widely implemented by most hospitals and other public health institutions. Based on the aforesaid objectives, we first transformed the floor plan of a hospital into a strong orientation connected graph for implementing graph algorithms [10]. Then, the patient node pair sets are treated as the union of different sets, the direction of edges, and the color of links are assigned based on the DFS-XOR algorithm to distinguish the walking paths of COVID-19 and non-COVID-19 patients. Finally, the minimum shared edge algorithm is implemented to determine the minimization of shared links between paths connecting different sets of unions and components. The maximized throughput is achieved by reducing the number of shared links and alternating links. The contrast experiment indicates that compared with brute force algorithm to split the walking paths of COVID-19 and non-COVID-19 patients, the algorithm proposed in this paper improves the maximum throughput of patients in public health institutions such as hospitals.

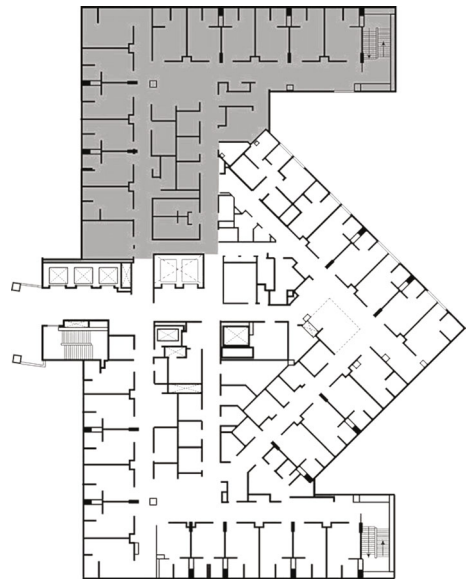

Figure 1: The floor plan of McGill University Health Centre.

2. Materials and Methods

2.1. Convert Hospital Floor Plans to Graphics. The throughput maximization algorithm proposed in this paper is based on the graph algorithm. Therefore, the first step of the method is to transform the floor plans of hospitals and other public health facilities into graphs. A floor pan of the McGill University Health Centre is displayed in Figure 1. The graph is composed of the set of nodes and the set of edges. Nodes can be further divided into ordinary nodes and special nodes [11]. In a hospital floor plan, the corridors are the edges of the graph.

The entrances or exits of rooms can be considered as the ordinary nodes of the graph. The main entrance of the floor, the main exit of the floor, and the intersections of the corridors are decided as the special nodes of the graph.

Based on the above definition of nodes and edges in the graph, the hospital floor plan can be transformed into an undirected graph $G = (V, E)$, where V is the set of nodes and E is the set of edges. Automatic understanding of floor plan images and converting floor plans to graphs could be accomplished by the deep recognition framework proposed by Lu et al. [12]. A sample of transformation and the result are displayed in Figure 2.

Under the background of the COVID-19 pandemic, some consulting rooms of hospitals are required to treat the COVID-19 patients; the other consulting rooms are receiving non-COVID-19 patients [13]. In public health, social distancing, also called physical distancing, is a set of nonpharmaceutical interventions or measures intended to prevent the spread of a contagious disease by maintaining a physical distance between people and reducing the number of times people come into close contact with each other [14]. Canada adopted a two-meter (approximately 6 ft) social distancing policy [15]. Although the requirement of social distance in public places has been gradually abolished, the

Figure 2: A sample of transformation from a floor plan to a graph: (a) the floor plan; (b) the transformed graph.

restriction of social distance is still strictly enforced in public health facilities such as hospitals [16].

Hospital corridors are clearly inadequate for social distance rules, especially when there is a large flow of people. Therefore, COVID-19 patients and other patients cannot share the same corridor at the same time. When one corridor is shared by both COVID-19 patients and other patients, we consider the edge of this corridor as the shared edge.

Therefore, the hospital floor plan further consists of the following parts: consulting rooms for COVID-19 and non-COVID-19 patients with entrances and exits, the main entrance and exit of the floor, corridors for patients to move, and intersections of corridors. The sample floor plan of a

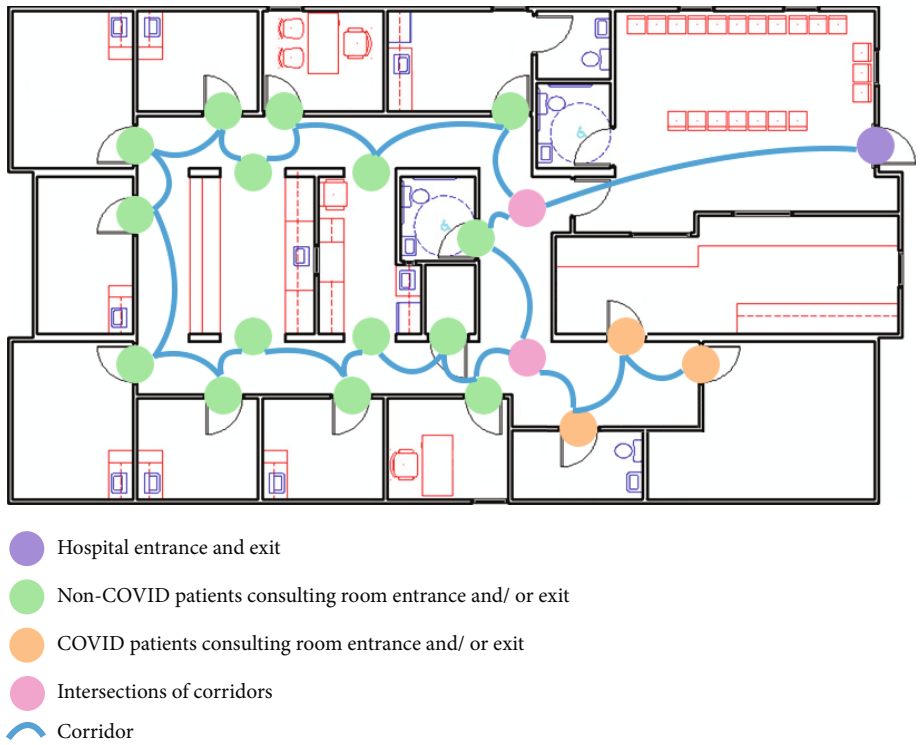

Figure 3: The sample floor plan of a hospital with COVID-19 and non-COVID-19 node sets.

hospital in a graph with COVID-19 and non-COVID-19 node sets is displayed in Figure 3.

The hospital floor plan is eventually converted into an undirected graph. In the graph, we require that each consulting room must have (1) at least one path from the main entrance of the floor to the entrance of the consulting room; (2) at least one path from the exit of the consulting room to the main exit of the floor; and (3) at least one path from the exit of any consulting room to the entrance of any other consulting room within the same node set, to meet the accessibility. Therefore, there must be some edges that need to be considered as shared edges as defined above. In the graph algorithm, the edge is undirected, and the link is directed [17]. The flow of people on one edge can be maximized when the edge is oriented as a one-way link, while to satisfy the accessibility, some of the edges must be determined as two-way links; these links are defined as alternating links. Alternating links are the links that are used in both directions, utilized alternately in each direction, with the usage of a single direction at any given time and a waiting area at each end of the links associated with alternating links. Throughput is rate of production or the rate at which something is processed [18]. In the context of the paper, throughput is the number of people reaching their destination per time unit [19]. As the shared links defined and discussed above, the existence of alternating links and shared links reduces the throughput of patients in a hospital because when one group is passing, the other group must stay at one end and wait, which significantly weakens the traffic efficiency of the flow. Shared links and alternating links contain waiting areas at their origins, which correspond to converge flows, and therefore lead to a source of flow slowdown [20].

Hence, the essence of the throughput maximization algorithm is to minimize the number of shared links and alternating links in the graph of the hospital floor plan.

2.2. Label Colors of the Edges. Given the undirected graph of a floor plan $G = (V, E)$ computed from the above section, two sets of node pairs are generated: SD1: the non-COVID-19 node pairs set, and SD2: the COVID-19 node pairs set. Sample SD1 and SD2 is shown in Figure 3, as the non-COVID-19 and COVID-19 patients consulting room entrances and/or exits separately. Nodes from SD1: s_1, $s_2, \cdots, s_n \in V$. Nodes from SD2: $s_1', s_2', \cdots, s_n' \in V$. Particularly, special nodes can be considered as belonging to both node pairs set, as the main entrance of the floor, the main exit of the floor, and the intersections of the corridors can be passed by both non-COVID-19 and COVID-19 patients. Corridors $l_1, l_2, \cdots, l_n \in E$. The goal is to label the same color link paths for individual node sets, such that COVID-19 patients walk along the red color link paths, and non-COVID-19 patients walk along the green color link paths, therefore, to detect all edges $l \in E$ and $l' \in E$ in the graph G where $l(u, v)$, $u \in$ SD1, $v \in$ SD1, and $l'(u', v')$, $u' \in$ SD2, $v' \in$ SD2.

The breadth-first search (BFS) algorithm is implemented on the undirected graph $G = (V, E)$ to make sure that all nodes in each set are reachable from the root nodes which are the main entrance [21]. The algorithm is described below in Algorithm 1.

```
1:  procedure BreadthFirstSearch (G(V, E), SD, root)
2:    for each vertex u in G(V)
3:        u.color ⟵ WHITE
4:        //initializing all vertices in the given graph
5:        u.d ⟵ ∞
6:        u.π ⟵ NIL
7:    end for
8:    u ⟵ root
9:    P ⟵ EmptyArrayList
10:   P ⟵ P ∪ MODIFIEDBFS(G, SD, u)
11:   //ModifiedBFS algorithm with specified root vertex
12:   for each vertex u ∈ G(V) − {root}
13:       if u.color is WHITE
14:           P ⟵ P ∪ MODIFIEDBFS(G, SD, u)
15:   //ModifiedBFS algorithm with unreached vertices
16:       end if
17:   end for
18:   return P
```

Algorithm 1: Breadth-first search algorithm.

Apply BFS search with the condition that only the node with SD1 or SD2 sets can be added to the queue [22]. The breadth-first tree formed after running the traditional algorithm may not visit all the vertices in some graphs for instance directed cyclic and acyclic graphs. Therefore, the traversing may be incomplete. We traverse the graphs with the usage of a modified BFS algorithm discussed below in Algorithm 2 [23].

The result of Algorithm 1 and Algorithm 2 will be the data structure of linked list as edges to form a path. It stores the node objects for COVID-19 patients and non-COVID-19 patients. We implement a Color Path Algorithm to color the original graph with two undirected paths consists of edges, as discussed in the Algorithm 3.

The total running time of the proposed algorithm is $O(V + E)$ [24], since the most time taken part is custom BFS by using the linked list data structure to store the whole graph. After above steps, two datasets are formed. There are two undirected paths in the datasets. One is for COVID-19 patients, and the other one is for non-COVID-19 patients.

2.3. Define Orientation to Minimize Alternating Links. In this section, we define the orientation of edges in the undirected paths. The aim is to minimize the alternating links in the process of orientation, and meanwhile, satisfy the requirements of accessibility. The one-way street problem is a graph orientation problem, which means to define the orientation of edges (undirected links) subject to conditions [25]. The definition of the one-way street problem is as follows: consider an undirected graph, is it possible to choose a direction for each edge, turning it into a directed graph that has a path from every vertex to every other vertex [26]? Strongly connected components satisfy the requirement of the one-way street problem [27]. Therefore, we need to detect the strongly connected components inside each graph formed by the undirected paths.

```
1:  procedure ModifiedBFS (G(V, E), SD, u)
2:    u.color ⟵ GREY
3:    u.d ⟵ 0
4:    //tree from the specified root vertex
5:    u.π ⟵ NIL
6:    Q ⟵ EmptyQueue
7:    P ⟵ EmptyArrayList
8:    ENQUEUE(Q, u)
9:    while not EMPTY(Q)
10:       u ⟵ DEQUEUE(Q)
11:       if u ∈ SD
12:           P ⟵ P ∪ {u}
13:       end if
14:       for each vertex v in ADJ[u]
15:           if v.color is WHITE
16:               u.color ⟵ Grey
17:               u.d ⟵ u.d + 1
18:               u.π ⟵ u
19:               ENQUEUE(Q, v)
20:           end if
21:       end for
22:       u.color ⟵ BLACK
23:   end while
24:   return P
```

Algorithm 2: Modified BFS algorithm.

For the two undirected graph generated by the two undirected paths, we first consider all the edges as alternating links to make the graph directed. Then, we detect the strongly connected components inside the graph. If inside the node sets, there exist cycle component connected nodes, the direction of the links formed the cycle can be defined as one side, and the cycle is considered as strongly connected component [28]. Otherwise, inside the component, some nodes may not be reachable under the one-direction way street problem's condition; hence, alternating links will be

```
1:  procedure GetAllEdges(P)
2:    P1 ⟵ EmptyArrayList
3:    //path P is an array list with node objects
4:    for i ⟵ 1 to length of P
5:        if i + 1 ≤ length of P
6:          P1 ⟵ P1 ∪ (P[i], P[i + 1])
7:  procedure RemoveUsedPath (G(V, E), P)
8:    Edges ⟵ GETALLEDGES(P)
9:    for each e ∈ Edges
10:       if e ∈ G(E)
11:         G ⟵ G − {e}
12:       end if
13:   end for
14:   return G
15:  procedure TraverseEdges (G(V, E), SD1, SD2)
16:   ///Assume that SD1 is non-COVID nodes dataset
17:   ///Assume that SD2 is COVID nodes dataset
18:   G1 ⟵ DirectedGraphConvert(G)
19:   P ⟵ BreadthFirstSearch(G1, SD1, root)
20:   if P covers all nodes in SD1:
21:       P1 ⟵ GetAllEdges(P)
22:       G2 ⟵ RemoveUsedPath(G1, P1)
23:   end if
24:   P2 ⟵ BreadthFirstSearch(G2, SD2, root)
25:   ifP2 covers all nodes in SD2:
26:       P3 ⟵ GetAllEdges (P2)
27:   end if
28:   resultG ⟵ ColorPath(G1, P1, P2)
29:   return resultG
30:  procedure ColorPath (G(V, E), P1, P2)
31:   //P1 belongs to non-COVID edges generated from BFS algorithm
32:   //P2 belongs to COVID edges generated from BFS algorithm
33:   for each e ∈ G(E)
34:       if e ∈ P1
35:         Color(e, GREEN)
36:       else if e ∈ P2
37:         Color(e, RED)
38:       else
39:         Color(e, GREY)
40:   return G
```

Algorithm 3: Color path algorithm.

implemented. The direction of a strongly connected component cycle path will be defined from the entry to the exit or vice versa. The DFS-XOR algorithm is implemented for detecting whether there are cycle components in the graph or not as Algorithm 4 displayed below.

The total running time of the proposed algorithm is $O(V + E)$ [29], since the most time taken part is custom depth-first search (DFS) by using the queue data structure to store the whole graph. The graph with define orientation paths after processing the cycle detection algorithm is displayed in Figure 4.

2.4. Define Orientation to Minimize Shared Links. We intend to confirm the orientation of the left alternating links in the graph, detect, and minimize the shared links to achieve the goal of maximum throughput. The current graph of a floor plan is shown in Figure 5. As displayed, there are links with already defined orientation, such as the red links and the green links in the graph. There also exist alternating links which required to be further oriented, such as the grey links in the graph.

A strong orientation is an orientation that results in a strongly connected graph. Robbins' theorem states that a graph has a strong orientation if and only if it is two-edge-connected, for example, if the graph has no bridge assuming the graph is connected [30]. An orientation of a graph G is an assignment of a direction to each edge of G, which obtains, as a result, a digraph. Let G be a connected graph and B be one of its edges. We define B as a bridge of G if the graph $G1$ obtained by removing B from G is disconnected [31]. We can conclude from the above description that the shared link is the bridge.

Identification of bridges can be done in linear time using Trajan's algorithm [32]. Multiple techniques can be

```
1:  procedure DFSCycleCountXOR (G(V, E))
2:    //initialization
3:    n ⟵ 0
4:    //n stores number of discovered cycles in operation
5:    CycleQueue ⟵ NIL
6:    //stores the discovered cycles
7:    TotalCycleQueue ⟵ NIL
8:    //stores the discovered cycles
9:    //end of initialization
10:     DFSVisit(u)
11:     //calling DFS for computing initial set of cycles
12:     TotalCycleQueue ⟵ TotalCycleQueue + CycleQueue
13:     for l = 2 to n
14:     //l stores the level of XOR to be done between the unique cycles
15:           for each combination comp of size = l in CycleQueue
16:                 cycle ⟵ XOR all cycles in comp
17:                       if cycle is a valid cycle
18:                       then TotalCycleQueue ⟵ cycle + TotalCycleQueue
19:     DFSVisit(u)
20:     set u to gray
21:     time ⟵ time + 1
22:     d[u] ⟵ time
23:     for each v ∈ Adjacent[u]
24:           if v is white
25:                 then DFSVisit(v)
26:           if v is white
27:                 then CycleQueue ⟵ CycleQueue + new cycle
28:   //discovered using back tracking the DFS path from vertex V to itself
29:           n = n + 1
30:           //count number of discover cycles
31:           set u to black
```

Algorithm 4: DFS cycle count XOR algorithm.

implemented to minimize the number of shared links. Computing a Hamiltonian path or a cycle (Hamiltonian path with the option of going several times through the same nodes) is a mechanism for reducing the number of shred links [33]. The algorithm to compute a Hamiltonian path or a cycle is the DFS and backtracking algorithm [34]. Overall, the minimum shared edges (MSE) problem is defined as follows.

Given a directed graph $G = (V, E)$, two special nodes s, $t \in V$, and integer $k > 0$. Find a set P of k paths from s to t in G so as to minimize $c(P) = \sum_{e \in E} \lambda(e)$, where $\lambda(e) = 0$ if e is used in at most one path of P, and $\lambda(e) = 1$ otherwise. An edge e with $\lambda(e) = 1$ is called a shared edge. As discussed by Omran et al., the MSE problem is NP-hard [35].

We implement a modified depth-first search (DFS) method to detect and minimize the number of bridges. The DFS algorithm generates four types of links: tree, forward, backward, and transversal [36]. Consider the DFS algorithm, while we are looking for vertices adjacent to vertex v, will be a bridge if and only if none of the vertex's u or any of its descendants in the DFS traversal tree has a back edge to vertex v or any of its ancestors. We can check the existence of back edges in $O(V + E)$ time as the domain time to do the depth-first search. Let $\mathrm{TIN}(v)$ denotes the entry time for node v. We introduce an array LOW which will let us check the fact for each vertex v. $\mathrm{LOW}(v)$ is the minimum of $\mathrm{TIN}(v)$, entry times $\mathrm{TIN}(p)$ for each node p that is connected to node v via a back-edge (v, p), and the values of $\mathrm{LOW}(w)$ for each vertex w which is a direct descendant of v in the DFS tree:

$$\mathrm{LOW}(v) = \begin{cases} \mathrm{TIN}(v), \\ \mathrm{TIN}(p), \text{ for all p such that } (v, p) \text{ is a back edge}, \\ \mathrm{TIN}(v), \text{ for all w such that } (v, w) \text{ is a tree edge}. \end{cases} \tag{1}$$

After the above processes, there is a back edge from vertex v or one of its descendants to one of its ancestors if and only if vertex v has a child w for which $\mathrm{LOW}(w) \leq \mathrm{TIN}(v)$. If $\mathrm{LOW}(w) = \mathrm{TIN}(v)$, the back edge comes directly to v; otherwise, it comes to one of the ancestors of v. Therefore, the current edge (v, w) in the DFS tree is a bridge if and only if $\mathrm{LOW}(w) > \mathrm{TIN}(v)$ [37].

The minimized number of shared links is detected according to the method. The shared link is used by both COVID-19 and non-COVID-19 patients; therefore, such should be orientated in both directions. Figure 6 shows the graph of a hospital's floor plan with the designed movement

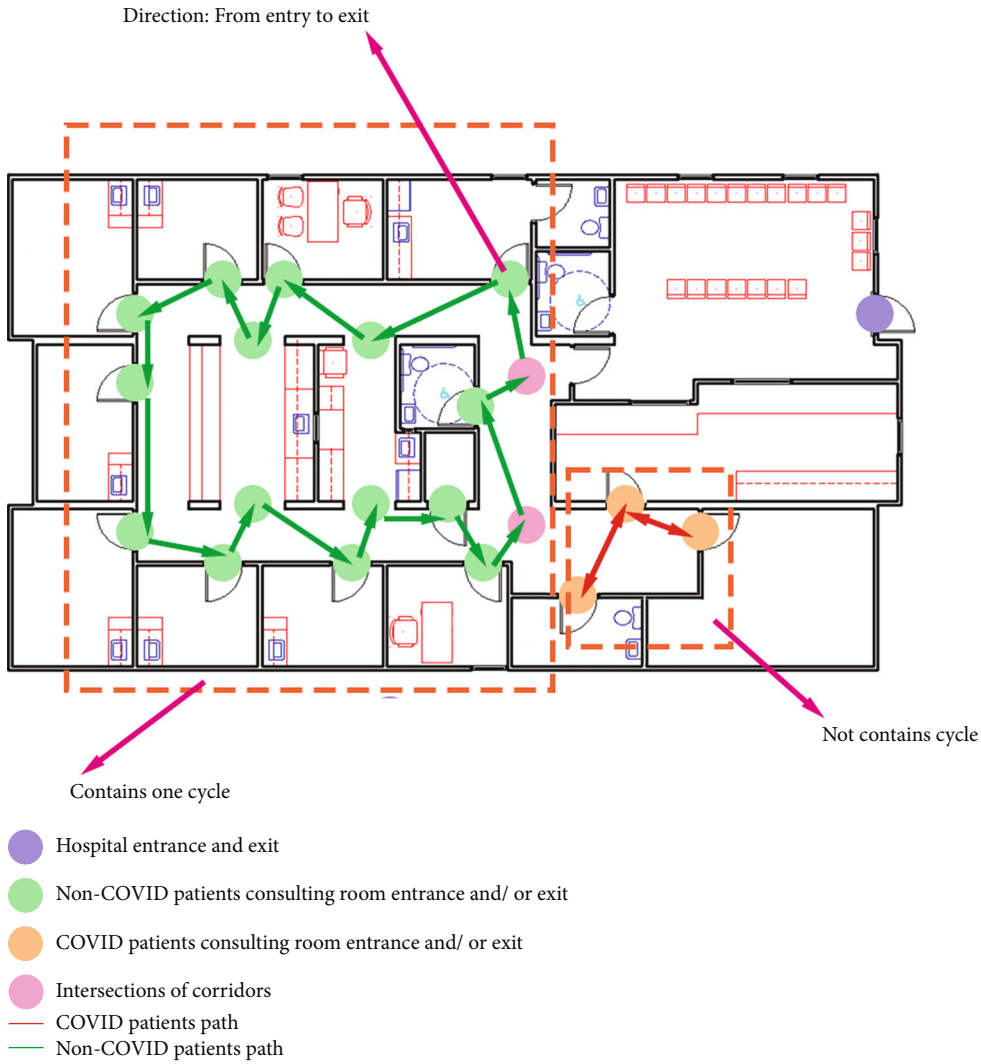

Figure 4: The graph with direction after algorithm modification.

flow of patients after all the algorithms' modifications. In the movement flow designed in the figure, the maximum throughput of the floor plan is obtained by reducing the number of alternating links and shared links.

3. Results and Discussion

3.1. Results. This section presents the analysis result of the designed hospital throughput maximization algorithm. There are two crowd movement path flows for one general hospital; one is according to the brute force method, and the other one is designed based on maximum throughput algorithm proposed in this paper. We establish the crowd flow simulation model of two different paths to calculate and count the time of the crowd consumed by moving from the exits of the consulting rooms to the main exit of the floor. The time difference between the two paths is compared to achieve the purpose of contradistinguishing throughput. Since throughput is the number of people reaching their destination per time unit. Based on the same amount of people in the crowd, the longer the consumption on the path, the smaller the corresponding throughput.

Pathfinder is selected for simulation in this paper. Pathfinder is a simulator based on human movement simulation. It provides users with a graphical user interface for simulation design and operation, as well as 2D and 3D visualization tools for analysing results [38]. Pathfinder utilizes a geometric model that supports 3D. This model includes rooms, doors, stairs, exits, and other structures. The three-dimensional structure diagram of a general hospital is shown in Figure 7.

The human is the main body of the simulation function, and the simulation model of the software allows to test the speed of the human, the width of the human model, the priority level, and special behaviours of the human. Pathfinder supports both steering and SFPE mobile simulation modes [39]. By using the hypothesis group in the SPFE handbook, the simulated personnel will not try to avoid each other when moving and will be crowded with each other [40]. The traveling speed of the crowd is affected by the space density of the room, and the pedestrian flow at the exit is

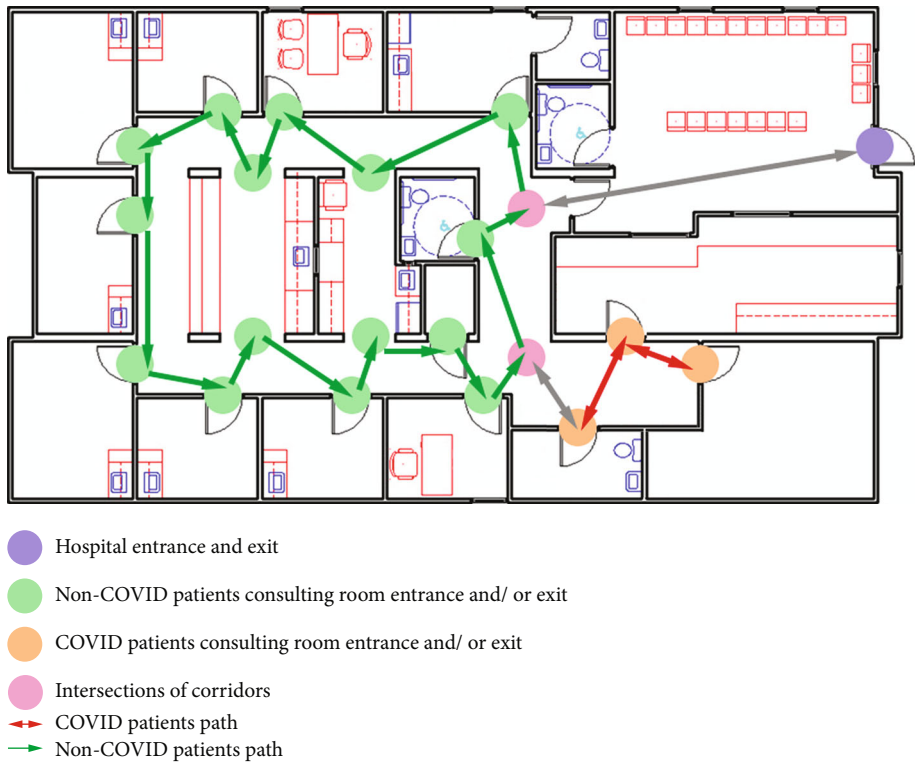

Figure 5: The current graph of a floor plan with oriented links and links to be oriented.

determined by the width of the door. In the steering mode, a reasonable distance will be maintained between people [41]. If the distance between moving people and the path of the nearest point reach or exceed a certain threshold, the system will automatically select other feasible paths and change the walking path of simulated personnel. Since the steering mode is closer to the real moving situation, the paper implements the steering mode in the simulation.

In the analysis of this paper, the population in the building is divided into eight types: adult male, sick male, adult female, sick female, normal old people, sick old people, normal children, and sick children. Simulated speed and simulated shoulder width of all kinds of personnel are adjusted according to the set parameters. The average shoulder width of personnel is set as 45 cm. According to the information provided by the hospital and field investigation, during the peak period of medical treatment, the flow of people on each floor of a hospital at a certain point is about 200 people. The building area of each floor is 1,500 square meters, and the crowd density is less than one person per square meter.

The movement speed and agility of eight different categories of personnel are different [42]. In the simulation analysis of personnel flow, the proportion and speed of personnel in the simulation software are shown in Table 1.

After generating corresponding simulators from various personnel data, we input the corresponding number of simulators into the system according to the expected personnel distribution and obtain the graph of generating simulators, as shown in Figure 8.

The two kinds of hospital personnel movement paths are generated based on the brute force method and the algorithm proposed in this paper. The simulation model with simulators in consulting rooms and corridors of the hospital moving to the main exit of the floor along the movement paths is displayed in Figure 9.

In this paper, the first floor, second floor, and third floor plans of the hospital are selected for the establishment and research of simulation model. The path diagram of personnel movement is shown in Figure 10. Randomly distributed people at each floor will choose the nearest path to the exit.

The thermal map of personnel density is shown in Figure 11.

From the simulated personnel movement path and personnel density heat map, it can be seen that the randomly distributed people on the first, second, and third floors of the hospital will choose the path to the main exit of the whole floor nearby for movement. According to the statistical time, there are 450 people on the whole three floors. The total time to reach the main exit of each floor using the movement path generated by the brute force method is 335.9 seconds, while the total time to reach the main exit of each floor using the movement path generated by the algorithm proposed in this paper is 227.6 seconds. The algorithm introduced in this paper can improve the hospital throughput.

3.2. Discussion. The present study developed algorithms for maximizing the patients' throughput in public health institutions such as hospitals under the requirements of social distancing. Different various methods previously designed by other scholars to improve patient acceptance are the scale-up approach to managing residents' clinical practices

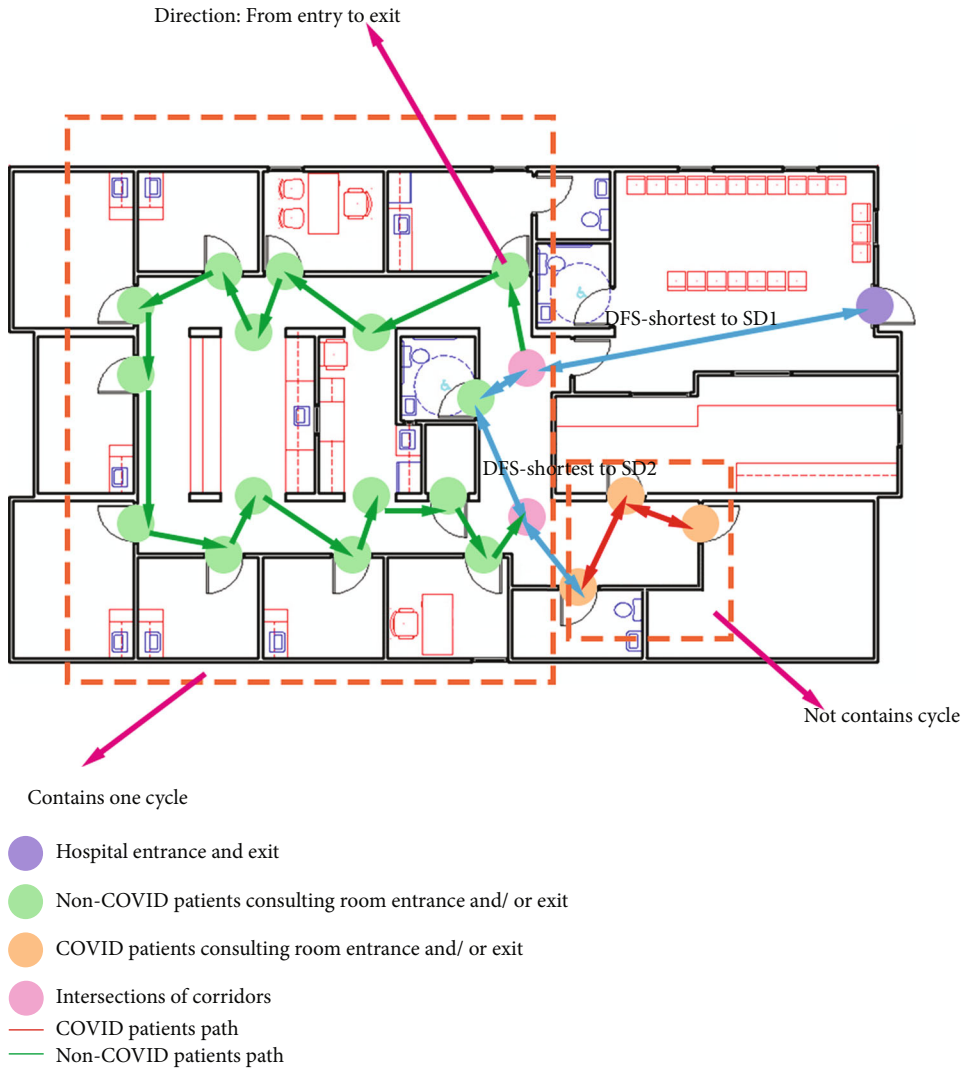

Figure 6: The movement flow of a floor plan graph after algorithm modification.

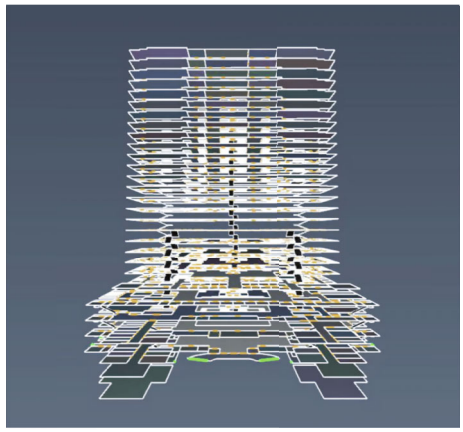

Figure 7: The three-dimensional structure diagram of a general hospital.

Table 1: Proportion of eight types of people and the walking speed.

Type of people	Proportion (%)	Walking speed (m/s)
Adult male	13	1.3
Sick male	25	1.0
Adult female	12	1.1
Sick female	25	0.85
Normal old people	3.25	0.8
Sick ole people	9.75	0.65
Normal children	3	1.0
Sick children	9	0.8

during the COVID-19 pandemic [5], the model for evaluating strategies to improve hospital patient handling capacity during the COVID-19 pandemic [6], and the approach of transferring patients to nursing institutions during the COVID-19 pandemic to shorten hospital stay and maximize the number of patients accepted by hospitals [8]. This paper

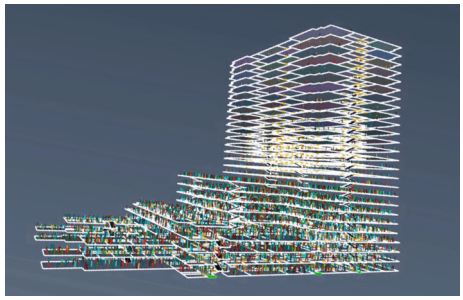

Figure 8: The three-dimensional structure diagram of a general hospital with simulators.

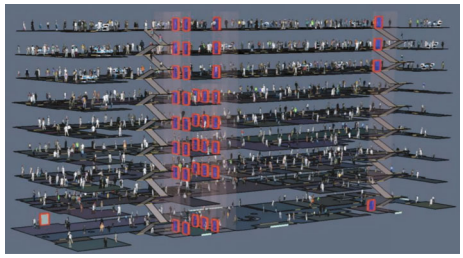

Figure 9: The simulation model with simulators.

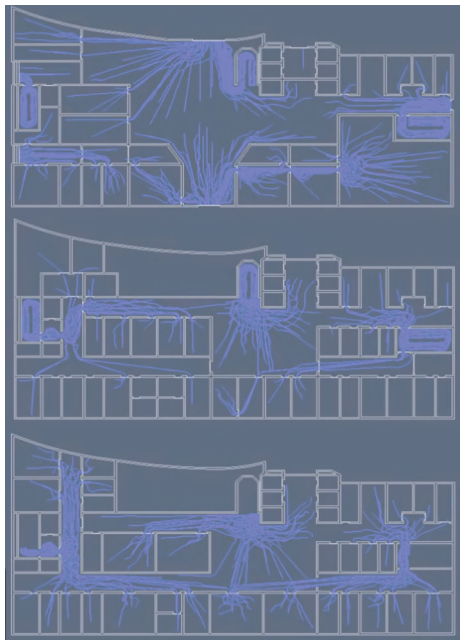

Figure 10: The path diagram of personnel movement.

focuses on the walking path of patients in the hospital, by applying the concept of maximum flow in the field of computer science and algorithm and reducing the number of shared links and alternating links, to achieve the goal of maximization the hospital throughput. The results of comparative experiments indicate that compared with the paths generated by the brute force method, the paths designed by the algorithm proposed in this paper can improve the throughput of hospitals by nearly 1.5 times. The study extends the current literature. Researchers can expand this study by including other public health institutions and exploring other factors affecting the maximum throughput.

The maximum flow problem is a combinatorial optimization problem, which discusses how to make full use of the capacity of the equipment to maximize the flow and achieve the best effect [43]. The labelling algorithm for maximum flow was first proposed by Ford and Fulkerson in 1956. The "network flow theory" established by Ford and Fulkerson in the 1950s is an important component of network applications [44]. Network flow is a kind of specific flow solving method, which is closely related to linear programming. The theory and application of network flow are developing continuously, and new topics such as flow with gain, multiterminal flow, multicommodity flow, and the decomposition and synthesis of network flow appear [45]. Network flow has been widely used in communication, transportation, power, engineering planning, task assignment, equipment updating, and computer-aided design. In this paper, the application of the maximum flow problem is extended to medical fields such as public health facilities to meet social distancing requirements under the COVID-19 pandemic.

The COVID-19 pandemic and the emergence of COVID-19 variants such as Omicron have put a strain on already stretched public health resources, with existing facilities overwhelmed by the soaring number of people needing to visit hospitals. Based on the concept of the maximum flow algorithm, walking path algorithms satisfying social distance are designed in this paper. On the basis of the existing public health resources, the hospital can maximize the throughput of people by minimizing unnecessary waiting time and preventing dangerous situations happen such as crossinfection. At the same time, the results of this paper can also be applied to other places to prevent crossinfection of infectious diseases, such as mobile cabin hospitals. Efforts should be made to reduce the waste of public medical resources which are already scarce.

Our study focuses on developing pseudocode-based algorithms for maximizing the throughput in hospitals. Since different public health institutions implement different programming languages for their Hospital Information Systems (HIS), the original intention of designing algorithms utilizing pseudocode is to hope that public health institutions such as hospitals and clinics can implement the algorithm by themselves by applying the programming language they utilize. However, this may prove difficult. Meanwhile, when applying the algorithms to some relatively complex floor plan scenes, the results generated in each step of the algorithms may need to be slightly improved according to the actual situation. These improvements require algorithms, graph theory, and other related knowledge for relevant medical staff, which might cause inconvenience. The above-mentioned points lead to the limitations of the research. Thus, future studies should design programs and systems which can be run on portable devices [46], in order to achieve the automatic generation of walking paths that can help hospitals and other public health facilities obtain maximum flow. What is more, it is the goal of future

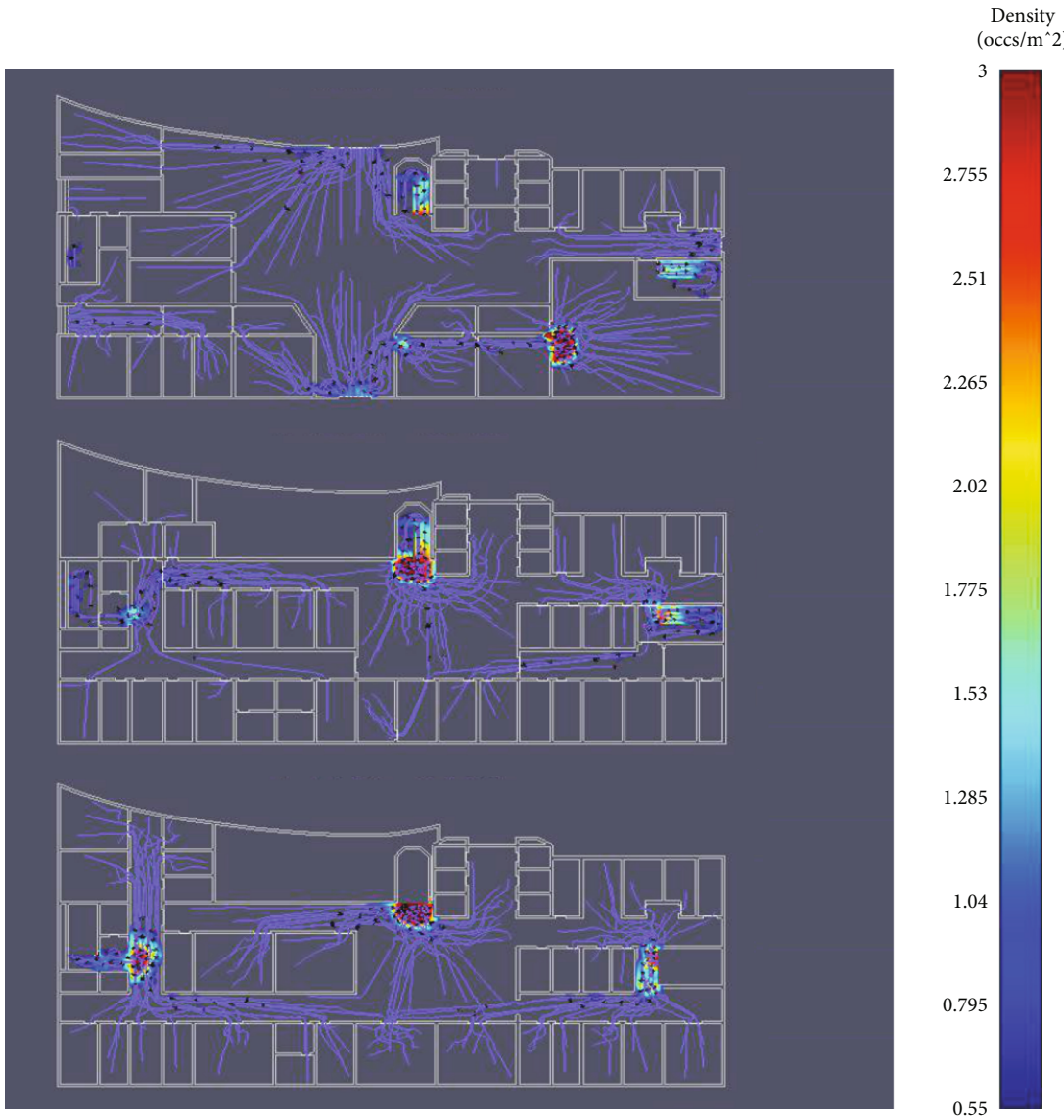

Figure 11: The path diagram of personnel movement.

research and works to improve the matching degree and accuracy of the results of the designed algorithm with the real public health institutions environment, so as to reduce the subsequent modification operations for medical staff. Meanwhile, future work will focus on reducing the number of iterations in the algorithm, such as loops and recursion, to improve the efficiency of the algorithm as much as possible and reduce the time and space complexity of the algorithm.

4. Conclusions

Due to the COVID-19 pandemic, hospitals and other public health facilities are being requested to redesign the way people walk in corridors to meet social distancing requirements. In this paper, algorithms based on the maximum flow problem are proposed in order to present movement flows and satisfy social distancing requirements. The core idea of the algorithm is to minimize the number of shared links and alternating links. The experimental results indicate that compared with the traditional methods, the designed algorithms can improve the throughput of public health institutions and achieve the aim of maximizing the usage of public medical resources.

Data Availability

The data underlying the results presented in the study are available within the manuscript.

Conflicts of Interest

The authors declare that they have no conflicts of interest.

References

[1] M. Misra, H. Joshi, and R. Sarwal, "Exit strategies from lockdowns due to COVID-19: a scoping review," *BMC Public Health*, vol. 22, pp. 1–16, 2022.

[2] J. Wong, Q. Y. Goh, Z. Tan et al., "Preparing for a COVID-19 pandemic: a review of operating room outbreak response measures in a large tertiary hospital in Singapore," *Canadian Journal of Anesthesia/Journal Canadien D'anesthésie*, vol. 67, no. 6, pp. 732–745, 2020.

[3] Y. Akkuş, Y. Karacan, R. Güney, and B. Kurt, "Experiences of nurses working with COVID-19 patients: a qualitative study," *Journal of Clinical Nursing*, vol. 31, no. 9-10, pp. 1243–1257, 2022.

[4] F. Grabowski, M. Kochańczyk, and T. Lipniacki, "The spread of SARS-CoV-2 variant Omicron with a doubling time of 2.0–3.3 days can be explained by immune evasion," *Viruses*, vol. 14, no. 2, p. 294, 2022.

[5] K. Bowden, E. L. Burnham, A. Keniston et al., "Harnessing the power of hospitalists in operational disaster planning: COVID-19," *Journal of General Internal Medicine*, vol. 35, no. 9, pp. 2732–2737, 2020.

[6] M. Sarier, M. Demir, M. Emek et al., "Comparison of spermiograms of infertile men before and during the COVID-19 pandemic," *Revista da Associação Médica Brasileira*, vol. 68, no. 2, pp. 191–195, 2022.

[7] B. Shahverdi, E. Miller-Hooks, M. Tariverdi, H. Ghayoomi, D. Prentiss, and T. D. Kirsch, "Models for assessing strategies for improving hospital capacity for handling patients during a pandemic," *Disaster Medicine and Public Health Preparedness*, pp. 1–10, 2022.

[8] S. L. Chang, N. Harding, and C. Zachreson, "Modelling transmission and control of the COVID-19 pandemic in Australia," *Nature Communications*, vol. 11, pp. 1–13, 2020.

[9] T. Olanipekun, "The impact of COVID-19 testing on length of hospital stay and patient flow in hospitals," *Journal of Community Hospital Internal Medicine Perspectives*, vol. 11, no. 2, pp. 180–183, 2021.

[10] R. Gao, M. Zhao, and T. Ye, "Jigsaw: indoor floor plan reconstruction via mobile crowdsensing," in *In Proceedings of the 20th annual international conference on Mobile computing and networking*, pp. 249–260, Maui, Hawaii, USA, 2014.

[11] F. Radicchi, C. Castellano, F. Cecconi, V. Loreto, and D. Parisi, "Defining and identifying communities in networks," *In Proceedings of the National Academy of Sciences*, vol. 101, no. 9, pp. 2658–2663, 2004.

[12] Z. Lu, T. Wang, J. Guo et al., "Data-driven floor plan understanding in rural residential buildings via deep recognition," *Information Sciences*, vol. 567, pp. 58–74, 2021.

[13] E. Yong, "Why health-care workers are quitting in droves," *The Atlantic*, 2021.

[14] K. Prem, Y. Liu, T. W. Russell et al., "The effect of control strategies to reduce social mixing on outcomes of the COVID-19 epidemic in Wuhan, China: a modelling study," *The Lancet Public Health*, vol. 5, no. 5, pp. e261–e270, 2020.

[15] S. Tremblay-Huet, T. McMorrow, E. Wiebe, M. Kelly, M. Hennawy, and B. Sum, "The impact of the COVID-19 pandemic on medical assistance in dying in Canada and the relationship of public health laws to private understandings of the legal order," *Journal of Law and the Biosciences*, vol. 7, no. 1, p. lsaa 087, 2020.

[16] S. Grundel, S. Heyder, T. Hotz, T. K. S. Ritschel, P. Sauerteig, and K. Worthmann, "How much testing and social distancing is required to control COVID-19? Some insight based on an age-differentiated compartmental model," *SIAM Journal on Control and Optimization*, vol. 60, no. 2, pp. S145–S169, 2022.

[17] M. Cheng and L. Yin, "Transmission scheduling in sensor networks via directed edge coloring," in *In Proceeding of the 2007 IEEE International Conference on Communications*, pp. 3710–3715, Glasgow, UK, June 2007.

[18] R. Rizvi, E. P. Nguyen, M. D. Kowal et al., "High-throughput continuous production of shear-exfoliated 2D layered materials using compressible flows," *Advanced Materials*, vol. 30, no. 30, p. 1800200, 2018.

[19] H. Zhang and X. Lu, "Vehicle communication network in intelligent transportation system based on internet of things," *Computer Communications*, vol. 160, pp. 799–806, 2020.

[20] M. Ameli, J. P. Lebacque, and L. Leclercq, "Simulation-based dynamic traffic assignment: meta-heuristic solution methods with parallel computing," *Computer-Aided Civil and Infrastructure Engineering*, vol. 35, no. 10, pp. 1047–1062, 2020.

[21] R. K. Ghosh and G. P. Bhattacharjee, "Parallel breadth-first search algorithms for trees and graphs," *International Journal of Computer Mathematics*, vol. 15, no. 1-4, pp. 255–268, 1984.

[22] A. Bundy, *Catalogue of Artificial Intelligence Tools. Catalogue of Artificial Intelligence Tools*, Springer, Berlin, Heidelberg, 1986.

[23] I. Baidari and A. Hanagawadimath, "Traversing directed cyclic and acyclic graphs using modified BFS algorithm," in *In 2014 Science and Information Conference*, pp. 175–181, London, UK, 2014, August.

[24] B. Awerbuch and R. G. Gallager, "Distributed BFS algorithms in proceeding of the 26th annual symposium on foundations of computer science sfcs," in *26th Annual Symposium on Foundations of Computer Science (sfcs 1985)*, pp. 250–256, Portland, OR, USA, October 1985.

[25] V. Verbavatz and M. Barthelemy, "From one-way streets to percolation on random mixed graphs," *Physical Review E*, vol. 103, no. 4, article 042313, 2021.

[26] R. Lewis, "Algorithms for finding shortest paths in networks with vertex transfer penalties," *Algorithms*, vol. 13, no. 11, p. 269, 2020.

[27] S. Illgen and M. Höck, "Literature review of the vehicle relocation problem in one-way car sharing networks," *Transportation Research Part B: Methodological*, vol. 120, pp. 193–204, 2019.

[28] A. Volkova, M. Niedermeier, and R. Basmadjian, "Security challenges in control network protocols: a survey," *IEEE Communications Surveys & Tutorials*, vol. 21, pp. 619–639, 2018.

[29] X. Wan and H. Wang, "Efficient semi-external depth-first search," *Information Sciences*, vol. 599, pp. 170–191, 2022.

[30] S. Špacapan, "The diameter of strong orientations of Cartesian products of graphs," *Discrete Applied Mathematics*, vol. 247, pp. 116–121, 2018.

[31] S. I. Khalaf, V. Mathad, and S. S. Mahde, "Edge hub number in graphs," *Online Journal of Analytic Combinatorics*, vol. 14, pp. 1–8, 2019.

[32] G. Yan, Q. Li, D. Guo, and X. Meng, "Discovering suspicious APT behaviors by analyzing DNS activities," *Sensors*, vol. 20, no. 3, p. 731, 2020.

[33] R. Pereira, J. Oliveira, and M. Sousa, "Bioinformatics and computational tools for next-generation sequencing analysis in

clinical genetics," *Journal of Clinical Medicine*, vol. 9, no. 1, p. 132, 2020.

[34] G. B. Mertzios and D. G. Corneil, "A simple polynomial algorithm for the longest path problem on cocomparability graphs," *SIAM Journal on Discrete Mathematics*, vol. 26, no. 3, pp. 940–963, 2012.

[35] M. T. Omran, J. R. Sack, and H. Zarrabi-Zadeh, "Finding paths with minimum shared edges," *Journal of Combinatorial Optimization*, vol. 26, no. 4, pp. 709–722, 2013.

[36] V. Ojha and G. Nicosia, "Backpropagation neural tree," *Neural Networks*, vol. 149, pp. 66–83, 2022.

[37] L. Roditty and U. Zwick, "A fully dynamic reachability algorithm for directed graphs with an almost linear update time," *SIAM Journal on Computing*, vol. 45, no. 3, pp. 712–733, 2016.

[38] I. Lochhead and N. Hedley, "Mixed reality emergency management: bringing virtual evacuation simulations into real-world built environments," *International Journal of Digital Earth*, vol. 12, no. 2, pp. 190–208, 2019.

[39] Y. H. Kim, J. S. Choi, T. F. Yuan, and Y. S. Yoon, "Building-information-modeling based approach to simulate strategic location of shelter in place and its strengthening method," *Materials*, vol. 14, no. 13, p. 3456, 2021.

[40] A. D'Orazio, L. Grossi, and D. Ursetta, "Egress from a hospital ward during fire emergency," *International Journal of Safety and Security Engineering*, vol. 10, pp. 1–10, 2020.

[41] M. Li, S. Zhu, J. Wang, and Z. Zhou, "Research on fire safety evacuation in a university library in Nanjing," *Procedia Engineering*, vol. 211, pp. 372–378, 2018.

[42] V. Alonso-Gutierrez and E. Ronchi, "The simulation of assisted evacuation in hospitals," in *Proceeding of Fire and Evacuation Modelling Technical Conference*, Malaga, Spain, 2016Malaga, Spain.

[43] J. Wu, A. Abbas-Turki, and A. El Moudni, "Cooperative driving: an ant colony system for autonomous intersection management," *Applied Intelligence*, vol. 37, no. 2, pp. 207–222, 2012.

[44] D. R. Fulkerson, "Flow networks and combinatorial operations research," *The American Mathematical Monthly*, vol. 73, no. 2, pp. 115–138, 1966.

[45] M. Klimm, M. E. Pfetsch, R. Raber, and M. Skutella, "On the robustness of potential-based flow networks," *Mathematical Programming*, pp. 1–38, 2022.

[46] H. Zou, K. Cao, and C. Jiang, "Spatio-temporal visual analysis for urban traffic characters based on video surveillance camera data," *ISPRS International Journal of Geo-Information*, vol. 10, no. 3, p. 177, 2021.

Hindawi
Computational and Mathematical Methods in Medicine
Volume 2022, Article ID 2382458, 9 pages
https://doi.org/10.1155/2022/2382458

Research Article

Nursing Countermeasures of Continuous Renal Replacement Treatment in End-Stage Renal Disease with Refractory Hypotension in the Context of Smart Health

Liya Ma, Jianli Guo, Hongwei Sun, Nan Li, MeiXuan Lv, and Bing Shang

Endoscopy Center, The First Affiliated Hospital of Qiqihar Medical University, Qiqihar, 161006 Heilongjiang, China

Correspondence should be addressed to Jianli Guo; smaller@qmu.edu.cn

Received 21 June 2022; Revised 14 July 2022; Accepted 22 July 2022; Published 10 August 2022

Academic Editor: Plácido R. Pinheiro

This work is aimed at exploring the nursing strategies and effects of continuous renal replacement therapy (CRRT) for end-stage renal disease (ESRD) with refractory hypotension under the background of smart health. 40 ESRD patients with refractory hypotension who received CRRT treatment were enrolled as the research objects and were randomly rolled into the intervention group and the control group, with 20 cases in each group. Patients in the control group received routine nursing, and those in the intervention group received individualized nursing. The incidence of hypotension, dry body weight, serous cavity effusion, renal function indicators (blood urea nitrogen (BUN) and creatinine (Cre)), and patient satisfaction were compared between the two groups. The results showed that the probability of hypotension in the intervention group was 9.38%, which was lower than that in the control group (34.38%). The probability of early termination of dialysis in the intervention group was 0%, which was lower than that in the control group (18.75%), and the difference was statistically significant ($P < 0.05$). The decreases of BUN and Cre in the intervention group were significantly greater than those in the control group, and the differences were statistically significant ($P < 0.05$). The proportion of water growth less than 10% during dialysis in the intervention group was 98.44%, which was greater than that in the control group (93.45%), and the difference was statistically significant ($P < 0.05$). The ultrafiltration volume after dialysis in the intervention group was 2850 ± 400 mL, which was greater than that in the control group 2350 ± 350 mL. After intervention, the proportion of patients with pleural effusion in the intervention group was 10% less than that in the control group (20%), and the difference was statistically significant ($P < 0.05$). The satisfaction rate of the intervention group was 97.66%, which was higher than that of the control group (65.63%). In conclusion, individualized nursing was more helpful to the recovery of ESRD patients with refractory hypotension treated with CRRT than routine nursing.

1. Introduction

End-stage renal disease (ESRD) refers to a disease in which chronic kidney disease develops to the end stage, with changes in renal structure and substantial loss of renal function, also known as uremia [1]. Chronic kidney disease is divided into 5 stages. When the glomerular filtration rate of patients in stage 5 is maintained at a level of less than 15 mL/(min.1.73 m^2), it can be diagnosed as ESRD. According to relevant statistics, the probability of chronic kidney disease in China can reach 10.8%, that is, the number of chronic kidney disease patients is about 130 million, of which about 3 million will develop ESRD [2]. ESRD is extremely detrimental to the patient's body and mind. The current treatment for ESRD patients is mainly renal replacement therapy, namely, hemodialysis, also known as blood purification [3]. Hemodialysis is a treatment method in which the patient's blood is drained to the outside of the body, the toxins in the blood are removed through a filtering device, and then, the blood is returned to the patient's body. In this process, the blood has to undergo extracorporeal circulation. Therefore, it is very important to disinfect and sterilize the relevant instruments and ensure the sterility of the operating environment to prevent blood infection. At

the same time, the extracorporeal circulation of blood is established on the basis of our artificial construction of access, so the establishment of vascular access before hemodialysis is the first important preparation work. During the dialysis, medical staff should also pay attention to ensuring the smoothness of the access, to prevent the pipeline from being damaged due to human factors, or to block the access by coagulation, which will affect the dialysis effect [4]. Hemodialysis, as a widely used clinical treatment method with outstanding therapeutic effect, prolongs the life of countless kidney disease patients. However, long-term hemodialysis will also be accompanied by certain side effects. Common side effects experienced by patients includes the following aspects. Firstly, the patients may suffer from dialysis imbalance syndrome. This is because there is a significant gradient difference between the plasma osmotic pressure and the osmotic pressure of the brain, resulting in intracranial edema and high pressure causing nausea, vomiting, dizziness, and headache. Secondly, hemodialysis patients will have allergies in the early stage. Some patients are allergic to dialyzers or dialysate and may experience rashes and fever. In severe cases, chest tightness, difficulty breathing, and palpitation may occur. Thirdly, early side effects may cause muscle cramps. Fourthly, patients may have conditions that can lead to hypotension or high blood pressure. Fifthly, there will also be infections, which are rare now, and sometimes contagious hepatitis C and hepatitis B. Sixthly, patients on long-term dialysis will have carpal tunnel syndrome, or chronic osteoarthropathy, and other manifestations of dialysis-related amyloidosis. Seventhly, hemodialysis patients may also experience anemia or malnutrition. Finally, cardiac problems may occur, such as heart failure, arrhythmia, or complications such as vascular calcification [5, 6]. Among them, the probability of hypotension caused by dialysis is about 20%-40% according to statistics. However, due to the difference of each person's constitution and the ability to adapt to hemodialysis, the probability of hypotension in some patients can reach 50%-70% [7]. In the existing research, targeted treatment measures for patients with hypotension during dialysis are as follows. Firstly, it should identify the etiology. The causes of hypotension in dialysis patients include hypovolemia, decreased peripheral blood flow resistance, heart problems, malnutrition, and dialysis-related infections. Secondly, it should cooperate with the doctor to look for the specific reasons actively and carefully, and sometimes, the reasons may interact at the same time. Thirdly, it should have a reasonable diet, ensure calories and energy, and maintain a good nutritional state. Long-term salt prohibition is not advisable. Fourthly, it should evaluate the dry body weight well and avoid excessive dialysis dehydration. Fifthly, it should protect the heart function, and pericardial effusion needs to be dealt with in time. Sixthly, drugs that raise blood pressure are effective for some patients. Seventhly, refractory hypotension, such as amyloidosis and severe failure, are difficult to respond to various treatments, so that hemodialysis cannot be performed, and peritoneal dialysis can be changed [8]. Continuous renal replacement therapy (CRRT) is mainly a blood purification treatment method. It is performed continuously for several hours or nearly 24 hours a day to relieve the pressure of kidney metabolism and purification and reduce the burden on organs [9]. The working principle of this technology is to imitate the filtration function of the glomerulus, using a semipermeable membrane filter to help remove water and solutes from the blood, and to separate the substances needed by the body from the waste substances that are metabolized. Next, it can import the substances needed by the body into the body to maintain the balance of electrolytes in the body and the normal operation of the body [10]. While performing blood filtration, it can also help eliminate inflammatory mediators in the blood, improve the patient's physical condition, reduce the chance of infection and concurrent inflammation, and improve the function of the autoimmune system. At the same time, regular blood purification can maintain the overall physical state of the patient. It is mainly suitable for severe kidney, liver, heart, and other organ diseases, such as acute renal failure, uremia, hepatic encephalopathy, acute pancreatitis, and congestive heart failure. It can reduce the burden on the organs and maintain the function of the organs. It can also be used to treat autoimmune system diseases, such as sepsis and systemic inflammatory response syndrome, to help inflammatory factors to be excreted from the body, so as to reduce the damage to organs caused by the disease [11, 12].

Until now, the nursing model of some hospitals has tended to be standardized, so that patients follow the same standard for postoperative recovery plans. Although such a nursing model can have a clear standard specification, it is difficult to guarantee the surgical effect of patients [13]. But in fact, each patient is an independent individual, and their psychological situation, living environment, eating habits, etc. are different. If these individual differences are not taken into account, and only a set of standards is used to require them, it will be difficult for some patients to meet the standard requirements, and the effect of surgery will naturally be greatly reduced. Standardized care requirements can ensure patient safety, while individualized care can lead to better surgical outcomes [14]. Individualized care is not just about designing recipes based on taste preferences, but about gaining a deep understanding of the patient's heart and living environment [15]. For example, psychological counselling is carried out according to the patient's situation, and a psychological intervention plan is formulated according to his reaction. Understand the patient's usual living habits, in addition to behaviors that have a negative impact on the effect of surgery, should try to adapt to these habits when formulating a recovery plan, so as to reduce the patient's resistance to the recovery plan. At the same time, the recovery status and quality of life of patients are regularly and objectively assessed, and the plan is adjusted in time [16]. Therefore, the routine nursing and nursing strategies (i.e., individualized nursing) were adopted for ESRD patients with refractory hypotension using CRRT in this work. By comparing and observing the hypotension occurrence, dry body weight, serous effusion, blood index, nursing satisfaction, and other performances of patients under the two nursing strategies, the effect of nursing strategies can be judged.

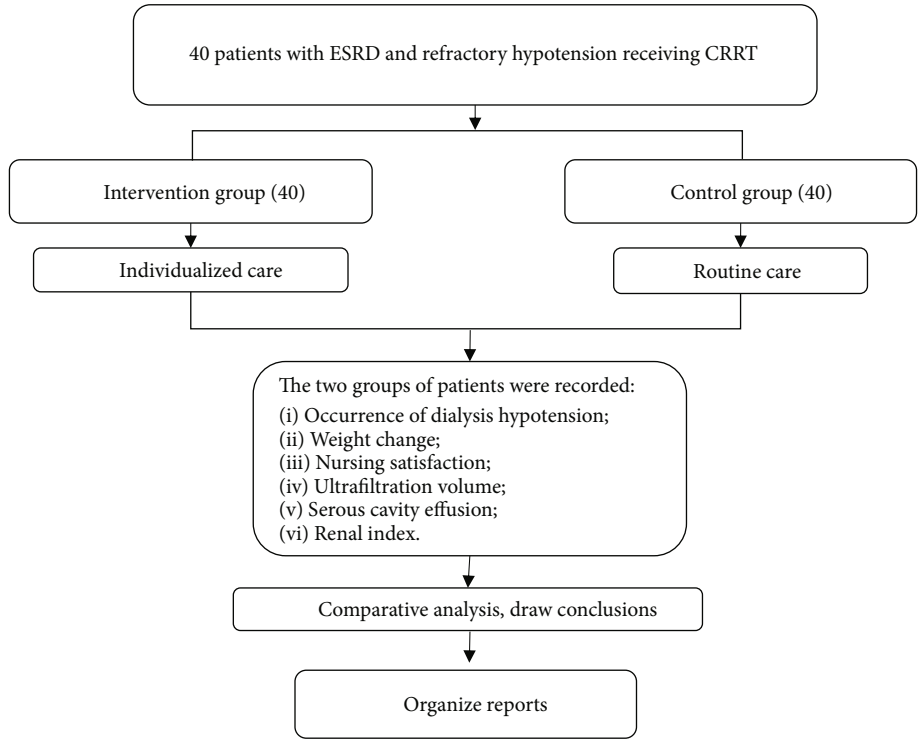

Figure 1: Technical route.

2. Materials and Methods

2.1. Experimental Subjects. 40 ESRD patients with refractory hypotension who received CRRT in The First Affiliated Hospital of Qiqihar Medical College from 2019 to 2021 were enrolled as the research subjects, including 21 males and 19 females. The age ranged 22-75 years old, with the mean age of 57.13 ± 9.75 years old. The 40 subjects were randomly rolled into the intervention group and the control group, with 20 cases in each group. There were 12 males and 8 females in the control group, while there were 11 males and 9 females in the intervention group. The experiment had been approved by the Medical Ethics Committee of The First Affiliated Hospital of Qiqihar Medical College, and the patients and their families understood the research content and methods and signed the corresponding informed consent.

Inclusion criteria were set as follows: (I) patients who were diagnosed according to ESRD diagnostic criteria, (II) patients whose systolic blood pressure (SBP) before dialysis was less than 100 mmHg or MAP decreased by more than 20 mmHg during dialysis, and (III) patients with complete clinical data.

Exclusion criteria were defined as follows: those with cardiac dysfunction, those unable to complete the experimental process, and those with incomplete clinical data.

2.2. Experimental Methods. The patients in the intervention group received individualized nursing on the basis of CRRT. Individualized nursing measures were tailored according to the complications that were prone to occur in patients with ESRD with refractory hypotension during treatment. The subjects in the control group received routine nursing on the basis of CRRT. The occurrence of hypotension, weight change, and nursing satisfaction in each dialysis group were recorded during the three months of nursing intervention (a total of 640 times of dialysis in the intervention group and in the control group). In addition, the performance of ultrafiltration volume, serous effusion, and renal indicators before and after three months of intervention were also recorded. Through comparative analysis, the effect of individualized nursing strategies can be determined. The specific experimental process was shown in Figure 1.

2.3. Flowchart of CRRT. CRRT, also known as bedside hemofiltration, is a long-term continuous extracorporeal blood purification therapy for 24 hours or nearly 24 hours a day to replace damaged kidney function, as shown in Figure 2.

2.4. Nursing Measures. Nursing routine procedures included standardized disinfection treatment, operation to ensure sterile state, and regular observation and recording of clinical indicators of patients.

Compared with routine nursing, scientific countermeasures are applied for the individualized nursing according to the specific situation of the patient, not only the nursing of the condition but also the psychological nursing. Table 1 showed the specific content of individualized nursing [17].

2.5. Observation Indicators. The observation indicators included the incidence of hypotension, early dialysis end rate, ultrafiltration volume, weight change, BUN, Cre, serous effusion, and nursing satisfaction.

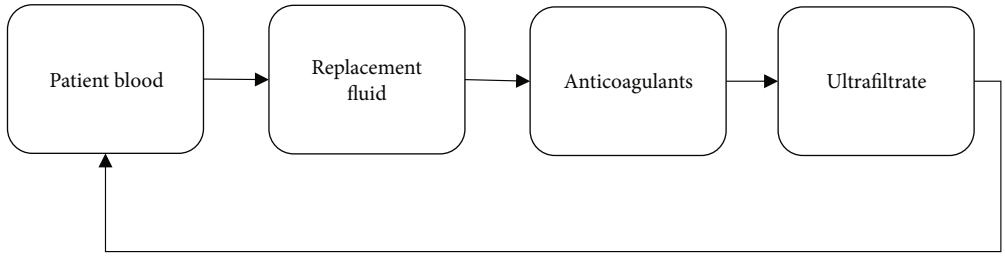

Figure 2: Flowchart of CRRT.

Table 1: Specific contents of individualized nursing.

Measures	Specific contents
Condition nursing	Nursing staff should pay close attention to the changes in the patient's condition. For dialysis patients, it was necessary to regularly observe the changes of vital signs, ask more about the patient's feeling, and detect abnormal changes in the patient's condition in time. It should monitor vital signs once per hour for general patients, and once every 15-30 minutes for critically ill patients to detect the aura symptoms and typical symptoms of hypotension in time, such as yawning, palpitation, nausea, vomiting, and cold sweats. In addition, it should timely inform the dialysis doctor of various changes in the dialysis process and give corresponding treatment.
Dietary guidance	Dialysis patients should strengthen nutrition, improve anemia, and eat high-quality high-protein, low-sodium, and vitamin-rich foods to prevent hypoproteinemia. It should inform the patients and their families to strictly limit the intake of sodium salt and water during dialysis, increase body weight by no more than 3%-5% of body weight, and avoid rapid ultrafiltration, and ultrafiltration of water per hour does not exceed 1% of the body weight. It was not advisable to eat during dialysis. If the condition requires, it should inform the patient that eating during hemodialysis was best within 1-2 hours of the start of dialysis. At this time, the solute and water removed by dialysis only account for 20%-40% of the expected target, which had little effect on peripheral effective circulating blood volume and would not cause blood pressure to drop.
Exercise program	Firstly, postural adaptation exercise should be taken: it should keep the patient in a concave lying position, raise the upper body by 30°, place a soft pillow under the feet, raise it by 15°, and train twice a day, and each training time is 20-30 minutes. Secondly, it should turn over regularly: an alarm clock was placed on the bedside of the hemodialysis treatment, and the alarm clock would ring once every 2 hours. After hearing the alarm, the patient used the healthy limb to grasp the bed rail and perform the ipsilateral turning movement. Nursing staff need to monitor during exercise to ensure that the turning movement does not affect the patency of the pipeline and monitor it effectively. Thirdly, according to the actual situation of the patient, acupuncture was mainly based on aerobic exercise, such as walking and playing Taijiquan. The specific exercise time and amount depended on the patient's tolerance. In addition, it should avoid large movements during exercise.
Psychological nursing	Compared with other treatments, hemodialysis is more likely to cause anxiety, fear, and other adverse emotions in patients, which not only increases the psychological burden but also is not conducive to the treatment of the disease, increasing the probability of hypotension. It can provide targeted psychological care according to the actual situation of the patient, explain the knowledge of the disease to the patient, eliminate the patient's fear of the disease, assist the patient to vent their negative emotions, and maintain a good psychological state. Nursing staff increased the number and time of visits, communicated with patients as much as possible, encouraged, and comforted patients more, and kept patients in the best condition.

Diagnostic criteria for hypotension during dialysis: a decrease in SBP > 20 mmHg or a decrease in MAP > 10 mmHg accompanied by hypotension symptoms such as headache, nausea, and sweating.

Target ultrafiltration volume = the body mass before dialysis − dry body mass + fluid return volume at the end of dialysis,

The ultrafiltration volume after dialysis = the actual ultrafiltration volume displayed by the dialysis machine at the end of dialysis.

In the early end of dialysis, the patient's dialysis time was less than the length of dialysis prescribed by the doctor.

2.6. Statistical Methods. SPSS 20.0 was used for statistical analysis, count data were expressed as frequency and percentage, and χ^2 test was used for comparison between groups. Measurement data were expressed as mean ± variance, and independent samples t test was used for comparison between groups. $P < 0.05$ meant difference was statistically significant.

3. Results

3.1. Basic Data. There was no significant difference between the two groups in age, gender, course of disease, and the number of weekly dialysis ($P > 0.05$). The patients in two groups were comparable, as shown in Table 2.

3.2. Comparison on Incidence of Hypotension. The incidence of hypotension and the early termination rate of dialysis

Table 2: Comparison on basic data of patients.

Item	Intervention group	Control group	t/χ^2	P
Age	57.13 ± 3.78	56.98 ± 2.67	0.056	0.735
Gender				
Males	11	12	0.018	0.987
Females	9	8		
Course of disease	9.31 ± 2.96	9.28 ± 4.13	0.127	0.396
Number of weekly dialysis	2.79 ± 0.56	2.81 ± 0.13	0.421	0.213

Table 3: Comparison on incidence of hypotension and early termination of dialysis.

Group	Times pf hypotension	Incidence of hypotension	Times of early termination of dialysis	Incidence of early termination of dialysis
Intervention group	60	9.38%	0	0
Control group	220	34.38%	120	18.75%
χ^2	59.673		27.164	
P	0.000		0.000	

Table 4: Comparison of renal function in intervention group before and after intervention.

Indicators	Intervention group		t	P
	Before intervention	After intervention		
BUN (mmol/L)	28.46 ± 7.31	15.14 ± 7.56	4.128	0.048
Cre (umoL/L)	360.67 ± 141.84	149.12 ± 140.32	4.063	0.030

between the two groups were obviously different ($P < 0.05$). In the 640 times of dialysis, the probability of hypotension was 9.38% in the intervention group and 34.38% in the control group. The probability of hypotension in the intervention group was lower ($P < 0.05$). The probability of early termination of dialysis due to hypotension was 0% in the intervention group, which was much lower than 18.75% in the control group ($P < 0.05$). The specific results were shown in Table 3.

3.3. Comparison of Renal Function Indicators. The BUN and Cre levels of the two groups of patients before and after the intervention were observed, and the results were given in Tables 4 and 5. The BUN and Cre levels of the two groups of patients were decreased to a certain extent compared with those before the intervention ($P < 0.05$). The two indicators in the intervention group decreased significantly more than that in the control group.

3.4. Comparison of Body Weight Changes. The weight changes of the two groups before and after the intervention were compared, and the results were given in Table 6. Before intervention, the proportion of water growth less than 10% in the intervention group during dialysis was 93.75%, and the proportion in the control group was 91.72%, showing statistical difference ($P > 0.05$). After the intervention, the proportion of water growth less than 10% in the intervention group during dialysis was 98.44%, and the proportion in the control group was 93.45%, showing statistically great difference ($P < 0.05$). The number of patients with water growth less than 10% during dialysis before and after the intervention, the number of patients in the intervention group was significantly more than that in the control group.

3.5. Comparison of Target Dialysis Ultrafiltration Volume before Dialysis and Ultrafiltration Volume after Dialysis. The target dialysis ultrafiltration volume before dialysis was compared between the two groups, and the difference was not statistically significant ($P > 0.05$). The ultrafiltration volume after dialysis was 2850 ± 400 mL in the intervention group and 2350 ± 350 mL in the control group. The intervention group was larger than the control group ($P < 0.05$). The details were shown in Table 7.

3.6. Comparison on Serous Effusion. The proportion of patients with pleural effusion in the intervention group was 35% before the intervention and 10% after the intervention, and the difference was statistically obvious ($P < 0.05$). The proportion of patients with pleural effusion in the control group was 30% before the intervention and 20% after the intervention, with statistically observable difference ($P < 0.05$). The reduction in pleural effusion patients in the intervention group was significantly greater than in the control group. The details were shown in Table 8.

Table 5: Comparison of renal function before and after intervention in the control group.

Indicator	Control group		t	P
	Before intervention	After intervention		
BUN (mmol/L)	27.72 ± 7.65	18.32 ± 6.23	4.241	0.007
Cre (umoL/L)	361.68 ± 132.86	169.52 ± 110.67	5.013	0.041

Table 6: Comparison of results of weight gain as a percentage of body weight.

Time	Intervention group		Control group		χ^2	P
	<10%	>10%	<10%	>10%		
Before intervention	600 (93.75%)	40 (6.25%)	587 (91.72%)	53 (8.28%)	2.376	0.312
After intervention	630 (98.44%)	10 (1.56%)	598 (93.45%)	42 (6.56%)	27.869	0.000

Table 7: Comparison on targeted ultrafiltration volume before dialysis and ultrafiltration volume after dialysis.

Ultrafiltration volume	Intervention group	Control group	t	P
Targeted ultrafiltration volume before dialysis	3100 ± 500	3000 ± 400	1.545	0.128
Ultrafiltration volume after dialysis	2850 ± 400	2350 ± 350	18.517	0.000

Table 8: Comparison on serous effusion before and after the intervention.

Pleural effusion	Intervention group (20 cases)	Control group (20 cases)
Before intervention	7 (35%)	6 (30%)
After intervention	2 (10%)	4 (20%)
χ^2	10.564	9.708
P	0.006	0.007

3.7. Comparison of Nursing Satisfaction. The satisfaction questionnaires of the two groups of patients after each dialysis were collected. After integration, it was found that the number of satisfactions in the intervention group was 625, and the satisfaction rate was 97.66%; while the number of satisfactions in the control group was 420, and the satisfaction rate was 65.63%. The satisfaction of the intervention group was obviously higher with statistical difference ($P < 0.05$). The details were shown in Table 9.

Table 9: Comparison on nursing satisfaction.

Group	Satisfied	General	Unsatisfied	Satisfaction
Intervention group	568	57	15	97.66%*
Control group	212	208	220	65.63%

Note: compared with the control group, the difference was statistically notable ($P < 0.05$).

4. Discussion

ESRD refers to the end stage of various chronic kidney diseases, which is previously called the late stage of uremia. In recent years, the diagnostic criteria for the disease are also changing due to the continuous changes in disease guidelines. Currently, chronic kidney disease stage 5 is end-stage renal disease [18]. Dialysis is often used clinically to reduce the burden on the kidneys, so as to relieve the patient's condition. Dialysis can be clinically divided into two types: hemodialysis and peritoneal dialysis. Both dialysis modes have advantages and disadvantages, but comprehensive hemodialysis has fewer disadvantages. Prehemodialysis often leads to complications such as dialysis imbalance syndrome. Patients will experience nausea, vomiting, dizziness, headache, and even intolerance to hemodialysis. Other patients may have allergic reactions to the dialyzer or dialysis water, and hypotension in hypertensive patients may occur. For patients with late hemodialysis, dialysis-related amyloidosis may occur [19, 20]. Long-term dialysis patients are prone to gastrointestinal bleeding, cerebral hemorrhage, etc. due to the use of anticoagulants, and some patients may have heart failure due to circulatory instability caused by hemodialysis. For peritoneal dialysis patients, peritoneal dialysis-related peritonitis is prone to occur, and the patient presents with abdominal pain, chills, fever, etc., and severe patients may lead to septic shock [21]. Peritoneal dialysis patients are prone to abdominal distension due to the instillation of peritoneal dialysis fluid in their stomachs, and chest tightness may occur after the diaphragm is on the stage [22]. Hemodialysis in the hypotension state is easy to aggravate the patient's hypotension state after the dialysis starts to draw blood [23]. Symptoms of hypoperfusion of systemic organs may occur, such as cardiac ischemia such as palpitations and chest tightness, cerebral ischemia such as dizziness

and headache, peripheral circulation ischemia symptoms of numbness of the limbs, and severe hypotension shock [24]. In these cases, the doctor may return the blood to the patient in advance. In this way, the dialysis is insufficient, the patient's toxin and water excretion are significantly reduced, and there will be accumulation of toxins and capacity in the body. In addition, the blood drawn from some patients in the hypotension state is also prone to coagulation in the pipeline, which also affects the dialysis adequacy of the patient and the effect of dialysis [25]. Among them, the occurrence of hypotension in dialysis is considered to be caused by the reduction of effective circulating blood volume due to the ultrafiltration rate and ultrafiltration volume being greater than and bearing the range. In addition, studies have found that high dialysate temperature, low sodium dialysate, acetate dialysate, etc. can promote the occurrence of hypotension during dialysis. Elevated parathyroid hormone levels, bioincompatibility and allergic reactions, and decreased vasopressin can also promote inappropriate vasodilation, resulting in hypotension during dialysis [26].

CRRT is to replace the renal function of patients with acute renal failure by circulating blood through a continuous bradycardia hemofilter and to improve the morbidity through the following effects [27]. It can relieve pulmonary edema and edema, secure the infusion space by removing water from the blood (water removal), and improve the symptoms of pulmonary edema and edema. At the same time, by removing water, the space (infusion space) for dripping the drug into the blood can be guaranteed. Maintaining electrolyte balance can maintain blood pH and electrolyte balance quickly and for a long time. In addition, it should remove the metabolic wastes such as urea and Cre and disease-related substances and eliminate the low-molecular-weight metabolic wastes such as urea and Cre accumulated in the blood. In addition, it can also remove medium molecular weight substances in the range of 20,000 to 30,000 molecular weights such as inflammatory mediators. These substances contain disease-related humoral factors, and the clearance of these substances contributes to the improvement of morbidity [28]. Its treatment modes include the following four. First, continuous veno-venous hemofiltration (CVVH): the filtration pump applies negative pressure from the outside of the hollow fiber and uses the principle of filtration to remove the water and metabolic waste in the blood as filtrate. Second, continuous veno-venous hemodialysis (CVVHD): the dialysate flows from the outside of the hollow fiber, and the metabolic waste is removed by the principle of dispersion. Third, continuous veno-venous hemodiafiltration (CVVHDF) requires fluid replacement and dialysate and uses two principles of filtration and dispersion to remove water and metabolic waste. The pipeline combination is more complicated, but the solute removal performance can be adjusted by adjusting the filtration flow rate and the dialysate flow rate, so that the solute removal performance is between the two modes of CVVH and CVVHD. Four, slow continuous ultrafiltration (SCUF), which uses the same filtration principle as the CVVH mode, discharges water and metabolic waste as filtrate, and is suitable for the treatment of pulmonary edema and edema caused by congestive heart failure and accompanied by lack of urine. Clinically, CRRT intervention can be considered for patients with indications for renal replacement therapy and any of the following conditions: severe acute kidney injury, hemodynamic instability, risk of transport, inability to tolerate other renal replacement therapy (such as intermittent hemodialysis or peritoneal dialysis, and continuous removal of water from the body is required [29]. CRRT has no absolute contraindications, relative contraindications include inability to establish vascular access, severe low, or solute renal or nonrenal disease. Metabolic waste is removed with the movement of water, and electrolytes are removed at the same time, so to maintain electrolyte balance, it is necessary to add fluids. In addition, from small molecular weight substances to medium molecular weight substances in the molecular weight range of 20,000 to 30,000, it can be effectively removed [30].

Existing studies suggest that reducing the incidence of hypotension in patients with dialysis hypotension can be achieved by controlling dry body weight, reducing the intake of watery foods in the daily diet, and limiting the intake of salt, soy sauce, and various preserved foods; changing the dialysis mode; actively treating complications; and rationally applying antihypertensive drugs [31]. In the introduction of individualized nursing, it is pointed out that moderate exercise and psychological guidance can also be added. Therefore, this work integrated the above practices in the content design of individualized nursing strategies and applied them to the nursing of the research subjects. It was compared with the routine nursing, and the nursing effects were analyzed. The results showed that the probability of hypotension during dialysis in the intervention group was lower than that in the control group, and the probability of early termination of dialysis due to hypotension was also lower than that in the control group. The reason is that compared with routine care, individualized care is more detailed in monitoring the patient's condition and incorporates relevant measures to prevent hypotension in patients, so the probability of hypotension is significantly reduced. In the intervention group, the cases of early termination due to discomfort caused by hypotension were significantly reduced, which indirectly improved the effectiveness of the treatment. BUN and Cre are important clinical indicators reflecting renal function. The higher the level, the more serious the renal failure. The results of the work showed that the levels of BUN and Cre in the two groups were decreased to a certain extent compared with those before the intervention, and the decrease of blood urea nitrogen and creatinine in the intervention group was significantly greater than that in the control group. It indicates that the renal function recovery of patients is better under individualized care. Dry body weight, also known as target body weight or ideal body weight, refers to the body weight when the patient has neither water or sodium retention nor dehydration, that is, the body weight when the water metabolism is balanced, that is, the desired body weight at the end of dialysis [32]. In this work, the proportion of water growth during dialysis in the intervention group was greater than that in the control group, the patients with good water control in the

intervention group were significantly more than those in the control group, and the amount of ultrafiltration after dialysis in the intervention group was also greater than that in the control group. It means that individualized nursing based on a health science-based diet and strict fluid control can help patients achieve ideal body weight. Long-term dialysis patients are prone to serous effusion due to hypoalbuminemia, infection, and water retention. The satisfaction of the intervention group was significantly higher than that of the control group, indicating that the overall treatment of the patients from the disease itself, daily diet, exercise, and psychology will increase the patients' enthusiasm for treatment and enhance the treatment effect.

5. Conclusion

This work compared the effect of individualized nursing and routine nursing in the treatment of ESRD with refractory hypotension using CRRT. The results showed that individualized nursing can reduce the occurrence of dialysis hypotension, help patients achieve ideal body weight, and reduce the occurrence of serous cavity effusion. In addition, the overall satisfaction of patients was high, which can help improve the clinical treatment effect. However, due to the limited sample size of the work, the next step was to expand the research scope and increase the research volume to ensure the accuracy of the research results.

Data Availability

The datasets used and analyzed during the current study are available from the corresponding author upon reasonable request.

Conflicts of Interest

The authors declare that they have no conflicts of interest.

Acknowledgments

This work was supported by the Qiqihar Science and Technology Plan joint Guidance Project (Contract no. LHYD-2021090).

References

[1] E. I. Mandel, R. E. Bernacki, and S. D. Block, "Serious illness conversations in ESRD," *Clinical Journal of the American Society of Nephrology*, vol. 12, no. 5, pp. 854–863, 2017.

[2] C. Zoccali, U. Moissl, C. Chazot et al., "Chronic fluid overload and mortality in ESRD," *J Am Soc Nephrol.*, vol. 28, no. 8, pp. 2491–2497, 2017.

[3] M. Santos, H. Yin, D. Steffick, R. Saran, and M. Heung, "Predictors of kidney function recovery among incident ESRD patients," *BMC Nephrology*, vol. 22, no. 1, p. 142, 2021.

[4] J. Perl, E. McArthur, V. S. Tan et al., "ESRD among immigrants to Ontario, Canada: a population-based study," *J Am Soc Nephrol.*, vol. 29, no. 7, pp. 1948–1959, 2018.

[5] B. S. Park, M. Seong, J. Ko et al., "Differences of connectivity between ESRD patients with PD and HD," *Brain and Behavior: A Cognitive Neuroscience Perspective*, vol. 10, no. 8, article e01708, 2020.

[6] P. Formanek, E. Salisbury-Afshar, and M. Afshar, "Helping patients with ESRD and earlier stages of CKD to quit smoking," *American Journal of Kidney Diseases*, vol. 72, no. 2, pp. 255–266, 2018.

[7] T. Li, C. S. Wilcox, M. S. Lipkowitz, J. Gordon-Cappitelli, and S. Dragoi, "Rationale and strategies for preserving residual kidney function in dialysis patients," *American Journal of Nephrology*, vol. 50, no. 6, pp. 411–421, 2019.

[8] A. Karkar and C. Ronco, "Prescription of CRRT: a pathway to optimize therapy," *Annals of Intensive Care*, vol. 10, no. 1, p. 32, 2020.

[9] B. R. Griffin, K. D. Liu, and J. P. Teixeira, "Critical care nephrology: core curriculum 2020," *American Journal of Kidney Diseases*, vol. 75, no. 3, pp. 435–452, 2020.

[10] J. Wang, Z. Wu, Q. Wen, and X. Wang, "Effects of CRRT on renal function and toxin clearance in patients with sepsis: a case-control study," *The Journal of International Medical Research*, vol. 49, no. 9, p. 3000605211042981, 2021.

[11] M. Heung and B. A. Mueller, "Prevention of hypophosphatemia during continuous renal replacement therapy—an overlooked problem," *Seminars in Dialysis*, vol. 31, no. 3, pp. 213–218, 2018.

[12] P. Pattharanitima, A. Vaid, S. K. Jaladanki et al., "Comparison of approaches for prediction of renal replacement therapy-free survival in patients with acute kidney injury," *Blood Purification*, vol. 50, no. 4-5, pp. 621–627, 2021.

[13] M. Zuo, J. Tang, M. Xiang, Q. Long, J. Dai, and X. Hu, "Characteristics and factors associated with nosocomial pneumonia among patients undergoing continuous renal replacement therapy (CRRT): a case- control study," *International Journal of Infectious Diseases*, vol. 68, pp. 115–121, 2018.

[14] C. L. Yen, P. C. Fan, G. Kuo et al., "Prognostic performance of existing scoring systems among critically ill patients requiring continuous renal replacement therapy: an observational study," *Journal of Clinical Medicine*, vol. 10, no. 19, p. 4592, 2021.

[15] H. Saunders and D. Sanghavi, *Continuous Renal Replacement Therapy*, Stat Pearls Publishing, Treasure Island (FL), 2022.

[16] M. W. Kang, S. Kim, Y. C. Kim et al., "Machine learning model to predict hypotension after starting continuous renal replacement therapy," *Scientific Reports*, vol. 11, no. 1, p. 17169, 2021.

[17] W. Chen, F. Wang, Y. Zhao, L. Zhang, Z. Chen, and M. Dai, "Efficacy and safety of furosemide for prevention of intradialytic hypotension in haemodialysis patients: protocol for a multicentre randomised controlled trial," *BMJ Open*, vol. 11, no. 7, article e048015, 2021.

[18] C. Vangala, M. Shah, N. N. Dave et al., "The landscape of renal replacement therapy in veterans affairs medical center intensive care units," *Renal Failure*, vol. 43, no. 1, pp. 1146–1154, 2021.

[19] I. Baldwin and N. Fealy, "Nursing for renal replacement therapies in the intensive care unit: historical, educational, and protocol review," *Blood Purification*, vol. 27, no. 2, pp. 174–181, 2009.

[20] W. Y. Chen, L. H. Cai, Z. H. Zhang et al., "The timing of continuous renal replacement therapy initiation in sepsis-associated acute kidney injury in the intensive care unit: the CRTSAKI Study (Continuous RRT Timing in Sepsis-associated AKI in ICU): study protocol for a multicentre,

randomised controlled trial," *BMJ Open*, vol. 11, no. 2, article e040718, 2021.

[21] J. Wu, H. Zhang, Y. Gao, and X. Huang, "Nursing effect of ECMO combined with CRRT in the treatment of fulminant myocarditis: a protocol of randomized controlled trial," *Medicine (Baltimore)*, vol. 100, no. 3, article e24085, 2021.

[22] A. Stavropoulou, M. G. Grammatikopoulou, M. Rovithis, K. Kyriakidi, A. Pylarinou, and A. G. Markaki, "Through the patients' eyes: the experience of end-stage renal disease patients concerning the provided nursing care," *Healthcare (Basel).*, vol. 5, no. 3, p. 36, 2017.

[23] Y. Kim, L. S. Evangelista, L. R. Phillips, C. Pavlish, and J. D. Kopple, "The End-Stage Renal Disease Adherence Questionnaire (ESRD-AQ): testing the psychometric properties in patients receiving in-center hemodialysis," *Nephrology Nursing Journal*, vol. 37, no. 4, pp. 377–393, 2010.

[24] Z. Yang, R. Xu, M. Zhuo, and J. Dong, "Advanced nursing experience is beneficial for lowering the peritonitis rate in patients on peritoneal dialysis," *Peritoneal Dialysis International*, vol. 32, no. 1, pp. 60–66, 2012.

[25] J. Kuipers, J. K. Oosterhuis, W. P. Krijnen et al., "Prevalence of intradialytic hypotension, clinical symptoms and nursing interventions–a three-months, prospective study of 3818 haemodialysis sessions," *BMC Nephrology*, vol. 27, no. 17, p. 21, 2016.

[26] R. K. Al-Za'abi, E. P. Tolmie, A. M. Rice, N. Mohsin, and A. S. Al-Busadi, "Epidemiology of end-stage kidney disease on renal replacement therapy: 35 years analysis study nephrologists," *Saudi Journal of Kidney Diseases and Transplantation*, vol. 32, no. 1, pp. 183–190, 2021.

[27] W. S. Shiferaw, T. Y. Akalu, and Y. A. Aynalem, "Risk factors for anemia in patients with chronic renal failure: a systematic review and meta-analysis," *Ethiopian Journal of Health Sciences*, vol. 30, no. 5, pp. 829–842, 2020.

[28] M. S. ALEissa, I. A. AlGhofaili, H. F. Alotaibe et al., "Incidence and risk factors associated with hypoglycemia among patients with chronic kidney disease: a systematic review," *Journal of Family and Community Medicine*, vol. 27, no. 3, pp. 157–162, 2020.

[29] N. B. Mascarenhas, Á. Pereira, R. S. da Silva, and M. G. da Silva, "Systematization of nursing assistance to patients with diabetes mellitus and chronic renal failure," *Revista Brasileira de Enfermagem*, vol. 64, no. 1, pp. 203–208, 2011.

[30] L. Pham and K. Ziegert, "Ways of promoting health to patients with diabetes and chronic kidney disease from a nursing perspective in Vietnam: a phenomenographic study," *International Journal of Qualitative Studies on Health and Well-Being*, vol. 10, no. 11, p. 30722, 2016.

[31] C. B. Bowling, L. Plantinga, R. K. Hall, A. Mirk, R. Zhang, and N. Kutner, "Association of nondisease-specific problems with mortality, long-term care, and functional impairment among older adults who require skilled nursing care after dialysis initiation," *Clinical Journal of the American Society of Nephrology*, vol. 11, no. 12, pp. 2218–2224, 2016.

[32] P. O'Halloran, H. Noble, K. Norwood et al., "Nurse-led advance care planning with older people who have end-stage kidney disease: feasibility of a deferred entry randomised controlled trial incorporating an economic evaluation and mixed methods process evaluation (ACReDiT)," *BMC Nephrology*, vol. 21, no. 1, p. 478, 2020.

Hindawi
Computational and Mathematical Methods in Medicine
Volume 2023, Article ID 9797525, 1 page
https://doi.org/10.1155/2023/9797525

Retraction

Retracted: Serum TGF-β1 and VEGF Levels Reflect the Liver Hardness and Function in Children with Biliary Atresia

Computational and Mathematical Methods in Medicine

Received 17 October 2023; Accepted 17 October 2023; Published 18 October 2023

This article has been retracted by Hindawi following an investigation undertaken by the publisher [1]. This investigation has uncovered evidence of one or more of the following indicators of systematic manipulation of the publication process:

(1) Discrepancies in scope

(2) Discrepancies in the description of the research reported

(3) Discrepancies between the availability of data and the research described

(4) Inappropriate citations

(5) Incoherent, meaningless and/or irrelevant content included in the article

(6) Peer-review manipulation

The presence of these indicators undermines our confidence in the integrity of the article's content and we cannot, therefore, vouch for its reliability. Please note that this notice is intended solely to alert readers that the content of this article is unreliable. We have not investigated whether authors were aware of or involved in the systematic manipulation of the publication process.

Wiley and Hindawi regrets that the usual quality checks did not identify these issues before publication and have since put additional measures in place to safeguard research integrity.

We wish to credit our own Research Integrity and Research Publishing teams and anonymous and named external researchers and research integrity experts for contributing to this investigation.

The corresponding author, as the representative of all authors, has been given the opportunity to register their agreement or disagreement to this retraction. We have kept a record of any response received.

References

[1] D. Chang, X. Geng, L. Zhou, and G. Hou, "Serum TGF-β1 and VEGF Levels Reflect the Liver Hardness and Function in Children with Biliary Atresia," *Computational and Mathematical Methods in Medicine*, vol. 2022, Article ID 5802548, 5 pages, 2022.

Hindawi
Computational and Mathematical Methods in Medicine
Volume 2022, Article ID 5802548, 5 pages
https://doi.org/10.1155/2022/5802548

Research Article

Serum TGF-β1 and VEGF Levels Reflect the Liver Hardness and Function in Children with Biliary Atresia

Dongzhe Chang, Xianjie Geng, Liang Zhou, and Guangjun Hou

General Surgery Department, Henan Provincial Children's Hospital, Affiliated Hospital of Zhengzhou University, China

Correspondence should be addressed to Guangjun Hou; houguangjun0227@163.com

Received 8 June 2022; Revised 13 June 2022; Accepted 17 June 2022; Published 21 July 2022

Academic Editor: Plácido R. Pinheiro

Objective. This study further explored the wind direction correlation analysis between serum levels of TGF-β1 and VEGF and liver function assessment in children with biliary atresia. *Methods*. A total of 62 children with biliary atresia (BA) who received surgical treatment in our hospital from October 2020 to October 2021 were selected as the research objects (BA group), and 50 normal healthy children who received routine physical examination in our hospital during the same period were selected as blank control group. Outcome measures included postoperative total bilirubin levels and conjugality of enrolled patients. Bilirubin level, unbound bilirubin level, serum transforming growth factor-beta-1 (TGF-β1), vascular endothelial growth factor (VEGF), liver function indicators albumin (ALB), alanine aminotransferase (ALT), aspartate aminotransferase (AST), and other observation indicators were included. All data in this study were collected and analyzed by SPSS 23.0 software, and t-test was performed. *Results*. The serum levels of TGF-β1, VEGF, ALT, AST, GGT, and liver hardness were significantly higher in children with jaundice than those without jaundice, and the serum ALB level was significantly lower than that in children without jaundice ($P < 0.05$). The levels of TGF-β1 and VEGF in BA group were positively correlated with the levels of ALT, AST, GGT, and liver hardness ($P < 0.05$) but negatively correlated with the level of ALB ($P < 0.05$). *Conclusion*. The levels of serum TGF-β1 and VEGF in children with biliary atresia have a certain risk correlation with liver function damage, which will become a research focus on the mechanism of liver fibrosis in the diagnosis and treatment of biliary atresia in children.

1. Introduction

Biliary atresia (BA) is a severe neonatal disease with unknown etiology characterized by progressive inflammation of the bile duct and biliary fibrous obstruction [1]. If BA is not timely intervention, most children will die due to liver failure at the age of 2 years. Surgical intervention is the only effective treatment [2]. BA is one of the common causes of neonatal obstructive jaundice, and its pathogenesis is not fully defined [3–5]. There are significant regional and ethnic differences in BA incidence, with higher rates in Asian countries than in European and American countries [6]. Biliary atresia refers to a series of serious malformations characterized by cholestatic liver injury due to progressive inflammatory or fibrotic atresia of the intrahepatic bile ducts, with persistent jaundice as the main clinical manifestation [7]. The disease progresses rapidly and can cause death within 2 years of age. Kasai surgery in early stage is the preferred treatment for this disease, but due to the lack of specific indications, it is difficult to prompt diagnosis based on clinical manifestations [8]. In order to make up for this deficiency, researchers based on the characteristics of biliary atresia lead to more obvious liver fibrosis. Shear wave elastography was used to measure and compare the liver cirrhosis of biliary atresia and other pathological jaundice, and the results of hardness difference support the identification of biliary atresia [9]. In theory, if the influence of individual baseline biochemical level can be fully considered in the application, it is expected to improve the practical diagnostic value of elastography in different populations [10].

It has been reported that few cytokines and growth factors, including TGF-β1, can increase in VEGF protein levels and induce its secretion in different types of cells [11]. Our

previous study has demonstrated that TGF-β1 can regulate steroidogenesis, cell proliferation, and differentiation in hGL cells [12]. A previous study showed that TGF-β1 increases the secretion of VEGF and stimulates angiogenic activity in rat granulosa cells [13]. However, whether the same effect is true for human granulosa cells remains unknown. In order to avoid bias of disease progression, the interval between blood sample collection and elastography examination was compressed to within 3 days on the premise of ensuring medical arrangement [14]. Biliary atresia (BA) is the most common cause of obstructive jaundice in neonates, with an incidence of approximately 1/10000 [15]. The pathological feature of BA is that the lesion involves the intrahepatic bile duct system, resulting in progressive bile duct destruction [16]. Successful hilar jejunostomy (Kasai) allows bile to be drained and some children to survive [17]. However, due to the occurrence of progressive liver fibrosis, cholestatic cirrhosis, and portal hypertension, most children must choose liver transplantation. Progressive liver fibrosis is a major constraint on Kasai's surgical results which show that in cervical, preventing the progression of liver fibrosis will significantly improve the outcome of Kasai surgery, and the transforming growth factor-β1 (TGF-β1) protein regulates cell growth [18].

In order to explore the expression level and diagnostic value of TGF-1 and VEGF in BA hepatic fibrosis, the general clinical data of 62 children with biliary atresia admitted to our hospital from March 2016 to 83 Months 2019 were collected, and TGF-1 and VEGF were detected and analyzed, to explore the expression level and diagnostic value of TGF-1 and VEGF in biliary atresia liver (BA) fibrosis.

2. Materials and Methods

2.1. General Clinical Features. The inclusion criteria were as follows: (1) BA was diagnosed by clinical and pathological sections, (2) complete clinical data and samples, (3) mild hepatic fibrosis was judged by liver HE staining, (4) the postoperative recovery was good without postoperative complications, and (5) the informed consent of the family members of the children was obtained.

Exclusion criteria were as follows: (1) combined with other hepatobiliary diseases, (2) combined with other congenital diseases, and (3) liver transplantation was received within 2 months after operation. According to the level of total bilirubin, BA group was divided into children with jaundice (total bilirubin $\geq 34.2\,\mu$mol/L) and children without jaundice (total bilirubin $< 34.2\,\mu$mol/L).

Another 50 healthy children who underwent physical examination in our hospital in the same period were taken as the control group. There were 35 males and 27 females in BA group, aged from 5 to 18 months, with an average of 12.47 ± 2.28 months. There were 28 males and 22 females in the control group, aged from 5 to 20 months, with an average of 13.11 ± 2.94 months. There was no significant difference in gender and age between BA group and control group ($P > 0.05$). All patients had the written consent explained to them. All patients have signed written informed consent. This study was approved by the medical ethics committee of the Hospital of Zhengzhou University.

2.2. Detection of Serum Indicators. Children in BA group collected 3 ml of fasting venous blood 2 months after operation, and children in control group collected 3 ml of fasting venous blood during physical examination. After standing for 30 minutes, 3000 revolutions/heart separation for 10 minutes, serum was separated. TGF was detected by ELISA kit. The ELISA kit was purchased from Beyotime Biotechnology Company, and the operation was carried out according to the instructions of the kit.

2.3. Detection of Liver Hardness Value. The children in the BA group were tested for liver hardness at 2 months after operation, and the children in the control group were tested for liver hardness at physical examination. The detection method was instantaneous elastic imaging. The elastic ultrasonic probe was placed in the axillary midline on the right side of the body and recorded continuously. It was successfully tested for 10 times, and the median number was taken as the liver hardness value.

2.4. Statistical Analysis. Load extension packages (RMS, RMDA, pROC, and resources election) use R Software 3.61 to analyze the data. Since the measurement data did not conform to the normal distribution, they were represented by M (P25 and P75), and the difference between groups was compared by Mann-Whitney U test. The counting data were represented by example (ratio), and the differences between groups were compared by Pearson's chi-square test. Due to collinearity among the indicators, according to the data of the training set, the LASSO regression was used to include liver hardness measurements, blood biochemical results, and epidemiological characteristics as independent variables and whether biliary atresia was defined as dependent variables. The 10-fold cross validation method was used to test the fitting results of all the regular penalty terms. The regularization parameter (λ) of the person with minimum deviation (binomial deviance) was calculated, and the simplest model corresponding to one standard error range of the parameter was confirmed, and its construction indexes were screened. Then, the diagnostic model was reconstructed by the odds ratio (OR) of binary logistic regression. The cut-off value was defined by maximum approximation index, and sensitivity, specificity, and corresponding 95% confidence interval (95% CI) were refined. The differentiation degree of the model was evaluated by area under ROC curve (AUC), and the calibration degree was evaluated by Hosmer-Lemeshow test and calibration curve. Statistical graphs were drawn by R Software except ROC curve using GraphPad Prism 8.0. $P < 0.05$ was considered as statistically significant difference.

3. Results

3.1. Comparison of Serum Indexes and Liver Hardness. Compared with the control group, serum TGF in BA group, The levels of VEGF, ALT, AST, and GGT increased significantly ($P < 0.05$), but there was no significant difference in serum ALB level ($P > 0.05$) (Figure 1).

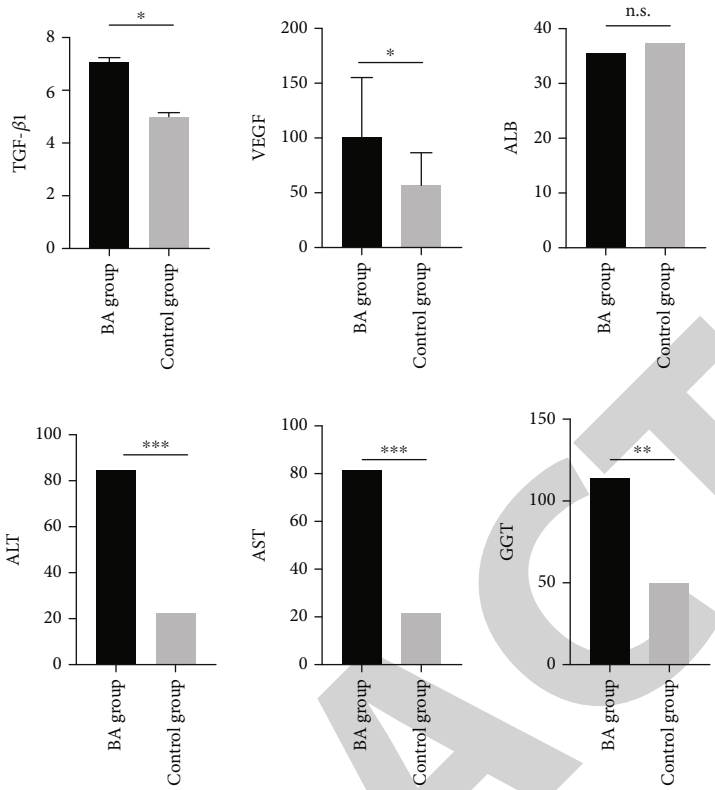

Figure 1: Comparison of serum indexes and liver hardness values between the two groups.

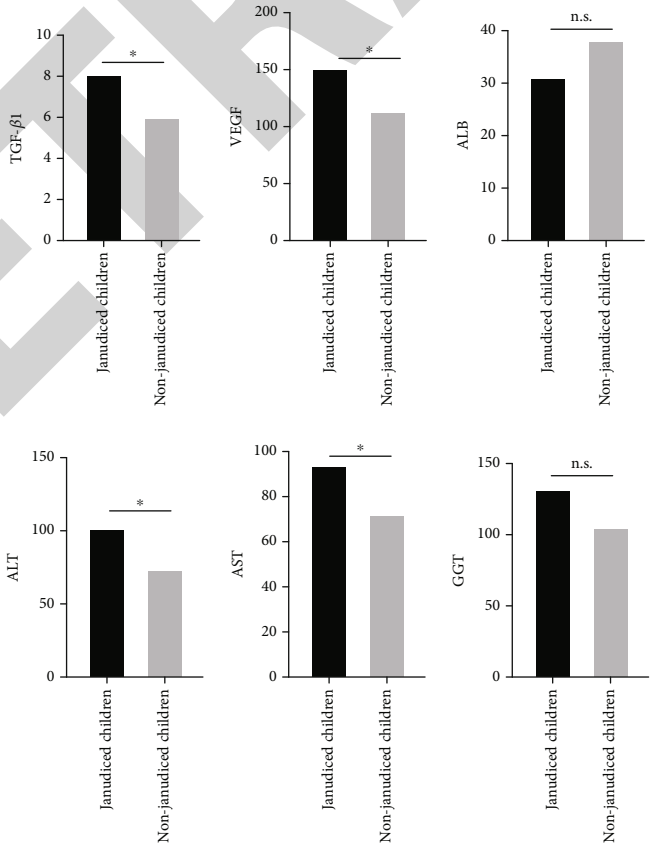

Figure 2: Comparison of serum indexes and liver hardness values of children with jaundice and children without jaundice in the BA group.

Table 1: Correlation of serum TGF-1 and VEGF with liver hardness values and liver function in the BA group.

Index	Liver hardness		ALB		ALT		AST		GGT	
	r	*P*	*r*	*P*	*r*	*P*	*r*	*P*	*r*	*P*
TGF-β1	0.378	0.004	-0.247	0.012	0284	0.014	0.284	0.004	0.254	0.008
VEGF	0.292	0.010	-0.362	0.002	0.213	0.012	0.364	0.001	0.236	0.004

3.2. Comparison of Children with Jaundice and Children without Jaundice. In BA group, there were 24 children with jaundice and 38 children without jaundice. Compared with children without jaundice, serum TGF in children with jaundice, The levels of VEGF, ALT, AST, GGT, and liver hardness increased significantly, while the level of ALB decreased significantly ($P < 0.05$) (Figure 2).

3.3. Serum TGF in BA Group: Correlation between Liver Hardness and Liver Function. Pearson's correlation analysis showed the serum TGF in BA group. There was a positive correlation between liver hardness and serum VEGF ($P < 0.05$). The level of VEGF was positively correlated with the levels of ALT, AST, and GGT and negatively correlated with the level of ALB ($P < 0.05$) (Table 1).

4. Discussion

The surgical effect of biliary atresia depends on the age of the child, the severity of liver fibrosis, and postoperative complications, and progressive liver fibrosis is an important factor affecting the surgical effect [19]. Studying the mechanism of liver fibrosis and preventing liver fibrosis is a major topic for domestic and foreign scholars [20]. In this study, the positive rate of TGF-1 and VEGF in biliary atresia group was higher than that in the control group ($P < 0.05$), and the expression level of TGF-1 was higher than that in biliary dilatation group and the control group ($P < 0.05$). The expression level of TGF-1 in grades I to II patients was significantly increased [21]. Ttgf-1 expression level was significantly decreased in grades III to IV patients ($P < 0.05$), suggesting that TGF-1 expression level was significantly increased in the early stage of fibrosis and significantly decreased in the late stage of TGF-1 [22]. The reason for the decreased late expression is that the transcription of TGF-1 mRNA in BA hepatosclerosis stage was inhibited, its content decreased, and its promoting fibrosis effect weakened. Some scholars believe that during the cirrhosis of children with BA, due to intrahepatic fibrous hyperplasia and blood circulation disorder, TGF-1 and VEGF proteins are greatly reduced, which is consistent with the results of this experiment [23].

Conventional ultrasound has been widely used in the evaluation of jaundice in infants due to its unique advantages of noninvasive, simple, and repeatable. In order to improve the diagnostic level of biliary atresia, based on the long-term accumulated clinical experience, previous researchers have summarized the characteristics of biliary atresia represented by gallbladder morphology and hilar triangle abnormality (TC). However, due to the difficulty in timely detection of TC in children in small age groups and low sensitivity in early stage, the actual clinical value of TC has been doubted [24, 25]. In addition, since pathological jaundice without biliary atresia (such as hepatitis syndrome in infants) can also present with poor gallbladder filling, it has been reported that although the diagnostic sensitivity based on abnormal gallbladder morphology is as high as 97.8%, its specificity is only 54.1% [26–28]. Therefore, a considerable number of jaundice cases evaluated by conventional ultrasound still need to rely on radionuclide angiography, gallbladder puncture angiography, and even open exploration to confirm the diagnosis, and the accompanying risk of radiation injury and surgical complications is inevitable. However, this study also has its limitations, such as the incomplete information for all patients included in this retrospective study. Therefore, more prospective clinical studies and mechanical verifications should be performed in the future study.

5. Conclusion

The levels of serum TGF-β1 and VEGF in children with biliary atresia have a certain risk correlation with liver function damage, which will become a research focus on the mechanism of liver fibrosis in the diagnosis and treatment of biliary atresia in children.

Data Availability

The data used to support this study are available from the corresponding author upon request.

Conflicts of Interest

The authors declare that they have no conflicts of interest.

References

[1] P. A. Derusso, M. R. Spevak, and K. B. Schwarz, "Fractures in biliary atresia misinterpreted as child abuse," *Pediatrics*, vol. 112, no. 1, pp. 185–188, 2003.

[2] K. Tsugumichi, O. Kensuke, O. Kakou, H. Kaneda, and T. Furuya, "Obliterative cholangiopathy in acquired cystic biliary atresia type III after cyst perforation: a case report," *Pediatrics*, vol. 18, no. 1, pp. 1–7, 2018.

[3] S. Xu, D. Mei, X. Wu, W. Cheng, M. Ye, and L. Li, "A prospective study comparing laparoscopic and conventional Kasai portoenterostomy in children with biliary atresia," *Journal of Pediatric Surgery*, vol. 51, no. 3, pp. 374–378, 2016.

[4] M. H. Lee, H. J. Shin, H. Yoon, S. J. Han, H. Koh, and M. J. Lee, "Periportal thickening on magnetic resonance imaging for hepatic fibrosis in infantile cholestasis," *Journal of Gastroenterology*, vol. 26, no. 21, pp. 2821–2830, 2020.

[5] S. Hanquinet, D. S. Courvoisier, A. L. Rougemont et al., "Acoustic radiation force impulse sonography in assessing children with biliary atresia for liver transplantation," *Pediatric Radiology*, vol. 46, no. 7, pp. 1011–1016, 2016.

Hindawi
Computational and Mathematical Methods in Medicine
Volume 2023, Article ID 9827631, 1 page
https://doi.org/10.1155/2023/9827631

Retraction

Retracted: Lentinan Enhances the Function of Oxaliplatin on the Esophageal Tumors by Persuading Immunogenic Cell Death

Computational and Mathematical Methods in Medicine

Received 3 October 2023; Accepted 3 October 2023; Published 4 October 2023

This article has been retracted by Hindawi following an investigation undertaken by the publisher [1]. This investigation has uncovered evidence of one or more of the following indicators of systematic manipulation of the publication process:

(1) Discrepancies in scope

(2) Discrepancies in the description of the research reported

(3) Discrepancies between the availability of data and the research described

(4) Inappropriate citations

(5) Incoherent, meaningless and/or irrelevant content included in the article

(6) Peer-review manipulation

The presence of these indicators undermines our confidence in the integrity of the article's content and we cannot, therefore, vouch for its reliability. Please note that this notice is intended solely to alert readers that the content of this article is unreliable. We have not investigated whether authors were aware of or involved in the systematic manipulation of the publication process.

Wiley and Hindawi regrets that the usual quality checks did not identify these issues before publication and have since put additional measures in place to safeguard research integrity.

We wish to credit our own Research Integrity and Research Publishing teams and anonymous and named external researchers and research integrity experts for contributing to this investigation.

The corresponding author, as the representative of all authors, has been given the opportunity to register their agreement or disagreement to this retraction. We have kept a record of any response received.

References

[1] X. Huo, Z. Pei, W. Wang et al., "Lentinan Enhances the Function of Oxaliplatin on the Esophageal Tumors by Persuading Immunogenic Cell Death," *Computational and Mathematical Methods in Medicine*, vol. 2022, Article ID 2296574, 9 pages, 2022.

Hindawi
Computational and Mathematical Methods in Medicine
Volume 2022, Article ID 2296574, 9 pages
https://doi.org/10.1155/2022/2296574

Research Article

Lentinan Enhances the Function of Oxaliplatin on the Esophageal Tumors by Persuading Immunogenic Cell Death

Xiaolei Huo,[1] Zhen Pei,[1] Weiwei Wang,[1] Yu Liu,[1] Jing Sun,[1] Hui Wang,[2] and Nanping Ai[1]

[1]*Department of Basic Medicine, Changzhi Medical College, Changzhi, Shanxi Province, China*
[2]*Changzhi Maternal and Child Health Care Hospital, Changzhi, Shanxi Province, China*

Correspondence should be addressed to Nanping Ai; ainanping@qq.com

Received 28 May 2022; Revised 1 June 2022; Accepted 4 June 2022; Published 8 July 2022

Academic Editor: Plácido R. Pinheiro

Objective. The focus of this research was to look at the effects of the combination of the lentinan (LNT) and oxaliplatin (Oxa) on the apoptosis of human esophageal cancer cells, as well as the underlying mechanism. *Methods*. LNT and Oxa were used to treat EC-109 human esophageal cancerous cells at various doses, and the cell survival rate was measured using the Cell Counting Kit-8 (CCK-8) assay. In addition, 24 h after treatment of EC-109 cells with a combination of LNT and Oxa, flow cytometry was used to analyze their apoptotic effect on these cells. Additionally, LNT on EC-109 cell apoptotic upshot was assessed via measuring the consequence of LNT on the mRNA and protein expression levels pertaining to immunogenic cell death factors CALR, HSP90, and HSP70 by qPCR (quantitative real-time polymerase chain reaction) and western blot analysis, correspondingly. *Results*. Cell proliferation was inhibited only when EC-109 cells were added with LNT at 1,200 μg/mL to the maximum concentrations, but the combination of LNT and Oxa at a low dose (800 μg/mL and 20 μM, respectively) significantly increased their sensitivity to Oxa and reduced their proliferation ($P < 0.05$), and their apoptosis was significantly increased by LNT ($P < 0.05$). The immunogenic cell death-related genes CALR, HSP90, and HSP70 had dramatically enhanced mRNA and protein expression levels after therapy with a combination of LNT and Oxa ($P < 0.05$). *Conclusion*. These data imply that LNT increases the susceptibility of esophageal cancerous cells to Oxa by driving EC-109 cells to display immunogenic death. Therefore, LNT combined with Oxa may be an effective method in esophageal cancer management.

1. Introduction

Human tumor incidence and death have been steadily rising in recent years, and the incidence of esophageal cancer, in particular, remains high. Esophageal cancer is the sixth leading cause of cancer-related deaths of men, and the overall 5-year survival rate diverses from 15 to 25% worldwide [1]. Squamous cell carcinoma (SCC) and adenocarcinoma (AC) are two major subtypes of esophageal cancer.

The current main treatment technique for esophageal cancer is surgery, either alone or in conjunction with chemotherapy and/or radiotherapy, and the prevalence of esophageal malignancy has remained high in recent years [2, 3]. However, although surgical treatment and systemic chemotherapy can be used to treat esophageal cancer and prolong the patient survival to some degree, they cannot effectively treat advanced esophageal cancer. Currently, there are no effective drugs for esophageal cancer treatment except for those targeting PD-L1 in PD-L1-positive cancer [4, 5]. Oxaliplatin- (Oxa-) based chemotherapy regimens are still one of the main clinical regimens for esophageal cancer treatment, but the development of resistance to Oxa and its toxicity limits its efficacy in the treatment of esophageal cancer [6, 7]. Reducing its cytotoxicity and preventing the development of resistance to Oxa in esophageal cancer remains an unsolved challenge in the treatment of this cancer.

Extracts from natural foods and herbs for cancer treatment have received widespread attention from researchers due to their advantages of little side effects [8, 9]. Lentinan (LNT) is a polysaccharide compound derived from shiitake mushroom (Lentinula edodes) mycelium, thus exhibits therapeutic effects such as antioxidative stress, anti-inflammatory, and anticancer and has been widely used in cancer

adjuvant therapy clinical trials [10–12]. Oxa is a commonly used platinum-based chemotherapeutic agent and is used in combination with other drugs. LNT in combination with paclitaxel or cisplatin efficiently inhibits gastric cancer cell growth and promotes apoptosis, and LNT in conjunction with cisplatin greatly minimises the adverse effects of cisplatin and can successfully enhance the standard of life of lung cancer patients. However, its role in esophageal cancer is currently unclear. In the current research, we appraised the antitumor immune outcome of LNT alone and with Oxa combination against esophageal cancer by determining the alteration of the apoptotic mechanism in esophageal cancer cells.

This study will demonstrate the role of lentinan and Oxa on the esophageal tumors and explain the underlying mechanism, which will bring light on the treatment of patients.

2. Results

2.1. Both LNT and Oxa Inhibit Proliferation and Induce Apoptosis in EC-109 Esophageal Tumor Cells. We cocultured EC-109 cells with different concentrations of LNT (0 1,600 g/mL) and Oxa (0 80 m) for 24 to 72 hours to test the impacts of LNT and Oxa on the proliferation of EC-109 esophageal cancer cells and then used the Cell Counting Kit-8 (CCK-8) assay to determine the growth inhibitory effects of LNT and Oxa on EC-109 cells. Both LNT (Figure 1(a)) and Oxa (Figure 1(b)) decreased the growth of EC-109 cells, and cytotoxicity was inversely linked with drug concentration and duration of treatment as measured by the cell value-added rate. The following formula was used to estimate cell viability:

$$\text{Cell viability}(\%) = \frac{(\text{ODtreated} - \text{ODbackground})}{\text{ODunterated} - \text{ODbackground}} * 100\% \quad (1)$$

We used flow cytometry and an Annexin V-fluorescein isothiocyanate (FITC)/propidium iodide (PI) apoptosis assay to determine the rate of apoptosis of EC-109 cells after treatment with LNT for 48 hours to see if the inhibitory effect of LNT on EC-109 cell growth was related to its apoptosis-inducing effect. The apoptosis rate of EC-109 cells rose in a dose-dependent manner as the LNT concentration was increased, similar to the results of the CCK-8 experiment. These findings revealed that LNT induced apoptosis in EC-109 cells ($P < 0.05$) (Figure 2).

2.2. LNT Enhances the Sensitivity of EC-109 Cells to Oxa. The use of drug combinations in the therapeutic practice of malignancies is a frequent practice. The impacts of the conjunction of LNT and Oxa on the proliferation and apoptosis of EC-109 cells were assessed using the CCK-8 assay and flow cytometry to see if the combination of LNT and Oxa may increase the cell proliferation inhibition activity and apoptosis-inducing effect of Oxa on EC-109 cells. The outcomes explored it, and the TLN and Oxa combination significantly enhanced both the proliferation inhibitory effect and apoptosis-inducing effect of Oxa on EC-109 cells (Figures 3(a) and 3(b)).

Using qPCR and western blot analysis, we examined the mRNA and protein expression levels of BAX, Bcl-2, and caspase 3 in EC-109 cells to see if the combination of LNT and Oxa was linked with elevated mRNA and protein expression levels of genes involved in apoptotic pathways. The results demonstrate the effectiveness of LNT and Oxa in increased BAX and caspase 3 mRNA and protein expression ($P < 0.01$) while inhibiting Bcl-2 mRNA and protein expression ($P < 0.05$) (Figures 3(c) and 3(d)).

The combination index (CI) is one of the important measurement indexes to assess the degree of interaction between drugs. A CI < 1 denotes that there could be a synergistic impact between two medicines, a CI > 1 indicates that the relationship between 2 medicines is antagonistic, and a CI = 1 denotes the cumulative effect of the two drugs. To learn more about how the combination of LNT mechanism and Oxa to determine whether it was a cumulative or synergistic effect mechanism, we analyzed the combination index (CI) using the CompuSyn software. The results showed that the CI was <1, implying that Oxa and LNT's combined action on EC-109 cells was primarily synergistic (Figure 3(e)).

2.3. LNT Augments the Sensitivity of the EC-109 Cells to Oxa by Activating the Immunogenic Cell Death Pathway in EC-109 Cells. Immunogenic cell death (ICD), a type of controlled cell death, is linked to DAMPs (damage-associated molecular patterns), which occur when antigens are released intracellularly and cause self-damage in cells [13]. It has been shown that LNT can promote H22 cell death by inducing the expression of more CALR, HMG1, and HSP70 on the surface of H22 cells. We further investigated how LNT, in combination treatment with Oxa, enhances Oxa-induced apoptosis in EC-109 cells using ELISA, analysis of qRT-PCR, and western blot analysis to measure levels of key molecules associated with ICD and ATP, in addition to flow cytometry to assess the expression of surface (cell) immune antigens on EC-109 cells. The results of the ELISA of supernatants showed significantly higher release of CXCL10 and IL17 ($P < 0.05$) and significantly upregulated levels of HSP90 and HSP70 ($P < 0.05$) in the supernatants of the LNT and Oxa+LNT groups related to control. The relative mRNA expression levels of HMGB1, CALR, ANXA1, and IFNA1 were considerably greater ($P < 0.05$), while the relative protein expression levels of HSP70, HSP90, and CALR were dramatically increased, according to the results of the qRT-PCR and western blot studies ($P < 0.05$). These results indicated that LNT can enhance the toxicity of Oxa to cells by activating the release of ICD proteins in EC-109 cells (Figure 4).

3. Materials and Methods

3.1. Cell Culture. The human esophageal melanoma EC-109 cells (Shanghai Cell Bank of the Chinese Academy of Sciences, Shanghai, China) have been cultured in RPMI-1640 complete medium (Invitrogen, Carlsbad, CA, USA)

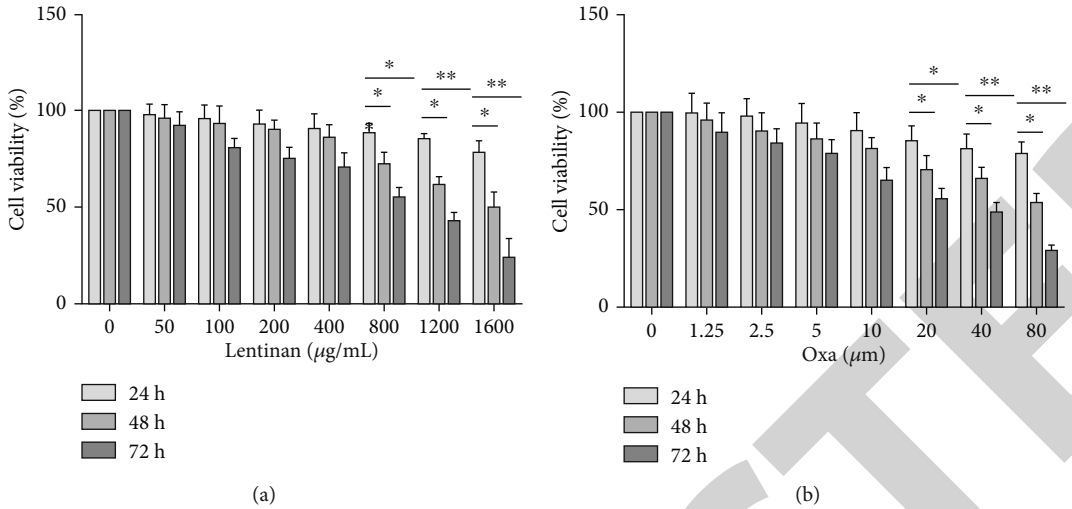

Figure 1: Both LNT and Oxa showed growth inhibitory effects against EC-109 cells. The vitality of EC-109 cells was measured using the CCK-8 assay after they were exposed to various amounts of LNT or Oxa for 24 to 72 hours. Each experiment was repeated three times, with the findings given as the mean minus the standard deviation. *24 h compared with 48 h and 72 h, $P < 0.05$.

containing 100 U/mL penicillin and streptomycin (Invitrogen) and 10% foetal bovine serum (Invitrogen) at 37°C in an incubator with 5% CO_2.

3.2. CCK-8 Assay. The Cell Counting Kit-8 (CCK-8) test (Beyotime Biotechnology, Shanghai, China) was used to calculate the cell survival rate. EC-109 cells in the logarithmic growth phase were collected and planted at a density of 5,000 cells per well in 96-well plates, and afterwards, the cells were attached and grown to 60% confluence, and each plate was incubated for 24 or 48 h with the corresponding concentration of the drug. The plate was then incubated at 37°C for 1-4 hours after 10 mL of CCK-8 solution was introduced to each well. The cell survival rate percent was then estimated for each group by detecting the optical density value at 450 nm (OD450), as follows: cell survival rate% = (OD_{450} value of drug group − OD_{450} of blank wells)/(OD_{450} of the control group − OD_{450} of the blank group) × 100%.

3.3. Analysis of Drug Synergy Using the CompuSyn Software. Based on the findings of the CCK-8 test, OD_{450} value and survival rate percentage at each drug concentration were obtained and analyzed with the CompuSyn software [ComboSyn Inc., Paramus, (NJ), 2005. http://www.combosyn.com [Donated to biomedical communities for free download, upon registration, beginning August 1. 2012 via http://www.combosyn.com of PD Science LLC].]. If CI < 1, the drug has synergistic effect, and the smaller the value, the more significant the synergistic effect; if CI = 1, it means that the drug has a cumulative effect; if CI > 1, it means that the drug has an antagonistic effect, and the value The larger the value, the more significant the antagonistic effect.

3.4. Apoptosis Assay. To determine the manner of cell death, researchers employed an Annexin V-fluorescein isothiocyanate (FITC)/propidium iodide (PI) apoptosis detection kit (Keygentec, Nanjing, China) (apoptosis versus necrosis). As mentioned in Collect cells as in step 2.2, log-phase grown EC-109 cells were harvested, plated in 96-well plates, and treated with the appropriate drug dose. Flow cytometry was used to examine EC-109 cells in the logarithmic growth phase for apoptosis using the Annexin V-FITC/PI double-staining method. The cells from each group were collected, centrifuged at 1,000*g* for 35 minutes, washed twice with precooled phosphate-buffered saline (PBS), and finally resuspended at a concentration of 1×10^6/mL.

The cell suspension was then mixed with 250 mL of diluted binding buffer, and 100 mL of the mixture was put into a 5 mL flow cytometry tube. The cell suspension was blended well and incubated for 15 minutes at ambient temp in the dark after adding 5 μL of Annexin V-FITC and 10 μL of 20 g/mL PI solution. The cell suspension was then examined using flow cytometry after 400 L PBS was added to the reaction tube.

3.5. Quantification of Secreted ATP, IL-17, CXCL10, HSP70, and HSP90. After 48 hours of incubation with 800 g/mL LNT or 20 M Oxa, the supernatant was collected, and the cell pellet was discarded after centrifugation (15,000 rpm, 30 min). Western blot analysis and enzyme-linked immunosorbent assays were used to evaluate the quantities of IL17, CXCL10, HSP70, and HSP90 released into the supernatant (ELISA). According to the manufacturer's instructions, the total protein content in the supernatant was determined using the Pierce bicinchoninic acid (BCA) Protein Assay Kit (Thermo Fisher Scientific Inc., Waltham, MA, USA). Following the determination of the total protein content in the supernatant, aliquots of 20-30 g of protein were combined with loading buffer, boiled in a boiling water bath for 5 minutes, and chilled to room temperature. The proteins in the aliquots were then separated on 10 percent SDS-PAGE gels and transferred to PVDF membranes using sodium dodecyl sulfate-polyacrylamide gel electrophoresis (SDS-PAGE). The membranes were then blocked for 1 hour

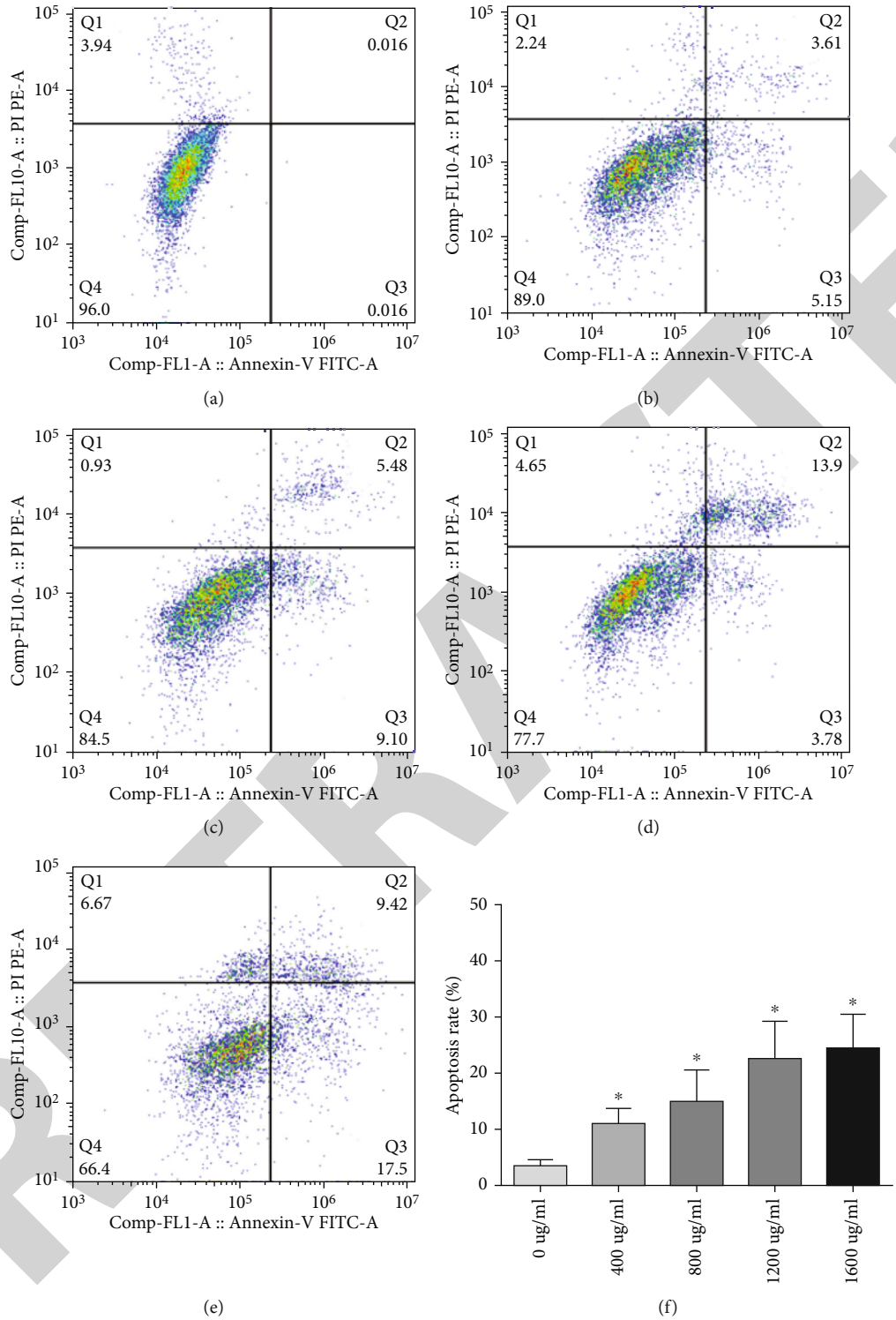

Figure 2: LNT induces apoptosis of EC-109 cells. (a–e) Rate of EC-109 cells apoptosis under the action of different concentrations of LNT. (f) Apoptosis rate of cells; each experiment was repeated 3 times, uttered like mean ± standard deviation. $^{*}P < 0.05$ vs. 0μg/mL LNT. Differences between groups have been detected by statistical analysis of one-way variance.

at room temperature with 5% fat-free dried milk in Tris-buffered saline (TBS) containing 0.1 percent Tween-20 (TBST), followed by overnight incubation with a primary antibody specific for HMGB1 (1 : 1,000, Sigma-Aldrich, Burlington, MA, USA). After that, the membranes were washed and incubated with a secondary antibody conjugated to horseradish peroxidase (1 : 2,000, MilliporeSigma) (HRP). The reference protein was bovine serum albumin (BSA). In addition, the levels of IL17, CXCL10, HSP70, and HSP90 in the collected supernatant were determined according to

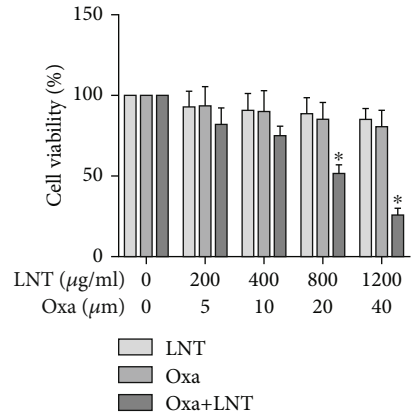

(a)

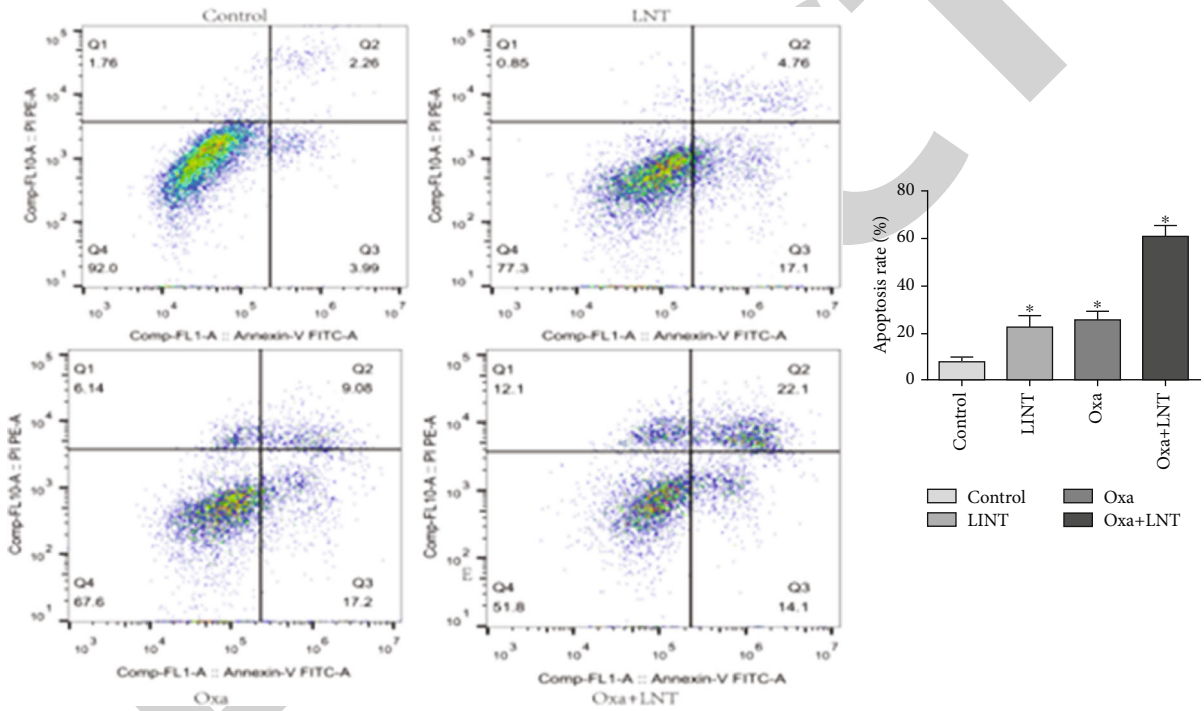

(b)

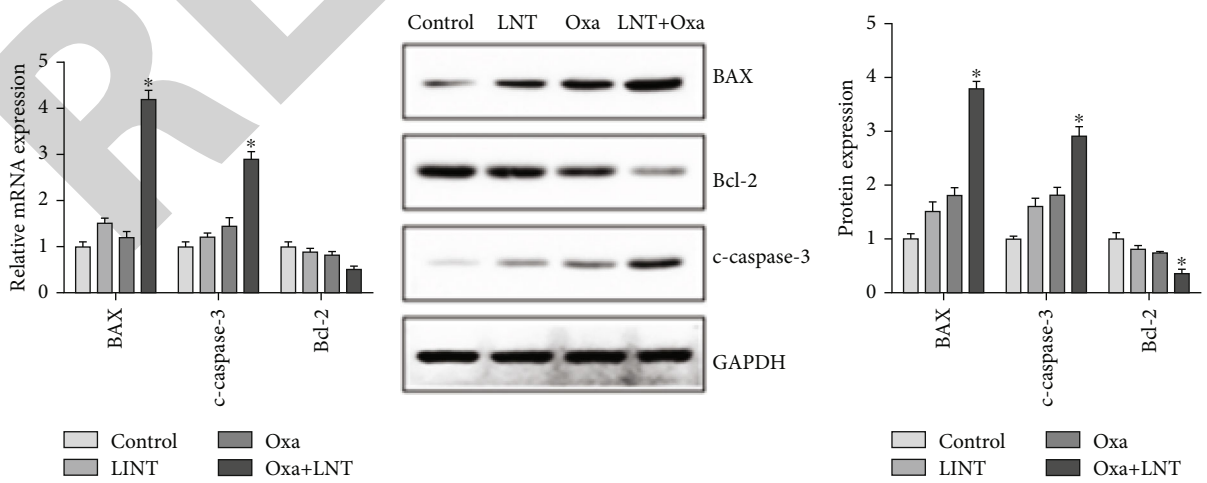

(c) (d)

Figure 3: Continued.

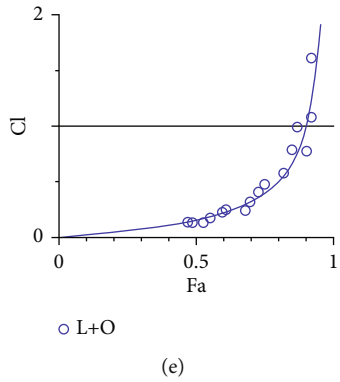

(e)

Figure 3: LNT enhances the sensitivity of EC-109 cells to Oxa. (a) The conjunction of LNT and Oxa greatly reduced EC-109 cell growth ($P < 0.05$). (b) The combination of LNT and Oxa persuaded programmed cell death in EC-109 cells ($P < 0.05$). (c) LNT combination and Oxa induced mRNA expression levels of *BAX* and *CASP3* and inhibited the mRNA expression *BCL2* ($P < 0.05$) level. (d) The conjunction of LNT and Oxa increased BAX and cleaved caspase 3 protein expression while suppressing BCL2 protein expression (P 0.05). (e) The analysis of the combination index (CI) of LNT and Oxa using the CompuSyn software revealed that both LNT and Oxa acted synergistically on EC-109 cells. The data were expressed as the mean standard deviation for each experiment, which was done in triplicate. $P < 0.05$ in comparison to 0 g to analyze the differences between groups; statistical analysis using one-way analysis of variance (ANOVA) was used.

the manufacturer's instructions using IL17, CXCL10, HSP70, and HSP90 ELISA kits (Clonecloud, Wuhan, China). A chemiluminescent ATP determination kit was used to determine the amount of ATP in the collected supernatants (A22066, Invitrogen, Shanghai, China). The fluorescence decay was measured using a luminometer after separately mixing each collected supernatant with the chemiluminescent ATP determination kit reagent (containing the reaction mixture of the luciferin and firefly luciferase without ATP). A series of ATP standard curves were developed with varied ATP concentrations to determine the quantity of ATP in the supernatant.

3.6. Quantitative Real-Time Polymerase Chain Reaction (qPCR) Analysis. TRIzol reagent (Invitrogen) was used to extract total RNA from cells in different treatments according to the manufacturer's instructions. The whole RNA was then utilised to convert mRNA to cDNA using a reverse transcription kit (Promega Corporation, Madison, WI, USA; Cat# A2801). The relative expression levels of *BAX*, *BCL2*, *CASP3*, CALR, *HSP90*, and *HSP70* in EC-109 cells were measured by qPCR analysis with a qPCR Master Mix kit (Cat# A6000; Promega Corporation), using *GAPDH* as the internal reference. The $2\text{-}\triangle\triangle^{ct}$ method was utilized to compute the relative mRNA expression levels.

3.7. Western Blot Analysis. The concentration of the extracted protein was measured using the BCA Protein Assay Kit after total protein was extracted from EC-109 cells in the three treatment groups according to the kit instructions (Thermo Fisher Scientific Inc.). SDS-PAGE was used to separate the proteins, which were subsequently transferred to PVDF membranes as described in section. Western blot analysis with the following antibodies was used to evaluate the protein expression levels of BAX, BCL2, caspase 3,CALR, HSP90, and HSP70: anti-BAX (Cat# ab3191; Abcam, Cambridge, UK), anti-BCL2 (Cat# ab196495; Abcam), anti-Caspase 3 (Cat# ab179517, Abcam), anti-HSP90 (Cat# ab203085, Abcam), and anti-HSP70 (Cat# ab2787, Abcam). The western blot analysis was performed utilizing anti-GAPDH (Cat# ab8227; Abcam) as the internal reference protein.

3.8. Statistical Analysis. Data from three independent studies are provided as mean standard deviation. A one-way ANOVA was used to find differences between groups during statistical analysis. All analyses were carried out using IBMSPSS Statistics 21.0. A difference of $P < 0.05$ was considered statistically significant.

4. Discussion

Human tumor incidence and death have been steadily rising in recent years, and the incidence of esophageal cancer, in particular, remains high. One of the main reasons for tumor recurrence or difficulty in treatment is the weak immunogenicity or lack of expression of tumor antigens, and the body's immune tolerance to the tumor can lead to escape response when the tumor is attacked by the body, resulting in treatment failure [14–18]. Therefore, reducing tumor drug resistance and improving tumor immunogenicity is the key to successful esophageal tumor treatment.

An increasing number of natural immunogenic enhancing substances are receiving more and more attention from researchers. The combination of conventional chemotherapeutic or radiotherapeutic drugs with extracts from natural plants is used to reduce the resistance of chemotherapeutic or radiotherapeutic drugs to tumors while at the same time increasing the effective rate of action of chemotherapeutic or radiotherapeutic drugs [19–23]. Currently, natural plant extracts are considered effective substances to enhance drug efficacy and reduce toxicity and are widely used in a variety of cancers. The polysaccharide complexes extracted from natural shiitake mushrooms have been widely used in

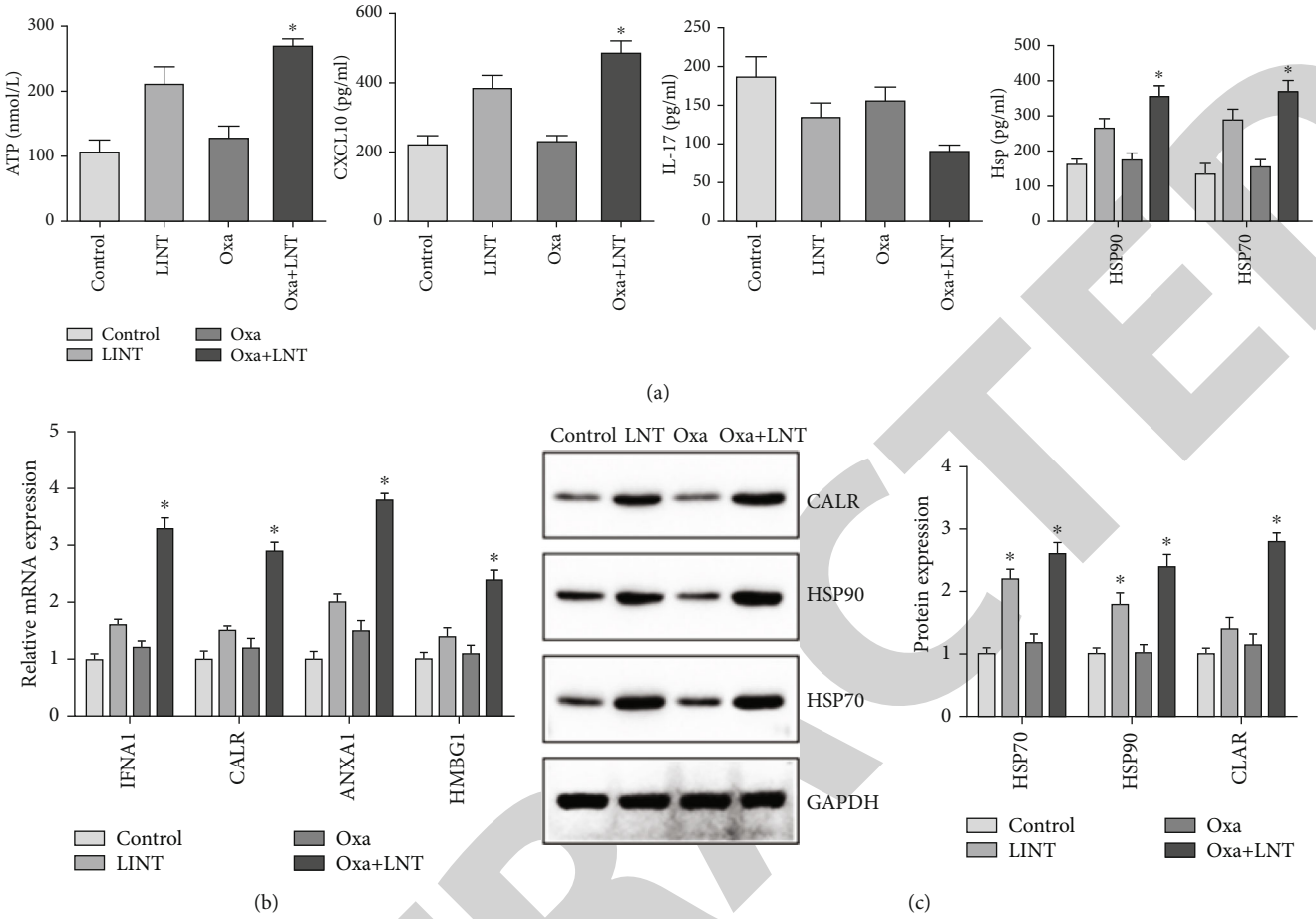

Figure 4: LNT-induced immunogenic cell death (ICD) pathway in EC-109 cells enhances the effectiveness of the combined Oxa intervention. (a) LNT alone or combined with Oxa induced the release of ATP, CXCL10, IL17, HSP70, and HSP90 ($P < 0.05$). (b) LNT alone or combined with Oxa induced the mRNA expression levels of *HMGB1*, *ANXA1*, *IFNA1*, and *CALR* ($P < 0.05$). (c) CALR, HSP70, and HSP90 protein expression levels were increased by LNT alone or in combination with Oxa ($P < 0.05$). Each experiment was repeated three times, with the findings given as mean ± standard deviation. *Contrast with control at $P < 0.05$. To find differences between the groups, statistical analysis using one-way analysis of variance (ANOVA) was used.

clinical practice. LNTs have been shown to have antioxidant, tumor-metastatic, tumor-proliferative, and immunomodulatory activities in vivo [24, 25]. However, the specific mechanism of its tumor-inhibitory activity is unclear. This work investigated the in vitro increase of the cellular level tumor suppression impact of LNT in conjunction with Oxa by activating ICD in esophageal cancer cells to elucidate the particular mode of action of LNT in esophageal cancer inhibition following treatment with Oxa.

Numerous studies have shown that LNT and Oxa can significantly inhibit tumor proliferation, metastasis, and invasion. LNT has been reported to inhibit SHG-44 human glioma cells [26], MCF-7 human breast cancer cell, and HepG2 human hepatocellular carcinoma cell [27] to varying degrees and can be used as an adjuvant in combination with chemotherapeutic agents to exert tumor-suppressive effects [28]. Oxa is a commonly used platinum-based chemotherapeutic agent and is used in combination with other drugs. LNT in combination with paclitaxel or cisplatin efficiently inhibits gastric cancer cell growth and promotes apoptosis, and LNT in conjunction with cisplatin greatly minimises the adverse effects of cisplatin and can successfully enhance the standard of life of lung cancer patients. Zhang et al. demonstrated [10] that LNT can regulate autophagy and apoptosis to inhibit the development of rectal cancer. The combination of LNT and Oxa was found to have significant synergistic antitumor effects in H22-bearing mice and effectively reduced the toxic side effects caused by Oxa. The antiproliferative effects of LNT and Oxa on EC-109 cells were time and dose dependent, according to the findings. The combination group significantly showed inhibited cell proliferation compared with LNT or Oxa alone. Moreover, CI analysis with the CompuSyn software also indicated the synergistic antiproliferative effects of LNT in combination with Oxa. Flow cytometric analysis revealed that the EC-109 cell apoptosis was significantly higher posttherapy in a combination of LNT and Oxa than with Oxa alone ($P < 0.05$), implying that the two medicines combined may suppress cell proliferation by increasing cell sensitivity to Oxa.

ICD is a distinct type of controlled cell death, thus related to DAMPs associated with the release of antigens

from cells leading to the production of self-damage in tumor cells [13]. Antigenic molecules released from the cell surface area are among the important markers of ICD, including ATP, HMGB1, HSP90, and HSP70. Natural plant extracts have been demonstrated to be effective in a number of investigations with the ability to induce an increase in the secretion of ATP, HSP90, and HSP70 from tumor cells which can more effectively inhibit tumor growth, proliferation, and metastasis. W. Wang et al. [29] showed that LNT can promote H22 cell death by inducing the expression of CALR, HMG1, and HSP70 on the surface of H22 cells. Similar results were obtained in this study, in which a significantly increased level of CALR was found in the culture supernatant of LNT-treated EC-109 cells, suggesting that CALR is transferred from inside the cells to the cell surface, which in turn promotes ICD in EC-109 cells. Oxa was not found to have a role in promoting ICD in Oxa-treated EC-109 cells. The combination of LNT and Oxa was found to induce the release of ATP, CALR, HSP70, and Hsp90 from EC-109 cells, which increased the cell death of EC-109 cells.

The advantage of this study was that this study demonstrated the role of LNT in assisting the function of Oxa in esophageal tumor cells, which will bring light for patients. However, there are also limits of this study. The mechanism was not clearly clarified and needs further studies deeply.

5. Conclusion

The results of this study showed that treatment of EC-109 cells with a combination of LNT and Oxa significantly increased their level of ATP and their release of CALR and other immunogenic signaling substances related to apoptosis, which increased the rate of apoptosis while at the same time increasing autoimmunogenicity. In future studies, we will analyze the ICD process in EC-109 cells induced by LNT combined with oxaliplatin and its specific mechanisms of action and pathways.

Data Availability

The data used to support this study is available from the corresponding author upon request.

Conflicts of Interest

The authors declare that they have no conflict of interest.

Authors' Contributions

Xiaolei Huo and Zhen Pei contributed equally to this work.

Acknowledgments

This research was supported by the 2020 Science and Technology Innovation Project of Colleges and Universities in Shanxi Province (2020 L0394).

References

[1] M. Watanabe, R. Otake, R. Kozuki et al., "Recent progress in multidisciplinary treatment for patients with esophageal cancer," *Surgery Today*, vol. 50, no. 1, pp. 12–20, 2020.

[2] F. Bray, J. Ferlay, I. Soerjomataram, R. L. Siegel, L. A. Torre, and A. Jemal, "Global cancer statistics 2018: GLOBOCAN estimates of incidence and mortality worldwide for 36 cancers in 185 countries," *CA: a Cancer Journal for Clinicians*, vol. 68, no. 6, pp. 394–424, 2018.

[3] F. Huang and S. Yu, "Esophageal cancer: risk factors, genetic association, and treatment," *Asian Journal of Surgery*, vol. 41, no. 3, pp. 210–215, 2018.

[4] E. Limagne, M. Thibaudin, L. Nuttin et al., "Trifluridine/tipiracil plus oxaliplatin improves PD-1 blockade in colorectal cancer by inducing immunogenic cell death and depleting macrophages," *Cancer Immunology Research*, vol. 7, no. 12, pp. 1958–1969, 2019.

[5] H. Zhu, Y. Shan, K. Ge, J. Lu, W. Kong, and C. Jia, "Oxaliplatin induces immunogenic cell death in hepatocellular carcinoma cells and synergizes with immune checkpoint blockade therapy," *Cellular Oncology*, vol. 43, no. 6, pp. 1203–1214, 2020.

[6] J. Zheng, J. Sun, J. Chen et al., "Oxygen and oxaliplatin-loaded nanoparticles combined with photo-sonodynamic inducing enhanced immunogenic cell death in syngeneic mouse models of ovarian cancer," *Journal of Controlled Release*, vol. 332, pp. 448–459, 2021.

[7] Z. Sun, Y. Peng, W. Zhao, L. L. Xiao, and P. M. Yang, "Purification, characterization and immunomodulatory activity of a polysaccharide from *Celosia cristata*," *Carbohydrate Polymers*, vol. 133, pp. 337–344, 2015.

[8] Y. Zi, B. Zhang, B. Jiang et al., "Antioxidant action and protective and reparative effects of lentinan on oxidative damage in HaCaT cells," *Journal of Cosmetic Dermatology*, vol. 17, no. 6, pp. 1108–1114, 2018.

[9] L. Zhao, Y. Xiao, and N. Xiao, "Effect of lentinan combined with docetaxel and cisplatin on the proliferation and apoptosis of BGC823 cells," *Tumour Biology*, vol. 34, no. 3, pp. 1531–1536, 2013.

[10] Y. Zhang, Y. Liu, Y. Zhou et al., "Lentinan inhibited colon cancer growth by inducing endoplasmic reticulum stress-mediated autophagic cell death and apoptosis," *Carbohydrate Polymers*, vol. 267, p. 118154, 2021.

[11] Y. Zhang, M. Zhang, Y. Jiang et al., "Lentinan as an immunotherapeutic for treating lung cancer: a review of 12 years clinical studies in China," *Journal of Cancer Research and Clinical Oncology*, vol. 144, no. 11, pp. 2177–2186, 2018.

[12] Y. Zhang, H. Mei, W. Shan et al., "Lentinan protects pancreatic β cells from STZ-induced damage," *J Cell Mol Med*, vol. 20, no. 10, pp. 1803–1812, 2016.

[13] Z. Asadzadeh, E. Safarzadeh, S. Safaei et al., "Current approaches for combination therapy of cancer: the role of immunogenic cell death," *Cancers*, vol. 12, no. 4, p. 1047, 2020.

[14] T. Zyrianova, B. Lopez, A. Liao et al., "BK channels regulate LPS-induced CCL-2 release from human pulmonary endothelial cells," *American Journal of Respiratory Cell and Molecular Biology*, vol. 64, no. 2, pp. 224–234, 2021.

[15] N. Zwink, V. Choinitzki, F. Baudisch et al., "Comparison of environmental risk factors for esophageal atresia, anorectal malformations, and the combined phenotype in 263 German families," *Diseases of the Esophagus*, vol. 29, no. 8, pp. 1032–1042, 2016.

Hindawi
Computational and Mathematical Methods in Medicine
Volume 2023, Article ID 9896832, 1 page
https://doi.org/10.1155/2023/9896832

Retraction

Retracted: Effects of Pelvic Floor Muscle Massage on the Pregnancy Outcome of Frozen Embryo Transfer in Patients with Thin Endometrium

Computational and Mathematical Methods in Medicine

Received 3 October 2023; Accepted 3 October 2023; Published 4 October 2023

This article has been retracted by Hindawi following an investigation undertaken by the publisher [1]. This investigation has uncovered evidence of one or more of the following indicators of systematic manipulation of the publication process:

(1) Discrepancies in scope

(2) Discrepancies in the description of the research reported

(3) Discrepancies between the availability of data and the research described

(4) Inappropriate citations

(5) Incoherent, meaningless and/or irrelevant content included in the article

(6) Peer-review manipulation

The presence of these indicators undermines our confidence in the integrity of the article's content and we cannot, therefore, vouch for its reliability. Please note that this notice is intended solely to alert readers that the content of this article is unreliable. We have not investigated whether authors were aware of or involved in the systematic manipulation of the publication process.

Wiley and Hindawi regrets that the usual quality checks did not identify these issues before publication and have since put additional measures in place to safeguard research integrity.

We wish to credit our own Research Integrity and Research Publishing teams and anonymous and named external researchers and research integrity experts for contributing to this investigation.

The corresponding author, as the representative of all authors, has been given the opportunity to register their agreement or disagreement to this retraction. We have kept a record of any response received.

References

[1] L. Shen, "Effects of Pelvic Floor Muscle Massage on the Pregnancy Outcome of Frozen Embryo Transfer in Patients with Thin Endometrium," *Computational and Mathematical Methods in Medicine*, vol. 2022, Article ID 2803363, 7 pages, 2022.

Hindawi
Computational and Mathematical Methods in Medicine
Volume 2022, Article ID 2803363, 7 pages
https://doi.org/10.1155/2022/2803363

Research Article

Effects of Pelvic Floor Muscle Massage on the Pregnancy Outcome of Frozen Embryo Transfer in Patients with Thin Endometrium

Longying Shen

Kuishan Health Center of Rizhao Economic and Technological Development Zone, China

Correspondence should be addressed to Longying Shen; sxc@qfnu.edu.cn

Received 27 May 2022; Revised 2 June 2022; Accepted 3 June 2022; Published 29 June 2022

Academic Editor: Plácido R. Pinheiro

Objective. To observe the effects of pelvic floor muscle mass on the priority outcome of frozen embryo transfer in patients with thin endometrium. *Methods.* The patients who were prepared for freeze-thaw embryo transfer were randomly divided into the study group and control group. Both groups of patients began to take estradiol valerate tablets 3 mg on the third day of menstrual cycle and added progesterone for luteal support after 14 days. Both groups selected high-quality embryos for embryo transfer on the day of embryo transfer. The basic information, embryo transfer, intimal thickness, intimal type, clinical pregnancy rate, and early abortion rate of the two groups were compared. *Results.* The intimal thickness of patients in the control group and the study group on the second day of menstruation was (0.49 ± 0.03) and (0.45 ± 0.02) and that before progesterone was (1.17 ± 0.03) and (1.20 ± 0.04), respectively ($P < 0.05$). At the same time, the number of excellent embryos in the study group was significantly higher than that in the control group ($P < 0.05$), but there was no significant difference in the number of transplants between the two groups ($P > 0.05$). The proportion of intimal blood flow of type III + II in the study group was significantly higher than that in the control group ($P < 0.05$). The main adverse pregnancy outcomes of the whole group included biochemical pregnancy, early abortion, and ectopic pregnancy. The incidence of biochemical pregnancy in the control group and the study group was 63.3% (38/60) and 40.0% (24/60), respectively. The incidence of biochemical pregnancy in the control group was significantly higher than that in the study group, but there was no significant difference in the incidence of early abortion and ectopic pregnancy between the two groups ($P > 0.05$). *Conclusion.* Pelvic floor muscle massage can improve endometrial thickness and subendometrial blood flow, so as to improve the pregnancy rate of frozen thawed embryo transfer patients.

1. Introduction

According to the statistics of the World Health Organization (WHO), 5-15% of couples of gestational age have the problem of infertility [1]. At present, there are nearly 40 million infertility patients in China, and they are increasing at the rate of hundreds of thousands every year, so that infertility has become the third largest disease after tumor and cardiovascular and cerebrovascular diseases [2]. Therefore, this problem has become a worldwide medical and social problem. The main reasons for the increase of infertility include the deterioration of environmental quality, the increase of infectious diseases such as sexually transmitted diseases, and the excessive social psychological pressure. In vitro fertilization embryo transfer (IVF-ET) [3], which appeared at the end of the 21st century, is not only the core part of assisted reproductive technology but also an important way to treat infertile patients in modern medicine, thus bringing fertility hope to the majority of infertile patients. However, the clinical pregnancy rate after embryo transfer (ET) did not reach a satisfactory level (30%~40%) [4]. For in vitro fertilization embryo transfer patients who have or may have severe ovarian hyperstimulation syndrome, in order to avoid further aggravation of their symptoms, embryos can be frozen and transferred after resuscitation. During embryo transfer [5], it is very difficult to intubate the uterine cavity,

wait for the diagnostic results after embryo biopsy, and patients who cannot carry out fresh embryo transfer for other special reasons can reduce the burden of patients and increase the cumulative pregnancy rate through freeze-thaw embryo transfer technology [6]. Therefore, embryo freezing has become one of the conventional technologies of reproductive centers [7, 8]. How to improve the endometrial receptivity of patients with frozen thawed embryo transfer, make it reach the endometrial thickness most suitable for embryo implantation [9], grasp the transfer opportunity, and improve the success rate of frozen thawed embryo transfer is a common problem faced by reproductive centers.

The center adopts the method of integrated traditional Chinese and Western medicine to improve endometrial receptivity and make it reach the most suitable endometrial thickness for embryo implantation, so as to improve the success rate of freeze-thaw embryo transfer [10]. Chinese acupoint massage has a long history in the diagnosis and treatment of infertility, which is one of the precious heritages of traditional Chinese medicine. Its characteristics are as follows: simple method, low-cost, nontoxic, and side effects. By adjusting the balance of yin and yang, it can adjust and strengthen the function of Zang Fu organs in both directions [11]. Combined with drugs, it can improve the absorption of drugs, enhance the exertion of drug properties, and reduce the possible toxic and side effects of drugs [12]. In this study, the medical massager produced by Shanghai Shengsheng Medical Equipment Co., Ltd. was used for pelvic floor muscle massage instead of traditional massage. The motor was used as the vibration element to massage the human pelvic floor through the massage pad in line with ergonomics. The massager stimulates the pelvic floor muscles through specific vibration frequency and intensity, so that the massage part can dredge the meridians, muscle contraction, accelerate blood circulation, and increase the blood perfusion rate of ovary uterus during embryo implantation, so as to improve the pregnancy rate in IVF-ET and improve the pregnancy outcome [13]. It can be seen that the combination of pelvic floor muscle massage and assisted reproductive technology (Art) is a direction worthy of further research and discussion. Compared with traditional massage, pelvic floor muscle massage instrument is safer, noninvasive, and painless, which is easy for patients to accept. More importantly, it can clearly quantify the stimulation intensity and has high repeatability. In addition to the traditional massage technology and art modern technology, the emergence of pelvic floor muscle massage is more conducive to clinical promotion and scientific research. Besides, pelvic floor muscle massage also provides a broader development space for art technology.

2. Method

2.1. Case Source. 120 patients who failed IVF/ICSI-ET treatment or cancelled fresh embryo transfer and underwent freeze-thaw embryo transfer in the reproductive center of our hospital were collected as the research objects. The patients were randomly divided into 60 cases in the study group and 60 cases in the control group. Fill in the observation form according to the requirements of clinical experiment. Our study was approved by the institutional review board of the hospital, and written informed consent was obtained from each participant. Inclusion criteria were as follows: (1) patients who meet the diagnostic criteria of infertility in western medicine; (2) comply with the indications of IVF-ET specified in the notice of the Ministry of Health on revising the technical specifications, basic standards, and ethical principles related to human assisted reproductive technology and human sperm bank; (3) no history of taking estrogen and progesterone drugs in recent 3 months; (4) those who do not get pregnant by transferring fresh embryos in the egg collection cycle; (5) avoid the occurrence of severe ovarian hyperstimulation syndrome; and (6) fresh cycle endometrium is too thin or endometrial lesions are not suitable for transplantation. Exclusion criteria were as follows: (1) comply with the contraindications of IVF-ET specified in the notice of the Ministry of Health on revising the technical specifications, basic standards, and ethical principles related to human-assisted reproductive technology and human sperm bank; (2) exclude hypertension, hyperthyroidism, and other endocrine diseases. (3) patients over 40 years old or with low ovarian response; (4) patients who cancel the cycle due to embryo quality, sudden diseases, and other factors on the day of transplantation; (5) and patients who are unwilling to participate in the study or do not insist on cooperation.

2.2. Treatment. During the freeze-thaw embryo transfer cycle, both groups began to take orally estradiol valerate 3 mg po bid on the third day of the menstrual cycle. After 14 days of continuous application, progesterone was added, and progesterone capsule 150 mg po bid was given every day, progesterone injection 40 mg im QD. On the day of transplantation, 2000 IU im QOD of chorionic gonadotropin for injection was added, and three of them were used for luteal support. The patients in the observation group received pelvic floor muscle massage for 15-20 minutes every day since their menstruation was clean, and the frequency of use was 50 Hz. The specific operations of pelvic floor muscle massage therapy are as follows: (1) preparation: the patient empties the bladder, and the treatment method is sitting; (2) input power: 40 VA; (3) operating frequency: 3400 rpm; and (4) pulse frequency: 75/min. The patients in the control group were not given pelvic floor muscle massage treatment, and the two groups underwent embryo transfer on the 20th day of menstruation (Figure 1).

2.3. Observation Index and Detection Method. Endometrial development in transplantation cycle is as follows: B-ultrasound was used to observe the thickness and type of endometrium in the two groups on the 2nd, 10th, and 17th day of menstrual cycle. The B-ultrasound instrument uses the vaginal probe of Aloka-SSD1700 color ultrasound imaging instrument and sector scanning (probe power 5.0 MHz).

Subendometrial blood flow in the two groups is as follows: the type and resistance of subendometrial blood flow were observed by B-ultrasound on the 10th and 17th days of menstrual cycle. Parameters such as peak systolic

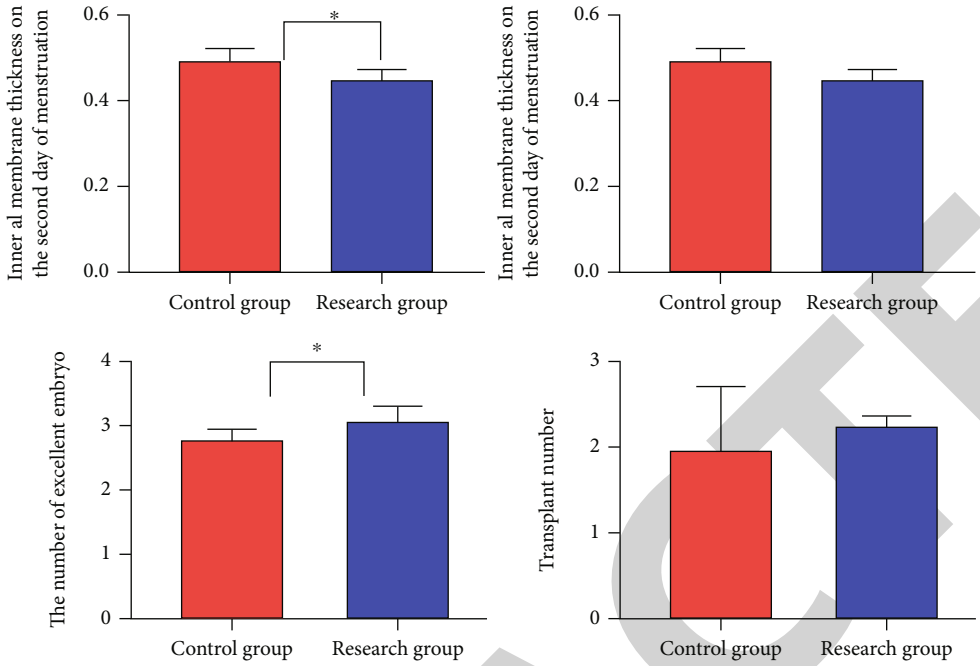

Figure 1: Classification criteria for subendometrial blood flow of each type.

velocity (s), end diastolic blood velocity (d), resistant index, RI = $(S - D)$/s, and pulsatility index, pi = $(S - D)$/vmean are obtained through the machine's own software. Subendometrial blood flow typing is as follows: the endometrial blood flow typing method first used by Chien and others: type I: endometrial blood flow cannot be detected, type II: only subendometrial blood flow can be detected, and type III: the blood flow in and under the endometrium can be detected.

2.4. In Vitro Culture and Embryo Transfer. After the embryos cultured in vitro meet the transfer conditions, the embryos are transferred under the guidance of abdominal B-ultrasound, and the conventional scheme is adopted for the transfer. After the patient's bladder is moderately filled, take the bladder lithotomy position, understand in detail the uterine position, the angle between the uterine body and the cervix, the length of the cervical tube, and the curvature of the cervix through abdominal ultrasound, measure the longest arc of the sagittal plane of the endometrium (i.e., the distance between the internal opening of the cervix and the endometrium of the uterine fundus) twice, and record the average value of the two. According to the direction and curvature of the cervical tube observed by the uterine exploration records and B-ultrasound, bend the outer tube of the transplantation tube (k pets 5000 transplantation tube, a product of cook company) into an appropriate curvature, insert it into the internal opening of the cervix along the endometrium, then place the inner tube in an appropriate position, and place the embryo at the thickest place of the endometrium or the place with the best echo of the endometrium under ultrasound.

2.5. Efficacy Criteria. The patients were asked to conduct self-test urine pregnancy test 14 days after transplantation, and the pregnancy outcomes of patients in each group were compared. Biochemical pregnancy is as follows: urine test showed positive reaction of HCG or blood 14 days after transplantation β – HCG > 10 IU/L; clinical pregnancy is as follows: 20 days after biochemical pregnancy, pregnancy sac, fetal bud, and fetal heart beat were found in utero under B-ultrasound. Early abortion is as follows: embryo loss occurs within 12 weeks of pregnancy.

2.6. Statistical Treatment. There is an SPSS 22.0 software package for statistical analysis. The counting data are expressed in percentage (n (%)), and chi square test is used. The measurement data were expressed by mean ± standard error and compared statistically by t-test, $P < 0.05$.

3. Results

3.1. Comparison of Intima and Embryo between the Two Groups. The intimal thickness of the control group and the study group on the second day of menstruation was (0.49 ± 0.03) and (0.45 ± 0.02), respectively. And that intimal thickness of the control group and the study group before progesterone was (1.17 ± 0.03) and (1.20 ± 0.04), respectively. The difference was statistically significant ($P < 0.05$). At the same time, the number of excellent embryos in the study group was significantly higher than that in the control group ($P < 0.05$), but there was no significant difference in the number of transplants between the two groups ($P > 0.05$). See Table 1 and Figure 2.

3.2. Comparison of Subintimal Blood Flow Type and Blood Flow Index between the Two Groups. On the 10th day of menstruation, the intimal blood flow of type III + II in the control group and the study group was 36 cases and 34 cases,

Table 1: Comparison of the intima and embryonic conditions of the patients in the two groups.

Index	Control group ($n = 60$)	Research group ($n = 60$)	Statistic value	P value
Inner al membrane thickness on the second day of menstruation	0.49 ± 0.03	0.45 ± 0.02	8.593	0.05
Flavestin anterior inner membrane thickness	1.17 ± 0.03	1.20 ± 0.04	-4.647	0.001
A-type intima	47	52	1.443	0.230
The number of excellent embryo	2.61 ± 0.15	2.89 ± 0.21	-8.404	0.001
Transplant number	1.85 ± 0.73	2.02 ± 0.24	-1.713	0.089

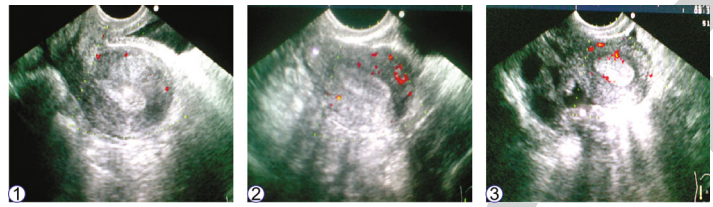

Figure 2: Comparison of the intima and embryonic conditions of the patients in the two groups.

respectively, and that of type I was 24 cases and 26 cases, respectively. There was no significant difference ($P > 0.05$). On the 17th day of menstruation, the intimal blood flow of type III + II in the control group and the study group was 37 and 56 cases, respectively, and that of type I was 23 and 4 cases, respectively. The proportion of intimal blood flow of type III + II in the study group was significantly higher than that in the control group ($P < 0.05$). See Table 2.

3.3. Comparison of Pregnancy Outcomes between the Two Groups. The main adverse pregnancy outcomes of the whole group included biochemical pregnancy, early abortion, and ectopic pregnancy. The incidence of biochemical pregnancy in the control group and the study group was 63.3% (38/60) and 40.0% (24/60), respectively. The incidence of biochemical pregnancy in the control group was significantly higher than that in the study group. However, there was no significant difference in the incidence of early abortion and ectopic pregnancy between the two groups ($P > 0.05$). See Table 3.

Table 2: Comparison of subendometrial blood flow type and blood flow index in the two groups.

Index	Control group ($n = 60$)	Research group ($n = 60$)	Statistic value	P value
Menstrual 10 d			0.137	0.711
III + II	36	34		
I	24	26		
Menstrual 17 d			1.725	0.001
III + II	37	56		
I	23	4		

Table 3: Comparison of pregnancy outcomes between the two patient groups.

Index	Control group ($n = 60$)	Research group ($n = 60$)	Statistic value	P value
Biochemical pregnancy	38	24	6.541	0.011
Clinical pregnancy	26	36	3.337	0.068
Early abortion	2	1	0.342	0.559
Eccyesis	1	0	0.135	0.843

4. Discussion

Frozen thawed embryo transfer (FET) is a further treatment measure after the failure of in vitro fertilization (IVF)/intracytoplasmic sperm injection (ICSI). The theoretical basis of frozen embryo storage is that tissue cells can inhibit metabolism and biochemical reaction rate during low-temperature freezing storage, which can make frozen thawed embryos survive. And because it increases the cumulative pregnancy rate [14], reduces the risk of multiple pregnancies in the in vitro fertilization cycle, and reduces the occurrence of moderate and severe ovarian hyperstimulation syndrome (OHSS), at the same time, there are many advantages, such as less cost, relatively simple and easy, and shorter time than the repeated egg retrieval cycle. This has attracted the attention of various reproductive centers, and embryo freezing technology has been carried out. As we all know [15], the key to the success of frozen thawed embryo transfer pregnancy is the synchronization of endometrium and embryo development, because embryo implantation is a process of mutual recognition, mutual accommodation, and interaction between embryo and maternal endometrium [16]. In this process, both embryo and endometrium are in a dynamic process of growth and development, only when the embryo develops to the blastocyst stage. Embryo implantation is allowed only when the endometrium proliferates and differentiates to a receptive state. The synchronization of the two is a necessary condition to ensure the successful

implantation of embryos [14]. In FET, too thick or too thin endometrium will affect embryo implantation. How to prepare the endometrium for freeze-thaw embryo transfer is an important topic to be discussed in the field of reproductive medicine. Therefore, the best endometrial preparation scheme is the key to ensure successful implantation. At present, there are many endometrial preparation schemes for freeze-thaw embryo transfer. In our center, endometrial blood flow in natural cycle, hormone replacement cycle, and ovulation induction cycle is often used as one of the influencing factors of endometrial receptivity. At present, the most commonly used blood flow parameters are blood pulsatility index (PI) and resistance index (RI). It is generally believed that high PI and RI reflect the increase of blood flow resistance and the decrease of uterine artery blood flow, poor uterine blood perfusion, and blood supply disorder, which may be one of the reasons for the low pregnancy rate. The study found that before embryo transfer, the uterine artery blood flow PI and RI of patients treated with IVF-ET were measured. It was found that there were significant differences between the pregnant group and nonpregnant group. It was considered that the uterine artery Doppler spectrum was related to the time of endometrial embryo reception, and PI and RI were effective indicators to predict the outcome of IVF-ET. Cheng and others believe that endometrial perfusion index can better reflect endometrial receptivity, so as to guide clinical medication to improve endometrial function and select transplantation time, which will have a far-reaching impact on improving the implantation rate and pregnancy rate of IVF-ET. Therefore, how to improve the distribution of subendometrial blood flow in hormone replacement cycle, reduce blood flow resistance, and improve pregnancy rate is a problem to be solved at present. Based on the principle of simple use, exact curative effect, and economic application, this study applied massage to pelvic floor muscle to improve subendometrial blood flow and improve pregnancy rate.

The motor is used as the vibration source to massage the pelvic floor of the human body through a massage pad in line with ergonomics. It stimulates the pelvic floor muscles through specific vibration frequency and intensity, so that the massage part can dredge the meridians, contract the muscles, and accelerate the blood circulation. Massage integrates the European concept of pelvic floor rehabilitation with China's traditional medical bioinformatics theory and technology. It is a new and unique method. The stimulation time is set at 15-20 min with a fixed time frequency and intensity. The use of electrical stimulation and biofeedback technology can dredge the meridians and stimulate acupoints, so as to awaken the pelvic floor nerves and muscles, promote the blood circulation in the pelvic cavity, regulate the internal environment, contract the pelvic muscles and ligaments, regulate the function of hypothalamus pituitary gonad axis, and increase the uterine blood flow and subendometrial blood flow. Massage is an early method used in clinical prevention and treatment of pelvic floor muscle injury and atrophy at home and abroad. At present, our center uses it to treat infertility. At present, studies have found that the mechanism of electrical stimulation is as follows: by inducing passive muscle contraction and activating some active molecules, it can promote the increase of the number of muscle cells to a certain extent, induce passive muscle contraction, promote muscle blood circulation, improve venous reflux, prevent the accumulation of harmful metabolites in muscle, and indirectly affect the metabolic process of atrophic muscle cells.

The characteristics of basin massage include the following: ① safe and effective, nontoxic, and side effects. For a safe and effective method, the treatment purpose is achieved through physical methods, which not only avoids the possible toxic and side effects of drugs but also solves the patients' doubts that the use of a large number of drugs may have an impact on fetal health in the future; ② two-way regulation can kill many birds with one stone. Pelvic floor muscle massage can regulate the balance of yin and yang, regulate the profit and loss of qi and blood of Zang Fu organs, strengthen the function of Zang Fu organs, and improve the ovarian uterine blood perfusion during embryo implantation, so as to improve the pregnancy rate; and ③ Simple operation and low cost. In this study, ssa-600e massager of Shanghai Shengsheng medical instrument company is used, which has no trauma and pain, good patient compliance, simple operation, low-cost, and no economic burden. The pelvic floor muscle belongs to the perineum muscle, which is a group of pelvic diaphragm and urogenital diaphragm separating the small pelvic cavity and perineum. It is composed of three layers of muscles and fascia to close the pelvic outlet. There is a pelvic diaphragm fissure in the front of the pelvic diaphragm. The urogenital diaphragm strengthens the pelvic floor from below, with urethra and vagina passing through. The pelvic diaphragm is located in the anal triangle, with rectum passing through, supporting and maintaining the pelvic organs in the normal position. It can control urination, maintain vaginal contraction, and enhance pleasure and other physiological functions. Under normal circumstances, pelvic floor muscle contraction is mostly caused by orgasm. For many infertile patients, it is difficult to reach orgasm and even have difficulty in sexual life, which is difficult to cause pelvic floor muscle contraction. Therefore, pelvic floor muscle cannot be exercised for a long time, its contractility is poor, and it cannot be congested, resulting in ischemia of various pelvic organs and insufficient nutrition. Patients with secondary infertility suffer from excessive pressure on pelvic floor muscles, muscle fiber deformation, decreased muscle tension, and pelvic muscle relaxation due to previous pregnancy, resulting in dissatisfaction with sexual life, stress urinary incontinence, uterine prolapse, incomplete closure of internal sphincter, and so on. Pelvic floor muscle weakness syndrome and pelvic congestion syndrome can lead to reduced uterine blood filling, endometrial dysplasia, difficult embryo implantation, and an increase in infertility patients. Therefore, the use of pelvic floor muscle massage can significantly improve the function of pelvic floor muscle through the massage effect of pelvic floor muscle, so as to improve the development of endometrium and improve the clinical pregnancy rate.

All kinds of literatures show that the application of traditional Chinese medicine in IVF-ET has made a beneficial

attempt. The research shows that the role of traditional Chinese medicine in regulating endometrial receptivity is positive. In assisted reproductive technology, the application of various traditional Chinese medicine means to improve the pregnancy rate reflects the idea of "prevention before disease" in traditional Chinese medicine. Zhang and others conducted a series of studies on the use of kidney tonifying traditional Chinese medicine to promote angiogenesis. On this basis, they put forward the theory of "tonifying the kidney and generating blood vessels," which enriched the theoretical connotation of "kidney governing reproduction" and further revealed the essence of kidney tonifying theory. Traditional Chinese medicine uses the prescriptions of tonifying the liver and kidney, supplementing qi, harmonizing blood and promoting blood circulation to improve the pregnancy rate of assisted reproductive technology, and mainly tonifying the kidney. In this study, combined with the shock method in traditional Chinese medicine massage, the simple use of physical therapy enables many patients who are unwilling to take traditional Chinese medicine or have concerns about drugs to better cooperate with the treatment. Through the combination of massage and acupoint massage, the overall adjustment is carried out in multiple ways, multiple levels, and multiple targets, so as to combine the syndrome differentiation and treatment of traditional Chinese medicine with the pregnancy assistance technology of Western medicine, develop their strengths, and avoid their weaknesses. It opens up a new way to improve the success rate of assisted reproductive technology. With the development of in vitro fertilization embryo transfer technology, laboratory technology is becoming more and more perfect, because the impact of technical reasons on embryos is becoming smaller and smaller. The main factors affecting the success rate of IVF-ET focus on the patient's own embryo quality, endometrial receptivity (ER) ,and so on. Pelvic floor muscle massage can improve endometrial receptivity. Endometrial receptivity refers to the ability of endometrium to accept embryos [17]. In the normal reproductive cycle of human and mammals, there is only a very short period of endometrium that allows embryo implantation. This period is called "implantation window period," at which the endometrium shows the greatest receptivity. If embryonic development is not synchronized with endometrial receptive development, or poor receptivity is not suitable for embryo implantation, it will lead to pregnancy failure. At present, the research on endometrial receptivity mainly focuses on pinopodes, subendometrial blood flow, integrins, leukemia inhibitory factor (LIF), etc. Pelvic floor muscle massage mainly affects the blood flow under the endometrium.

In conclusion, this study found that pelvic floor muscle massage can effectively improve the clinical pregnancy rate. The mechanism is to induce muscle contraction, increase intra-abdominal pressure, accelerate pelvic blood flow, reduce the blood flow resistance of uterine artery, and increase the subendometrial blood flow and blood perfusion, so as to improve the thickness and structure of endometrium and improve the active function and hormone level of uterus and ovary. The improvement of the intrauterine environment, the development of pinocytes, the expression of integrin and leukemia inhibitory factor, and the increase of endometrial receptivity are conducive to embryo implantation.

Data Availability

The data used to support this study are available from the corresponding author upon request.

Conflicts of Interest

The author declares that he/she has no conflicts of interest.

References

[1] B. Dhital, F. Gul-E-Noor, K. Downing, S. Hirsch, and G. S. Boutis, "Pregnancy-induced dynamical and structural changes of reproductive tract collagen," *Biophysical Journal*, vol. 111, no. 1, pp. 57–68, 2016.

[2] W. Li, Q. Hu, Z. Zhang, F. Shen, and Z. Xie, "Effect of different electrical stimulation protocols for pelvic floor rehabilitation of postpartum women with extremely weak muscle strength," *Medicine*, vol. 99, no. 17, article e19863, 2020.

[3] M. H. Davenport, T. S. Nagpal, M. F. Mottola et al., "Prenatal exercise (including but not limited to pelvic floor muscle training) and urinary incontinence during and following pregnancy: a systematic review and meta-analysis," *British Journal of Sports Medicine*, vol. 52, no. 21, pp. 1397–1404, 2018.

[4] Y. Snyder, C. Donlin-Smith, E. Snyder, E. Pressman, and E. Ciafaloni, "The course and outcome of pregnancy in women with nondystrophic myotonias," *Muscle & Nerve*, vol. 52, no. 6, pp. 1013–1015, 2015.

[5] X. Qi, J. Shan, L. Peng, C. Zhang, and F. Xu, "The effect of a comprehensive care and rehabilitation program on enhancing pelvic floor muscle functions and preventing postpartum stress urinary incontinence," *Medicine*, vol. 98, no. 35, article e16907, 2019.

[6] Y. Zhao, M. Xiao, F. Tang et al., "The effect of water immersion delivery on the strength of pelvic floor muscle and pelvic floor disorders during postpartum period," *Medicine*, vol. 96, no. 41, article e8124, 2017.

[7] M. Ishikawa, H. Ide, T. Tsujii et al., "Preferential freezing avoidance localised in anthers and embryo sacs in wintering Daphne kamtschatica var. jezoensis flower buds visualised by magnetic resonance imaging," *Plant, Cell & Environment*, vol. 45, 2022.

[8] A. Maheshwari, J. L. Bell, P. Bhide et al., "Elective freezing of embryos versus fresh embryo transfer in IVF: a multicentre randomized controlled trial in the UK (E-freeze)," *Human Reproduction*, vol. 37, no. 3, pp. 476–487, 2022.

[9] A. J. Wein, "Re: Preoperative pelvic floor muscle exercise and postprostatectomy incontinence: a systematic review and meta-analysis," *Journal of Urology*, vol. 197, no. 4, pp. 1115-1116, 2017.

[10] C. Panman, M. Wiegersma, B. Kollen et al., "Effectiveness and cost-effectiveness of pessary treatment compared with pelvic floor muscle training in older women with pelvic organ prolapse: 2-year follow-up of a randomized controlled trial in primary care," *Journal of the North American Menopause Society*, vol. 23, no. 12, pp. 1307–1318, 2016.

[11] M. Hagovska and J. Svihra, "Evaluation of duloxetine and innovative pelvic floor muscle training in women with stress

Hindawi
Computational and Mathematical Methods in Medicine
Volume 2022, Article ID 9535254, 8 pages
https://doi.org/10.1155/2022/9535254

Research Article

Health Index Estimation of Wind Power Plant Using Neurofuzzy Modeling

Shahanaz Ayub,[1] **Rajasekhar Boddu**,[2] **Harshali Verma**,[3] **Sri Revathi B**,[4] **Bal Krishna Saraswat**,[5] **and Anandakumar Haldorai**[6]

[1]*Electronics and Communication Engineering Department, Bundelkhand Institute of Engineering and Technology, Uttar Pradesh, Pin-284128, Jhansi, India*
[2]*Department of Software Engineering, College of Computing and Informatics, Haramaya University, Dire Dawa, Ethiopia*
[3]*Digital Communication, Bundelkhand Institute of Engineering and Technology, UP, Jhansi, India*
[4]*School of Electrical Engineering, Vellore Institute of Technology, Chennai, India*
[5]*Department of Computer Science & Engineering, Faculty of Engineering & Technology, SRM Institute of Science & Technology, NCR Campus, Modinagar, 201204, Ghaziabad, Uttar Pradesh, India*
[6]*Department of Computer Science and Engineering, Sri Eshwar College of Engineering, 641202, Coimbatore, Tamil Nadu, India*

Correspondence should be addressed to Rajasekhar Boddu; rajsekhar.boddu@haramaya.edu.et

Received 30 March 2022; Revised 7 May 2022; Accepted 10 May 2022; Published 29 May 2022

Academic Editor: Plácido R. Pinheiro

According to the Tamil Nadu Energy Development Agency (TEDA) in the 2019-20 academic year, the wind power plant produces 23% of the biomass power supply in the Indian electrical commodities. To maintain the power withstanding capability needed for future electrical commodities, a yearly power shutdown program is implemented. An additional wind power plant unit will be erected and create more electricity, thereby balancing India's commercial electricity needs. Even in a nonstationary working environment, continuous monitoring and analyzing the efficiency of wind turbines is a more difficult task. Consequently, in this paper, a health index calculation for wind power plants is proposed utilizing neurofuzzy (NF) modeling. Wind generator efficiency can be measured mathematically by recording three crucial primitivistic such as observed rotation speed, generation wound temperature, and gearbox heat. Fuzzy rules are used to design the parameters of the neural network (NN), and the accumulated signal is compared using the nonlinear extrapolation approach to determine the wind generator's behavior and evaluate the hazards. During the experimental study, two windows of 24 hours and 60 hours are used, where the deviation signal required for the hazard induction is investigated. The proposed approach can accurately calculate the wind generator's health state. As a result of an improved health operating and management (HOM) system, the amount of power generated by industrials and domestic appliances has increased dramatically.

1. Introduction

Wind turbines have a lower fuel cost than other renewable energy sources in large-scale applications [1–3]. A wind generator's efficacy might fluctuate depending on the situation due to various geological characteristics, climate conditions, and wind farm characteristics [4, 5]. Power suppliers will have more useful data to aid in power generation planning if the total output of windy power plants (WPP) can be projected with high precision [6]. With this information, a WPP may be managed in a flexible and intelligent way (e.g., enhanced wind farm operating schedules and reactive energy flow). Estimating wind power generation can be done using physical procedures, analytical methodologies, fuzzy-based techniques [7], and even hybrid approaches [8]. Because of the detection and tracking limitations imposed by WPP's detectors and tracking systems, physical techniques must rely mostly on numerical weather forecasts [9]. Variable factors, calculation time, time limitations, and sampling frequency all affect WPP's capacity to provide

reliable information. It is easier to predict the efficiency of a single wind turbine than the entire WPP's output [10]. Low-cost forecasting methods based on probabilistic and neuro-networking principles are available. A nonlinear model of the interactions between input and output information can be created based on previously observed information. However, the anticipated error may be large if additional data that was not previously included in the collection of retraining data is used as intake into such a type of system [11].

According to [11], wind farms have a large prediction error and a wide range of failures. If an abnormal wind farm is not discovered and corrected in a timely manner, it could cause lengthy outages and even lead to a lack of electricity generation. Wind farms, on the other hand, have a major challenge due to their high operational expenses. Because of this, it is becoming increasingly important to improve wind turbine O&M technology such as state tracking and wind farm problem diagnostics [12]. Evaluating wind turbines' real-time operational conditions and discovering emergent faults requires conducting an electronic health review. Administrators of wind farms can use it as a timely reminder to prioritize and construct time-based condition-based repair plans. A wind farm's operating costs and loss risk can be reduced by monitoring the operational state of all its wind generators [13]. Consequently, the safety and efficiency of the wind farm have been improved.

There is still a lot of work to be done in terms of healthcare performance measurements and assessment concepts, which are still in the early phases of development [14]. The three types of wind farm healthcare evaluation strategies outlined in the research include neural network- (NN-) based approaches, knowledge-based techniques, and data-based techniques [15]. Many various components and functions make up the wind farm's electromechanical structure. In addition, the many elements' linkages are intricate. It is so difficult to construct a precise numerical model for a wind farm of this size and complexity [16].

Assessment of wind turbine maintenance will raise several difficulties, the majority of which are addressed in the following sections. To begin, the wind farm will receive numerous (false) alerts due to multiple state tracking systems and the segregation of designs in subassemblies of the wind farm (separate modeling for gearboxes, one modeling for bearings, etc.) [17]. As a result, it is nearly impossible to keep track of operations. Furthermore, because there is only one model for each WT, wind farms with many large wind farms will be impossible to operate. As a result, it is difficult to scale state monitoring equipment in large wind farmlands. Keeping track of each WT's data for a long period of time would be the next challenge in setting alarm thresholds. Because of the lack of standardization in the system's characteristics, operations are more costly as a result. Consequently, it is necessary to significantly improve the status tracking methods [18].

A lot of attention is being paid to NN-based systems (especially multilayered perceptron), which can handle nonlinear effects. When developing a neural network model, it is customary to use characteristics such as GWT, rotation speed (RS), windy speed (WS), gearbox temperatures (GT), AT, and pitching angle PA, as well as NT, to anticipate the resultant active energy (AP) for such WT. Anomalies are recognized in the same way as in anomaly identification methods when the gap between expected and observed AP is greater than a specified level [19]. Several of the new components of the study mentioned in this research are the utilization of this signaling to construct a probabilistic health state model for such a WT because it has data about its healthcare.

In this paper, a health index calculation for wind power plants is proposed. Wind generator efficiency can be measured mathematically by recording three crucial primitivistic such as rotation speed, generation wound temperature, and gearbox heat. Fuzzy rules are used to design the parameters of the neural network (NN). The proposed approach can accurately calculate the wind generator's health state. During the experimental study, two windows of 24 hours and 60 hours are used, where the deviation signal required for the hazard induction is investigated.

The rest of the paper is structured as follows: Section 2 focuses on related work, in which the authors' contributions to wind power plant healthcare are examined. A neurofuzzy model and mathematical approach to changing window sliding are discussed in Section 3. For operating and management systems, Section 4 presents experimental findings that demonstrate how well the wind generator's healthcare parameters are evaluated. Finally, Section 5 provides a conclusion and a look at what the future holds.

2. Literature Review

For the most part, condition monitoring systems (CMS) in this industry demand a deeper knowledge of the monitored process. Sadly, this information is hard to obtain by and often does not exist [20]. Physical representations of such a network are rarely generated with great precision because of its complex interplay across several dynamical components. Furthermore, vibrations are the primary focus of the current CMS. As a means of assessing the health of machines, vibration testing has recently gained in popularity [21]. Unfortunately, vibrating detectors are rarely installed on all rotors and modules due to their high cost. A lack of state tracking has resulted in many turbines that are merely equipped with a vibrating sensor at each of their primary components. On the other hand, it appears that a large amount of operational (SCADA) data will be used to determine the generator's status. According to [22], wind farm CMS construction is the most cost-effective when such data is used. Data on the state of the turbine or observations of indicators such as current flow, temperatures, or tensions will be used as performance information in the turbine.

Using turbine condition data, problems can be predicted 5–60 minutes in advance in [23]. Performing preventive maintenance during this predicted timeframe would be difficult due to the lack of time available for workers to complete tasks. Signal processing techniques that focus on the trending of key data or combinations of signals can be used to detect major fluctuations in turbine performance at an early stage. Using neural network (NN) design techniques, [24]

shows that signaling activity can be predicted weeks, days, and even months in advance. These methods are more suited to allowing workers to correct problems before the component fails [25]. Model-based techniques are used to build conventional behavioral patterns that can predict a specific output signal when given one or more data inputs [25]. Many signals could be discovered to be linked to other information monitored simultaneously, such as wind speed or power generation. This is perfect for wind farm signaling. To analyze wind farm signals, the use of a typical behavioral notion is advantageous because it does not require any prior knowledge of signaling behavior. The availability of signal tracking seems to be a fundamental component of the normal behavioral idea, as mentioned, as well [26].

When the turbine parts are considered normal (usually functional), which is typically at the beginning of the device's lifespan, the conventional behavioral modeling is constructed. Learned systems are then used to predict signals, and the forecasting error indicates signal behavioral changes that lead to flaws in the system. The scientific community is quite interested in this technique [26]. Autoregressive using exogenous input (ARX) modeling is used in this case to determine the status of a wind farm generator bearing using SCADA signals. Unfortunately, this approach involves human involvement in variable selection to produce a decently functioning system. Due to the large number of signals and generators that need to be inspected, human activity must be restricted. It is common for many operations to apply artificial intelligence approaches (learning capacity), and SIMAP and MARS are two of the most recent sophisticated technology that employs this strategy (MAS). There are two ways to create SCADA information typical behavioral models using artificial neural networks [27]. Such a NN design approach is often pursued, with the creation and demonstration of NN's exceptional efficiency in this scenario being one of the most common examples. Wind farm drive train parts were tracked using neural networks (NNs) in prior investigations in [28].

In [29], it is suggested that additional research be conducted on the impacts of duration, deterioration, and failure predicting, as well as anomaly identification on the state tracking of such a specific section of WT (generating heat). In addition, regression techniques are used to develop a polynomial framework for predicting the generation of heat. The system's input variables are generated output and additional variables created by integrating generator ambient temperatures (AT), nacelle temperatures (NT), and coolant temperature. By using its descriptive language, the system is used to improve total power generation while also providing an empirical basis for managing a single subassembly. A later version of the system will incorporate enhancements to allow its use in real-world WT scenarios that may include varying environmental conditions. While considering the ninth-degree polynomials, the energy curve of a WT is often the primary focus of research publications in this area that use descriptive modeling. However, most of the descriptive modeling for WTs are in research centers upon endurance, fault detection, and deterioration of the devices. As a result of the failure of the dataset or simulations, proportionate hazard modeling (PHM) was employed in this scenario. Diagnostics rely heavily on the usage of PHMs, a sort of failure model [30]. Covariates and a baseline are the two main components of this typical design.

3. System Model

To evaluate a WT's current and comprehensive health status, the healthcare state tracking alerts if the established health state signal deviates from expected regular healthcare circumstances. As a result, the system's application can be characterized as precautionary actions necessary to ensure a successful performance. Such a paper suggests a method for developing a parameterized health situation surveillance design (like a usual behavioral concept) that monitors the WT's actual time as well as actual health situation via its subassemblies but also elevates an aware flag when such WT's ailment deviates from the anticipated normal situation. To achieve that, NN modeling will be first built for every characteristic under consideration (GT, RS, and GWT). The deviating signal is then recovered, and that is responsive to variations in the healthy state of every characteristic. Next, using these signals, a parameterization model with such a PHM-based shape for every one of the characteristics is created. Depending upon the effectiveness of such NN and PHM-based modeling, such produced designs having PHM aspects are integrated to generate the ultimate incremental parameterized health state modeling of such WT. This final design is utilized to evaluate the WT's entire condition in actual time, providing support to the controller and assets administration group in improving performance and servicing schedule.

The HMS created in this study seeks to recognize features and structures in SCADA information, in addition, to anticipating potential problems, allowing wind farm operators sufficient time to adjust servicing schedules or undertake other precautions to avoid unplanned hardware failure. For it though, 10 minutes averaging SCADA information that are routinely accessible to controllers are employed. Figure 1 depicts the basic structure of such HMS that was created. The functions of the various HMS units (see Figure 1) are discussed here.

3.1. Training Module. When modeling is still not accessible or further learning is necessary, the typical behavior modeling is learned within the learning program. If an element is changed as well as the signaling relationships alter as a result, the converse is accurate. The dataset is normalized before building the models using the methods provided, which comprises a validation checking, a dataset ranging check, and absent data analysis, as well as latency elimination. Various training stages are provided in the learning program to enable quick evaluation. Over one month of continuous practical data collecting, the initial model development is undertaken. If three, six, and following nine months additional information is collected, more workouts are conducted. The developed ANFIS system and standardized criteria designating the typical operating region of wind

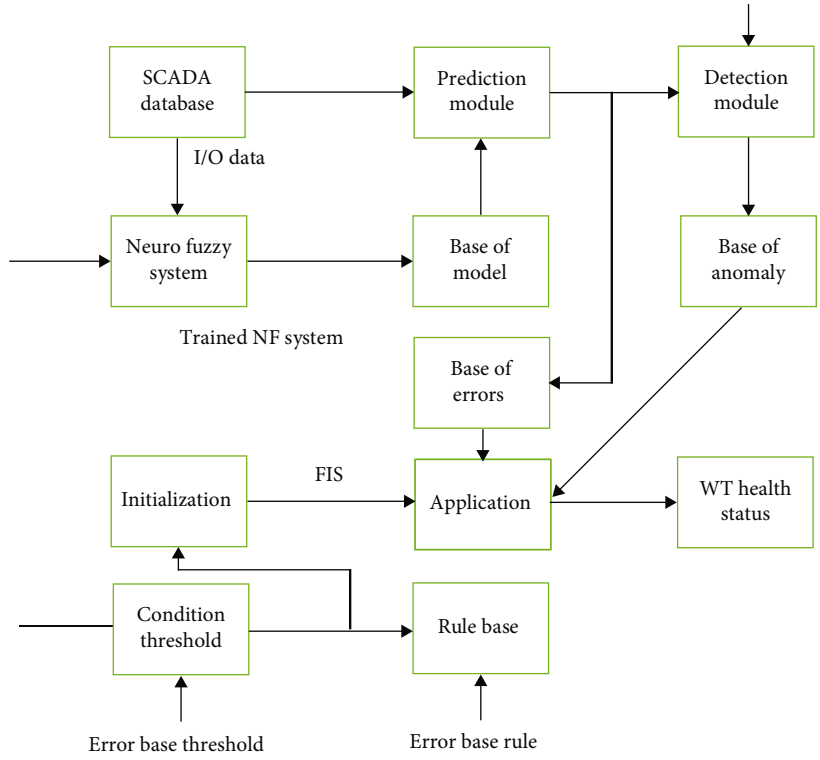

Figure 1: The proposed health management systems (HMS).

generators utilizing the estimation inaccuracy are the outputs of such a learning program.

3.2. Prediction Module. When one training modeling of the sampled signal is accessible on a modeling basis, the forecasting unit becomes operational. The predicted inaccuracy is computed and saved using the created normal behavioral framework.

3.3. Anomaly Recognition Module. Discrepancies in forecast mistakes are found in this section. This will be done using the learning module's calculated normal behavior criteria but rather expert-defined parameters. The result is an anomalous matrix with data on the incidence but also the date of incidence and the present anomaly's period on weekdays.

3.4. Initializing Module for Fuzzy Experts. Number of intakes and outlets, and also respective MFs, are initialized as in FIS frameworks utilized for anomaly detection and element conditional assertions. Every element that needs to be checked will have its unique FIS, whereas the inputs vary depending on the element or system being investigated, and every FIS architecture includes the corresponding output data: diagnostic (details regarding the signal's aberrant activity) state possible root causes.

3.5. Fuzzy Expert Application Module. Using the forecasting failures and data about current abnormalities, the updated FIS architecture is assessed within that component. The result is saved in a textual form then displayed to provide the analyzer with a complete picture of such turbine's state.

NN has been made up of neurons, whose parameters are interpolated among the input parameters as well as the targeted variable via an optimizing process (e.g., gradient of weighted conjugates). For ordinary behavioral analysis of GT, GWT, and RS impulses, a multilayered perceptron feed-forward neural network will be used in this paper. Among the inlet and outlet nodes, it has a unique architecture wherein one or more buried tiers with various counts of neurons occur. Furthermore, the architecture lacks interaction between tiers and neurons, allowing data to pass simply from the source to the destination tier.

$$\begin{aligned} V &= \{v_1, v_2, \cdots, v_n\}, \\ \mathrm{AF}_1 &= f_1\left(w_i^h v_i^{\mathrm{in}} + b^h\right), \\ \mathrm{AF}_2 &= f_2\left(w_i^o v_i^h + b^o\right). \end{aligned} \tag{1}$$

Every layer's result gets computed using the V transferring functional (or activating function) as well as input variables. Biased variables in the export layer, bias variables in the buried layer, activating functional of the buried layer, and activating functions of the exit layer are represented by b^o, b^h, and AF_1 as well as AF_2, correspondingly. Because this research has two levels, two transferring equations are used. The first transferring functional (f_1) predicts the buried layer's results as well as is specified like a sigmoid functional

of hyperbolic tangential pattern, as shown below.

$$f_1\left(w_i^h v_i^{\text{in}} + b^h\right) = \frac{2}{1 + e^{-2\left(w_i^h v_i^{\text{in}} + b^h\right)}} - 1. \quad (2)$$

Transferring functional 2 (f_2) determines the exit layer's result and is described as a sequential transferring function, as shown below.

$$f_2\left(w_i^o v_i^h + b^o\right) = w_i^o v_i^h + b^o. \quad (3)$$

The performing metric, that is employed in learning, seems to be the summation of squared erroneous (SSE). A guided training approach called scaling conjugated gradients is used to build the NN. This approach analyses the incoming dataset then adjusts its NN's values and impairments to reduce SSE.

$$\text{SSE} = \sum_{j=1}^{n} \left(O_j - O_j^{`}\right)^2, \quad (4)$$

in which O_j is the predicted value while $O_j^{`}$ is the result of NN across n incoming data sets. The NNs' correctness is determined using a linear extrapolation among the NN result as well as the destination parameters, with the highest attainable efficiency of 100%.

3.5.1. Preprocessing. The information set utilized in the suggested approach comes from such a WT that did not have any notable failures or anomalies over one year. Erroneous data sets must be cleaned out to format such data for examination. Four filters are being created and implemented for such an objective. Filter tries to replace not-a-number (NaN) results with such an averaging value created as from NaN point's following and preceding accessible data sources. Every WT variable has such a realistic and established limit, while data sets outside of such limits are filtered out. (e.g., AP was found to be negative). It is worth noting that such filters are however implemented to produce clear information for the systems in mind. Moreover, because the WT behaved normally, the results cannot go beyond a confidence level. For example, to be labeled unusual, two of three successive data values have to be beyond a set range. Filter incorporates this under account using power-curve measurements, while filter adjusts and adjusts every variable in a defined limit now at a conclusion.

The sources are however verified to ensure that such recorded values for every parameter approximate the dispersion of such optimum values. It stops the system from producing an output based on uncertain input data, which helps to reduce the model's inaccuracy. Modeling for characteristics using NN, these NN types are created in this stage to imitate the typical functioning of GWT and GT, as well as RS. This NN for such three NN types seems to be a multilayered perceptron feed-forward having the architecture of one concealed layer having 50 neurons and also one convolution layer. The AP, NT, and AP-1, as well as AP-2 along with the matching GT as well as GWT predictor parameter, represent the inputs to NNGT as well as NNGWT. AP-1, as well as AP-2, is still the A*P* values obtained from the two preceding periods. The purpose of including such two factors is to look at the effect of the previous action on ongoing operations. The WS, as well as AP, seems to be the NNRS's sources, having RS as the objective parameter. A year's worth of information (37,000 measuring values) averaging at 10-minute intervals was arbitrarily split into 70 percent, 15%, and 15% for learning, testing, and verification, correspondingly.

The "randomized" sample method was selected since it ensures that every collected data is similarly likely, such that 70 observations are picked for learning, 15 for tests, as well as 15 for verification out of each 100 observations. Even though it may lessen some relationships among some associated activity moments in duration, it has proven to become the most effective method. When "block-type" but rather "time-dependent" sample strategies are used, for example, they directly split specific intervals and limit the system from learning as many potential structures as feasible, which constitutes a disadvantage. The studies are being conducted to prevent several of the challenges that come with interacting using NNs, like overfitting.

As a result, the system is only allowed after every testing, whereas if changes in efficiency among the "learning," "testing," and "verification" data points are lower than 0.1 percent. As a result, just one graph reflects the entire dataset, like all three charts (learning, tests, and verification) are identical with 0.1 percent error, as shown in Figure 2. Instead, the modeling will be modified since this requirement is satisfied. Similarly, this knowledge is gained through running numerous tests and examining the model's results. After applying this requirement, the aggregate defect rates for every NN system are calculated by averaging the prediction error from the three databases. Furthermore, when a subassembly gets removed or the element is significantly modified, a separate NN system must be developed.

For highlighting and explaining the suggested parameterized model's characteristics, the established parameterized health state concept will be of relevance in a variety of ways, including how it handles many of the existing issues identified in such a current research review. It must be noted that such a paper proposes a way for modeling health conditions, and the generated model's parameterized shape will be a big characteristic. Furthermore, all studies are conducted by observing normal performance, which can mitigate against the absence of failing facts in the environment. The system excels in the below aspects, which can be investigated deeper in subsequent research:

3.5.2. Adaptability. Because most of the modeling deployed thus yet are dependent upon NNs, there seems to be a difficulty with adaptation, as NN-based estimates of specific WTs will not be used alternately. A modeling approach, on the other hand, has the benefit of being able to change the variables and reuse the prototype for different WT. In addition, to verify the improved variables, more research will be required.

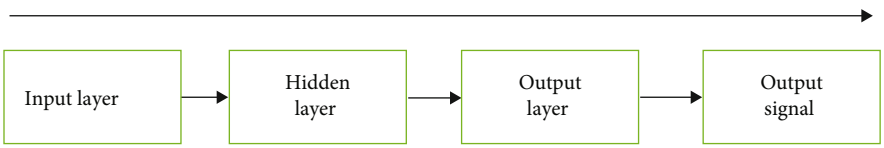

Figure 2: Structure of multilayer neural networks.

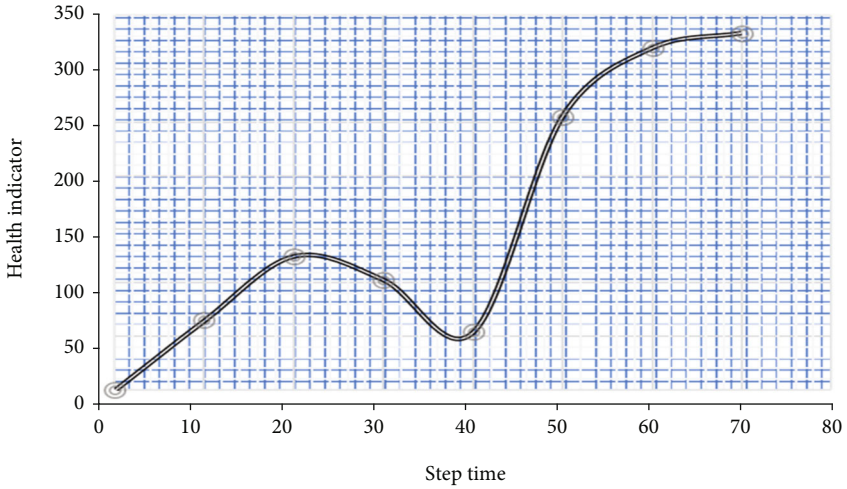

Figure 3: Performance of the health indicator of the wind turbine.

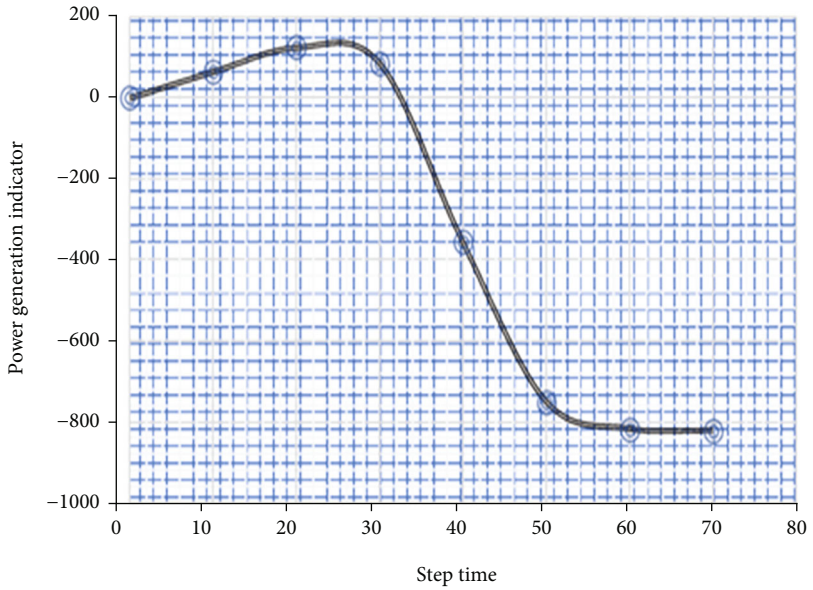

Figure 4: Performance of the power degradation indicator of the wind turbine.

3.5.3. Scalability. Developing unique NN modeling for every WT in such a wind turbine having a huge minority of WTs, in which the commonalities among simulations will not be simply studied, is a challenge for the field administrator and controller. One such research can be carried out using the suggested concept, and contrasts of simulations among a low minority of WTs will lead to a generic concept for such farmland. Evaluation of the residual usable lifetime is as follows: the parameterized approach presented herein will be for a one-year study span in which the WT does not experience any significant anomalies. This means the actual behavioral and modeling will be utilized like a guide. The effectiveness of every year can then be contrasted to such figures. An alternative perspective, a comparable simulation for every year, will be built, with correlations between the variables of the simulations potentially yielding insights on the deterioration matter. Certainly, it can lead to improvements in operational planning.

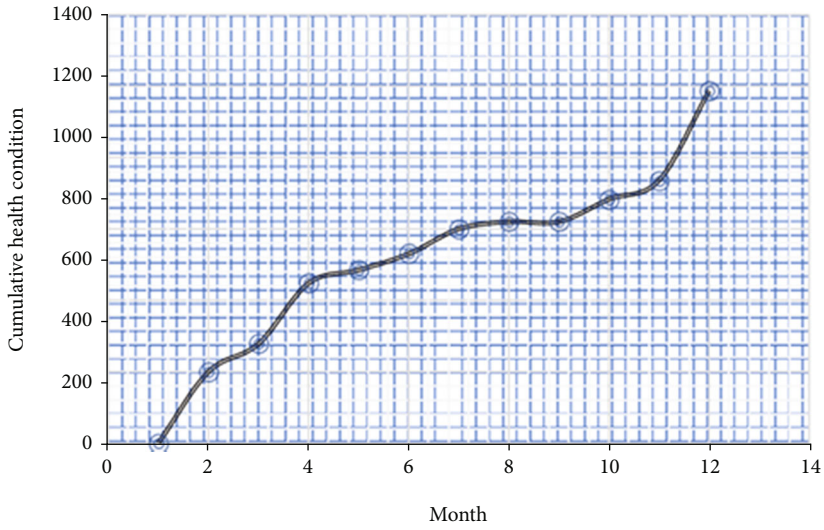

Figure 5: Cumulative health condition indicator of the wind turbine.

4. Results and Discussion

Neuronetworking simulators can be used in the proposed model to test the wind generator's proposed modeling for healthcare purposes. The suggested health monitoring systems make advantage of all available fuel efficiency parameters. Certain health markers change because of the aberrant operation of the wind farm generating systems. There was a 72-hour period in which wind speed and energy data from the wind farm SCADA were compared and evaluated using three state wellness indicators based on data linkages. The results of such investigations are depicted in Figures 3 and 4. The three wellness indices changed drastically after 40 hours, indicating that the status of these wind farm generator systems was unique.

A standardized dataset correlation model was developed based on SCADA information acquired during the ordinary operation of a wind farm on its first day of operation. The following is the relationship between wind velocity and energy data, as demonstrated using wind velocity and energy statistics as an example:

$$P_{\text{std}}(v) = 5316.85 - 2618.04v + 403.17v^2 - 17.34v^3. \quad (5)$$

The changing regulation of wind farm generator operational health indicator is generated by setting the window wide to 24 hours as well as the window increments to 1 hour.

The changing regulation of the operational health indicator of a wind farm generator is generated by setting the window width to 24 hours, and the window increments to one hour. Figure 5 displays a graphical representation of the cumulative development of health state following administration of the F. Various confidence range degrees are investigated for such Y, and the 99 percent confidence gap produced the best results in terms of accurately matching the genuine fluctuations as well as the input information. It should be noted that such a case study based on the proposed HCWT concept was generated with information that was free of significant anomalies, which should be noted.

5. Conclusions

This paper that is proposed a neurofuzzy modeling to check the dynamic health state of the wind turbines through typical behavioral characteristic is obtained from discrepancy real-time signal of the wind generator. The neural network can be utilized for state tracking and anomaly identification, an incremental approach built inside healthcare state modeling which recognizes state changes as in WT's action. The proposed system seems to have a simple design having a minimal set of variables, as well as it has been validated by evaluating real and synthetic information. Fuzzy logic can naturally handle available expertise information regarding anomaly/prediction mistake pattern analysis and underlying causes identification. Once criteria are specified, automatic fault diagnosis becomes possible. Hence, the accuracy rate, is contingent on the availability of varied SCADA signals, is addressed. Such requirement is frequently met, allowing the proposed system is applied to both current and newer rotors. Therefore, it has identified current problems in SCADA data and gives broad status and diagnosis remarks. Furthermore, the proposed model is implemented in the authorized private wind power plant to study practical circumstance facing by the wind generator.

Data Availability

The data used to support the findings of this study are available from the corresponding author upon request.

Conflicts of Interest

The authors declare that they have no conflict of interest.

Authors' Contributions

All authors have equal contribution.

References

[1] International Energy Agency, "Offshore wind outlook 2019," *World Energy Outlook Special Report*, International Energy Agency, 2019.

[2] International Renewable Energy Agency, "Future of Wind: Deployment, Investment, Technology," *Grid Integration and Socio-Economic Aspects*, 2019.

[3] K. Freeman, C. Frost, G. Hundleby et al., "Our energy, our future," *How offshore wind will help Europe go carbon-neutral*, 2019, WIND Europe.

[4] Z. Song, Z. Zhang, Y. Jiang, and J. Zhu, "Wind turbine health state monitoring based on a Bayesian data-driven approach," *Renewable Energy*, vol. 125, no. 960-1481, pp. 172–181, 2018.

[5] X. An, H. Zeng, W. Yang, and X. An, "Fault diagnosis of a wind turbine rolling bearing using adaptive local iterative filtering and singular value decomposition," *Transactions of the Institute of Measurement and Control*, vol. 39, no. 11, pp. 1643–1648, 2017.

[6] W. Yang, C. Liu, and D. Jiang, "An unsupervised spatiotemporal graphical modeling approach for wind turbine condition monitoring," *Renewable Energy*, vol. 127, no. 960-1481, pp. 230–241, 2018.

[7] M. Deveci, U. Cali, S. Kucuksari, and N. Erdogan, "Interval type-2 fuzzy sets based multi-criteria decision-making model for offshore wind farm development in Ireland," *Energy*, vol. 198, article 117317, 2020.

[8] M. Abdel-Basset, A. Gamal, R. Chakrabortty, and M. Ryan, "A new hybrid multi-criteria decision-making approach for location selection of sustainable offshore wind energy stations: a case study," *Journal of Cleaner Production*, vol. 280, article 124462, 2021.

[9] H. Niemann, N. Kjølstad Poulsen, M. Mirzaei, and L. C. Henriksen, "Fault diagnosis and condition monitoring of wind turbines," *International Journal of Adaptive Control and Signal Processing*, vol. 32, no. 4, pp. 586–613, 2018.

[10] H. D. M. De Azevedo, A. M. Araujo, and N. Bouchonneau, "A review of wind turbine bearing condition monitoring: state of the art and challenges," *Renewable and Sustainable Energy Reviews*, vol. 56, pp. 368–379, 2016.

[11] Q. Liu, Y. Sun, and M. Wu, "Decision-making methodologies in offshore wind power investments: a review," *Journal of Cleaner Production*, vol. 295, article 126459, 2021.

[12] M. Argin, V. Yerci, N. Erdogan, S. Kucuksari, and U. Cali, "Exploring the offshore wind energy potential of Turkey based on multi-criteria site selection," *Energy Strategy Reviews*, vol. 23, pp. 33–46, 2019.

[13] M. Deveci, E. Ozcan, R. John, D. Pamucar, and H. Karaman, "Offshore wind farm site selection using interval rough numbers based best- worst method and MARCOS," *Applied Soft Computing*, vol. 109, article 107532, 2021.

[14] M. Deveci, E. Ozcan, R. John, C.-F. Covrig, and D. Pamucar, "A study on offshore wind farm siting criteria using a novel interval-valued fuzzy-rough based Delphi method," *Journal of Environmental Management*, vol. 270, article 110916, 2020.

[15] K. Ullah, "Picture fuzzy Maclaurin symmetric mean operators and their applications in solving multiattribute decision-making problems," *Mathematical Problems in Engineering*, vol. 2021, Article ID 1098631, 13 pages, 2021.

[16] A. Martinez and G. Iglesias, "Multi-parameter analysis and mapping of the levelised cost of energy from floating offshore wind in the Mediterranean Sea," *Energy Conversion and Management*, vol. 243, article 114416, 2021.

[17] C. Kheirabadi and R. Nagamune, "A quantitative review of wind farm control with the objective of wind farm power maximization," *Journal of Wind Engineering and Industrial Aerodynamics*, vol. 192, pp. 45–73, 2019.

[18] R. B. Randall, *Vibration-Based Condition Monitoring*, Wiley, Chichester, West Susssex, UK, 2011.

[19] W. Yang and J. Jiang, "Wind turbine condition monitoring and reliability analysis by SCADA information," in *2011 Second International Conference on Mechanic Automation and Control Engineering*, pp. 1872–1875, Hohhot, 2011.

[20] L. Kusiak and W. Li, "The prediction and diagnosis of wind turbine faults," *Renewable Energy*, vol. 36, no. 1, pp. 16–23, 2011.

[21] M. Schlechtingen and I. F. Santos, "Comparative analysis of neural network and regression based condition monitoring approaches for wind turbine fault detection," *Mechanical Systems and Signal Processing*, vol. 25, no. 5, pp. 1849–1875, 2011.

[22] M. Süttmann, "Master thesis: condition monitoring in wind turbines – a drive train monitoring System," 2010.

[23] K. B. Abdusamad, D. W. Gao, and E. Muljadi, "A condition monitoring system for wind turbine generator temperature by applying multiple linear regression model," in *2013 North American Power Symposium (NAPS)*, Manhattan, KS, USA, 2013.

[24] P. M. Gebraad, F. W. Teeuwisse, J. W. van Wingerden et al., "A data-driven model for wind plant power optimization by yaw control," in *2014 American Control Conference*, Portland, OR, USA, 2014.

[25] P. M. O. Gebraad, F. W. Teeuwisse, J. W. van Wingerden et al., "Wind plant power optimization through yaw control using a parametric model for wake effects—a CFD simulation study," *Wind Energy*, vol. 19, no. 1, pp. 95–114, 2016.

[26] E. M. Carlini, A. Ianniciello, C. Pisani, A. Vaccaro, and D. Villacci, "An optimised methodology to predict the wind farms production," in *2015 International Conference on Clean Electrical Power (ICCEP)*, Taormina, Italy, 2015.

[27] H. Louie and J. M. Sloughter, "Probabilistic modeling and statistical characteristics of aggregate wind power," in *Large Scale Renewable Power Generation*, H. Louie and J. M. Sloughter, Eds., pp. 19–51, Springer, Singapore, 2014.

[28] M. Lydia, S. S. Kumar, and A. I. Selvakumar, "Condition based maintenance optimization for multi-component systems using proportional hazards model," *Reliability Engineering & System Safety*, vol. 96, no. 5, pp. 581–589, 2011.

[29] R. Moghaddass and C. Rudin, "The latent state hazard model, with application to wind turbine reliability," *The Annals of Applied Statistics*, vol. 9, no. 4, pp. 1823–1863, 2015.

[30] U. Leturiondo, O. Salgado, and D. Galar, "Estimation of the reliability of rolling element bearings using a synthetic failure rate," in *Current Trends in Reliability, Availability, Maintain Ability and Safety*, U. Kumar, A. Ahmadi, and A. Verma, Eds., pp. 99–112, Springer, Cham, 2015.

Hindawi
Computational and Mathematical Methods in Medicine
Volume 2023, Article ID 9795242, 1 page
https://doi.org/10.1155/2023/9795242

Retraction

Retracted: A Three-Dimensional Cement Quantification Method for Decision Prediction of Vertebral Recompression after Vertebroplasty

Computational and Mathematical Methods in Medicine

Received 3 October 2023; Accepted 3 October 2023; Published 4 October 2023

This article has been retracted by Hindawi following an investigation undertaken by the publisher [1]. This investigation has uncovered evidence of one or more of the following indicators of systematic manipulation of the publication process:

(1) Discrepancies in scope

(2) Discrepancies in the description of the research reported

(3) Discrepancies between the availability of data and the research described

(4) Inappropriate citations

(5) Incoherent, meaningless and/or irrelevant content included in the article

(6) Peer-review manipulation

The presence of these indicators undermines our confidence in the integrity of the article's content and we cannot, therefore, vouch for its reliability. Please note that this notice is intended solely to alert readers that the content of this article is unreliable. We have not investigated whether authors were aware of or involved in the systematic manipulation of the publication process.

Wiley and Hindawi regrets that the usual quality checks did not identify these issues before publication and have since put additional measures in place to safeguard research integrity.

We wish to credit our own Research Integrity and Research Publishing teams and anonymous and named external researchers and research integrity experts for contributing to this investigation.

The corresponding author, as the representative of all authors, has been given the opportunity to register their agreement or disagreement to this retraction. We have kept a record of any response received.

References

[1] Y. Zhang, T. Zhang, X. Ge et al., "A Three-Dimensional Cement Quantification Method for Decision Prediction of Vertebral Recompression after Vertebroplasty," *Computational and Mathematical Methods in Medicine*, vol. 2022, Article ID 2330472, 14 pages, 2022.

Hindawi
Computational and Mathematical Methods in Medicine
Volume 2022, Article ID 2330472, 14 pages
https://doi.org/10.1155/2022/2330472

Research Article

A Three-Dimensional Cement Quantification Method for Decision Prediction of Vertebral Recompression after Vertebroplasty

Yanming Zhang,[1] Tao Zhang,[2] Xiang Ge,[3] Yong Ma,[4] Zhenduo Cui,[1] Shuilin Wu,[1] Yanqin Liang,[1] Shengli Zhu,[1] and Zhaoyang Li[1]

[1]*Tianjin Key Laboratory of Composite and Functional Materials, School of Materials Science and Engineering, Tianjin University, Tianjin 300350, China*
[2]*Department of Orthopedic Surgery, Tianjin First Central Hospital, Tianjin 300190, China*
[3]*Key Laboratory of Mechanism Theory and Equipment Design of Ministry of Education, School of Mechanical Engineering, Tianjin University, Tianjin 300354, China*
[4]*Pain Department, The Third People's Hospital of Yunnan Province, Kunming 650010, China*

Correspondence should be addressed to Zhaoyang Li; zyli@tju.edu.cn

Received 15 March 2022; Accepted 25 April 2022; Published 12 May 2022

Academic Editor: Plácido R. Pinheiro

Objective. Proposing parameters to quantify cement distribution and increasing accuracy for decision prediction of vertebroplasty postoperative complication. *Methods*. Finite element analysis was used to biomechanically assess vertebral mechanics ($n = 51$) after percutaneous vertebroplasty (PVP) or kyphoplasty (PKP). The vertebral space was divided into 27 portions. The numbers of cement occupied portions and numbers of cement-endplate contact portions were defined as overall distribution number (oDN) and overall endplate contact number (oEP), respectively. And cement distribution was parametrized by oDN and oEP. The determination coefficients of vertebral mechanics and parameters (R^2) can validate the correlation of proposed parameters with vertebral mechanics. *Results*. oDN and oEP were mainly correlated with failure load ($R^2 = 0.729$) and stiffness ($R^2 = 0.684$), respectively. oDN, oEP, failure load, and stiffness had obvious difference between the PVP group and the PKP group ($P < 0.05$). The regional endplate contact number in the front column is most correlated with vertebral stiffness ($R^2 = 0.59$) among all regional parameters. Cement volume and volume fraction are not dominant factors of vertebral augmentation, and they are not suitable for postoperative fracture risk prediction. *Conclusions*. Proposed parameters with high correlation on vertebral mechanics are promising for clinical utility. The oDN and oEP can strongly affect augmented vertebral mechanics thus is suitable for postoperative fracture risk prediction. The parameters are beneficial for decision-making process of revision surgery necessity. Parametrized methods are also favorable for surgeon's preoperative planning. The methods can be inspirational for clinical image recognition development and auxiliary diagnosis.

1. Introduction

Osteoporosis compression vertebral fracture (OCVF) is a compression fracture of a single vertebral body or multiple vertebral bodies caused by a reduction in bone mineral density (BMD). It can lead to back pain, spinal deformity, decreased mobility in older people [1], and higher risk of age-adjusted mortality [2], all of which increase public health pressure. In most cases, percutaneous vertebroplasty (PVP) or kyphoplasty (PKP) is used to stabilize the wounded vertebrae to prevent further damage [3]. This kind of minimally invasive surgery improves the quality of life of patients with an OCVF by prompting pain reduction and mobility restoration [4]. Cemented vertebral failure can cause many complications, and research found that different cement distributions and volumetric factors greatly determine vertebral

mechanical stability and appearance of complications [5]. The cement distribution can largely affect the prediction on risk of vertebral recompression and decisions on revision surgery of poorly augmented vertebrae.

Volumetric factors were proposed to quantify the intravertebral cement distribution and evaluate the effect on vertebroplasty complications, such as intravertebral cement volume (CV), cement height in X-ray slices, cement morphology, and volume fraction [6–8]. Volume fraction (VF) is defined as the fraction of intravertebral cement volume to vertebral body volume and is meant to quantify the extent of cement filling given differences in vertebral size. Although these two risk factors can parametrically quantify the amount of cement, conflicting results on these factors have been presented in several studies [9, 10].

Research has shown that uneven mechanical support from the cement decreases the strength of augmented vertebrae [11, 12]. The compactness of cement is one of the risk factors that describes the cement distribution morphology, which is usually determined by X-ray or CT slices. In this case, the cement compactness was simply divided into lump and interdigitated types. The lump distribution pattern has been found to be a harmful distribution for augmented vertebrae. Since under this situation, the vertebrae are more easily to collapse again [6, 7]. Some clinical studies were conducted to parametrize cement morphology, suggesting that a more extensive and interdigitated distribution would increase the recuperative rate from OCVFs [8, 13, 14]. The obvious disadvantage of compactness factors is that two categories cannot parametrically parametrize the distribution cement. Also, the morphological information in two-dimension X-ray slices is difficult to replicate. Thus, the numerical relationship between three-dimensional cement distribution with vertebral mechanics remains unclear, and a new method for parametrizing the cement distribution is needed.

Patient-specific multidetector computational tomography- (MDCT-) based finite element analysis (FEA) is a promising tool for assessing clinically relevant parameters. For vertebroplasty, some homogeneous FEA research has studied different injection volumes, cement modulus, cement-endplate contacts, and so on [15, 16]. For kyphoplasty, a study of the placement and symmetry of cement clouds [11], the author stated that the symmetric distribution of cement clouds is favorable. Several heterogeneous nonlinear FEA studies have been conducted to understand the mechanical effect of using various modulus of cement. A time-lapse microcomputed tomography (μ-CT) FEA study showed that the VF% was related to the stiffness gain percentage [17]. Chevalier et al. [15] found that different cement-endplate contact modes can dominate the stiffening and strengthening effects of augmentation. Excluding the research above, FEA studies focused on how cement morphology parametrically affects cemented vertebral mechanics are rare. On the other hand, it lacks a substantial quantification method to evaluate the augmentation. Parameters that correlate well with augmented vertebral mechanics are needed.

Table 1: Statistical review of patients' augmented levels.

PVP ($n = 24$)		PKP ($n = 27$)	
Levels	Numbers	Levels	Numbers
T10	0	T10	1
T11	3	T11	6
T12	9	T12	7
L1	4	L1	6
L2	5	L2	4
L3	2	L3	0
L4	1	L4	3

This study is aimed at investigating and parametrizing different cement distribution modes. Correlated well with failure risk of cemented vertebrae, these parameters can be utilized as efficient postoperative evaluating scales like other clinic postoperative risk factors, such as VAS score, kyphotic restoration, and vertebral height restoration. Thus, it should be used as reference on decision-making of early revision surgery. Patient-specific FEA testing was used to assess mechanical properties of cemented vertebrae. By dividing intravertebral space into 27 portions (cubes) according to vertebral anatomy, the cement morphology and distribution inside vertebrae were parametrized. Regression studies revealed parameters that correlated well with vertebral mechanics. Different types of cement were also evaluated in this study.

2. Materials and Methods

2.1. Data Collection. The MDCT datasets of patients with OCVF who underwent vertebroplasty were collected from local clinics between April 2017 and December 2020. Data collection was performed under the supervision of a clinical ethical committee, and all datasets were anonymized to protect privacy. The MDCT scans were taken by a Siemens Somatom Definition AS scanner (Siemens, Malvern, PA), with 120 kVp tube voltage, 210 mA current, 0.4 mm pixel size, and 1 mm slice thickness. The reconstruction kernel was set as the standard (B30S).

The inclusion criteria for collection were as follows: (1) single or multiple vertebral levels between T10 and L4 in patients diagnosed with OCVFs who underwent PKP or PVP; (2) OVCFs without damaged vertebral posterior walls, nerve lesions, or intravertebral clefts (IVCs); and (3) clear visualization of cement cloud in digital imaging and communications in medicine (DICOM) sets. The exclusion criteria for collection were as follows: (1) severe cement leakage to the adjacent levels or spinal cord compression; (2) complete burst fracture at the cemented level due to its integrity that was not eligible for building a regular FEA model; and (3) vertebrae with posterior fixation constructs. A total of 51 vertebrae from 39 patients were eligible for inclusion and were investigated in the following study (Table 1).

2.2. Heterogeneous Finite Element Model Development. The workflow of model development is depicted in Figure 1. Briefly, MDCT data were imported into medical 3D reconstruction software Mimics (Materialise NV, Harislee, Belgium) to

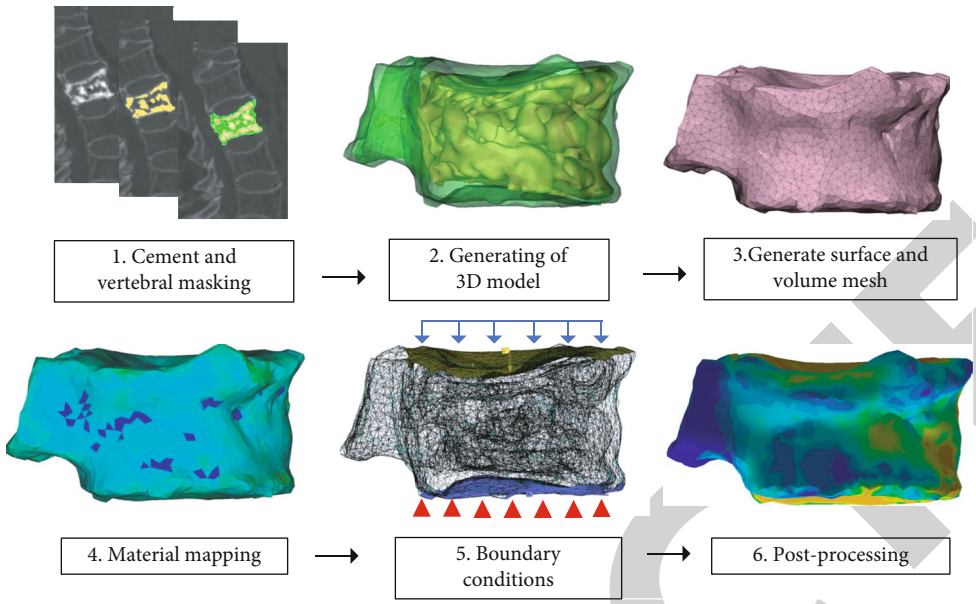

Figure 1: Overall flow chart of the imaging process and postvertebroplasty FEA model development. The boundary condition is imposed in step 5, blue arrows represent displacement compression, and red triangles represent fixation. Displacement was set at increments of 0.033 mm.

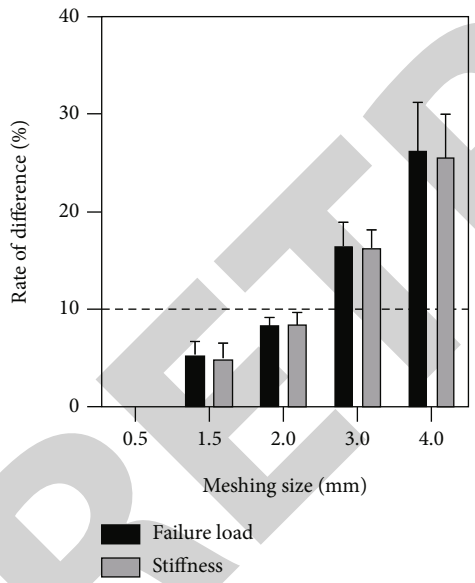

Figure 2: FEA mesh sensitivity validation. The rate of difference in mesh sizes was calculated by the mechanical difference of a 0.5 mm mesh size model.

perform level segmentation and bone reconstruction, and masks of vertebrae and radiopaque bone cement were generated separately. The posterior ligamentous complex (PLC), pedicle, vertebral arch, transverse process, and articular process were erased in this phase to reduce computational efforts. After masking and model generation, the STL model of cement and vertebrae was exported to preprocessing software 3-Matic (Materialise NV, Harislee, Belgium) to generate mesh. According to Anitha et al. [18], thoracolumbar vertebra MDCT-FEA is acceptable for meshing with sensitivity errors decreasing to less than 10%. After the validation of meshing quality sensitivity on three random models within criteria (Figure 2), the volume mesh size of this study was set to a maximum 2 mm for both vertebrae and cement, and the overall volume mesh element type was set as tetrahedral C3D10.

The HU to element mechanical property conversion equation is listed in Table 2. The conversion of HU to apparent density (ρ, g/cm^3) was performed according to previous FEA literature [19, 20]. The shift from elastic to postyield mechanical behavior of bone and cement was defined as bilinear isotropic hardening. Elastic modulus (E, MPa) was converted from apparent density according to Keller [21], and yield stress (S, MPa) was obtained from apparent density according to Morgan and Keveany [22]. The postyield modulus (E_{py}, MPa) of the bilinear isotropic hardening model was set as 5% element elastic modulus [22]. Although the retrospective study was unable to collect an adequate number of quantitative computed tomography (QCT) scanned DICOM files that were in line with the calibration phantom, some phantom-less heterogeneous FEA suggested that with consistent scanner and scanning parameter, the mechanical results were identical with phantom calibrated one [23, 24]. The regression test in our study only requires accuracy of relative bone mechanics (the difference of mechanical properties between different vertebrae samples), and our DICOM data was obtained from consistent CT scanner with consistent parameters throughout the scan, such as KVP, X-ray tube current, reconstruction kernel, and pixel size. This was sufficient to run the regression and other test in our study.

Moreover, this study also examined the mechanical behavior changes between 4 different homogeneous cement types. The elastic-perfect plastic model was assigned for

Table 2: Material property relations adopted from the literature.

Parameters	Mathematical relationship	References
Apparent density (g/cm^3)	$\rho = 0.001 \times (1.3465 + 0.945\text{HU})$	Mazlan et al. [19] [20]
Elastic modulus (MPa)	$E = 757 \times \rho^{1.94}$	Keller [21]
Yield stress (MPa)	$S = 21.7 \times \rho^{1.52}$	Morgan and Keaveny [22]
Postyield modulus (MPa)	$E_{\text{py}} = 0.05 \times 757 \times \rho^{1.94}$	Morgan and Keaveny [22]
Poisson ratio	0.3	

Table 3: Material properties of homogeneous bilinear bone cements adopted from the literature.

Types of cement	Young's modulus (GPa)	Strength (MPa)	References
Cement type A (low modulus PMMA)	1.5	85	Robo et al. [25]
Cement type B (medium modulus PMMA)	2.5	90	Wekwejt et al. [26]
Cement type C (high modulus PMMA)	3.5	95	López et al. [27]
Cement type D (calcium phosphate cement)	0.5	10	Palmer et al. [28]; Liu et al. [29]

cement. Cement strength and Young's modulus were adopted from literature in Table 3. The volume mesh file and material-to-element cross-reference file were fed to ANSYS workbench 19.0 (Ansys, Pennsylvania, USA).

2.3. Boundary Conditions and Convergence. Single vertebral uniaxial compression has been adopted in many studies, both in FEA and in vitro biomechanical tests [30–32]. A displacement load was applied to the upper endplate, as shown in Figure 1, to simulate uniaxial compression in a direction vertical to the lower endplate [33], and no degree of freedom was constrained. The step controls were defined by substeps. And the initial substeps were set as 30. The maximum substeps were set at 100. A fixed support was assigned at the lower endplate for complete constraint, and the reaction force of the fixed lower endplate was recorded while the displacement of the upper endplate continues (Figure 1). The failure load was defined as the resultant axial reaction force at compressive displacement of cranial endplate equal to 1.9% of minimum distance of two endplates [34], and stiffness was estimated as the slope of the linear range in force-displacement curves. The working environment was Ansys Mechanical APDL (ANSYS® Academic Research, Release 19.0, Pennsylvania, USA).

2.4. Quantification of Cement Distribution

(1) Quantification of cement distribution extensiveness

To quantify the overall cement distribution, this study developed a stand-alone parameter called the distribution number (DN), which is independent of the cement volume (CV) and the cement volume fraction (VF%). Briefly, the 3D reconstructed vertebrae and cement cloud were divided into 27 portions (cubes) in three anatomic planes according to the vertebral anatomical structure by 6 splitting surfaces (Figure 3). Two coronal splitting surfaces were parallel to the spinous process, which were located on intersection of pedicles and vertebral foramen. Two sagittal splitting surfaces were placed in third of coronal splitting surfaces. The axial splitting surfaces were placed in third of vertebral front and posterior heights. The number of cement-occupied cubes was noted as the overall distribution number (oDN). To prevent invalid occupation in cubes, cement contact with three or more cube walls or cortical bone is certified as cement occupation within the cube.

(2) Quantification of endplate contact

The number of cement cubes touched the endplate was defined as the overall endplate contact number (oEP), which was a distribution parameter for subsequent regression analysis with failure load and stiffness, respectively.

(3) Definition of intravertebral regions

To explore the effect of cement distribution in different intravertebral regions, 27 cubes were classified as frontier column, middle column, and posterior column in the coronal direction (Figure 3(b)). In the transverse direction, 27 cubes were classified as superior transverse, middle transverse, and inferior transverse (Figure 3(c)). In each region of vertebrae, the regional distribution number (rDN), regional endplate contact number (rEP), regional volume fraction (rVF%), and regional cement volume (rCV) were noted. Finally, the linear regression R^2 of CV, VF%, DN, and EP on the failure load and stiffness was calculated. The comparison of R^2 showed that dominant factors affect augmentation.

2.5. Statistical Analysis. t-tests and Wilcoxon rank sum tests were used to verify the differences in parameters between the PKP and PVP groups. The difference in failure load and stiffness between different types of cement was tested by the Wilcoxon rank sum test. The difference in the average was tested by a t-test ($n = 51$). Linear regression analysis was conducted to explore the possible relationship between multiple independent and dependent parameters, thus generating R^2.

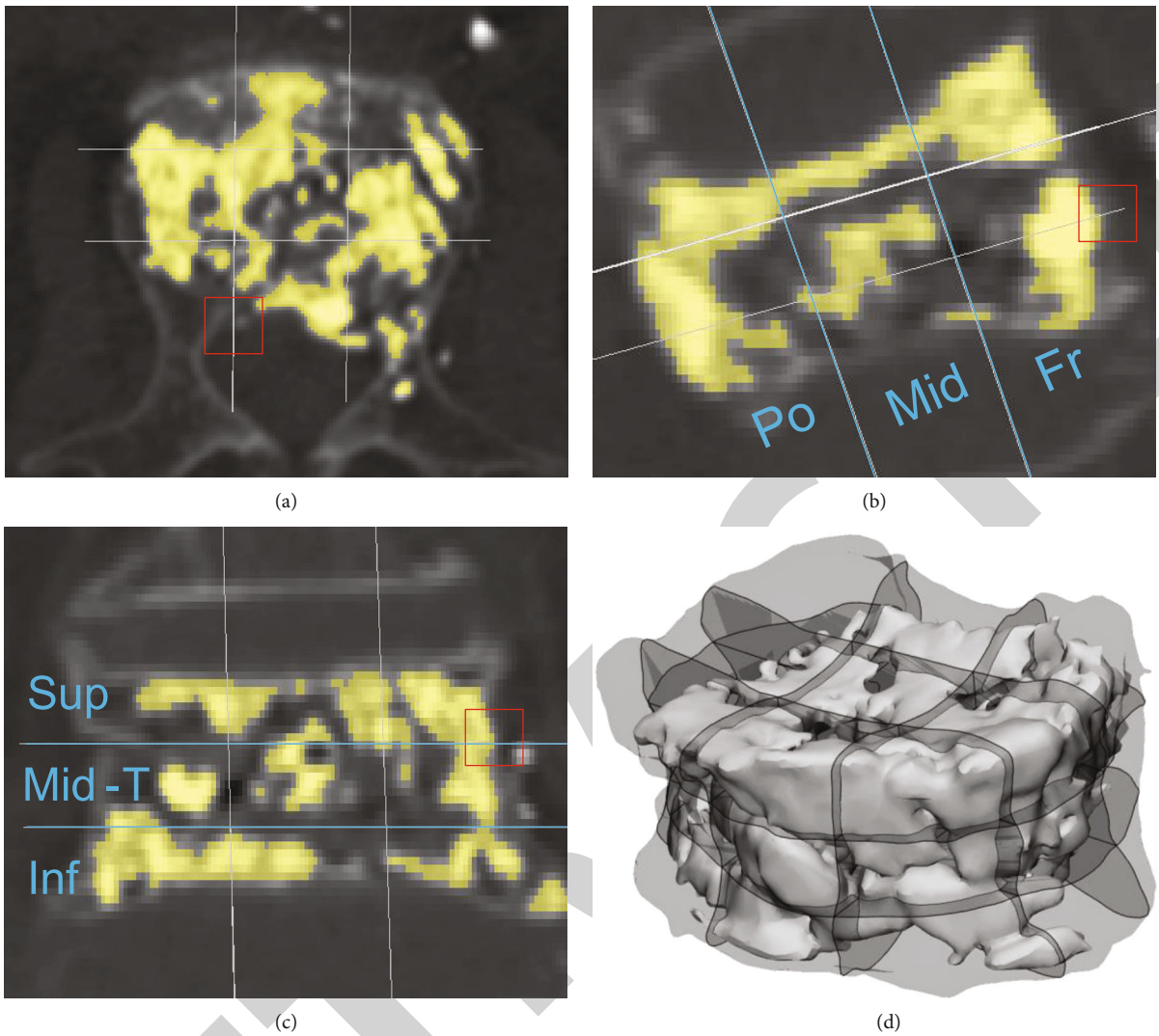

Figure 3: oDN quantification method: vertebrae and cement were anatomically divided into 27 portions. The red box indicates the alignment position of 6 splitting surfaces in three anatomical surfaces. Blue lines represent region division. Fr: front column; Mid: middle column; Po: postcolumn; Sup: superior transverse; Mid-T: middle transverse; Inf: inferior transverse. The number of cement-occupied cubes was noted as oDN, and the number of cement cubes touching the endplate was noted as oEP. (a) Transverse plane; (b) sagittal plane; (c) coronal plane; (d) overview in three dimensions.

3. Results

3.1. Cement Distribution Quantification in PVP and PKP. The comparison of variables in the PVP and PKP groups is presented in Table 4. There was no significant difference in cement volume between PVP and PKP ($P = 0.29$). In addition, all independent variables (distribution parameter) and dependent variables exhibited significant differences between the two groups. The vertebral volume of the PKP group was significantly larger ($34039.56 \pm 13716.6\,mm^3$) than that of the PVP group ($25001.29 \pm 5755.99\,mm^3$), so it is reasonable that the PVP group exhibited a significantly larger oVF% than the PKP group.

The oEP was also significantly larger in the PVP group. For PKP, the cancellous bone tamped by the inflated balloon might be denser and harder to penetrate by PMMA, thus decreasing the value of oDN and oEP. The contrast figures of typical cement morphology in PVP and PKP groups are in Figure S4. Except for the CPC group, the failure load and stiffness of the PVP group were significantly higher than those of the PKP group (Table 4). Since there was a significant difference between the PKP and PVP groups in terms of independent variables (distribution parameter), predicted vertebral failure load, and stiffness, the subsequent regression analysis and Wilcoxon rank sum test were conducted for pooled data with PVP or PKP adjusted.

Data were assessed by the Wilcoxon rank sum test; no significant mechanical difference was found between different groups of PMMA cement. The calcium phosphate cement group had significant lower failure load and stiffness than any PMMA cement group. $0.010 < {}^{*}P < 0.050$ and ${}^{**}P < 0.010$.

The mean oCV, oVF, oDN, and oEP for all vertebrae (pooled data) were $6259.6 \pm 1653.88\,mL$, $23.13 \pm 8.15\%$, 18.92 ± 3.43, and 4.18 ± 3.23, respectively. The predicted

Table 4: Comparison of different variables between the PVP and PKP groups (mean ± SD).

Variables	PVP ($n = 24$)	PKP ($n = 27$)	P value
Distribution parameter (independent variables)			
Vertebral volume (mm^3)	25001.29 ± 5755.99	34039.56 ± 13716.63	0.003
oCV (mm^3)	6515 ± 1167	6032 ± 1985	0.290
oVF% (mm^3/mm^3 %)	26.79 ± 5.41	19.88 ± 8.87	0.002
oDN (-)	20 ± 3.49	17.96 ± 3.14	0.033
oEP (-)	5.42 ± 3.12	3.07 ± 2.96	0.009
Mechanical parameters (dependent variables)			
Failure load with cement A (N)	2791.9 ± 1198.3	2177.89 ± 1045.83	0.048
Stiffness with cement A (N/mm)	10467.11 ± 4859.22	6916.67 ± 4498.73	0.001
Failure load with cement B (N)	3026.73 ± 1345.37	2301.25 ± 1178.22	0.045
Stiffness with cement B (N/mm)	11643.87 ± 5594	7502.66 ± 5277.48	0.001
Failure load with cement C (N)	3200.55 ± 1493.49	2370.1 ± 1248.52	0.042
Stiffness with cement C (N/mm)	12370.57 ± 6030.68	7911.84 ± 5822.76	0.001
Failure load with cement D (N)	2157.28 ± 788.03	1834.1 ± 680.6	0.117
Stiffness with cement D (N/mm)	7875.3 ± 3245.27	5461.26 ± 2687.45	0.001

P values of independent variables are from independent sample t-tests because they are normally distributed. P values of predicted mechanical variables are from Wilcoxon rank sum tests.

failure load of augmented vertebrae with four different types of cement was A: 2466.8 ± 1151.1 N, B: 2642.7 ± 1299.3 N, C: 2760.9 ± 1418.4 N, and D: 1986.19 ± 743.69 N, respectively. The predicted stiffness of augmented vertebrae with four different types of cement was A: 8587.5 ± 4958.7 N/mm, B: 9451.5 ± 5765 N/mm, C : 10010 ± 6277.9 N/mm, and D: 6597.28 ± 3175.08 N/mm, respectively. Different cement types had no significant impact on the predicted failure load and stiffness of augmented vertebrae except cement type D (calcium phosphate cement) in the Wilcoxon rank sum test (Figure 4).

3.2. Correlation of Overall Distribution Parameters with Strength and Stiffness. The linear regression analysis of vertebrae with cement type B is presented in Figure 5, and the corresponding analysis of the other three types of cement is available in the Supplementary materials (Table S1). The oDN exhibited a highest correlation with the failure load ($R^2 = 0.729$); thus, this parameter had potential to be utilized as a postoperative fracture rack predictor. The lower oDN could be a sign of augmented vertebrae endanger by vertebral recompression even refracture. The oEP was most correlated with stiffness ($R^2 = 0.684$) in this study (Figure 5(f)), indicating that cement-endplate contact could strongly affect augmented vertebrae stiffening. oCV and oVF% with determination coefficients of $R^2 = 0.4$ and $R^2 = 0.286$, respectively, indicating the oDN and oEP were better parameter for postoperative evaluation and prediction. No obvious collinearity was found between these overall distribution parameters and volumetric parameters after diagnosis (Figure 6). This statistically proves that oDN and oEP are independent of oCV and oVF%.

3.3. Correlation of Regional Parameters with Strength and Stiffness. The linear regression test for regional independent variables in coronal planes with vertebral failure load with cement type B is presented in Figure 7(a). The front and middle column rDNs exhibited identical determination coefficients on failure load ($R^2 = 0.508$ for front column and $R^2 = 0.49$ for middle column). R^2 of rEP on failure load was close between front and middle columns. A lower correlation was found between posterior column rDN and failure load ($R^2 = 0.206$). Corresponding analyses of the other three types of cement are available in the Supplementary materials (Figures S1a, S2a, S3a). In terms of stiffness, rEP in the front column dominated vertebral stiffness changing, with $R^2 = 0.59$ (Figure 7(b)).

For transverse planes, with cement type B, cement in the superior and inferior transverse planes produced a similar influence on the failure load when endplate contact occurred (Figure 7(c)). The rEP correlation on stiffness was highest ($R^2 = 0.421$) in the inferior transverse (Figure 7(d)). Corresponding analyses of the other three types of cement are available in the Supplementary materials (Figures S1c, S1d, S2c, S2d, S3c, S3d). All regressions of regional variables on failure load and stiffness were significant ($P < 0.05$).

4. Discussion

Many common complications are caused by vertebra mechanical failure after vertebroplasty. Appropriate parameters should be proposed to describe the augmented vertebral mechanics. In this study, the intravertebral space was divided into 27 cubes, with a consistent quantification method, and cement distribution was parameterized as

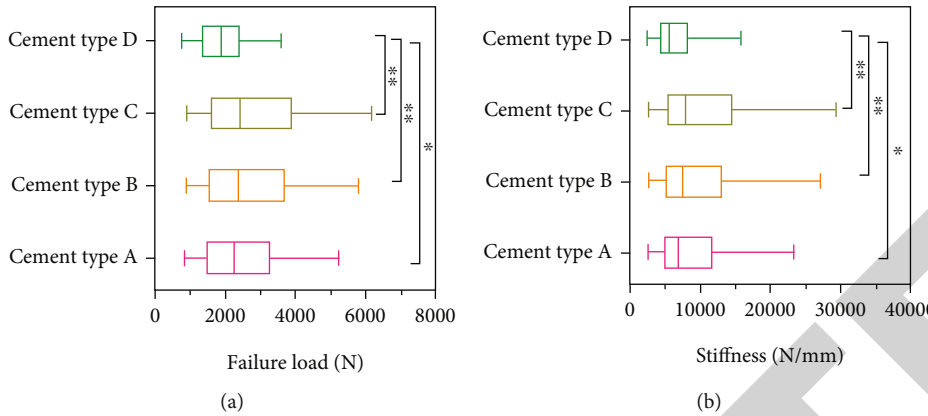

Figure 4: Mechanical properties of vertebrae with different types of cement. (a) Failure load in four types of cement and (b) stiffness in four types of cement.

overall distribution number (oDN) and overall endplate contact number (oEP). Overall cement volume (oCV) and overall cement volume fraction (oVF%) were also determined. Additionally, the distribution parameters in three transverse (superior, midtransverse, and inferior) and three coronal (front, middle, and post) regions were noted as regional distribution number (rDN) and regional endplate contact number (rEP). The predictive value of these parameters was assessed by their correlation with cemented vertebral mechanics. This analysis was helpful in selection of proper parameters during postsurgical decision prediction process.

4.1. Correlation of Distribution Parameters and Mechanical Properties. To quantify cement morphology inside vertebrae, it was intuitive to divide the vertebrae into 27 cubes in three dimensions according to patient-specific vertebral anatomy. The method can be easily adopted to risk parameter evaluation before postsurgical decision-making process, like VAS score, kyphotic restoration, and vertebral height restoration, thus increase accuracy on decision-making process of revision surgery necessity. This kind of vertebral dividing method had been adopted by some recent vertebral bone mineral heterogeneity studies [35, 36].

The results of the current study indicate that there was a strong positive correlation ($R^2 = 0.729$) between oDN and the failure load (Figure 5(a)). To the authors' understanding, the oDN assesses the extensiveness of space occupied by cement and the even distribution of cement mechanical support. Multiple clinical studies had noted that interdigitated cement distribution instead of lump distribution can significantly decrease the chances of refracture [6, 7], and some research had emphasized that refracture of the augmented level may be due to uneven loading, which is initiated by the uneven distribution of cement [11, 12]. With more extensive cement distribution (higher oDN), the mechanical support of cement was typically even, and less intravertebral space remained unsupported. The oDN in this study could effectively quantify this extensiveness. The high R^2 of oDN on failure load ($R^2 = 0.729$) made this parameter available for vertebral recompression prediction postoperatively. The lower value of oDN indicated more risk for augmented vertebrae to fail. The oEP was regarded as quantified parameter of endplate contact, and it was correlated with vertebral stiffness ($R^2 = 0.684$), and the R^2 was the highest of all the variables (Figure 5(f)). Considering that the vertebral stiffness was correlated with adjacent new vertebral fracture [37, 38], the oEP could be utilized as predictor of new adjacent segment vertebral fracture postoperatively. Preoperatively, low oEP cement insert strategy in severe osteoporosis patients could prevent new adjacent segment vertebral fracture.

CV and VF% have been investigated as cement distribution parameters, but whether these factors can dominate the mechanical behavior of cemented vertebrae remains conflicted [9]. oCV and oVF% were compared with oDN and oEP, and the oVF% and oCV obtained relatively low R^2 values for the predicted failure load and stiffness, which indicates that the mechanical properties of augmented vertebrae are not directly affected by VF% or CV (Figures 5(c), 5(d), 5(g), and 5(h)). The reason of that was the different dispersion resistances of various BMDs inside vertebrae can largely impact the final cement morphology for the same amount of CV or VF% [39]. Thus, the CV and VF% are inconsistent and unreliable scales to validate augmentation, and these parameters can be confounding for postsurgical decision-making. Different cement modulus cannot significantly decrease stiffness (Figure 4(b)) in our study.

4.2. Mechanical Differences between PVP and PKP. Grouping information for PVP and PKP was collected along with DICOM from clinic in this study. No significant difference in oCV was found between the two groups, but the oDN, oEP, and mechanics all exhibited significant differences between the PVP and PKP groups.

The significant difference in oDN between the PVP and PKP groups may be due to the cancellous bone tamped by inflated balloons in the PKP groups, which can make cancellous bone denser and harder to penetrate by PMMA. The lump distribution pattern exhibited a lower oDN in this study, and PVP with interdigitated distribution [14, 40] could achieve a significantly increased oDN. A similar

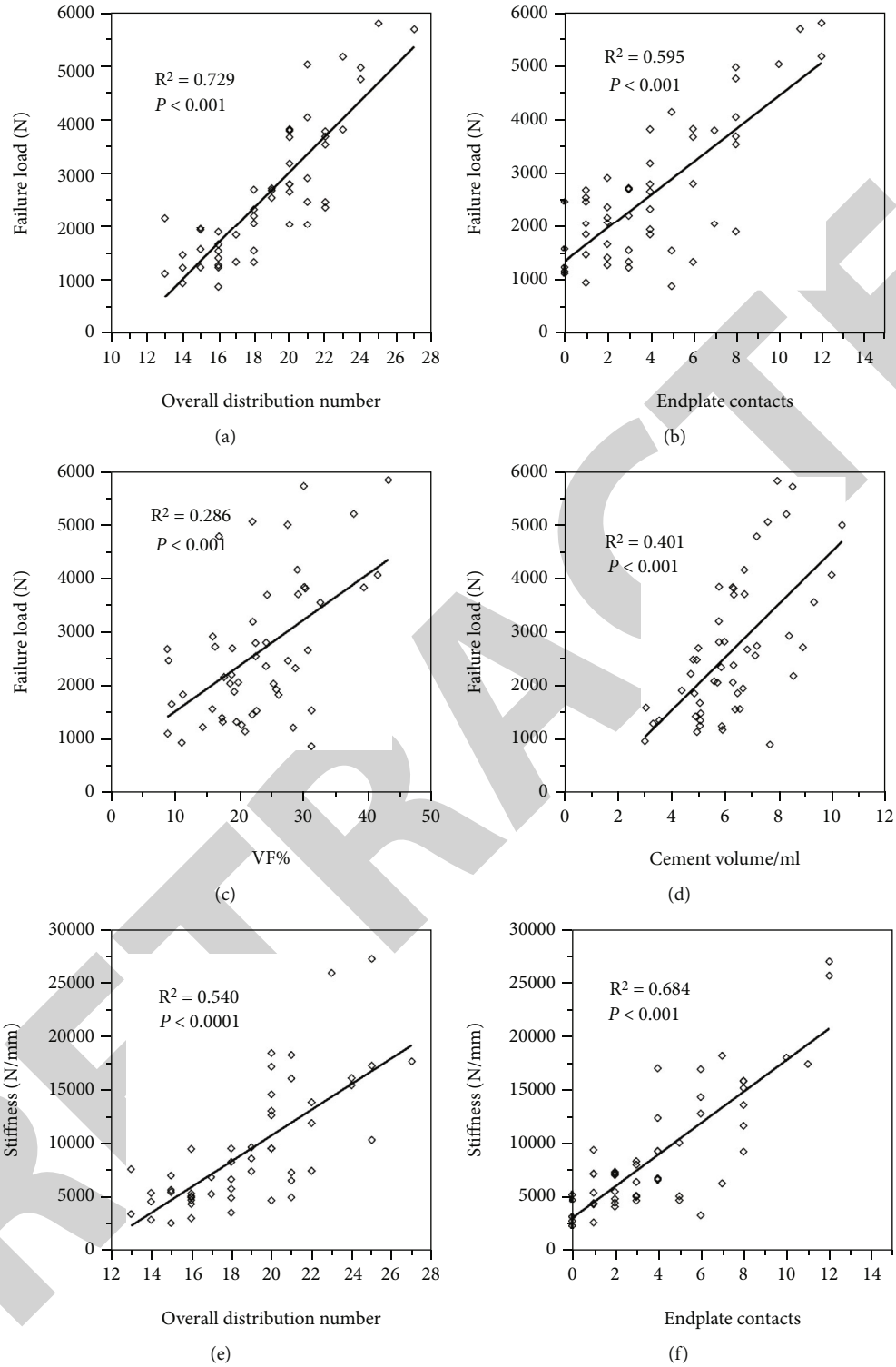

Figure 5: Continued.

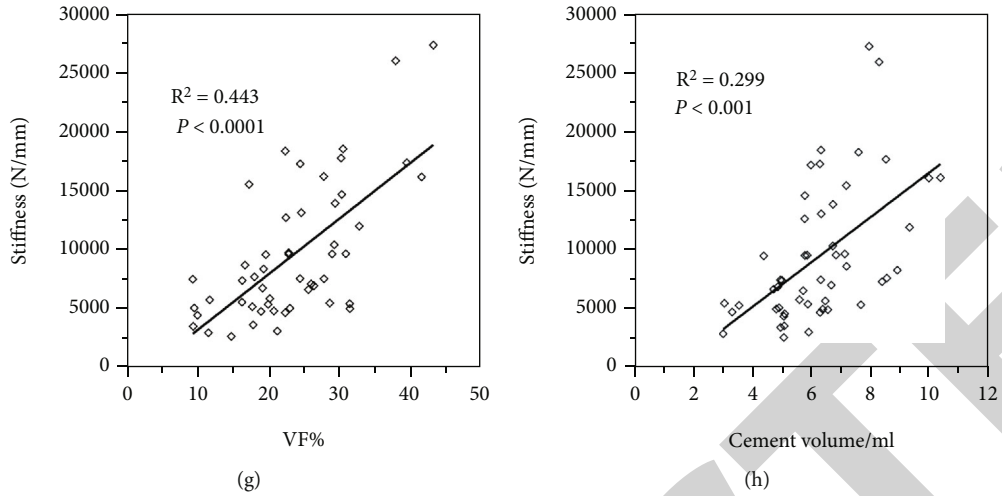

Figure 5: Linear regression analysis of distributional parameters on predicted (a–d) failure load and (e–h) stiffness; all regressions are significant ($P < 0.05$).

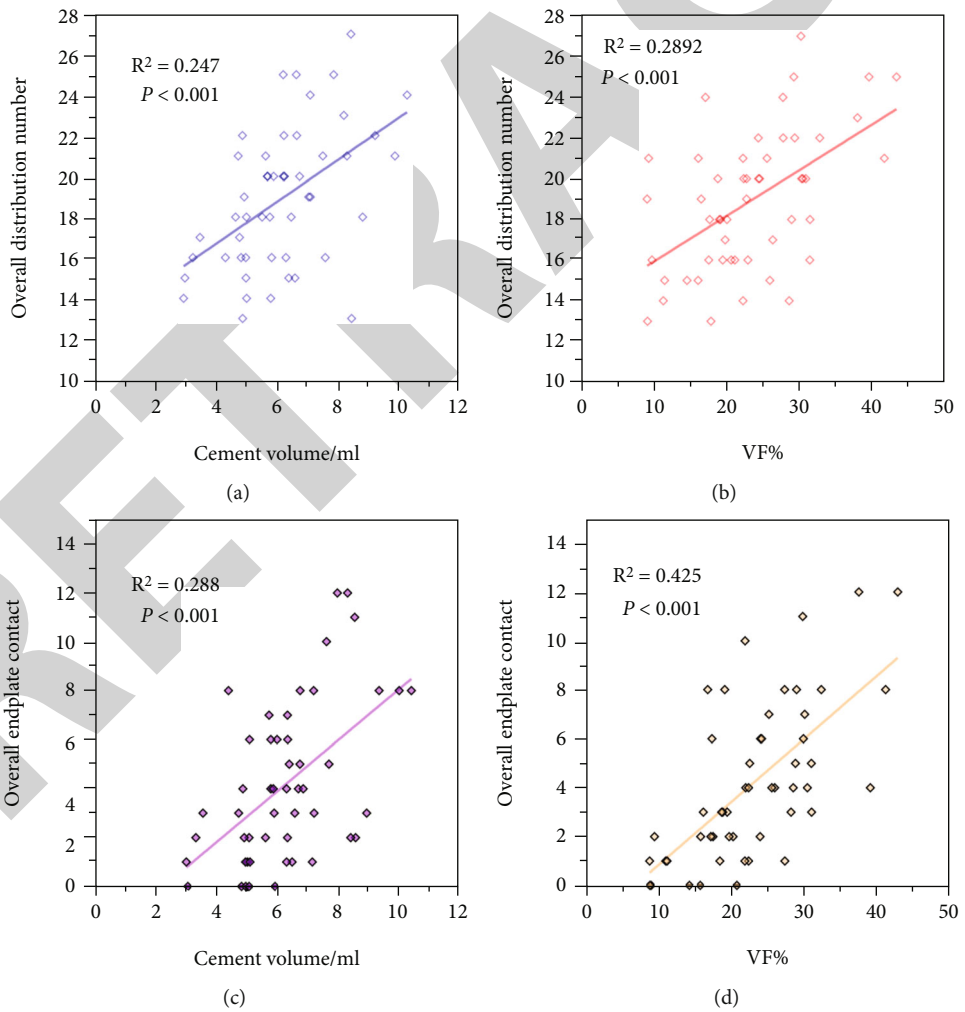

Figure 6: Collinearity diagnosis of overall independent variables. oDN and oEP are independent of oCV and oVF%.

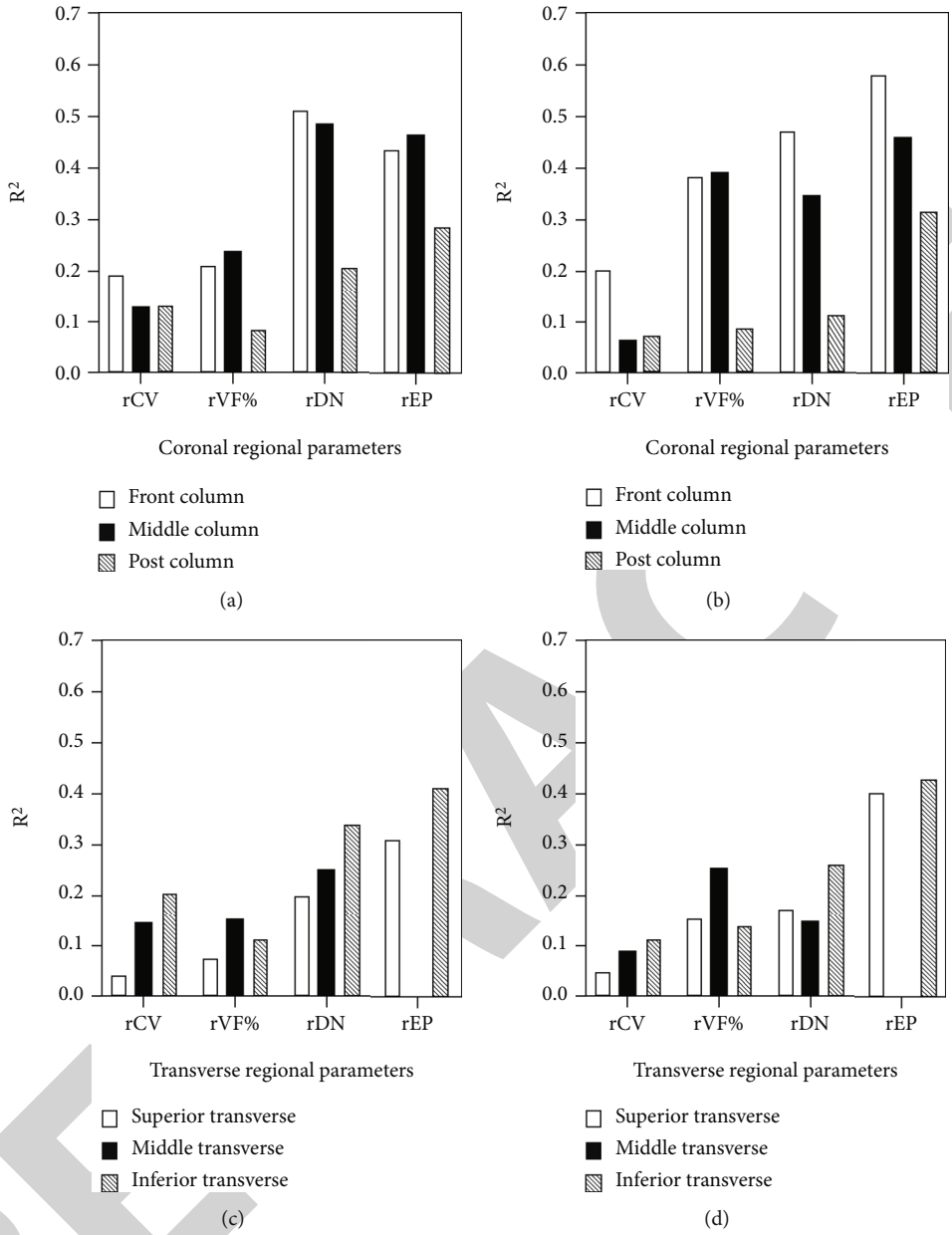

Figure 7: Determination coefficient of regional variables on failure load and stiffness of cement type B. (a) R^2 of different regional variables on failure load in three coronal regions, (b) R^2 of different regional variables on stiffness in three coronal regions, (c) R^2 of different regional variables on failure load in three transverse regions, and (d) R^2 of different regional variables on stiffness in three transverse regions.

situation was observed for oEP between PVP and PKP groups, and more retention of the cancellous structure in PVP makes it easier for cement to disperse to the endplate [14, 41]. Compared with that of the PKP group, the oVF% in the PVP group was significantly higher, and it is mainly because the frontier vertebral height is generally higher after inflation of the balloon in PKP than in the PVP group in many studies [40, 41], which could cause the vertebral volume of the PKP group to increase during the masking procedure (Figure 1). As quantified by the cement distribution in this study, oDN and oEP were both significantly higher in the PVP group, indicating that the cement dispersed better in the PVP group.

The predicted failure load was significantly higher in the PVP group than in the PKP group, which corresponds to previous studies [40, 41]. The PKP group exhibited greater refracture incidence or loss of frontier height, and different cement distribution patterns were key factors according to previous studies, which corresponds with the results of this study. Thus, differentiation of PVP and PKP technique is crucial in postsurgical evaluation process because of significant lower failure load in the PKP group. In a similar situation regarding stiffness, the more interdigitated distribution in PVP increases the oDN and strength, while simultaneously increasing the oEP. The R^2 of oEP on stiffness ($R^2 = 0.684$) suggested that a higher oEP indicates greater

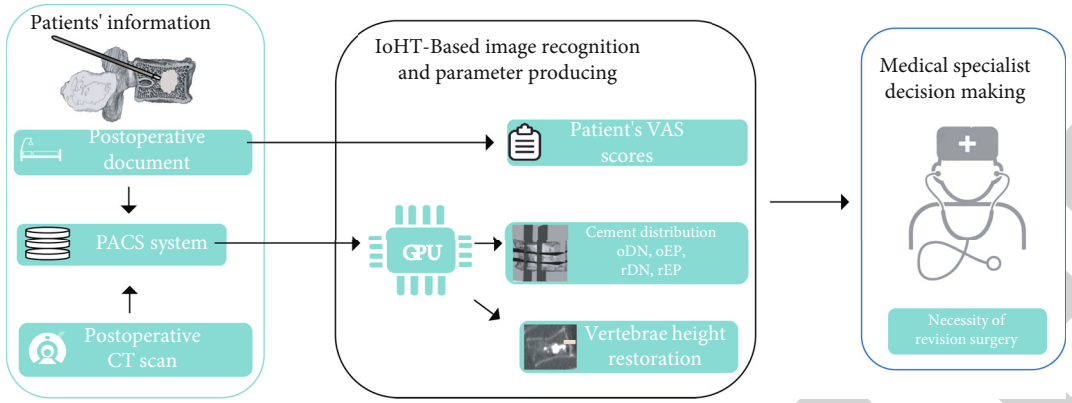

Figure 8: Application of patient-specific vertebroplasty parameters for postoperative decision-making process.

stiffness in the PVP group (Table 4). Corresponding to previous clinical research [7, 41], the "stress-riser" effect occurring in PVP was more intense than that in PKP, leading to more adjacent vertebral compression.

4.3. Distribution in Different Regions of Intravertebral Space. Different R^2 for rDN and rEP on failure load across three columns reflected the load bearing mechanism of vertebrae (Figure 7(a)). The result was not only helpful for postsurgical evaluation and decision-making, but also beneficial for injection technique such as needle placement and needle movement. The three-column theory [42] indicated that the front column bears most of the vertebral axial load, and the front column in the three-column theory is similar to the front and middle columns of the vertebrae in this study, which were correlated with the failure load. This conclusion was consistent with a previous X-ray retrospective study: a greater cement distribution in the middle column was a protective factor against repeat collapse after surgery [8]. Moreover, endplate contact in the front column can aggressively affect vertebral stiffness (Figure 7(b)). To prevent adjacent vertebral fracture, the rEP in this region should be controlled within a reasonable range, and the overly high rEP in this region can be an alert for newly adjacent segment fracture in postsurgical inspection. The postcolumn distribution in this study barely shows any correlation with failure load or stiffness; however, it is not the indication that the cement dispersion in this region is unimportant. On the contrary, it has been reported that the presence of a basivertebral foramen indicates weakness of vertebral load bearing and could lead to the superior endplate failure and burst fracture [43]; therefore, the augmentation of postcolumn region cannot be ignored. In terms of different transverse regions (Figure 7(d)), rEP in the superior and inferior transverse exhibits similar and strong influence on stiffness. Gustafson et al. [44] reported that when a large compressive strain develops in near superior and inferior endplate regions when experiencing axial compression, the cement-endplate contact in both regions can ease the strain, thus improving the stiffness of the augmented vertebrae.

There are some drawbacks in this study. First, the sample size was limited by the number of patients, and the patients' CT data after vertebroplasty were difficult to obtain because of the instant pain reduction after this type of surgery, and patients tend to not return to clinic and undergo the CT inspection. Second, phantom CT calibration requires QCT scans; unfortunately, this retrospective study was unable to collect an adequate number of QCT scanned DICOM files containing the calibration phantom. With that said, the DICOM data were obtained from a consistent CT scanner, with consistent parameters throughout the scan, such as KVP, X-ray tube current, pixel size, and reconstruction kernel. Thus, the predicted mechanical differences between vertebrae are reliable, and therefore sufficient to calculate the R^2 of cement distribution with vertebral mechanical properties.

4.4. Further Application of Proposed Methods and Parameters. The proposed parameters, oDN, oEP, and rEP in front column, are well correlated with vertebral mechanics, and the combination of these parameter with IoHT (Internet of Health Things) system is promising (Figure 8). For patients performed vertebroplasty, their postoperative CT images stored in PACS (picture archiving and communication system) are analyzed, and generate diagnostic parameters by proposed methods. These parameters can be extracted from postoperative CT image by IoHT-based image recognition system [45–48], which can be done by local or cloud GPU (Graphics Processing Unit) without the need for specific hardware and user knowledge [49–51]. In some recent research, deep learning algorithm, CNN (Convolutional Neural Networks), and other techniques have been adopted to medical image process [52–55], and some algorithm is developed specifically for CT image recognition [56]. This kind of solution can be adopted to bone cement automatic parametrization. After oDN and oEP are extracted from image recognition algorithm, these parameters can be inputted into specific empirical formula on IoHT to generate risk indicator as auxiliary diagnose. Thus, medical specialist can propose a low latency and accurate diagnose for necessity of revision surgery. Meanwhile, the proposed parameters can also be used preoperatively to help surgeons to reduce the risk of cement leakage during the injection process. On the other hand, lower oEP in severe osteoporosis patients can prevent new adjacent segment vertebral fracture.

5. Conclusion

Three-dimensional cemented vertebral models were reconstructed based on MDCT data. By dividing the intravertebral space into 27 sections (cubes), a stand-alone method was developed to quantify intravertebral cement morphology. Different R^2 values indicated that the extensive distribution of intravertebral cement (oDN) played an important role in augmented vertebral mechanical properties. The oDN and oEP were most correlated with the failure load and stiffness, respectively. Regionally, rDN in the front column and inferior transverse exhibited significant correlation with mechanical behavior. Proposed parameters have the potential to be used as a postoperative evaluation scale thus improving the quality of clinical decision-making, in this way to increase life quality of older people, reducing the public health pressure.

Data Availability

The datasets used and analyzed during the current study are available from the corresponding author on reasonable request.

Ethical Approval

This study was performed in line with the principles of the Declaration of Helsinki. Approval was granted by the Ethics Committee of The Third People's Hospital of Yunnan Province (2020KY008).

Conflicts of Interest

The authors have no competing interests to declare that are relevant to the content of this article.

Acknowledgments

This work was financially supported by the National Natural Science Foundation of China (Grant No. 51871163).

Supplementary Materials

The supplementary file includes regression results of different types of bone cement in FEA study. Table S1 shows determination coefficients of overall parameters on failure load and stiffness in four types of cement. Figure S1 shows determination coefficients of regional parameters on failure load and stiffness in cement type A. Figure S2 shows determination coefficients of regional parameters on failure load and stiffness in cement type C. Figure S3 shows determination coefficients of regional parameters on failure load and stiffness in cement type D. Figure S4 shows contrast of typical cement morphology in PVP and PKP groups. *(Supplementary Materials)*

References

[1] P. C. S. Parreira, C. G. Maher, R. Z. Megale, L. March, and M. L. Ferreira, "An overview of clinical guidelines for the management of vertebral compression fracture: a systematic review," *The Spine Journal*, vol. 17, no. 12, pp. 1932–1938, 2017.

[2] S. L. Silverman, "The clinical consequences of vertebral compression fracture," *Bone*, vol. 13, no. 2, pp. S27–S31, 1992.

[3] S. Han, S. Wan, L. Ning, Y. Tong, J. Zhang, and S. Fan, "Percutaneous vertebroplasty versus balloon kyphoplasty for treatment of osteoporotic vertebral compression fracture: a meta-analysis of randomised and non-randomised controlled trials," *International Orthopaedics*, vol. 35, no. 9, pp. 1349–1358, 2011.

[4] S. R. Garfin, R. A. Buckley, J. Ledlie, and Balloon Kyphoplasty Outcomes Group, "Balloon kyphoplasty for symptomatic vertebral body compression fractures results in rapid, significant, and sustained improvements in back pain, function, and quality of life for elderly patients," *Spine*, vol. 31, no. 19, pp. 2213–2220, 2006.

[5] Y. Li, J. Yue, M. Huang et al., "Risk factors for postoperative residual back pain after percutaneous kyphoplasty for osteoporotic vertebral compression fractures," *European Spine Journal*, vol. 29, no. 10, pp. 2568–2575, 2020.

[6] W. Yu, W. Xu, X. Jiang, D. Liang, and W. Jian, "Risk factors for recollapse of the augmented vertebrae after percutaneous vertebral augmentation: a systematic review and meta-analysis," *World Neurosurgery*, vol. 111, pp. 119–129, 2018.

[7] Y. J. Rho, W. J. Choe, and Y. I. Chun, "Risk factors predicting the new symptomatic vertebral compression fractures after percutaneous vertebroplasty or kyphoplasty," *European Spine Journal*, vol. 21, no. 5, pp. 905–911, 2012.

[8] J. Song, L. Ding, J. Chen, Y. Zhang, Y. Hou, and G. A. Zhang, "The filling proportion of bone cement affects recollapse of vertebrae after percutaneous vertebral augmentation: a retrospective cohort study," *International Journal of Surgery*, vol. 47, pp. 33–38, 2017.

[9] D. Martinčič, M. Brojan, F. Kosel et al., "Minimum cement volume for vertebroplasty," *International Orthopaedics*, vol. 39, no. 4, pp. 727–733, 2015.

[10] L. Cristofolini, N. Brandolini, V. Danesi, P. Erani, M. Viceconti, and S. J. Ferguson, "A preliminary *in vitro* biomechanical evaluation of prophylactic cement augmentation of the thoracolumbar vertebrae," *Journal of Mechanics in Medicine and Biology*, vol. 16, no. 5, article 1650074, 2016.

[11] A. Tsouknidas, S. Savvakis, Y. Asaniotis, K. Anagnostidis, A. Lontos, and N. Michailidis, "The effect of kyphoplasty parameters on the dynamic load transfer within the lumbar spine considering the response of a bio-realistic spine segment," *Clinical Biomechanics*, vol. 28, no. 9-10, pp. 949–955, 2013.

[12] J. L. Wang, C. K. Chiang, Y. W. Kuo, W. K. Chou, and B. D. Yang, "Mechanism of fractures of adjacent and augmented vertebrae following simulated vertebroplasty," *Journal of Biomechanics*, vol. 45, no. 8, pp. 1372–1378, 2012.

[13] X. He, H. Li, Y. Meng et al., "Percutaneous kyphoplasty evaluated by cement volume and distribution: an analysis of clinical data," *Pain Physician*, vol. 19, no. 7, pp. 495–506, 2016.

[14] Y. Y. Kim and K. W. Rhyu, "Recompression of vertebral body after balloon kyphoplasty for osteoporotic vertebral compression fracture," *European Spine Journal*, vol. 19, no. 11, pp. 1907–1912, 2010.

[15] Y. Chevalier, D. Pahr, M. Charlebois, P. Heini, E. Schneider, and P. Zysset, "Cement distribution, volume, and compliance in vertebroplasty: some answers from an anatomy-based nonlinear finite element study," *Spine*, vol. 33, no. 16, pp. 1722–1730, 2008.

[16] Y. Peng, X. Du, L. Huang et al., "Optimizing bone cement stiffness for vertebroplasty through biomechanical effects analysis

based on patient-specific three-dimensional finite element modeling," *Medical & Biological Engineering & Computing*, vol. 56, no. 11, pp. 2137–2150, 2018.

[17] V. A. Stadelmann, I. Zderic, A. Baur, C. Unholz, U. Eberli, and B. Gueorguiev, "Composite time-lapse computed tomography and micro finite element simulations: a new imaging approach for characterizing cement flows and mechanical benefits of vertebroplasty," *Medical Engineering and Physics*, vol. 38, no. 2, pp. 97–107, 2016.

[18] D. P. Anitha, T. Baum, J. S. Kirschke, and K. Subburaj, "Effect of the intervertebral disc on vertebral bone strength prediction: a finite-element study," *The Spine Journal*, vol. 20, no. 4, pp. 665–671, 2020.

[19] M. H. Mazlan, M. Todo, H. Takano, and I. Yonezawa, "Finite element analysis of osteoporotic vertebrae with first lumbar (L1) vertebral compression fracture," *International Journal of Applied Physics and Mathematics*, vol. 4, no. 4, pp. 267–274, 2014.

[20] L.-M. Ren, M. Todo, T. Arahira, H. Yoshikawa, and A. Myoui, "A comparative biomechanical study of bone ingrowth in two porous hydroxyapatite bioceramics," *Applied Surface Science*, vol. 262, pp. 81–88, 2012.

[21] T. S. Keller, "Predicting the compressive mechanical behavior of bone," *Journal of Biomechanics*, vol. 27, no. 9, pp. 1159–1168, 1994.

[22] E. F. Morgan and T. M. Keaveny, "Dependence of yield strain of human trabecular bone on anatomic site," *Journal of Biomechanics*, vol. 34, no. 5, pp. 569–577, 2001.

[23] Y. H. Lee, J. J. Kim, and I. G. Jang, "Patient-specific phantomless estimation of bone mineral density and its effects on finite element analysis results: a feasibility study," *Computational and Mathematical Methods in Medicine*, vol. 2019, 10 pages, 2019.

[24] F. Eggermont, N. Verdonschot, Y. van der Linden, and E. Tanck, "Calibration with or without phantom for fracture risk prediction in cancer patients with femoral bone metastases using CT-based finite element models," *PLoS One*, vol. 14, no. 7, article e0220564, 2019.

[25] C. Robo, C. Ohman-Magi, and C. Persson, "Compressive fatigue properties of commercially available standard and low-modulus acrylic bone cements intended for vertebroplasty," *Journal of the Mechanical Behavior of Biomedical Materials*, vol. 82, pp. 70–76, 2018.

[26] M. Wekwejt, N. Moritz, B. Świeczko-Żurek, and A. Pałubicka, "Biomechanical testing of bioactive bone cements – a comparison of the impact of modifiers: antibiotics and nanometals," *Polymer Testing*, vol. 70, pp. 234–243, 2018.

[27] A. López, G. Mestres, M. K. Ott et al., "Compressive mechanical properties and cytocompatibility of bone-compliant, linoleic acid-modified bone cement in a bovine model," *Journal of the Mechanical Behavior of Biomedical Materials*, vol. 32, pp. 245–256, 2014.

[28] I. Palmer, J. Nelson, W. Schatton, N. J. Dunne, F. Buchanan, and S. A. Clarke, "Biocompatibility of calcium phosphate bone cement with optimised mechanical properties: an in vivo study," *Journal of Materials Science. Materials in Medicine*, vol. 27, no. 12, p. 191, 2016.

[29] H. Liu, Y. Guan, D. Wei, C. Gao, H. Yang, and L. Yang, "Reinforcement of injectable calcium phosphate cement by gelatinized starches," *Journal of Biomedical Materials Research Part B-Applied Biomaterials*, vol. 104, no. 3, pp. 615–625, 2016.

[30] M. Y. Liu, P. L. Lai, and C. L. Tai, "Biomechanical evaluation of low-modulus bone cement for enhancing applicability in vertebroplasty — an experimental study in porcine model," *Biomedical Engineering: Applications, Basis and Communications*, vol. 30, no. 1, article 1850002, 2018.

[31] M. C. Costa, P. Eltes, A. Lazary, P. P. Varga, M. Viceconti, and E. Dall'Ara, "Biomechanical assessment of vertebrae with lytic metastases with subject-specific finite element models," *Journal of the Mechanical Behavior of Biomedical Materials*, vol. 98, pp. 268–290, 2019.

[32] Y. Matsuura, H. Giambini, Y. Ogawa et al., "Specimen-specific nonlinear finite element modeling to predict vertebrae fracture loads after vertebroplasty," *Spine*, vol. 39, no. 22, pp. E1291–E1296, 2014.

[33] J. M. Buckley, D. C. Leang, and T. M. Keaveny, "Sensitivity of vertebral compressive strength to endplate loading distribution," *Journal of Biomechanical Engineering*, vol. 128, no. 5, pp. 641–646, 2006.

[34] T. M. Keaveny, M. R. McClung, H. K. Genant et al., "Femoral and vertebral strength improvements in postmenopausal women with osteoporosis treated with denosumab," *Journal of Bone and Mineral Research*, vol. 29, no. 1, pp. 158–165, 2014.

[35] A. I. Hussein, D. T. Louzeiro, G. U. Unnikrishnan, and E. F. Morgan, "Differences in trabecular microarchitecture and simplified boundary conditions limit the accuracy of quantitative computed tomography-based finite element models of vertebral failure," *Journal of Biomechanical Engineering*, vol. 140, no. 2, article 0210041, 2018.

[36] J. Kaiser, B. Allaire, P. M. Fein et al., "Heterogeneity and spatial distribution of intravertebral trabecular bone mineral density in the lumbar spine is associated with prevalent vertebral fracture," *Journal of Bone and Mineral Research*, vol. 35, no. 4, pp. 641–648, 2020.

[37] C. Griffoni, J. N. M. Lukassen, L. Babbi et al., "Percutaneous vertebroplasty and balloon kyphoplasty in the treatment of osteoporotic vertebral fractures: a prospective randomized comparison," *European Spine Journal*, vol. 29, no. 7, pp. 1614–1620, 2020.

[38] L. Tan, B. Wen, Z. Guo, and Z. Chen, "The effect of bone cement distribution on the outcome of percutaneous vertebroplasty: a case cohort study," *BMC Musculoskeletal Disorders*, vol. 21, no. 1, p. 541, 2020.

[39] M. Loeffel, S. J. Ferguson, L. P. Nolte, and J. H. Kowal, "Vertebroplasty - experimental characterization of polymethylmethacrylate bone cement spreading as a function of viscosity, bone porosity, and flow rate," *Spine*, vol. 33, no. 12, pp. 1352–1359, 2008.

[40] M. J. Kim, D. P. Lindsey, M. Hannibal, and T. F. Alamin, "Vertebroplasty versus kyphoplasty: biomechanical behavior under repetitive loading conditions," *Spine*, vol. 31, no. 18, pp. 2079–2084, 2006.

[41] Y. X. Li, D. Q. Guo, S. C. Zhang et al., "Risk factor analysis for re-collapse of cemented vertebrae after percutaneous vertebroplasty (PVP) or percutaneous kyphoplasty (PKP)," *International Orthopaedics*, vol. 42, no. 9, pp. 2131–2139, 2018.

[42] F. Denis, "The three column spine and its significance in the classification of acute thoracolumbar spinal injuries," *Spine*, vol. 8, no. 8, pp. 817–831, 1983.

[43] X. Zhang, S. Li, X. Zhao et al., "The mechanism of thoracolumbar burst fracture may be related to the basivertebral foramen," *The Spine Journal*, vol. 18, no. 3, pp. 472–481, 2018.

[44] H. M. Gustafson, A. D. Melnyk, G. P. Siegmund, and P. A. Cripton, "Damage identification on vertebral bodies during

Hindawi
Computational and Mathematical Methods in Medicine
Volume 2022, Article ID 9923214, 11 pages
https://doi.org/10.1155/2022/9923214

Research Article

The Effects of Different Reference Methods on Decision-Making Implications of Auditory Brainstem Response

Zhenzhen Liu,[1] Xin Wang,[2,3,4] Mingxing Zhu,[2,3,4] Yuchao He,[2,3,4] Lin Li,[1] Li Chen,[5] Weimin Huang,[6] Zhilong Wei,[2,3,4] Shixiong Chen,[2,3,4] Yan Chen,[1] and Guanglin Li[2,3,4]

[1]*Surgery Division, Epilepsy Center, Shenzhen Children's Hospital, Shenzhen 518038, China*
[2]*The CAS Key Laboratory of Human-Machine Intelligence-Synergy Systems, Shenzhen Institutes of Advanced Technology, Chinese Academy of Sciences, Shenzhen 518055, China*
[3]*Shenzhen College of Advanced Technology, University of Chinese Academy of Sciences, Shenzhen 518055, China*
[4]*Guangdong-Hong Kong-Macao Joint Laboratory of Human-Machine Intelligence-Synergy Systems, Chinese Academy of Sciences, Shenzhen 518055, China*
[5]*Department of Neurology, Shenzhen Children's Hospital, Shenzhen 518038, China*
[6]*Department of Neonatology, Shenzhen Children's Hospital, Shenzhen 518038, China*

Correspondence should be addressed to Shixiong Chen; sx.chen@siat.ac.cn and Yan Chen; ccflysz@126.com

Received 5 January 2022; Accepted 10 March 2022; Published 8 April 2022

Academic Editor: Plácido R. Pinheiro

Hearing loss is a common disease affecting public health all around the world. In clinic, auditory brainstem response (ABR) has been widely used for the detection of hearing loss based on its convenience and accuracy. The different reference methods directly influence the quality of the ABR waveform which in turn affects the ABR-based diagnosis. Therefore, in this study, a reference electrode standardization technique (REST) was adopted to systematically investigate and evaluate the effect of different reference methods on the quality of ABR waveform in comparison with the conventional average reference (AR) and mean mastoid (MM) methods. In this study, ABR signals induced by click stimulus were acquired via an EEG electrode cap arrays, and those located on the six channels along the midline were compared systemically. The results showed that, when considering the different channels, the ABR in the Cz channel showed the best morphology. Then, the ABR waveforms acquired via the REST method possessed better morphologies with large amplitude ($0.06 \pm 0.02\,\mu$V for wave I, $0.07 \pm 0.02\,\mu$V for wave III, and $0.21 \pm 0.04\,\mu$V for wave V) when compared with the traditional method. Summarily, we found that the REST and MM methods improved the quality of ABR on both amplitude and morphology under different stimulation rates and levels without changing the latencies of ABR when compared with the conventional AR method, suggesting that the REST and MM methods have the potential to help physicians with high accurate ABR-based clinical diagnosis. Moreover, this study might also provide a theoretic basis of reference methods on the acquisition of electroencephalogram over public health issues.

1. Introduction

Hearing loss has been reported to affect over 1.1 billion individuals across different age groups, which causes a huge public health issue. In clinical settings, auditory brainstem response (ABR) has a decision-making implication on hearing loss diagnosis based on its accuracy, convenience, and efficiency. ABR was firstly described in detail by Jewett et al. in 1971 as a potential change in the auditory nerve pathway from the cochlea to the brainstem evoked by an acoustic stimulus and could be recorded noninvasively on the scalp of the subjects [1]. As a matter of fact, ABR is the

most commonly applied auditory-evoked responses in clinical settings because it allows adequate assessment of the auditory neural pathway and hearing sensitivity [2, 3]. Fundamentally, ABR is composed of seven waveform peaks, in which the first five are often used for hearing loss assessment in clinical practice. The peaks are classified based on their temporal appearance as described by Jewett and Williston (waves I-V) [4]. Each of the five waves (waves I-V) has been characterized and attributed to different anatomical region in auditory pathway [5]. The indexes used to recognize an ABR waveform are wave latency, interwave latency, waveform repeatability, and so on. The occurrence of abnormality in ABR waveform, like a disappearance of subsequent waves and the change of wave latency, provides a basis for the localization of the auditory nerve and brainstem auditory pathway lesions.

The quality of the ABR waveform is considered as a core determinant for the effective assessment of hearing loss and its associated cause. Many research focus on the improvement of physiological signal's quality by applying deep learning methods [6–10]. Similar as other physiological electrical signals, ABR is a potential difference-based signal that is recorded against a specific reference point. However, ABR signals are mainly characterized by weak amplitudes that typically range between 0.1 and 0.9 μV [11], thereby making it susceptible to interferences resulting from the electrical activity of the reference electrode. In electroencephalogram (EEG) studies, the commonly employed reference electrode methods include vertex (Cz), mean mastoid (MM), and average reference (AR) approaches [12]. Characterized by various advantages, each method also has some limitations in some ways. For instance, when the Cz reference approach is utilized, the recorded signals are usually affected by the electrophysiological activities around the Cz point [13]. For the MM approach, the average of the two mastoid electrodes is subtracted from the potential per time, which is a function of the potential changes associated with the mastoid electrodes [14]. Meanwhile, for the AR approach, the recorded data per electrode is subtracted from the overall average across electrodes per time, which is the most commonly adopted scheme, especially in the context of multichannel EEG signal analysis [15, 16]. Despite its wide adoption, the AR approach is characterized by some issues that have limited its adoption in large-scale clinical and commercial settings. One of such critical issues is that the potentials evoked based on the AR method do not only depend on the changes in the reference point but also on the potential changes that occur in the other surrounding electrodes. Besides, in situations where the selected reference points are different from absolute zero potentials, the ABR signals become inevitably affected.

In selecting a reference electrode, the potential should be as close to zero as possible; however, such point rarely exists on the scalp [17]. Meanwhile, inevitable alterations in the voltages at the reference electrode will cause a change in the recorded potential of the active electrode [18]. Therefore, in situations where the reference electrodes are different, the waveforms recorded from the same active electrode position would vary largely leading to inconsistent results [19]. In other words, the choice of the reference electrode is a key issue in obtaining reliable evoked potentials during EEG signal acquisition. In order to minimize the impact of reference electrode on evoked potential detection, previous studies have proposed the use of different kinds of reference methods [20–24]. For instance, in 2001, Yao proposed a "reference electrode standardization technique (REST)" that could approximately convert brain response recordings with a point on the scalp and an average potential as a reference with respect to a spatial infinity point [25]. The physical basis of the method is that the potentials before and after the conversion are generated by real neural activity in the brain or its equivalent distribution, such that the potentials before and after the conversion can be linked by a common physical source [26]. Yao et al. also proved the effectiveness of their proposed REST in the context of EEG spectral mapping [27], EEG default mode networks [28], and other event-related potentials (ERPs) [29–31].

To date, to the best of our knowledge, the application of REST in ABR for an effective assessment of hearing loss has not been conducted. Therefore, as a crucial step towards the effective evaluation of hearing loss, we systematically investigated the possibility of adopting REST technique for qualitative ABR signal assessment and subsequently compared its effectiveness with the commonly applied conventional AR and MM reference methods. Furthermore, we examined the influence of different reference methods on the quality of the acquired ABR waveforms with respect to the AR, REST, and MM methods while considering different stimulus rates and test levels. Meanwhile, we utilized 30 channels from a 64-channel EEG acquisition system to record ABR signals and compared the ABR waveforms at midline positions, especially the Cz channel. Finally, we studied the differentiable characteristics of the ABR waveforms across the three examined methods especially considering waves I-III-V and their amplitude properties to ascertain their merits and demerits with respect to hearing loss assessment. Finally, we studied the characteristics of ABR across the three examined methods by considering those typical wave (I, III, and V) morphologies and their amplitudes to ascertain their merits and demerits on hearing loss assessment.

2. Methods

2.1. Participants. In this study, a total of ten subjects without hearing defect (6 males and 4 females) with age range between 20 and 28 years (mean age = 24.6 years) were recruited for the EEG data collection. Prior to the experimental design, a standard audiogram test was carried out, and those whose audiogram thresholds were 20 dB hearing level (HL) or less for frequencies between 250 and 8000 Hz were chosen. The participants were properly briefed about the aim of the study and details of the experiments; afterward, a consent form indicating their willingness to participate in the study was signed by all the subjects. The entire experimental protocols were approved by the Institutional Review Board (IRB) of the Shenzhen Institutes of Advanced Technology, Chinese Academy of Sciences (SIAT-IRB-180415-H0252).

2.2. Equipment and Setup. The EEG recordings used to extract the evoked ABR signals were recorded using a Neuroscan SynAmps^2 (*NeuroScan, Inc.*) acquisition system. In the amplifier settings section, the sampling rate was configured to 20000 Hz and AC mode was selected. Then, the low pass filter was set to 3000 Hz, while the high pass filter was configured with a cut-off frequency of 100 Hz. Afterwards, the corresponding ABR signals were recorded using Ag/Agcl with 64-channel Quik-cap (*Neuromedical Supplies, Sterling, USA*), and according to the international extended 10/20 montage, 32 channels out of the 64 channels were considered for the analysis in the study [32]. Meanwhile, 30 channels out of the 32 channels are presented in Figure 1(a), and these channels are FP1, FP2, F7, F3,Fz, F4,F8,FT7,FC3,FCz, FC4, FT8, T7, C3, Cz,C4, T8, TP7,CP3, CPz, CP4, TP8,P7, P3, Pz, P4, P8, O1, Oz, and O2. Among these electrode channels, Fz, FCz, Cz, CPz, Pz, and Oz channels were arranged along the midline of the skull, while the remaining electrodes were located symmetrically on both sides of the midline (Figure 1(a)). Besides, the GND and REF electrodes on the EEG cap served as ground and online references, respectively. The remaining two channels were placed on the left and right mastoids (M1 and M2), which were later used for rereference purpose. For reconstructing the head model, a three-dimensional (3D) digitizer (*Polhemus, Colchester, VT, USA*) was used to measure the EEG electrodes' location on the scalp. As shown in Figure 1(b), the receivers of the 3D digitizer are placed on the left and right temples and occipital bulge, forming a triangular plane. The transmitter is placed on a tripod that is about 30 cm away from the subject's face, while the x-axis is positively oriented towards the subject's face. Sequentially, the selected electrodes were located according to the amplifier setting file.

2.3. Stimuli and Procedures. Generally, click-induced ABR method has been considered as a benchmark approach for estimating hearing loss [33]; hence, it was utilized as the stimulus mechanism produced by a customized printed circuit board (PCB) controlled by a MATLAB program in this study. Basically, click is referred to as a broadband signal, which is generated by an electric pulse with a width of 100 μs into the earphone. It should be noted that during the experiment, the stimuli were presented to the subject's left ear by an ER-2 insert earphone (*Etymotic Research Inc.*), with an earplug in the right ear. Besides, the stimuli were calibrated in normal hearing level (nHL) with an occluded ear simulator. Click-evoked ABRs that employed AR, REST, and MM reference methods were compared at different stimulus rates and levels.

Prior to the experiments, the participants were required to properly clean their hair so as to minimize the impedance between the electrodes of the Quik-cap and their scalp. Afterwards, they were told to sit in a comfortable chair in an acoustically and electromagnetically shielded room in a relatively calm/quiet manner. The Quik-cap was worn on the subject's head, and all the electrode impedances were maintained below 5 kΩ. Before the ABR acquisition commenced, the locations of the selected electrodes on the scalp were measured by the abovementioned 3D digitizer, and the 3D coordinates of the electrodes were captured and stored for further processing.

In the experiment, the ABR signal acquisition was accomplished in two sessions. In the first experimental session, we considered various stimulus rates including 10/s, 25/s, 50/s, and 100/s, in which the stimulus level was set at 75 dB nHL. Meanwhile, in the second experimental session, a constant stimulus rate of 25/s was applied, while the stimulus level was varied between 45 and 80 dB nHL, with the interval of 5 dB nHL. Meanwhile, each trial consisted of 4000 averages, and two independent trials were recorded for each stimulus condition to verify the repeatability of the response. It should be noted that the subjects were allowed to rest for about five minutes after every four trials to avoid nervous system-inclined fatigue which may affect the quality of the ABR recordings. Thereafter, the experiments for each subject lasted for about two hours, and the raw recorded data were saved on a storage device for subsequent offline processing and analysis.

2.4. Data Analysis. The acquired data were analyzed using the EEGLAB toolbox [34] that was integrated into MATLAB (*MathWorks Inc., USA*) computing software environment. The raw signals were firstly preprocessed by applying a 3 order butter worth band pass filter with cut-off frequencies of 100~1500 Hz. To investigate the effects of different reference electrode configurations on the signals' characteristics, the preprocessed EEG data (recorded via Ref as reference electrode) was reconstructed offline based on the AR, MM, and REST methods, respectively (Figure 2).

The AR and MM methods were implemented via the *pop_reref* inbuilt function in EEGLAB toolbox. In principle, the AR reference method could be realized by computing the average of all channels, while the MM method could be achieved by averaging the signals obtained from the left and right mastoids (also known as the average of the data from the M1 and M2 channels). Further, the REST method was implemented by converting the reconstructed signals via the REST EEGLAB plugin module developed by a group of researchers from the University of Electronic Science and Technology, Chengdu, China [25].The reconstruction process, which was shown in Figure 3, based on the REST module actually began with the execution of a program file named the *LeadField.exe* that firstly converted the 3D coordinates of the previously acquired signals to obtain a transfer matrix. Then, the EEG signal and the transfer matrix were converted to the REST-referenced data by utilizing *pop_REST_reref* inbuilt function. Thereafter, the EEG data reconstructed based on the three reference methods (AR, MM, and REST) were exported to the MATLAB programming environment for further analysis. It was worth noting that the continuous EEG data were divided into epochs with 10 msat the onset of each stimulus. Because the ABR is a low-amplitude signal and auditory-evoked potential, the ABR was extracted from the noised EEG signals by averaging technique to average all the segmentations. In this study, the target ABR signals were obtained by averaging 4000 epochs.

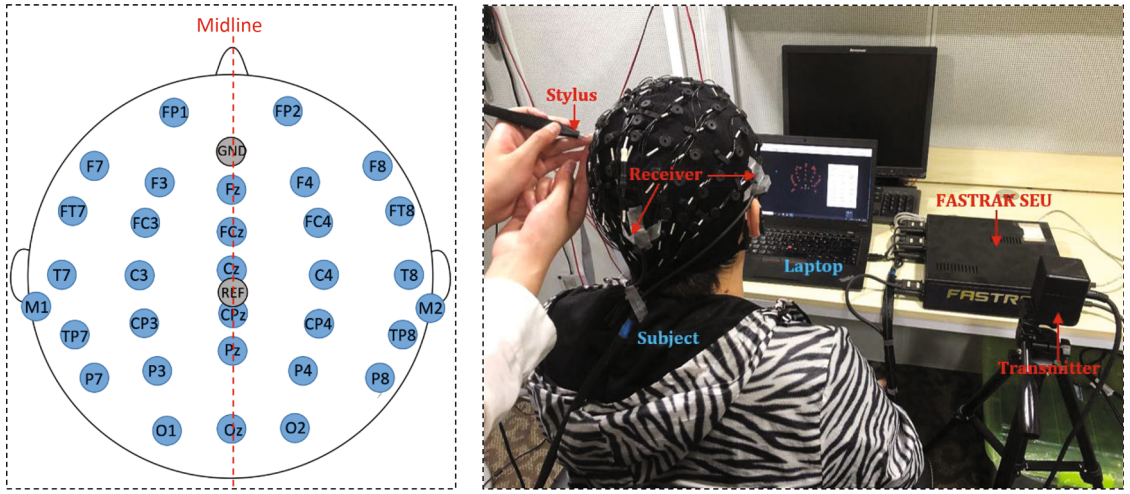

Figure 1: Electrode position distribution map and demonstration of 3D location of the electrodes on the scalp of a representative subject. (a) The distribution of the selected electrodes on the scalp of a representative subject according to the 10/20 international system standard. (b) The constructed head model based on the locations of the selected electrodes on the scalp by a 3D digitizer.

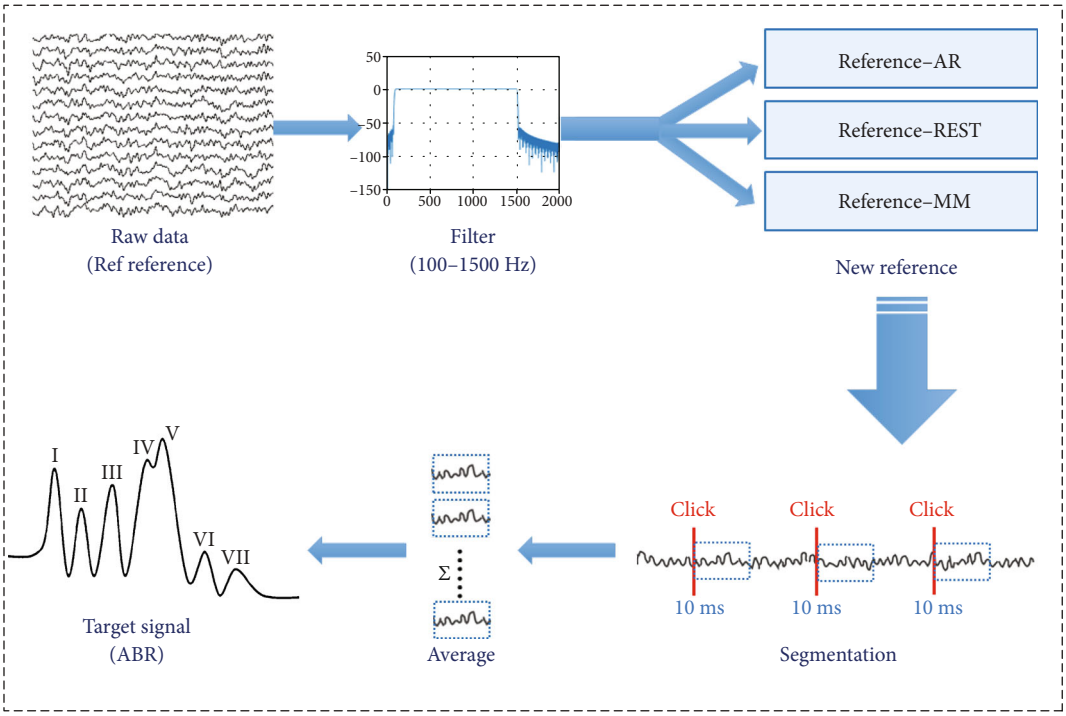

Figure 2: The schematic diagram of ABR acquisition and processing from raw EEG signals.

After a successful reconstruction process which took around 10 minutes, the effects of the different reference methods on the ABR waveform characteristics were examined by comparing the waveforms of the following electrode locations: Fz, FCz, Cz, CPz, Pz, and Oz in the midline using AR and REST reference methods. In addition, we compared the waveforms of the Cz channel when the reference methods were the AR, MM, and REST, focusing on the extent of waveform differentiation and wave V latency of ABR in the Cz channel with the stimulus rate and level.

3. Results

3.1. Analysis of ABRs Obtained along the Midline Channels via the AR and REST Methods. In this analysis, the ABR signals obtained via the AR and REST methods from the

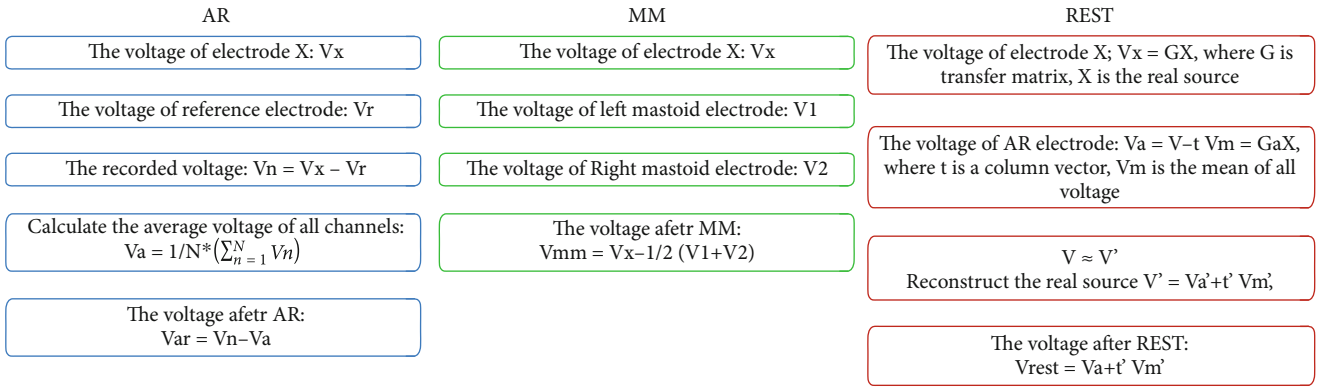

Figure 3: The flow chart of the given three algorithms.

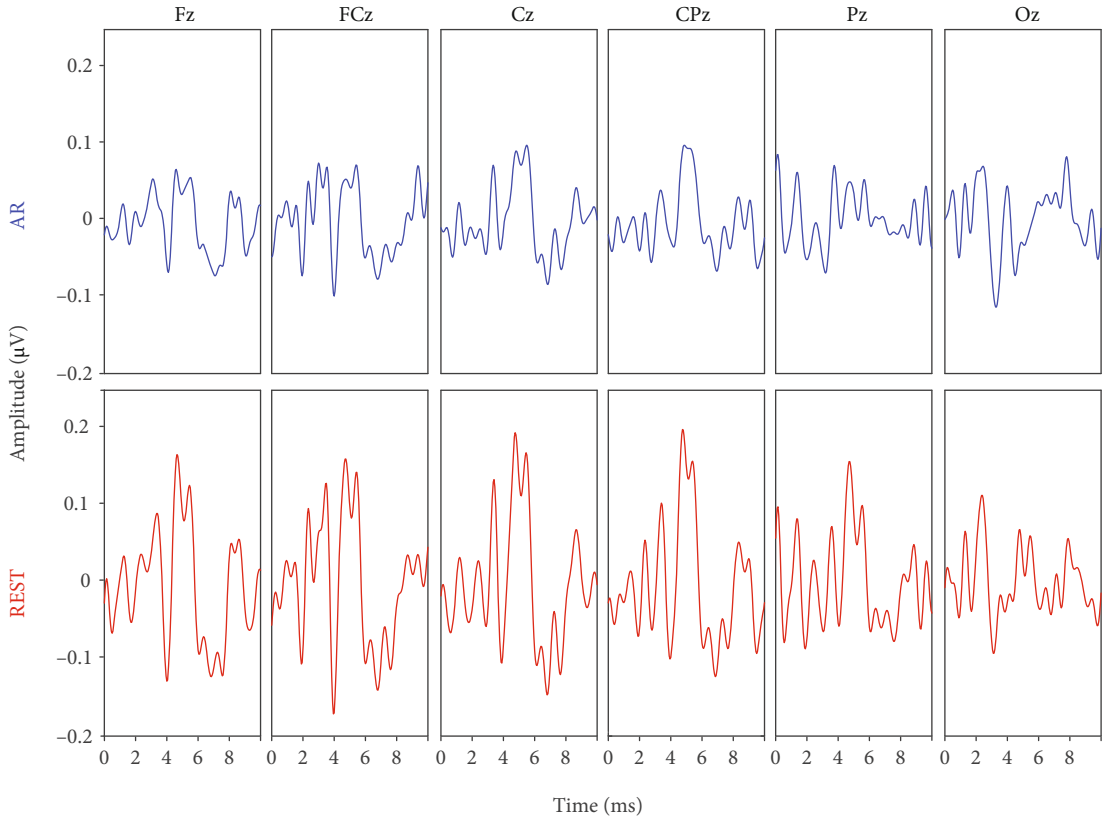

Figure 4: A representation of ABR waveforms of six channels along the midline (Fz, FCz, Cz, CPz, Pz, and Oz) at 75 dB nHL and a rate of 10/s. (a) Top row panels represented ABR obtained via the AR method. (b) Bottom row panels represented ABR obtained via the REST method.

electrodes placed along the midline channels on the Quikcap were analyzed and compared. From the processed data, it was observed that the signals picked up by the electrodes at the midline were better than those at other locations on the scalp. Therefore, we considered the ABR waveforms on Fz, FCz, Cz, CPz, Pz, and Oz electrodes located on the midline of the scalp in our subsequent analysis. As shown in Figure 4, a comparative analysis of the ABR waveforms obtained via the AR and REST methods from the abovementioned electrode channels at 75 dB nHL with a rate of 10/s was carried out. From the results, waves I, III, and V of ABR obtained from AR and REST on the Fz, FCz, Cz, CPz, and Pz channels could be clearly identified, while the ABR waveform processed by the REST method was observed to have a larger amplitude compared to that of the AR method. Moreover, the ABR waveform constructed from the Oz channel located on the occipital region using the AR method is poorly differentiated, thereby making it relatively difficult to identify the peaks in waves I, III, and V. Meanwhile, the ABR signals recorded at the Oz channel via the REST method were seen to be better than those obtained via the AR method, with clearly distinct wave V. In summary, regardless of the selected channel, the quality of the ABR waveform obtained via the REST method was

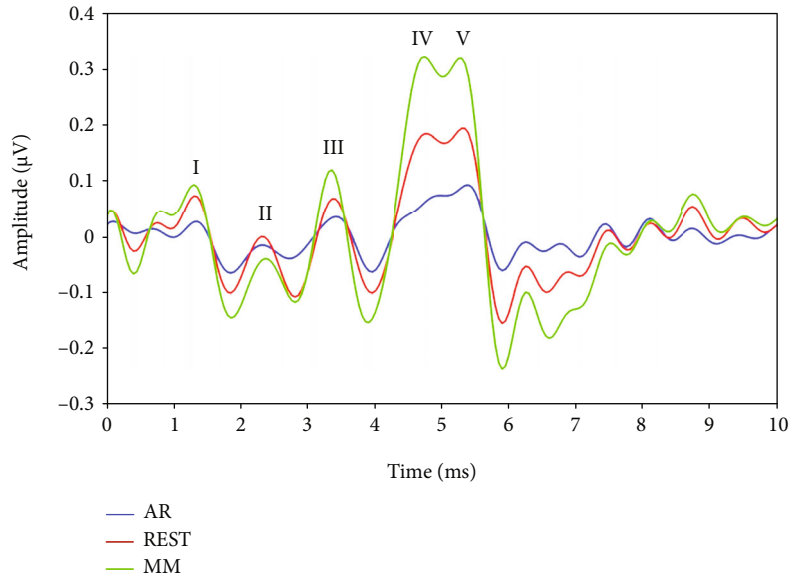

Figure 5: Representation of ABR waveforms of the Cz channel using the AR, REST, and MM reference methods under the condition of 75 dB nHL and 25/s.

observed to be better than that obtained from the AR method. Furthermore, we discovered that the ABR waveforms' differentiation in the Cz channel appeared to be the best irrespective of whether the AR or REST method was adopted for obtaining the ABR recordings. Hence, we considered the ABR recordings obtained from the Cz electrode channel in our subsequent analysis.

3.2. Comparison of ABR Signals in the Cz Channel Using the AR, REST, and MM Methods. In view of the above findings, we selected and compared the responses of the Cz channel recorded via the AR, REST, and MM methods under the condition of 75 dB nHL and 25/s (Figure 4). By carefully observing the waveforms in Figure 5, it could be seen that the amplitude of the ABR signals obtained via the AR method was slightly lower (only 0.1 μV) compared to that of the other two methods. Although the waves I-V could be adequately recognized, their differentiation seemed to be poor, especially those of waves IV and V. Compared with the AR method, the ABR waveform obtained via the REST method has better differentiation and higher amplitude characteristics, while the waveform differentiation of the ABR recordings obtained via the MM method was similar to that of REST but with relatively higher amplitudes. Although the amplitude of ABR signals was different with different reference methods, the latency of ABR waves I-V obtained was the same.

Table 1 shows the mean amplitudes and the standard deviation of waves I, III and V for ABRs obtained by the AR, REST, and MM methods across all the subjects ($N = 10$ ears). Obviously, the ABR obtained by the MM method had the highest mean amplitudes, and its wave V mean amplitude was as high as 0.27 μV. The mean amplitudes of the ABR obtained via the REST method were lower than those of the MM method, in which the mean amplitude of wave V was 0.21 μV. The mean amplitude of the ABR by the AR method was the lowest, with the mean amplitude of wave V of 0.08 μV. Table 2 showed the mean and standard deviation of interwave latencies for waves I-III and III-V of ABRs obtained by the AR, REST, and MM methods, which were derived from the same raw data as Table 1. As shown in Table 2, the ABRs obtained by the three reference methods (AR, REST, and MM) had the same interwave latencies for waves I-III and III-V, which proved that the reference methods could improve the ABR on the aspect of amplitude but without essentially affecting the waveform on the latency.

Table 1: The amplitudes (μV) of waves I, III and V of the ABRs obtained by the AR, REST, and MM methods at a level of 75 dB nHL and a rate of 25/s (mean and standard deviation; $N = 10$ ears).

Method	Wave I		Wave III		Wave V	
	Mean	SD	Mean	SD	Mean	SD
AR	0.02	0.02	0.03	0.01	0.08	0.03
REST	0.06	0.02	0.07	0.02	0.21	0.04
MM	0.09	0.04	0.11	0.05	0.27	0.07

Table 2: The interwave latencies (ms) for waves I-III and III-V of the ABRs obtained by the AR, REST, and MM methods at a level of 75 dB nHL and a rate of 25/s (mean and standard deviation; $N = 10$ ears).

Method	Wave I-III		Wave III-V	
	Mean	SD	Mean	SD
AR	2.05	0.11	1.95	0.08
REST	2.05	0.11	1.95	0.08
MM	2.05	0.11	1.95	0.08

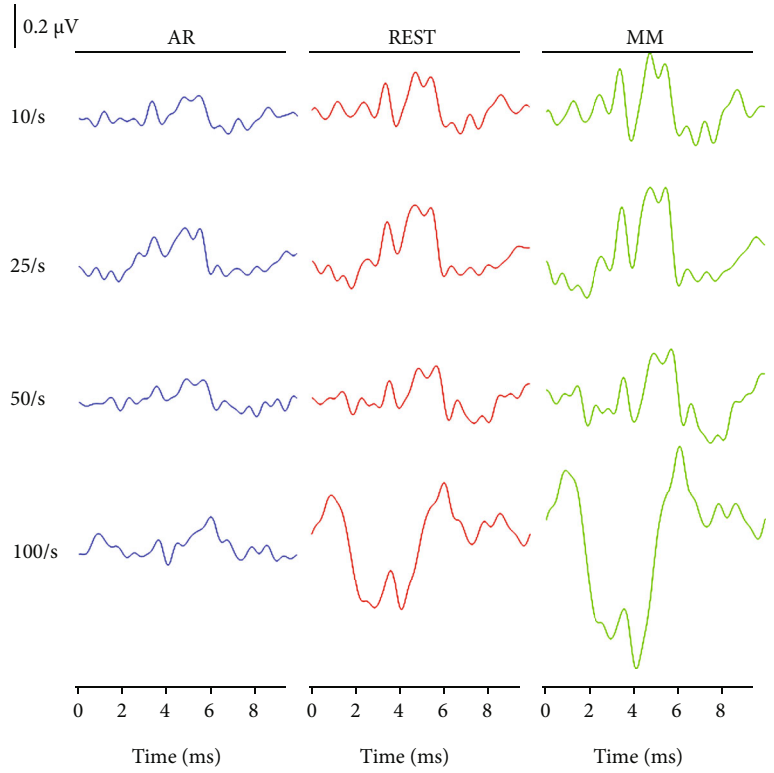

Figure 6: The ABR waveforms of the Cz channel obtained via the AR (left panel), REST (middle panel), and MM (right panel) methods, correspondingly. Note: the stimulation level is 75 dB nHL, and the stimulus rate varies from 10 to 100/s, as indicated.

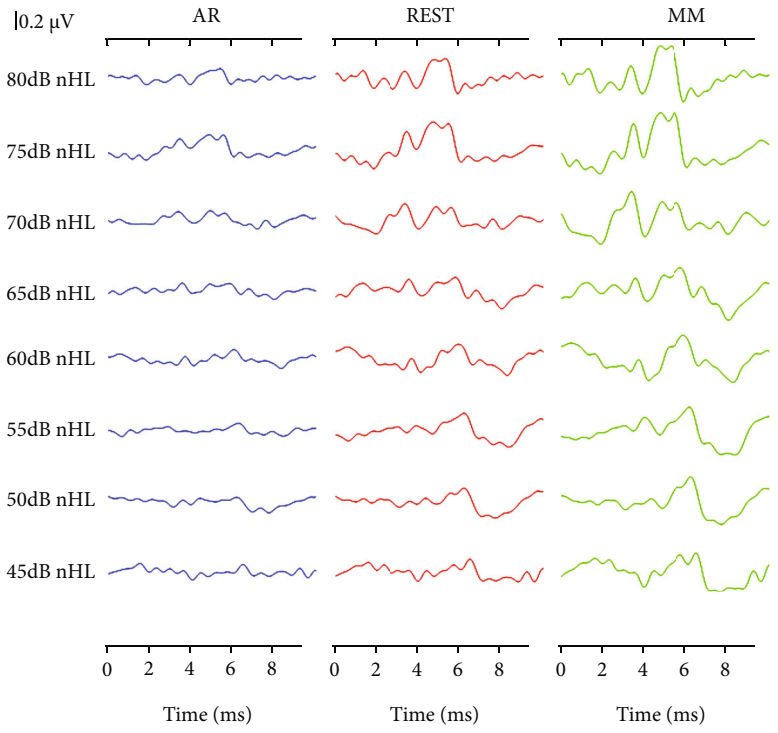

Figure 7: The ABR waveforms of the Cz channel obtained via the AR (left panel), REST (middle panel), and MM (right panel) methods, respectively. The stimulation level varied from 80 to 45 dB nHL, and the stimulus rate was 25/s.

3.3. ABRs of the Three Reference Methods in the Cz with Different Stimulus Rate and Intensity. To further examine whether the conclusion reached in the previous analyses (Figure 4) could be influenced by variation in stimulus rates and levels, we compared the ABR waveforms of the Cz channel using the AR, REST, and MM methods under the influence of varying stimulus rates and levels, and the experimental results were presented in Figures 6 and 7. Figure 6 represented the ABR waveforms obtained using the Cz channel at a stimulus level of 75 dB nHL under stimulus rates of 10/s, 25/s, 50/s, and 100/s. It could be noticed in Figure 6 that the latency of wave V increased with a corresponding increase in stimulus rate, while the waveform at lower stimulus rate was observed to have better waveform differentiation characteristics (waves I-V). These findings were in line with the conclusion of a previous study [35], and we also found that a correlation existed between the latency and stimulus rate regardless of the reference method adopted. This invariably meant that regardless of the stimulus rate (10/s, 20/s or 50/s) applied, the five peaks (waves I-V) of the ABR waveform obtained via the AR method would still be inadequately differentiated. Meanwhile, the waveforms of the ABR obtained via the REST and MM methods at the stimulus rates of 10/s, 20/s, and 50/s, were well differentiated, especially when the stimulus rate was set to 10/s (Figure 6). This phenomenon exhibited by the examined reference methods would result in easy recognition of the ABR waveforms in the context of the five peaks (waves I-V). Furthermore, the amplitudes of the ABR signals obtained through the REST and MM methods were obviously higher than those of the AR method. When considering the ABR under stimulus rate of 100/s, the waveforms obtained via the three reference methods become less distinguishable, which might be due to the stimulus interval of only 10 ms, resulting from the middle latency component of the response induced by the previous stimulus affecting the ABR induced by the latter stimulus. Compared with the ABR obtained via the AR method at the rate of 100/s, waves III and V could also be clearly identified using the REST and MM methods.

From Figure 7, it could be observed that the ABR recordings of the Cz channel obtained via the three reference methods at a rate of 25/s exhibited different characteristics. Moreover, the ABR latency was delayed, and the waveform differentiation became worse with a decrease in stimulus intensity. It should be noted that these trends were independent of the reference methods. Therefore, regardless of the stimulus level, the ABR waveform differentiation obtained via the AR method was not as good as the ones obtained through the REST and MM methods. Meanwhile, at the same stimulus level, the MM method had the largest amplitude followed by the REST method, and the AR method was with the smallest ABR amplitude. It should be noted that this phenomenon was consistent with the conclusion drawn from Figure 5.

4. Discussion

The main contribution of this study was to investigate the characteristics of the REST technique of ABR signal processing in comparison to the commonly applied reference methods, which helped with the improvement of the ABR-based decision-making implication on hearing loss. Although we utilized the Quik-cap EEG system to acquire 30 channels of ABR signals, only the recordings of 6 channels located along the midline were considered for the study, based on the analysis of the signal quality. Specifically, we compared the ABR signals corresponding to the Cz channel obtained via the AR, REST, and MM methods and their characteristics when subjected to different stimulus rates and levels. From series of experimental results, we found that the REST method would be effective for ABR signal recording, and the quality of the ABR signal obtained via the REST technique was much better than that of the conventional AR method, but not superior to that of the MM method. In addition, a similar phenomenon for the three methods was observed across different stimulus rates as well as levels.

4.1. ABRs in the Midline Channels via the AR and REST Methods. In order to verify the feasibility of applying the REST method for ABR signal acquisition, we compared the ABR recordings obtained by the REST method with that obtained via the traditionally applied AR method. Preliminary processing of the raw data showed that the quality of ABR waveforms obtained from the midline channels was better than that of the other channels. Besides, the electrodes located at the vertex or forehead were usually chosen as the active electrode in the single-channel ABR acquisition [36]. Similar to the findings of this study, Moulton et al. proposed a midline electrode configuration that could avoid priority recording from either side of a subjects' head [37]. In line with these previous studies, we compared the ABR signals of the six channels (Fz, FCz, Cz, CPz, Pz, and Oz) along with the midline position as shown in Figure 3, and the experimental results showed that the ABR waveforms obtained via the REST method were obviously distinguishable compared to those of the AR method, which was also consistent with the findings on event-related potential by Dong et al. [38]. It should be noted that the AR method was based on the average potential of all recording electrodes, which was affected by the density of the electrodes. Theoretically, when the scalp electrodes are dense enough, the potential obtained via the AR method would approach the expected value [39]. Thus, the REST method can approximately correct the reference value to the infinite point and therefore make up for the disadvantage that the conventional method has.

4.2. ABRs in Cz Channel Obtained via AR, REST, and MM Methods. From Figure 3, the ABR signal at the Cz channel appeared to provide best performance among the electrodes on the midline, which was consistent with the findings from the previous studies on auditory-evoked potentials [40, 41]. In this direction, Beattie and Lipp compared the latency and amplitude of the ABR collected from the vertex and the forehead as active electrodes, respectively [40]. Their results showed that there was no significant difference in the latency and interwave latency between the two active electrode positions, but the wave V amplitude of the ABR obtained from the vertex was larger than the one obtained

from the forehead. Therefore, the ABR waveform of the Cz channel was mainly focused and compared as presented in Figure 4. Meanwhile, the results indicated that the amplitude of the ABR waveform obtained through the MM method was the highest, followed by the REST method, while the AR method was the smallest. This conclusion was consistent with the findings from a previous study on auditory mismatch negativity by Mahajan et al. [42]. Hence, we concluded that the ABR amplitude obtained via the MM method was larger than that of REST, which may be due to the fact that bilateral mastoids are adjacent to the ankle occipital region, where task-related electrical activities are inevitably incorporated into the calculation of MM reference method. In most cases, this weakens the signal in the bilateral occipital region, while the amplitude of the signal away from the bilateral mastoid site (i.e., the central frontal region) may increase erroneously. The potential error at the mastoid may also increase the amplitude of the Cz channel, resulting in a larger amplitude of ABR for the MM method than for the REST method.

4.3. Characteristics of the ABRs Obtained across Stimulus Rates and Levels. The morphology of the ABR waveforms obtained via the REST and MM methods was obviously better than that obtained via the AR method. When the stimulus condition was set at 75 dB nHL and a rate of 25/s, the ABR amplitude of the MM method appeared to be the largest, followed by the REST method, and the AR method ranked last, which was verified in Figure 4. Meanwhile, Figures 5 and 6 presented the comparative results of ABR obtained by the three reference methods with adjustments in stimulus rates and levels. Regardless of what stimulus rates and levels were applied, the ABR obtained via the MM and REST methods was often better than the AR method. This invariably meant that the conclusions from Figure 4 were valid. However, the latency of the ABR obtained based on the three reference methods was always the same, even if the stimulus rate and level change. This meant that the reference method only changes the representation of the ABR signal, without affecting the nature of the signal, since the physician always make the diagnosis based on the characteristics of the latency. This clearly demonstrated that an effective reference method could efficiently reconstruct the target signal towards improving its quality.

In addition, the latency of the ABR waveform was observed to be highly prolonged with a corresponding increase in the stimulus rate. Moreover, the lower the stimulus rate, the better the waveform differentiation of waves I-V. However, when the stimulus rate was much high, for instance, 100/s, the ABR obtained through the three reference methods becomes very poor (Figure 5). This is possible for the following reasons. The ABR is an early component of auditory-evoked potential (AEP), which occurs between 0 and 10 ms after an acoustic stimulus, and it is characterized by an auditory middle latency response (MLR) after the acoustic stimulus 10 ms [43]. When the stimulus rate is 100/s, the stimulus interval is only 10 ms, which results in the MLR induced by the previous stimulus superimposed on the ABR waveform induced by the latter stimulus. Therefore, whether reference methods are applied, it is necessary to keep the stimulus rate lower than 100/s to assure a meaningful ABR can be acquired.

4.4. REST for Medical ABR Application Scenarios. In clinical, the physicians make diagnosis based on the characteristics of ABR such as the morphology, the amplitude of waves, the wave latency, and the interwave latency [44, 45]. However, all these parameters needed are heavily related to the ABR signal quality and the morphology. For example, the interwave latency of waves III and IV could be used to infer the axonal conduction time, while the interwave latency of IV and V represents a synaptic delay [46]. Besides, as reported by J. Lee et al., the amplitude of wave II was regarded as an indicator that helped in diagnosing vestibular paroxysmia [47].Therefore, once the ABR quality or morphology is poor, the parameters needed will be obscure which will also cause difficulty for the physicians to make corresponding diagnosis. Hence, it is meaningful and helpful to improve the ABR quality on the aspects of morphology and amplitude. In this manuscript, the REST-based ABR had been systematically investigated in comparison with the traditional AR method. Our results suggested that the REST method could significantly improve the amplitude of waves I (0.06 ± 0.02 μV), III ($0.07 \pm 0.02\,\mu$V), and V ($0.21 \pm 0.04\,\mu$V) when compared with the traditional AR methods ($0.02 \pm 0.02\,\mu$V for wave I, $0.03 \pm 0.01\,\mu$V for wave III, and $0.08 \pm 0.03\,\mu$V for wave V). Moreover, it should be pointed out that the improvement on the morphology and amplitude of ABR was achieved by unchanging the latency of each wave, which meant that the REST method-based ABR could provide physicians as the consistent latency-based information as the traditional AR method did. In consequence, the REST method would assist physicians in ABR-based diagnosis of hearing loss and other auditory diseases, with the significant improvement in ABR morphologies, making it more meaningful in medical application scenarios.

5. Conclusions

The study demonstrated that the REST method could be effectively applied for high-quality ABR signal recording, which might be potential for the improvement of ABR-based decision-making implications over the public health issue like hearing loss. The ABRs obtained via the MM and REST methods had better waveform morphologies in comparison to that of the AR method. Moreover, the ABR amplitude obtained through the MM method was observed to be the highest, followed by the REST, and subsequently the AR method. In addition, the latency of the ABRs obtained by the AR, REST, and MM methods appeared to be the same under the same stimulus conditions. This phenomenon was also observed across different stimulus rates and levels, which meant that the reference methods only affected the degree of differentiation and amplitude of the ABR waveform, without changing the latency of each peak. For the ABR signals, the amplitude, which was an important indicator in EEG research, would be directly affected by the selected reference method as shown in our experiments.

Therefore, the selection of an objective and effective reference method could help improve the quality of the ABR waveform and aid efficient signal analysis and processing that may be potential in clinical applications.

Data Availability

The data used to support the findings of this study are available from the corresponding author upon request.

Conflicts of Interest

The authors declare that they have no competing interests.

Authors' Contributions

Zhenzhen Liu and Xin Wang contributed equally to this work.

Acknowledgments

This work was supported in part by the National Natural Science Foundation of China (#61771462, #81927804, and #62101538), Science and Technology Planning Project of Shenzhen (#JCYJ20180507182241622, #JCYJ20210324135211030, and #JSGG20210713091808027), CAAE Epilepsy Research Funding (CU-C-2021-02), Sanming Project of Medicine in Shenzhen (SZSM201812005), Shenzhen Fund for Guangdong Provincial High Level Clinical Key Specialties (SZGSP012), Shenzhen Key Medical Discipline Construction Fund (SZXK033), Science and Technology Planning Project of Guangdong Province (#2019A050510033), SIAT Innovation Program for Excellent Young Researchers (E1G027), and Science and Technology Program of Guangzhou (#201803010093).

References

[1] D. L. Jewett, M. N. Romano, and J. S. Williston, "Human auditory evoked potentials: possible brain stem components detected on the scalp," *Science*, vol. 167, no. 3924, pp. 1517-1518, 1970.

[2] S. Khullar and R. Babbar, "Presbycusis and auditory brainstem responses: a review," *Asian Pacific Journal of Tropical Disease*, vol. 1, no. 2, pp. 150–157, 2011.

[3] A. R. D. Thornton, L. Kimm, and C. R. Kennedy, "Methodological factors involved in neonatal screening using transient-evoked otoacoustic emissions and automated auditory brainstem response testing," *Hearing Research*, vol. 182, no. 1-2, pp. 65–76, 2003.

[4] D. L. Jewett and J. S. Williston, "Auditory-evoked far fields averaged from the scalp of humans," *Brain*, vol. 94, no. 4, pp. 681–696, 1971.

[5] A. R. Møller and P. Jannetta, "Neural generators of the auditory brainstem response," in *The auditory brainstem response*, pp. 13–31, College-Hill Press San Diego, 1985.

[6] K. Muhammad, S. Khan, J. D. Ser, and V. H. C. . Albuquerque, "Deep learning for multigrade brain tumor classification in smart healthcare systems: a prospective survey," *IEEE Transactions on Neural Networks and Learning Systems*, vol. 32, no. 2, pp. 507–522, 2021.

[7] M. Miao, W. Hu, B. Xu, J. Zhang, J. J. Rodrigues, and V. H. C. de Albuquerque, "Automated CCA-MWF algorithm for unsupervised identification and removal of EOG artifacts from EEG," *IEEE Journal of Biomedical and Health Informatics*, p. 1, 2021.

[8] K. Muhammad, A. Mustaqeem, A. S. Ullah et al., "Human action recognition using attention based LSTM network with dilated CNN features," *Future Generation Computer Systems*, vol. 125, pp. 820–830, 2021.

[9] H. Zhang, H. Zhang, S. Pirbhulal, W. Wu, and V. H. C. D. Albuquerque, "Active balancing mechanism for imbalanced medical data in deep learning–based classification models," *ACM Transactions on Multimedia Computing, Communications, and Applications (TOMM)*, vol. 16, no. 1s, pp. 1–15, 2020.

[10] J. Cui, L. Wang, X. He, V. H. C. De Albuquerque, S. A. AlQahtani, and M. M. Hassan, "Deep learning-based multidimensional feature fusion for classification of ECG arrhythmia," *Neural Computing and Applications*, 2021.

[11] G. Moushegian, A. L. Rupert, and R. D. Stillman, "Scalp-recorded early responses in man to frequencies in the speech range," *Electroencephalography and Clinical Neurophysiology*, vol. 35, no. 6, pp. 665–667, 1973.

[12] C. Hesse, E. Seiss, R. Bracewell, and P. Praamstra, "Absence of gaze direction effects on EEG measures of sensorimotor function," *Clinical Neurophysiology*, vol. 115, no. 1, pp. 29–38, 2004.

[13] D. Lehmann, W. Strik, B. Henggeler, T. König, and M. Koukkou, "Brain electric microstates and momentary conscious mind states as building blocks of spontaneous thinking: I. visual imagery and abstract thoughts," *International Journal of Psychophysiology*, vol. 29, no. 1, pp. 1–11, 1998.

[14] A. Gevins and M. E. Smith, "Neurophysiological measures of working memory and individual differences in cognitive ability and cognitive style," *Cerebral Cortex*, vol. 10, no. 9, pp. 829–839, 2000.

[15] J. Dien, "Issues in the application of the average reference: review, critiques, and recommendations," *Behavior Research Methods, Instruments, & Computers*, vol. 30, no. 1, pp. 34–43, 1998.

[16] P. L. Nunez, B. M. Wingeier, and R. B. Silberstein, "Spatial-temporal structures of human alpha rhythms: theory, microcurrent sources, multiscale measurements, and global binding of local networks," *Human Brain Mapping*, vol. 13, no. 3, pp. 125–164, 2001.

[17] P. L. Nunez and R. Srinivasan, "A theoretical basis for standing and traveling brain waves measured with human EEG with implications for an integrated consciousness," *Clinical Neurophysiology*, vol. 117, no. 11, pp. 2424–2435, 2006.

[18] Y. Tian and D. Yao, "Why do we need to use a zero reference? Reference influences on the ERPs of audiovisual effects," *Psychophysiology*, vol. 50, no. 12, pp. 1282–1290, 2013.

[19] J. Kayser and C. E. Tenke, "In search of the Rosetta Stone for scalp EEG: converging on reference-free techniques," *Clinical Neurophysiology: Official Journal of the International Federation of Clinical Neurophysiology*, vol. 121, no. 12, pp. 1973–1975, 2010.

[20] P. Yang, C. Fan, M. Wang, and L. Li, "A comparative study of average, linked mastoid, and REST references for ERP components acquired during fMRI," *Frontiers in Neuroscience*, vol. 11, p. 247, 2017.

[21] L. T. Trujillo, C. T. Stanfield, and R. D. Vela, "The effect of electroencephalogram (EEG) reference choice on information-theoretic measures of the complexity and integration of EEG signals," *Frontiers in Neuroscience*, vol. 11, p. 425, 2017.

[22] F. Chella, A. D'Andrea, A. Basti, V. Pizzella, and L. Marzetti, "Non-linear analysis of scalp EEG by using bispectra: the effect of the reference choice," *Frontiers in Neuroscience*, vol. 11, p. 262, 2017.

[23] F. Chella, V. Pizzella, F. Zappasodi, and L. Marzetti, "Impact of the reference choice on scalp EEG connectivity estimation," *Journal of Neural Engineering*, vol. 13, no. 3, 2016.

[24] X. Lei and K. Liao, "Understanding the influences of EEG reference: a large-scale brain network perspective," *Frontiers in Neuroscience*, vol. 11, p. 205, 2017.

[25] D. Yao, "A method to standardize a reference of scalp EEG recordings to a point at infinity," *Physiological Measurement*, vol. 22, no. 4, pp. 693–711, 2001.

[26] Y. Zhai and D. Yao, "A study on the reference electrode standardization technique for a realistic head model," *Computer Methods and Programs in Biomedicine*, vol. 76, no. 3, pp. 229–238, 2004.

[27] D. Yao, L. Wang, R. Oostenveld, K. D. Nielsen, L. Arendt-Nielsen, and A. C. Chen, "A comparative study of different references for EEG spectral mapping: the issue of the neutral reference and the use of the infinity reference," *Physiological Measurement*, vol. 26, no. 3, pp. 173–184, 2005.

[28] Y. Qin, P. Xu, and D. Yao, "A comparative study of different references for EEG default mode network: the use of the infinity reference," *Clinical Neurophysiology*, vol. 121, no. 12, pp. 1981–1991, 2010.

[29] F. Li, T. Liu, F. Wang et al., "Relationships between the resting-state network and the P3: evidence from a scalp EEG study," *Scientific Reports*, vol. 5, no. 1, p. 15129, 2015.

[30] D. Yao, L. Wang, L. Arendt-Nielsen, and A. C. Chen, "The effect of reference choices on the spatio-temporal analysis of brain evoked potentials: the use of infinite reference," *Computers in Biology and Medicine*, vol. 37, no. 11, pp. 1529–1538, 2007.

[31] Y. Tian, W. Xu, H. Zhang et al., "The scalp time-varying networks of N170: reference, latency and information flow," *Frontiers in Neuroscience*, vol. 12, p. 250, 2018.

[32] R. Oostenveld and P. Praamstra, "The five percent electrode system for high-resolution EEG and ERP measurements," *Clinical Neurophysiology*, vol. 112, no. 4, pp. 713–719, 2001.

[33] S. Zirn, J. Louza, V. Reiman, N. Wittlinger, J. M. Hempel, and M. Schuster, "Comparison between ABR with click and narrow band chirp stimuli in children," *International journal of pediatric otorhinolaryngology*, vol. 78, no. 8, pp. 1352–1355, 2014.

[34] A. Delorme and S. Makeig, "EEGLAB: an open source toolbox for analysis of single-trial EEG dynamics including independent component analysis," *Journal of Neuroscience Methods*, vol. 134, no. 1, pp. 9–21, 2004.

[35] Y. Ben-David, H. Pratt, L. Landman, M. Fradis, L. Podoshin, and D. Yeshurun, "A comparison of auditory brain stem evoked potentials in hyperlipidemics and normolipemic subjects," *The Laryngoscope*, vol. 96, no. 2, pp. 186–189, 1986.

[36] G. M. Bidelman and A. S. Khaja, "Spectrotemporal resolution tradeoff in auditory processing as revealed by human auditory brainstem responses and psychophysical indices," *Neuroscience Letters*, vol. 572, pp. 53–57, 2014.

[37] B. Moulton, F. Milliken, R. Brey, and K. Jones, "Electrode placement for binaural auditory brainstem responses," *The Journal of the Acoustical Society of America*, vol. 68, no. S1, pp. S38–S38, 1980.

[38] L. Dong, F. Li, Q. Liu et al., "MATLAB toolboxes for reference electrode standardization technique (REST) of scalp EEG," *Frontiers in Neuroscience*, vol. 11, p. 601, 2017.

[39] D. B. Geselowitz, "The zero of potential," *IEEE Engineering in MedicineBiology Magazine*, vol. 17, no. 1, pp. 128–132, 1998.

[40] R. C. Beattie and L. A. Lipp, "Effects of electrode placement on the auditory brainstem response using ear canal electrodes," *The American Journal of Otology*, vol. 11, no. 5, pp. 314–319, 1990.

[41] S. K. Mamo, J. H. Grose, and E. Buss, "Speech-evoked ABR: effects of age and simulated neural temporal jitter," *Hearing Research*, vol. 333, pp. 201–209, 2016.

[42] Y. Mahajan, V. Peter, and M. Sharma, "Effect of EEG referencing methods on auditory mismatch negativity," *Frontiers in Neuroscience*, vol. 11, p. 560, 2017.

[43] K. T. Kavanagh and J. V. Beardsley, "Brain stem auditory evoked response: I. basic principles and clinical applications in the assessment of patients with nonorganic hearing loss," *Annals of Otology, Rhinology, and Laryngology*, vol. 88, 4_supplement, pp. 1–10, 1979.

[44] X. Wang, M. Zhu, O. W. Samuel et al., "The effects of random stimulation rate on measurements of auditory brainstem response," *Frontiers in Human Neuroscience*, vol. 14, pp. 78–78, 2020.

[45] X. Li, *Fundamental and Application of Auditory Evoked Repsponse*, Peoples Military Medical Press, Beijing, China, 2007.

[46] L. S. De Vries and H. C. Glass, *Neonatal Neurology: Handbook of Clinical Neurology Series*, Elsevier, 2019.

[47] J. H. Lee, S.-K. Hong, H.-J. Kim, and H.-J. Lee, "Is the auditory brainstem response diagnostic for vestibular paroxysmia?," *Research in Vestibular Science*, vol. 17, no. 2, pp. 55–59, 2018.

Hindawi
Computational and Mathematical Methods in Medicine
Volume 2023, Article ID 9828704, 1 page
https://doi.org/10.1155/2023/9828704

Retraction

Retracted: Retinal Vessel Automatic Segmentation Using SegNet

Computational and Mathematical Methods in Medicine

Received 17 October 2023; Accepted 17 October 2023; Published 18 October 2023

This article has been retracted by Hindawi following an investigation undertaken by the publisher [1]. This investigation has uncovered evidence of one or more of the following indicators of systematic manipulation of the publication process:

(1) Discrepancies in scope

(2) Discrepancies in the description of the research reported

(3) Discrepancies between the availability of data and the research described

(4) Inappropriate citations

(5) Incoherent, meaningless and/or irrelevant content included in the article

(6) Peer-review manipulation

The presence of these indicators undermines our confidence in the integrity of the article's content and we cannot, therefore, vouch for its reliability. Please note that this notice is intended solely to alert readers that the content of this article is unreliable. We have not investigated whether authors were aware of or involved in the systematic manipulation of the publication process.

Wiley and Hindawi regrets that the usual quality checks did not identify these issues before publication and have since put additional measures in place to safeguard research integrity.

We wish to credit our own Research Integrity and Research Publishing teams and anonymous and named external researchers and research integrity experts for contributing to this investigation.

The corresponding author, as the representative of all authors, has been given the opportunity to register their agreement or disagreement to this retraction. We have kept a record of any response received.

References

[1] X. Xu, Y. Wang, Y. Liang et al., "Retinal Vessel Automatic Segmentation Using SegNet," *Computational and Mathematical Methods in Medicine*, vol. 2022, Article ID 3117455, 11 pages, 2022.

Hindawi
Computational and Mathematical Methods in Medicine
Volume 2022, Article ID 3117455, 11 pages
https://doi.org/10.1155/2022/3117455

Research Article

Retinal Vessel Automatic Segmentation Using SegNet

Xiaomei Xu, Yixin Wang, Yu Liang, Siyuan Luo, Jianqing Wang, Weiwei Jiang, and Xiaobo Lai

School of Medical Technology and Information Engineering, Zhejiang Chinese Medical University, Hangzhou 310053, China

Correspondence should be addressed to Xiaobo Lai; dmia_lab@zcmu.edu.cn

Received 10 January 2022; Revised 10 March 2022; Accepted 12 March 2022; Published 26 March 2022

Academic Editor: Plácido R. Pinheiro

Extracting retinal vessels accurately is very important for diagnosing some diseases such as diabetes retinopathy, hypertension, and cardiovascular. Clinically, experienced ophthalmologists diagnose these diseases through segmenting retinal vessels manually and analysing its structural feature, such as tortuosity and diameter. However, manual segmentation of retinal vessels is a time-consuming and laborious task with strong subjectivity. The automatic segmentation technology of retinal vessels can not only reduce the burden of ophthalmologists but also effectively solve the problem that is a lack of experienced ophthalmologists in remote areas. Therefore, the automatic segmentation technology of retinal vessels is of great significance for clinical auxiliary diagnosis and treatment of ophthalmic diseases. A method using SegNet is proposed in this paper to improve the accuracy of the retinal vessel segmentation. The performance of the retinal vessel segmentation model with SegNet is evaluated on the three public datasets (DRIVE, STARE, and HRF) and achieved accuracy of 0.9518, 0.9683, and 0.9653, sensitivity of 0.7580, 0.7747, and 0.7070, specificity of 0.9804, 0.9910, and 0.9885, F_1 score of 0.7992, 0.8369, and 0.7918, MCC of 0.7749, 0.8227, and 0.7643, and AUC of 0.9750, 0.9893, and 0.9740, respectively. The experimental results showed that the method proposed in this research presented better results than many classical methods studied and may be expected to have clinical application prospects.

1. Introduction

Retinal vessel location actually is also important to serve as a structural marker to represent retinal anatomy. For example, prior studies have shown that retinal vessel locations are relatively stable in glaucoma and eyes with different retinal vessel locations correspond to different retinal anatomies, which can affect the diagnostic accuracy of using existing normative data.

With the change of lifestyles, the incidence of diseases such as diabetes, glaucoma, and hypertension has increased significantly in the modern society [1]. These diseases may cause retinopathy, and severe cases may result in visual impairment and blindness. And they can be diagnosed noninvasively by analysing the structural features of retinal vessels such as location [4] and tortuosity and diameter [2]. If these structural changes can be detected in the early stage, it will play an important role in the treatment of these diseases [3]. Clinical diagnosis of these diseases is done by experienced ophthalmologists who segment the retinal vessels manually to obtain their structural features. However, the manual segmentation of retinal vessels is tedious and requires a lot of time and energy [8]. The automatic segmentation of retinal vessels can reduce the work intensity of experienced ophthalmologists, and it has objectivity and repeatability. It can also solve the problem effectively that is a lack of experienced ophthalmologists in remote areas. Therefore, the automatic segmentation technology of retinal vessels is of great significance for clinical auxiliary diagnosis and treatment of ophthalmic diseases.

Due to the influence of uneven brightness, low contrast, retinopathy, and other retinal structures such as optic disc, automatic segmentation of retinal vessels in color fundus images is a challenging task. However, for its great significance of auxiliary medical treatment, there have been many findings in this field. To extract retinal vessels, Cao et al. proposed a method with matched filtering and automatic threshold and obtained the accuracy of 0.9174 on the DRIVE dataset [6].

Cai et al. presented a retinal vessel segmentation method based on phase stretch transform and multiscale Gaussian filter, which can improve the segmentation accuracy [5]. It is difficult for the thin vessel segmentation. Zhou et al. proposed a method with a line detector, hidden Markov model (HMM), and a denoising approach to resolve this problem. It tested on the DRIVE and STARE datasets and obtained high specificity of 0.9803 and 0.9992 [18]. Most of the above researches showed that thin or low-contrast vessels have low segmentation sensitivity. To improve the segmentation sensitivity, Soomro et al. proposed a method including modules such as principal component analysis-based color-to-gray conversion and scale normalization factors [7]. Khan et al. used some contrast normalization methods to extract the retinal vessels and fused them to obtain the final [21]. These methods which do not need ground truth (hand-labelled) images are unsupervised methods for automatic.

In addition to the unsupervised methods, some researchers have proposed supervised methods which need ground truth images to train the classifiers. Huang et al. realized a supervised learning method using an improved U-Net network with 23 convolutional layers, and the accuracy of the DRIVE, STARE, and HRF datasets was 0.9701, 0.9683, and 0.9698, respectively. However, its area under the curve (AUC) was only 0.8895, 0.8845, and 0.8686 [20]. Liang et al. fused the linear features, texture features, and the other features of retinal vessels to train a random forest classifier which realizes automatic segmentation of retinal vessels [9]. Lai et al. effectively fused mathematical morphology, matched filters, scale space analysis, multiscale line detection, and neural network models to achieve retinal vessel segmentation [10]. Fu et al. regarded retinal vessel segmentation as a boundary detection problem and segmented the vessels by combining the convolutional neural network and the connected conditional random field [11]. Orlando et al. proposed a discriminatively trained connected conditional random field model to segment retinal vessels [12]. Liskowski and Krawiec proposed a supervised segmentation method that used a deep neural network to extract retinal vessels from fundus images [13]. However, it is still a great challenge to segment vessels with high segmentation sensitivity and accuracy.

Although these methods have obtained some research findings, the performance of most methods still needs to be improved, especially the segmentation accuracy. In this research, a method using SegNet is proposed to obtain higher accuracy and AUC. Contributions of this research are highlighted:

(1) The training samples of fundus image dataset are generally small. A method for amplifying training samples is designed in this research to improve the accuracy and generalization ability of SegNet. It extracts image patches from fundus images and performs affine transformation

(2) The method proposed in this research can effectively improve the performance of retinal vessel segmentations, which not only can reduce oversegmentation on thin vessels but also can segment the vessels near optic disc and lesion area very well

(3) Lots of experiments are conducted on the DRIVE, STARE, and HRF datasets to evaluate the performance of the proposed method. The results show that the accuracy and AUC are higher than many other methods

This paper is organized as follows. In Section 2, the methods and materials are introduced in detail. Evaluation metrics for the proposed method is described in the Section 3. The experimental results and discussions are shown in Section 4. Finally, several conclusions are recapitulated in Section 5.

2. Methods and Materials

2.1. Materials. The proposed method is evaluated on the international public available datasets DRIVE [22], STARE [23], and HRF [24]. Fundus images of the DRIVE are from the diabetic retinopathy screening project in the Netherlands. They are collected by Canon CR5, and the age of the subjects is from 25 to 90 years old. The dataset consists of 40 color fundus images with resolution of 565×584. It is divided into two subsets including training and testing datasets. Each subset has the following: the training dataset contains 20 fundus images and their retinal vessel binary images which are segmented manually by an expert and the testing dataset contains 20 fundus images and each of them has two binary images which are segmented manually by two experts. In this paper, binary images segmented manually by the first expert are used as the ground truth images.

The STARE dataset was collected and published in 2000. It includes 20 fundus images, of which there are 10 images with pathological changes and the others are healthy fundus images. Their resolution is 605×700. Each image is segmented manually by two experts, and binary images segmented manually by the first expert are used as the ground truth images. There are 10 test images and 10 training images in the research.

The HRF dataset is the highest resolution of all fundus datasets at present. It includes 15 glaucoma retinal fundus, 15 diabetic retinopathy retinal fundus, and 15 healthy retinal fundus with a resolution of 3504×2336. Each image has a manual segmentation result. The training dataset contains 36 fundus images including 12 glaucoma retinal fundus, 12 diabetic retinopathy retinal fundus, and 12 healthy retinal fundus. And the left images are the test dataset.

In this paper, the machine learning library Keras in Python 3.6 is used to train and test the SegNet model for retinal vessel segmentation. In this research, PyCharm 2020.1 and Anaconda3 2020.2 are used as python IDE, while the back-end software needs tensorflow 1.15.0, Keras 2.3.1, Matplotlib 3.3.4, scikit-learn 0.22.1, and so on. The experimental platform for training and testing is NVIDIA Geforce Titan RTX 24G GPU of the Intel Xeon Silver 4210 2.2G GPU.

2.2. Methods. The overall flowchart of the method proposed in this research is shown in Figure 1. First, fundus images,

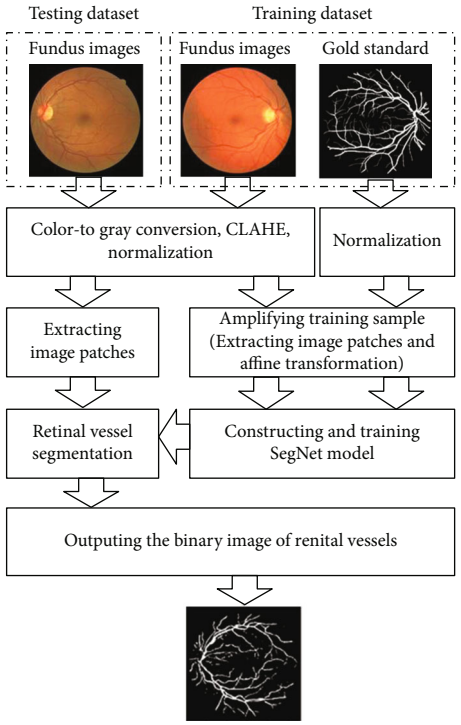

Figure 1: Structure diagram of the proposed method.

which are converted into gray images first, are preprocessed with contrast-limited adaptive histogram equalization (CLAHE) and normalized. Then, training samples are amplified with extracting image patches and affine transformation. Finally, SegNet model is constructed and trained to segment retinal vessels.

2.2.1. Preprocessing Fundus Images. In order to reduce the background interference and the influence of the noise, enhance the contrast of retinal vessels, accelerate the convergence speed of the algorithm, and improve the learning performance of SegNet model, preprocessing the fundus images is needed as shown in Figure 2. Retinal vessel segmentation is a very difficult task to extract thin vessels. According to the preexperiment, it could enhance well the thin vessels' contrast, using the method that the RGB image is converted to gray image. And considering with the color theory and the feature of each channel image, the color image "img" is converted to "gray" image with the following equation:

$$\text{gray} = \text{img}_R \times 0.299 + \text{img}_G \times 0.587 + \text{img}_B \times 0.114, \quad (1)$$

where img_R, img_G, and img_B are the red, green, and blue channel components of the image "img" in sequence, respectively.

After studying the feature of the converted gray image, to reduce the influence of the noise and to improve the contrast of retinal vessels, they are preprocessed with CLAHE. To facilitate data processing and improve the convergence speed of the model, fundus and their ground truth images are both normalized. They are normalized by Equation (2) and Equation (3), respectively. And the gray value of their pixels will be between 0 and 1.

$$\text{gray}^* = \frac{\text{gray} - \min(\text{gray})}{\max(\text{gray}) - \min(\text{gray})}, \quad (2)$$

where gray^* is the normalized image of the gray image gray.

$$\text{img}_{gt}^* = \frac{\text{img}_{gt}}{255}, \quad (3)$$

where img_{gt}^* is the normalized image of the ground truth image img_{gt}.

2.2.2. Amplifying Training Samples. The training samples of fundus image dataset are generally small. However, SegNet architecture has a large number of weight parameters. It needs a large number of training samples to improve their accuracy and generalization ability. If the network is trained directly with the fundus image, it would cause overfitting. So, the training samples should be amplified. Amplifying training sample algorithm includes extracting image patches and affine transformation, and they are described as follows:

(1) Extracting image patches. When extracting image patches, it is necessary to confirm whether the height and width of the reprocessed image gray^* can be divided exactly by the height and width of the patch, respectively. If it cannot be divided exactly, the reprocessed image gray^* should be extended by Equation (4) and Equation (5), and a new image gray_e^* will be obtained

The order of extracting images patches in the proposed method is from left to right and top to bottom, as shown in Figure 3. At first, the image patches of the first row are extracted, and then, the other rows are extracted in turn. Finally, the patches set a is obtained and $a = \{a_1, a_2, \cdots, a_6, a_7, \cdots\}$, where a_i is an image patch and i is the extracting order.

$$h' = h + h_{\text{extend}}, \quad (4)$$

$$w' = w + w_{\text{extend}}, \quad (5)$$

where h and w are the height and width of the reprocessed image gray^*, respectively; h' and w' are the height and width of the new image gray_e^*, respectively; h_{extend} and w_{extend} are the height and width of the area extended, which are expressed as Equation (6) and Equation (7), respectively.

$$h_{\text{extend}} = h_{\text{patch}} - h\%h_{\text{patch}}, \quad (6)$$

$$w_{\text{extend}} = w_{\text{patch}} - w\%w_{\text{patch}}, \quad (7)$$

where h_{patch} and w_{patch} are the height and width of the image patch, respectively. By comparing and analysing the model training curves and retinal vessel segmentation results under different patch sizes, the final values h_{patch} and w_{patch} both are 48 in the proposed method.

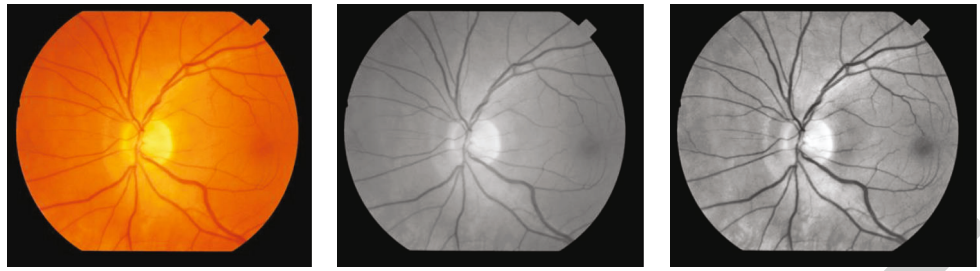

(a) (b) (c)

Figure 2: Preprocessing fundus image.

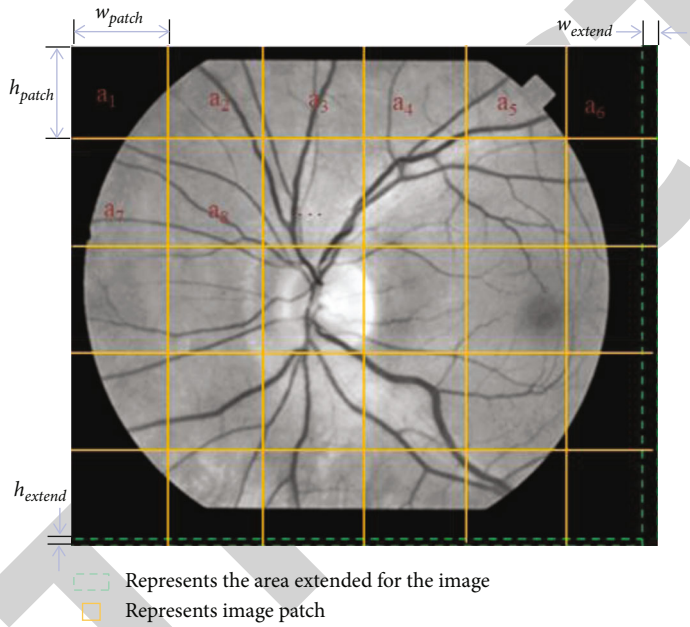

Figure 3: The diagram of the extracting image patches.

(2) Affine transformation. In order to further expand the size of training samples, each image patch is rotated clockwise with its center point, and the transformation matrix A is shown as follows:

$$A = \begin{bmatrix} \cos(\theta) & -\sin(\theta) & 0 \\ -\sin(\theta) & \cos(\theta) & 0 \\ 0 & 0 & 1 \end{bmatrix}, \quad (8)$$

where θ represents the angle of rotation and $\theta = 90°, 180°, 270°$.

2.2.3. Constructing and Training SegNet Model for Retinal Vessel Segmentation. The proposed method achieves end-to-end pixel segmentation with the SegNet model which is shown in Figure 4. SegNet developed by Badrinarayanan et al. [29] is an architecture for image segmentation. It is a semantic segmentation network and designed for scene understanding applications which need efficiently both memory and computational time during inference. Compared with other competing architectures such as FCN [30] and DeconvNet [31], it has significantly smaller trainable parameters and plays better performance with competitive inference time and memory-wise.

In the proposed method, the SegNet architecture includes encoder layer, decoder layer, and softmax layer. In the encoder layer, there are four convolutions and pooling layers. Each convolution used to extract features is followed by a batch normalization for accelerating learning speed, a rectified linear unit (ReLU), and a 2×2 maximum pooling operation (step size is 2) for downsampling. In each downsampling, the number of characteristic channels is doubled. In the decoder layer, there are four upsampling layers and four convolutions. After each upsampling is a convolution, and each convolution is followed by batch standardization and ReLU. The last layer of architecture is softmax layer which classifies each pixel using 1×1 convolution.

When SegNet is trained, 10-fold cross-validation is used to obtain the optimal model. The samples are divided randomly into ten subsets with the same size, and then set the proportion of training and validation dataset with 9 : 1. The

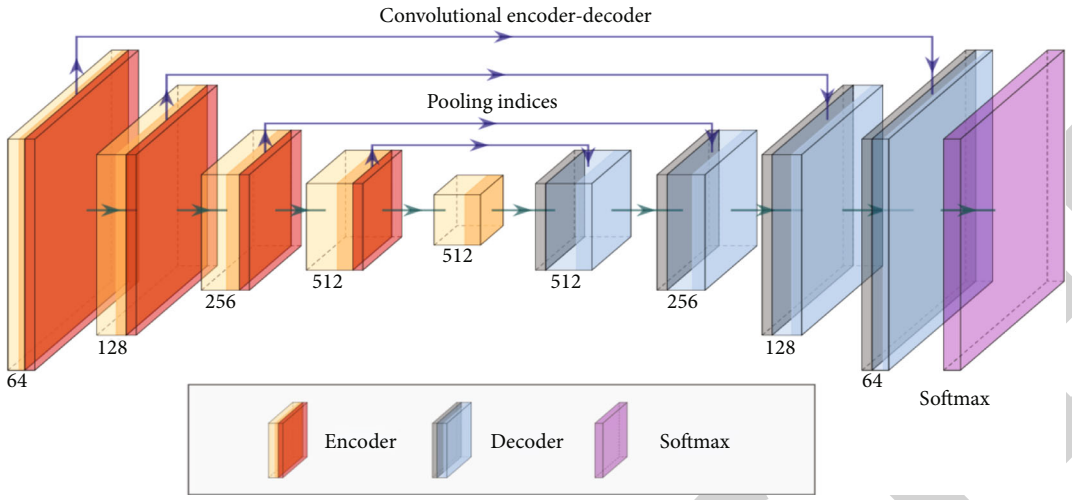

Figure 4: Schematic diagram of the proposed SegNet.

SegNet model is built by the training dataset and adjusted its parameters by the validation dataset. And the optimal model for retinal vessel segmentation is selected, which has the highest accuracy on the validation dataset.

In order to improve the imbalance between vessel pixels and nonvessel pixels, a class-balanced cross-entropy loss function Loss is adopted, as shown in the following equation.

$$\text{Loss} = -\sum_{i=1}^{N}[\alpha y_i \log(p_i) - (1-\alpha)(1-y_i) \times \log(1-p_i)], \quad (9)$$

where N is the total number of pixels in the validation dataset, y_i is the classification label of the ith pixel in the ground truth image, and $y_i \in \{0, 1\}$, where 0 is the background pixel and 1 is the vessel pixel. p_i is the predicted value of the ith pixel and α is shown in the following equation.

$$\alpha = \sum_{i=1}^{N}\frac{1-y_i}{y_i}. \quad (10)$$

In order to optimize the cross-entropy loss function Loss and to reduce the burden of debugging parameters, adaptive moment estimation (Adam) method [14] is adopted. The parameters of training are set as follows: the learning rate lr is set 0.001 initially, and it is set with 0.96 of the initial value of every 5 iterations; the iteration period epoch is 10.

3. Evaluation Metrics

To evaluate the performance of the proposed method, the evaluation metrics of accuracy, specificity, sensitivity, F_1 score (F_1), area under the receiver operating characteristic (ROC) curve (AUC), and Matthews correlation coefficient (MCC) are used. Accuracy is the ratio of the pixels segmented correctly to the total pixels of fundus image; specificity is the ratio of the nonvessel pixels segmented correctly to the total of nonvessel pixels; sensitivity is the ratio of the vessel pixels segmented correctly to the total of the vessel pixels. They are calculated as Equations (10)–(13). F_1 is calculated with Equation (14) that comprehensively considers the precision and recall of the model; ROC curve is a curve reflecting the relationship between sensitivity and specificity. The closer the curve is to the upper left corner (the smaller x and the larger y); that is, the larger the area below the curve and the higher the AUC value, the higher the segmentation accuracy is. MCC is computed with Equation (15), which measures the performance of unbalanced datasets very well. The value of 1 indicates the perfect segmentation on the test fundus images, while the value of -1 means that the segmentation is completely inconsistent with the ground truth.

$$\text{Accuracy} = \frac{\text{TP} + \text{TN}}{\text{TP} + \text{FN} + \text{TN} + \text{FP}}, \quad (11)$$

$$\text{Specificity} = \frac{\text{TN}}{\text{TN} + \text{FP}}, \quad (12)$$

$$\text{Sensitivity} = \frac{\text{TP}}{\text{TP} + \text{FN}}, \quad (13)$$

$$F_1 = \frac{2 \times \text{TP}}{2 \times \text{TP} + \text{FN} + \text{FP}}, \quad (14)$$

$$\text{MCC} = \frac{\text{TP} \times \text{TN} - \text{FP} \times \text{FN}}{\sqrt{(\text{TP} + \text{FP})(\text{FN} + \text{TP})(\text{FN} + \text{TN})(\text{FP} + \text{TN})}}, \quad (15)$$

where TP represents the vessel pixels classified as vessel pixels, FN represents the vessel pixels classified as nonvessel pixels, TN represents the nonvessel pixels classified as nonvessel pixels, and FP represents the nonvessel pixels classified as vessel pixels.

4. Experimental Results

The proposed method is tested and evaluated on the three datasets: DRIVE, STARE, and HRF. The training and test images of the three datasets are explained in Section 2.1.

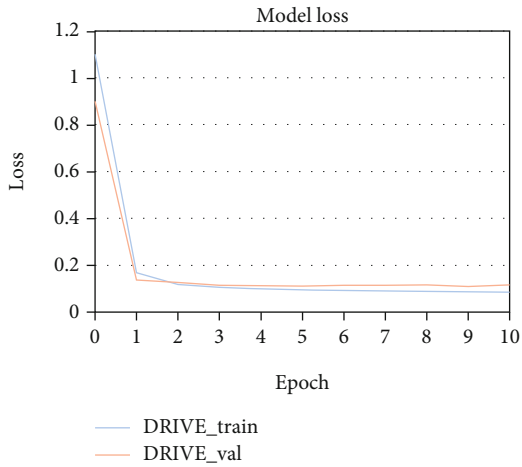

Figure 5: The loss curves of the proposed method trained on the DRIVE dataset.

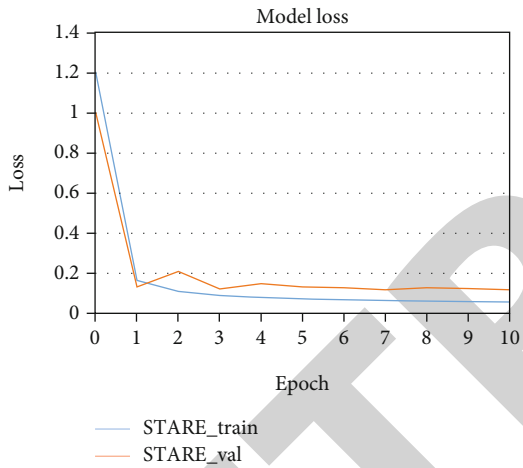

Figure 6: The loss curves of the proposed method trained on the STARE dataset.

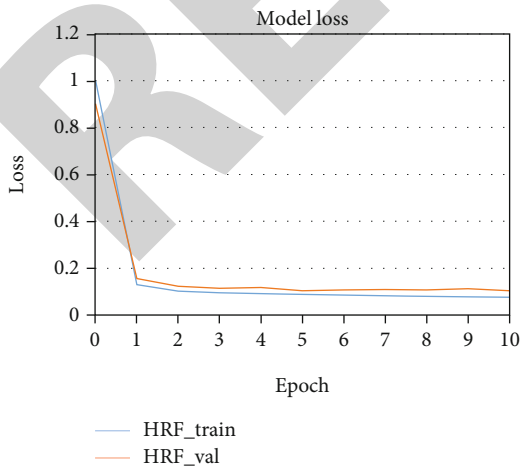

Figure 7: The loss curves of the proposed method trained on the HRF dataset.

Table 1: Statistical scores achieved on the DRIVE dataset.

Images	Sensitivity	Specificity	F_1	MCC	Accuracy	AUC
Test01	0.8220	0.9673	0.8064	0.7767	0.9483	0.9803
Test02	0.8290	0.9766	0.8452	0.8188	0.9545	0.9824
Test03	0.6793	0.9855	0.7699	0.7454	0.9408	0.9692
Test04	0.7507	0.9852	0.8128	0.7903	0.9539	0.9685
Test05	0.7266	0.9865	0.8019	0.7799	0.9513	0.9706
Test06	0.6949	0.9861	0.7811	0.7578	0.9450	0.9665
Test07	0.7180	0.9862	0.7940	0.7719	0.9507	0.9679
Test08	0.6919	0.9861	0.7738	0.7523	0.9492	0.9706
Test09	0.6914	0.9862	0.7702	0.7496	0.9515	0.9690
Test10	0.7495	0.9815	0.7948	0.7706	0.9538	0.9724
Test11	0.7629	0.9770	0.7957	0.7677	0.9492	0.9681
Test12	0.7460	0.9830	0.8001	0.7764	0.9533	0.9780
Test13	0.7289	0.9816	0.7922	0.7651	0.9458	0.9686
Test14	0.8022	0.9779	0.8153	0.7912	0.9572	0.9818
Test15	0.8086	0.9773	0.8067	0.7843	0.9598	0.9814
Test16	0.7720	0.9791	0.8079	0.7816	0.9520	0.9806
Test17	0.7112	0.9836	0.7781	0.7545	0.9500	0.9756
Test18	0.8137	0.9725	0.8034	0.7776	0.9542	0.9816
Test19	0.8522	0.9734	0.8327	0.8095	0.9588	0.9837
Test20	0.8100	0.9747	0.8012	0.7773	0.9571	0.9823

Table 2: Statistical scores achieved on the STARE dataset.

Images	Sensitivity	Specificity	F_1	MCC	Accuracy	AUC
Test01	0.7451	0.9924	0.8209	0.8087	0.9683	0.9902
Test02	0.8886	0.9818	0.8697	0.8542	0.9719	0.9931
Test03	0.8117	0.9883	0.8558	0.8388	0.9668	0.9907
Test04	0.8333	0.9927	0.8841	0.8709	0.9728	0.9942
Test05	0.7835	0.9922	0.8509	0.8367	0.9676	0.9912
Test06	0.8390	0.9907	0.8851	0.8693	0.9695	0.9946
Test07	0.7485	0.9933	0.8333	0.8197	0.9633	0.9912
Test08	0.7779	0.9951	0.8440	0.8369	0.9801	0.9930
Test09	0.6928	0.9925	0.7646	0.7560	0.9749	0.9878
Test10	0.5216	0.9909	0.6470	0.6427	0.9483	0.9675

Table 3: Statistical scores achieved on the HRF dataset.

Images	Sensitivity	Specificity	F_1	MCC	Accuracy	AUC
2_h	0.7325	0.9932	0.8508	0.7887	0.9592	0.9804
2_g	0.7094	0.9884	0.8209	0.7598	0.9638	0.9741
5_dr	0.7418	0.9859	0.8143	0.7565	0.9679	0.9743
10_g	0.7154	0.9888	0.7742	0.7599	0.9676	0.9755
11_dr	0.7063	0.9879	0.7782	0.7782	0.9596	0.9754
12_dr	0.6823	0.9861	0.7570	0.7377	0.9547	0.9702
12_g	0.7116	0.9871	0.7775	0.7598	0.9602	0.9714
14_h	0.6978	0.9836	0.7749	0.7654	0.9699	0.9794
15_h	0.6658	0.9954	0.7784	0.7731	0.9845	0.9651

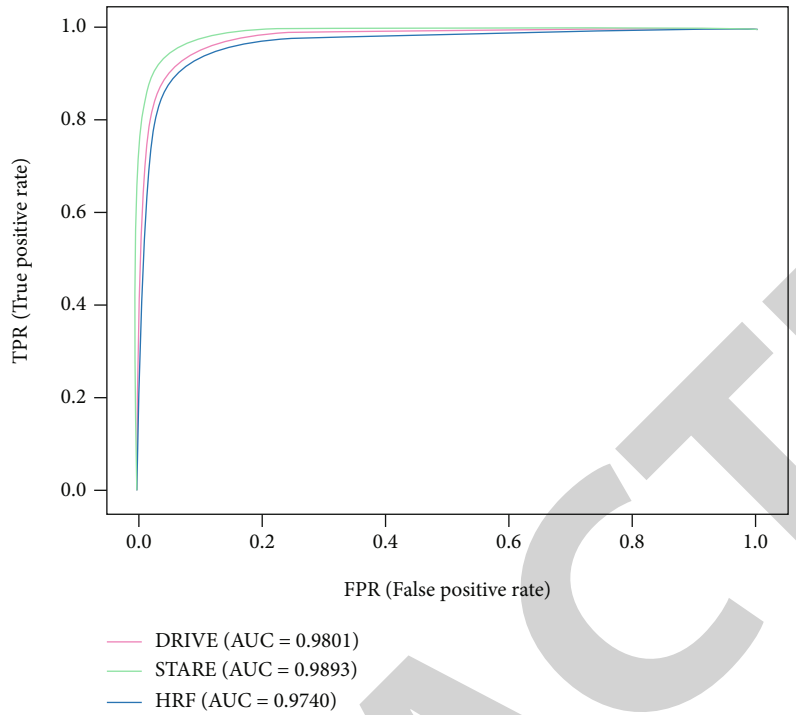

Figure 8: ROC curves of the proposed method tested on the DRIVE, STARE, and HRF datasets.

To illustrate the training and validation process, the loss curves of the proposed method trained on the three datasets are shown in Figures 5–7, respectively. The abscissa of the graph is the iteration period "Epoch," and the ordinate is the loss value "LOSS." Legend "train" represents training, and legend "val" represents validation. From Figures 5–7, it shows that the training loss values of the DRIVE, STARE, and HRF are all smaller than 2 after one epoch. It means that the loss of training and validation both converge quickly, when the proposed method is trained on the three datasets.

The evaluation metrics results of the DRIVE (20 test images), STARE (10 test images), and HRF (9 test images) are shown in Table 1, Table 2, and Table 3, respectively. The statistical scores show that the proposed method performs well all on the three datasets. In terms of retinal vessel segmentation AUC, the minimum value of the DRIVE dataset is 0.9665 and the maximum is 0.9837, while the minimum and maximum of the STARE dataset are 0.9675 and 0.9946 and of the HRF dataset are 0.9651 and 0.9804. In terms of F_1 score, the maximum of DRIVE is 0.8452, while STARE is 0.8851 and HRF is 0.8508; in terms of specificity, the minimum of DRIVE is 0.9865, and the minimum value of STARE is 0.9951 and HRF is 0.9954. That all, the proposed method could segment retinal vessels from fundus image well. It is robust to segment the low-resolution images of the DRIVE and STARE datasets and the high-resolution images of the HRF dataset.

Meanwhile, the ROC curves of the three datasets tested with the proposed method are shown in Figure 8. It can be seen that the ROC curve of the model tested on the STARE dataset is the closest to the upper left corner, and the curve of the model tested on HRF is the lowest. The different datasets have a slight impact on the model, but in general, the model can get good segmentation performance.

5. Discussions

Qualitative results of the proposed method are compared with the other methods which are shown in Figures 9–11. Figure 9 shows the methods tested on the DRIVE dataset. It can be seen that compared with the other two models, it shows that the segmentation performance of the proposed method is better than other methods, especially the thin vessels and the vessels in the optic disc region. For thin vessels in the fundus image test15, there is oversegmentation in the method proposed by Alom et al. [33], while the method proposed by Guo and Peng [17] also has this problem. In addition, the optic disc has a great influence on the retinal vessel segmentation, and the nonvessel pixels in this region are often mislabelled as vessel pixels, such as the fundus image test19 segmented by Guo and Peng [17]. And it can be seen from Figure 10 that the proposed method has better performance than the three methods proposed by Alom et al. [33], Hu et al. [32], and Guo and Peng [17], especially in thin vessels. For thin vessels in the fundus image test02, compared with its ground truth, there is oversegmentation in the method proposed by Hu et al. [32]. And they are not segmented well in the method proposed by Guo and Peng [17]. While the method proposed by Guo and Peng [17], tested on the HRF dataset shown in Figure 11, it can be found that the thin vessels are not segmented well, too. In short, the proposed method not only reduces

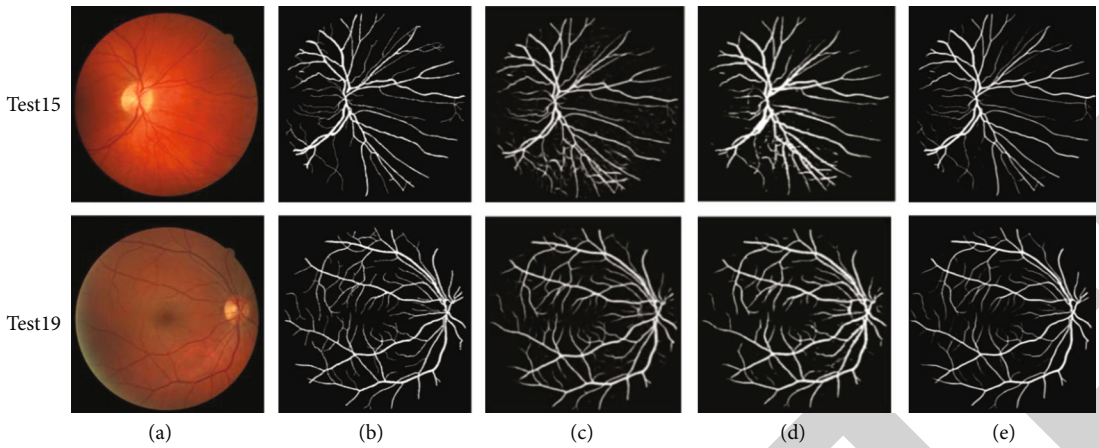

Figure 9: Qualitative results compared with other methods on the DRIVE dataset: (a) original image, (b) ground truth, (c) Alom et al., (d) Guo and Peng, and (e) the proposed method.

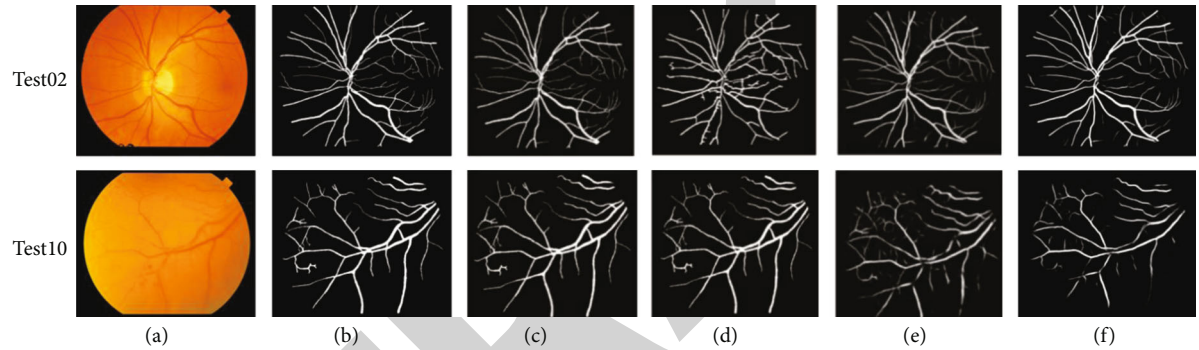

Figure 10: Qualitative results compared with other methods on the STARE dataset: (a) original image, (b) ground truth, (c) Alom et al., (d) Hu et al., (e) Guo and Peng, and (f) the proposed method.

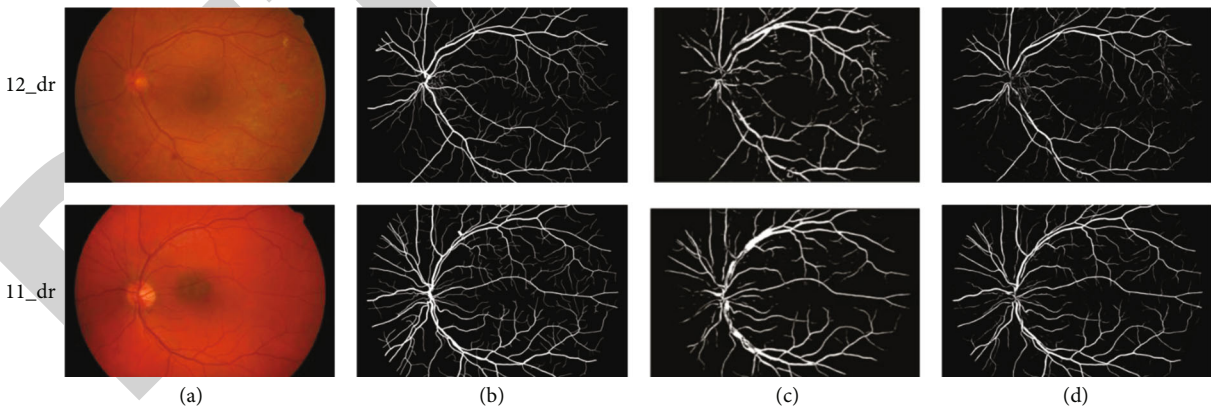

Figure 11: Qualitative results compared with other methods on the HRF dataset: (a) original image, (b) ground truth, (c) Guo and Peng, and (d) the proposed method.

oversegmentation on thin vessels but also segments thin vessels or vessels around optic disc well.

Compared with the other methods on the DRIVE, STARE, and HRF datasets, the quantization results are listed in Table 4, Table 5, and Table 6, respectively. These results reveal that the proposed method is superior to many other methods on the three datasets. On the DRIVE dataset, the proposed method has AUC of 0.9750, accuracy of 0.9518, sensitivity of 0.7580, specificity of 0.9804, F_1 score of 0.7992, and MCC of 0.7749. And there are 16 methods compared with the proposed method. The AUC of the proposed method is highest except Zhou et al. [18] which is 0.0004 and Wu et al. [19] which is 0.008 better than the proposed method. On the STARE dataset, the proposed method has

Table 4: Compared with other methods on the DRIVE dataset.

Method	Year	Sensitivity	Specificity	F_1 score	MCC	Accuracy	AUC
Neto et al.	2015 [7]	0.7806	0.9629	/	/	0.8718	/
Bahadar et al. [27]	2016	0.7462	0.9801	/	/	0.96075	0.882
Khan et al. [27]	2016	0.746	0.980	/	/	0.961	0.863
Khan et al. [28]	2017	0.754	0.964	/	/	0.944	0.859
Cao et al.	2017	0.7663	0.9311	/	/	0.9174	/
Soomro et al.	2017	0.7523	0.976	/	/	0.9432	/
Cai et al.	2019	0.7787	0.9701	/	/	0.9520	/
Mehmood et al. [15]	2019	0.737	0.976	/	/	0.953	/
Khan et al.	2019	0.754	0.964	/	/	0.944	/
Lai et al.	2019	0.7843	0.9815	/	/	0.9457	/
Yang et al. [34]	2019	0.7560	0.9696	0.7673	0.7365	0.9421	/
Zhou et al.	2020	0.7262	0.9803	/	/	0.9475	/
Khan et al.	2020	0.797	0.973	/	0.739	0.958	0.885
Zhou et al.	2020	0.8432	0.9681	0.8163	0.7905	0.952	0.9754
Wu et al.	2020	0.7996	0.9813			0.9582	0.9830
Huang et al.	2021	0.8011	0.9849	0.8099	/	0.9701	0.8895
The proposed method	2022	0.7580	0.9804	0.7992	0.7749	0.9518	0.9750

Table 5: Compared with other methods on the STARE dataset.

Method	Year	Sensitivity	Specificity	F_1 score	MCC	Accuracy	AUC
Neto et al.	2015 [7]	0.8344	0.9443	/	/	0.8894	/
Bahadar et al. [25]	2016	0.75805	0.9627	/	/	0.94585	/
Khan et al. [27]	2016	0.758	0.963	/	/	0.951	0.861
Soomro et al.	2017	0.784	0.981	/	/	0.9614	/
Khan et al. [28]	2017	0.752	0.956	/	/	0.948	0.854
Lai et al.	2019	0.7826	0.9803	/	/	0.9472	/
Mehmood et al. [15]	2019	0.741	0.982	/	/	0.957	/
Khan et al.	2019	0.791	0.970	/	/	0.957	0.880
Yang et al. [34]	2019	0.7202	0.9733	0.7260	0.7045	0.9477	/
Zhou et al.	2020	0.7865	0.9730	/	/	0.9535	/
Khan et al.	2020	0.792	0.998	/	0.707	0.996	0.895
Zhou et al.	2020	0.8630	0.9730	0.8233	0.8044	0.9620	0.9754
Wu et al.	2020	0.7963	0.9863			0.9672	0.9875
Huang et al.	2021	0.6329	0.9967	0.8049		0.9683	0.8845
Sun et al.	2021	/	/	0.8230	0.8075	0.9714	0.9882
The proposed method	2022	0.7747	0.9910	0.8369	0.8227	0.9683	0.9893

Table 6: Compared with other methods on the HRF dataset.

Method	Year	Sensitivity	Specificity	F_1 score	MCC	Accuracy	AUC
Yang et al.	2019	0.7915	0.9676	0.7449	0.7125	0.9517	/
Khan et al.	2020	0.732	0.979	/	0.710	0.960	0.863
The proposed method	2022	0.7070	0.9885	0.7918	0.7643	0.9653	0.9740

AUC of 0.9893, accuracy of 0.9683, sensitivity of 0.7747, specificity of 0.9910, F_1 score of 0.8369, and MCC of 0.8227. And it is compared with 15 methods in Table 5. The accuracy of the proposed method is highest except Sun et al. [35] which is 0.0031 and Khan et al. [26] which is 0.0277 higher than the proposed method. The proposed

method obtains the highest F_1 score, MCC, and AUC of all methods shown in Table 5. On the HRF dataset, the proposed method has AUC of 0.9740, accuracy of 0.9653, sensitivity of 0.7070, specificity of 0.9885, F_1 score of 0.7918, and MCC of 0.7643. It can be seen from Table 6 that the proposed method obtains the highest specificity, F_1 score, MCC, accuracy, and AUC. It proves the superiority of the proposed method.

It is difficult to segment retinal vessels accurately because of uneven illumination, low contrast, and retinopathy. From the experimental results, the performance of the proposed method in retinal vessel segmentation is improved, especially for the thin vessels and the vessels around the optic disc and the lesion area, which there is little oversegmentation. Compared with other methods, it has high MCC, AUC, accuracy, and specificity. However, the proposed method has some limitations. It can be seen from the quantitative data in Tables 4–6 that the sensitivity of the proposed method is lower than some methods. From the visualization results, the low sensitivity may be caused by the segmentation discontinuity of retinal vessels. Therefore, in the following study, it will be designed some appropriate postprocessing methods to improve the continuity of retinal vessels, which may improve the sensitivity of the algorithm. In addition, on the DRIVE, STARE, and HRF datasets, the sensitivity of current retinal vessel segmentation methods is generally low. From Tables 4–6, the maximum values of the three datasets are 0.8011, 0.8344, and 0.7915, respectively. Therefore, it is a great challenge to design a more ideal segmentation algorithm to improve the segmentation sensitivity of retinal vessels while maintaining high segmentation accuracy.

6. Conclusion and Future Work

It is important to extract retinal vessels accurately for detecting and analysing the progress of many eye diseases. At present, a variety of segmentation methods have been proposed, but most of them have low accuracy for thin vessels and lesion area. To improve the accuracy, a retinal vessel segmentation model with SegNet is constructed. The experimental results show that the proposed method has higher segmentation accuracy than the other methods on the DRIVE, STARE, and HRF datasets. The accuracy of the proposed method tested on the DRIVE, STARE, and HRF datasets is 0.9518, 0.9683, and 0.9653, respectively. It can segment the retinal vessels well but not with the thin vessels with low contrast and lesion area. In addition, the proposed method could provide a new methodological idea for extracting retinal vessels accurately and automatically from fundus images, which can promote the research of retinal vessel automatic segmentation model to serve the clinical practice better. In the future work, vessel's location, tortuosity, and diameter of fundus structural features will be extracted to predict some fundus diseases such as glaucoma and diabetes, which could improve the efficiency of their clinical diagnosis and treatment.

Data Availability

The raw/processed data required to reproduce these findings cannot be shared at this time as the data also forms part of an ongoing study.

Conflicts of Interest

The authors declare no conflict of interest.

Acknowledgments

This work is funded in part by the National Natural Science Foundation of China (Grant No. 62072413) and also supported by the Project of Domestic Visiting Scholar (Grant No. FX2020019 and Grant No. FX2020020).

References

[1] R. Zedan, A. A. Farouk, R. Azmy, R. Elhadidy, and E. Attya, "Role of pattern electroretinogram in assessment of retinal dysfunction in hypertensive patients," *International Journal of Neuroscience*, pp. 1–6, 2021.

[2] G. Wang, M. Li, Z. Yun et al., "A novel multiple subdivision-based algorithm for quantitative assessment of retinal vascular tortuosity," *Experimental Biology and Medicine*, vol. 246, no. 20, pp. 2222–2229, 2021.

[3] M. Wang, Q. Jin, H. Wang, D. Li, N. Baniasadi, and T. Elze, "The interrelationship between refractive error, blood vessel anatomy, and glaucomatous visual field loss," *Translational Vision Science & Technology*, vol. 7, no. 1, 2018.

[4] T. Elze, N. Baniasadi, Q. Jin, and H. Wang, "Ametropia, retinal anatomy, and OCT abnormality patterns in glaucoma. 1. Impacts of refractive error and interartery angle," *Journal of Biomedical Optics*, vol. 22, no. 12, article 121713, pp. 1–11, 2017.

[5] Z. Cai, P. Tang, and J. Hu, "Retinal vessel segmentation based on PST and multi-scale Gaussian filter," *Application Research of Computers*, vol. 36, no. 6, pp. 1893–1896, 2019.

[6] X. Cao, L. Xue, and J. Lin, "Retinal vessel segmentation method based on matched filtering and automatic threshold," *J. Electron. Meas. Instrumentation*, vol. 1, pp. 51–57, 2017.

[7] T. A. Soomro, M. A. U. Khan, J. Gao, T. M. Khan, and M. Paul, "Contrast normalization steps for increased sensitivity of a retinal image segmentation method," *Signal, Image and Video Processing*, vol. 11, no. 8, pp. 1509–1517, 2017.

[8] M. A. U. Khan, T. M. Khan, T. A. Soomro, N. Mir, and J. Gao, "Boosting sensitivity of a retinal vessel segmentation algorithm," *Pattern Analysis and Applications*, vol. 22, no. 2, pp. 583–599, 2019.

[9] L. M. Liang, B. W. Liu, and H. L. Yang, "Supervised blood vessel extraction in retinal images based on multiple feature fusion," *Chinese Journal of Computers*, vol. 41, no. 11, pp. 2566–2580, 2018.

[10] X. Lai, M. Xu, and X. Xu, "Automatic retinal vessel segmentation based on multi-model fusion and region iterative growth," *Acta Electonica Sinica*, vol. 47, no. 12, 2019.

[11] H. Fu, Y. Xu, D. W. K. Wong, and J. Liu, "Retinal vessel segmentation via deep learning network and fully-connected conditional random fields," in *2016 IEEE 13th International*

Hindawi
Computational and Mathematical Methods in Medicine
Volume 2022, Article ID 2868885, 8 pages
https://doi.org/10.1155/2022/2868885

Research Article

Modeling the Ranked Antenatal Care Visits Using Optimized Partial Least Square Regression

Maryam Sadiq,[1] **Alanazi Talal Abdulrahman**,[2] **Randa Alharbi**,[3] **Dalia Kamal Fathi Alnagar**,[3,4] **and Syed Masroor Anwar**[1]

[1]*Department of Statistics, University of Azad Jammu and Kashmir, Muzaffarabad, Pakistan*
[2]*Department of Mathematics, College of Science, University of Hail, Saudi Arabia*
[3]*Department of Statistics, University of Tabuk, Saudi Arabia*
[4]*Department of Statistics, Omdurman Islamic University, Sudan*

Correspondence should be addressed to Maryam Sadiq; hussainulahmad@gmail.com

Received 22 December 2021; Revised 9 February 2022; Accepted 11 February 2022; Published 14 March 2022

Academic Editor: Plácido R. Pinheiro

The frequency and timing of antenatal care visits are observed to be the significant factors of infant and maternal morbidity and mortality. The present research is conducted to determine the risk factors of reduced antenatal care visits using an optimized partial least square regression model. A data set collected during 2017-2018 by Pakistan Demographic and Health Surveys is used for modeling purposes. The partial least square regression model coupled with rank correlation measures are introduced for improved performance to address ranked response. The proposed models included PLSρ_s, PLSτ_A, PLSτ_B, PLSτ_C, PLS$_D$, PLSτ_{GK}, PLS$_G$, and PLS$_U$. Three filter-based factor selection methods are executed, and leave-one-out cross-validation by linear discriminant analysis is measured on predicted scores of all models. Finally, the Monte Carlo simulation method with 10 iterations of repeated sampling for optimization of validation performance is applied to select the optimum model. The standard and proposed models are executed over simulated and real data sets for efficiency comparison. The PLSρ_s is found to be the most appropriate proposed method to model the observed ranked data set of antenatal care visits based on validation performance. The optimal model selected 29 influential factors of inadequate use of antenatal care. The important factors of reduced antenatal care visits included women's educational status, wealth index, total children ever born, husband's education level, domestic violence, and history of cesarean section. The findings recommended that partial least square regression algorithms coupled with rank correlation coefficients provide more efficient estimates of ranked data in the presence of multicollinearity.

1. Introduction

Pakistan sets targets to minimize the maternal mortality ratio (MMR) to 140 per 100,000 live births by 2015 by increasing skilled birth attendants and improving access to reproductive health care as the fifth Millennium Development Goal (MDG) for improving maternal health suggested. The MDG progress assessment reported that Pakistan was not close to attaining the target in 2015. Recently, Pakistan has endorsed the Sustainable Development Goals (SDGs), committing to decrease the MMR to 70 per 100,000 live births by 2030 by increasing skilled birth attendance, facilitation to modern contraception, and extending coverage of health workers. The Government of Pakistan took initiatives and made good progress in maternal health indicators during the last decade, and a significant decline was reported in MMR from 276 to 178 [1, 2]. Pregnancy-related morbidity and mortality can be reduced by improving access and facilitation to maternal health care services. At least four antenatal care visits (ANC) are recommended to skilled personnel to avoid any pregnancy-related complication [3]. Nearly 12% Pakistani women reported no ANC throughout their pregnancy, 36% have less than four visits, and 52% claimed four or more visits [1]. Several studies have assessed the significant influential factors of antenatal care

attendance in Pakistan without considering the frequency of ANC [4, 5]. Poisson regression, negative binomial regression, zero-inflated, and hurdle regression models have been commonly used to model the count of ANC visits [6, 7]. Binary logistic regression and a multinomial logistic regression model are also found to study the use and ranks of ANC visits [5, 8]. Advancements in health research generate public health data having many covariates, where some or all may be correlated. Several studies have been conducted to identify influential factors of different public health concerns using multiple statistical tools and techniques [9–13]. The partial least square (PLS) regression model has been the concern of interest as a statistical method for modeling data having multicollinearity during the last few decades. A variety of modified PLS algorithms have been introduced for superior model performance [14]. Most PLS algorithms model continuous factors, and a few are specifically designed for categorical framework but no specific algorithm is projected to address the ranked data. To fill the gap of obtaining the optimal model for the ranked response variable, modified PLS algorithms based on ranked correlation loading weights are introduced. The main motivation of the present study is to propose the modified PLS algorithms to particularly address the ranked response factor in the presence of multicollinearity. To improve the PLS regression model, eight algorithms based on rank correlation measures including Spearman's rank correlation coefficient, Kendall's τ_A rank correlation coefficient. Kendall's τ_B rank correlation coefficient, the Stuart-Kendall τ_C rank correlation coefficient, Somers' delta (D), Goodman-Kruskal's tau τ_{GK}, Goodman-Kruskal's gamma (G), and Thiel's U correlation coefficient are proposed in this study. To the best of our knowledge, no previous research has considered multicollinear covariates in modeling the ranking of ANC visits of Pakistani women. Thus, the objectives of this study are twofold: (i) to develop a regression model for the ranked response covering the issue of multicollinearity and (ii) to determine the risk factors for inadequate use of antenatal care. This study introduced eight novel PLS algorithms addressing the concern of multicollinearity for a ranked response which is never discussed earlier. The proposed and standard algorithms are executed on a real-life application of ANC data for comparison purposes. These algorithms will facilitate users to obtain more efficient models than the standard PLS approaches for specifically ranked data. Regarding the clinical importance of this study, the influential selected variables of ANC will help maximize the chances for a normal pregnancy by providing priority interventions, increasing coverage, and improving health quality. The novel contribution of this study included:

(i) eight new PLS algorithms based on rank correlation loading weights are proposed to address rank response

(ii) the significant factors of ANC utilization of Pakistani women are identified

2. Methodology

2.1. Data Set. The data acquired from Pakistan demographic and health survey (PDHS) 2017-2018 for Baluchistan is used for the present study. A total of 943 observations (women) with 43 factors are included in the analysis. The frequency of ANC is considered the ordinal response factor (y) which is ranked as inadequate (0-3 visits), intermediate (4-7 visits), and adequate (8-9 visits).

2.2. Partial Least Square Regression (PLSR). Consider the regression model $y = \alpha + Z\beta + \varepsilon$, where α and β are the unknown regression parameters and ε is the error term. Let $Z_{(n,p)}$ is the matrix of explanatory variables and is assumed to be linearly related with the response $y_{(n,1)}$ and suppose some C (where $C \leq p$) to represent the number of components for prediction. Then, for $c = 1, \cdots, C$, the general algorithm executes as

(1) The loading weights are $w_c = Z'_{c-1} y_{c-1}$

(2) The score vector is $t_c = Z_{c-1} w_c$

(3) Evaluate Z-loadings (P_c) and Y-loadings (q_c) by $p_c = Z'_{c-1} t_c / t'_c t_c$ and $q_c = y'_{c-1} t_c / t'_c t_c$, respectively

(4) Deflate Z_{c-1} and y_{c-1} by $Z_c = Z_{c-1} - t_c p'_c$ and $y_c = y_{c-1} - t_c q_c$

(5) Repeat the algorithm, if $c < C$

Consider that W, S, P, and q are the matrices/vectors to compile the loading weights, scores, Z-loadings, and Y -loadings computed at each iteration of the algorithm, respectively. The regression estimators of the PLSR model are computed by $\widehat{\beta} = W(P'W)^{-1} q$ and $\widehat{\alpha} = \bar{y} - \bar{Z}\widehat{B}$ [15]. The general steps of standard PLSR are presented in Figure 1.

The standard PLS is designed for continuous dependent variable y but if the response is measured on a rank scale then this standard method may not work well. The most important phase of the PLS algorithm is to compute loading weight having the ability to choose significant factors. Loading weights compute the correlation between the dependent variable and predictors. If the data set is ranked then Spearman's rank correlation coefficient, Kendall's τ_A rank correlation coefficient, Kendall's τ_B rank correlation coefficient, the Stuart-Kendall τ_C rank correlation coefficient, Somers' delta (d), Goodman-Kruskal's tau τ_{GK}, Goodman-Kruskal's Gamma (G), and Thiel's U correlation coefficient are the recommended measures of rank correlation. These measures of association are used to compute the loading weights of the PLS algorithm. The modified loading weights of PLSR are visually displayed in Figure 2.

2.2.1. PLSρ_s. Spearman's rank correlation coefficient or Spearman's ρ (ρ_s) [16] is a nonparametric measure of rank correlation using a monotonic function. It is used to compute the weights of as

$$w_{\rho_s} = 1 - \frac{6\sum d_i^2}{n(n^2-1)}, \tag{1}$$

where d_i denotes the difference between the two ranks of

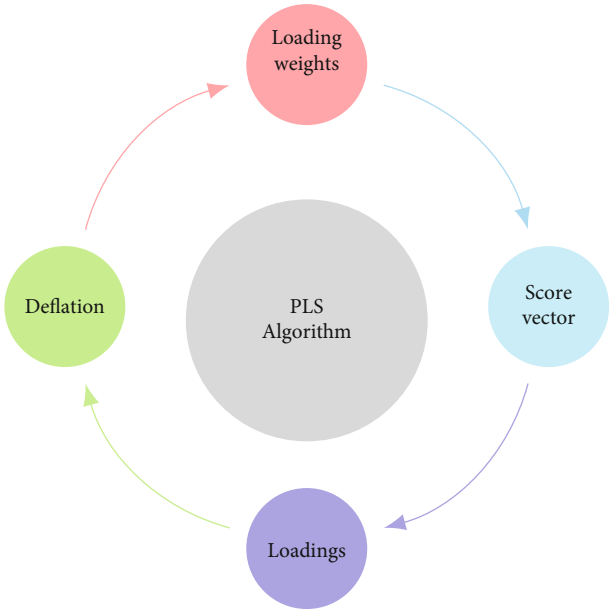

Figure 1: Standard PLS algorithm.

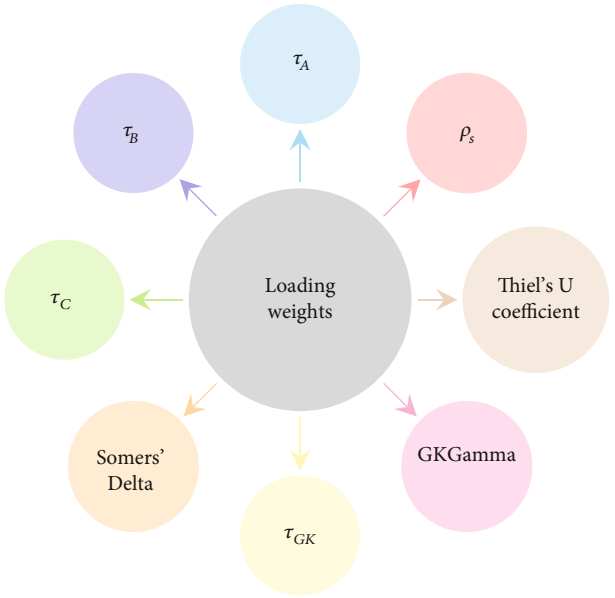

Figure 2: Modified loading weights of PLS.

each observation and n is the number of observations and the modified PLSR algorithm is referred to as PLSρ_s.

2.2.2. PLSτ_A. The Kendall rank correlation coefficient or Kendall's τ coefficient is a measure of rank correlation. The tau-A (τ_A) will not make any adjustment for ties [17]. It is used to define the PLS loading weights as

$$w_{\tau_A} = \frac{n_c - n_d}{n_0}, \tag{2}$$

where n_c is the number of concordant pairs, n_d is the number of discordant pairs, and $n_0 = n(n-1)/2$, and the modified algorithm is named as PLSτ_A.

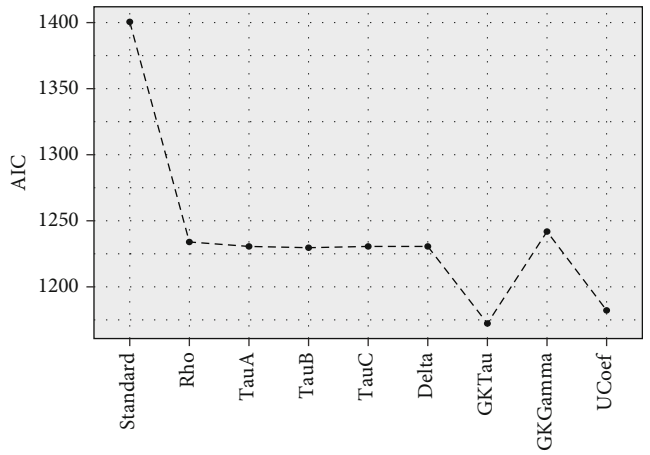

Figure 3: The AIC performance of PLSR models based on rank correlation coefficients' oversimulated data without considering any variable selection method is presented.

2.2.3. PLSτ_B. Kendall's tau-B makes adjustments for ties [18]. The PLS loading weights are altered by using τ_B as

$$w_{\tau_B} = \frac{n_c - n_d}{\sqrt{(n_0 - n_1)(n_0 - n_2)}}, \tag{3}$$

where $n_1 = \sum_i t_i(t_i - 1)$, $n_2 = \sum_j u_j(u_j - 1)$, t_i is the number of tied value in the i^{th} group of ties and t_j is the number of tied value in the j^{th} group of ties and the proposed model is termed as PLSτ_B.

2.2.4. PLSτ_C. The Stuart-Kendall (tau-c) is more suitable for contingency tables [19]. The τ_C replaced the weights of PLS as follows:

$$w_{\tau_C} = \frac{2(n_c - n_d)}{n^2((m-1)/m)} \tag{4}$$

where m is the minimun number among rows and coulmns, and the modified PLSR algorithm is called PLSτ_C.

2.2.5. PLS$_D$. The PLS loading weights based on Somers' delta(D) [20] of variable Y with respect to variable Z are defined as

$$w_D = \frac{\tau(Z, Y)}{\tau(Z, Z)}. \tag{5}$$

Kendall's tau τ is symmetric, whereas Somers' D is asymmetric in Z and Y, and the model is named as PLS$_D$.

2.2.6. PLSτ_{GK}. Goodman-Kruskal's tau τ_{GK} [21] is integrated as PLS loading weights as

$$w_{\tau_{GK}} = \frac{2(n_c - n_d)}{n_0}, \tag{6}$$

and the modified algorithm is called PLSτ_{GK}.

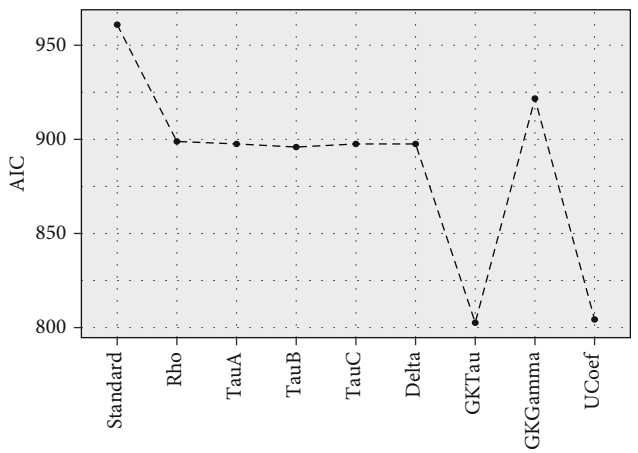

Figure 4: The AIC performance of PLSR models based on rank correlation coefficients' oversimulated data integrated with LW variable selection method is presented.

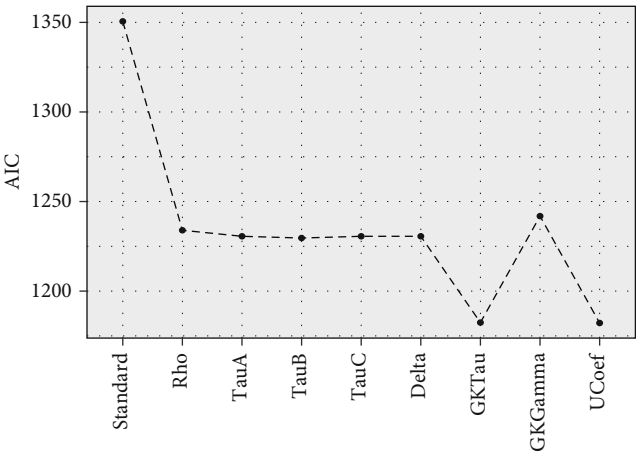

Figure 5: The AIC performance of PLSR models based on rank correlation coefficients' oversimulated data integrated with SMC variable selection method is presented.

2.2.7. PLS $_G$. The estimate of Goodman-Kruskal's gamma (G) [21] is used as loading weights of PLS

$$w_G = \frac{n_c - n_r}{n_c + n_r}, \tag{7}$$

where n_c is the number of concordant pairs and n_r is the number of reversed pairs. Goodman-Kruskal's gamma drop ties, and the PLSR model is named as PLS $_G$.

2.2.8. PLS $_U$. Thiel's U correlation coefficient or uncertainty coefficient [22] altered the PLS loading weights as

$$w_U = \frac{H(Z) - H(Z \mid Y)}{H(Z)}, \tag{8}$$

where $H(Z)$ represents the entropy of a single distribution and $H(Z \mid Y)$ represents the conditional entropy, and the modified PLSR algorithm is referred to as PLS $_U$.

2.3. Filter-Based Factor Selection Methods. Several variable selection methods integrated with PLSR have been introduced. The following are considered here.

2.3.1. The Loading Weight (LW). The loading weights w_j are used to measure of importance of predictors and are defined as [23].

$$\mathrm{LW} = \left| \frac{w_{a,j}}{\max(w_a)} \right|. \tag{9}$$

2.3.2. The Regression Coefficients (RC). The regression coefficient estimates are computed as [23]

$$\mathrm{RC} = W\left(P'W\right)^{-1} q. \tag{10}$$

2.3.3. Significance Multivariate Correlation (SMC). The significance multivariate correlation measure is used to reduce the effect of irrelevant predictors and enhance the influence of significant variables included in the model. The SMC [23] is computed as

$$\mathrm{SMC} = \frac{\mathrm{MeanSquareRegression}}{\mathrm{MeanSquareResidual}}. \tag{11}$$

3. Results

Initially, the PLS models with modified loading weights are executed for simulated data set for ranked variables. A sample of size 1000 with 100 predictors is generated. The response variable and 50% predictors are generated over 3 ranks, and the remaining explanatory variables are distributed over 4 ranks.

Spearman's coefficient, Kendall's coefficient-A, Kendall's coefficient-B, Stuart-Kendall's, Somers' delta, Goodman-Kruskal's tau, Goodman-Kruskal's gamma, and Thiel's U coefficient are used as loading weights of the PLS algorithm to fit oversimulated data set to observe the variation in performance of standard and proposed models based on Akaike information criterion (AIC).

Figure 3 showed the efficiency of models established by AIC and indicated that PLSR algorithms with modified loading weights have higher efficiency (lower mean AIC) compared to standard PLSR for a ranked response. The PLSR model with τ_{GK} as modified loading weight showed optimum performance compared to eight other models without integrating any variable selection method. All other proposed models also evidenced higher efficiency compared to standard PLSR. Figures 4 and 5 also demonstrated the higher accuracy of proposed models compared to standard PLSR algorithm integrated with LW and SMC variable selection methods. Both figures depicted that PLSτ_{GK} and PLS $_U$ have optimum performance compared to all other models. The standard and modified models are also executed over the real data set of ANC for comparison of accuracy. The data set of ANC visits had 43 predictors sampled over 943 samples (mothers). The Spearman rank correlation coefficient is used to examine the multicollinearity in the data.

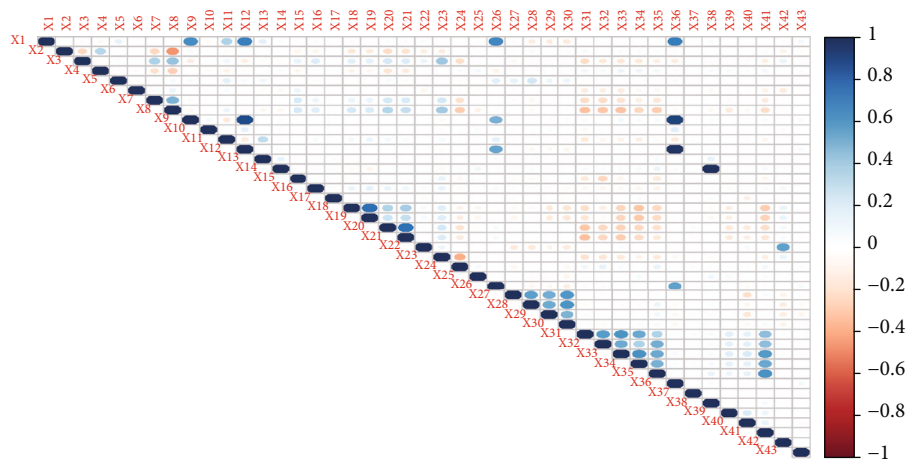

Figure 6: Correlogram by Spearman rank correlation matrix is presented. Color intensity and the size of the circle are proportional to the strength of the correlation among covariates.

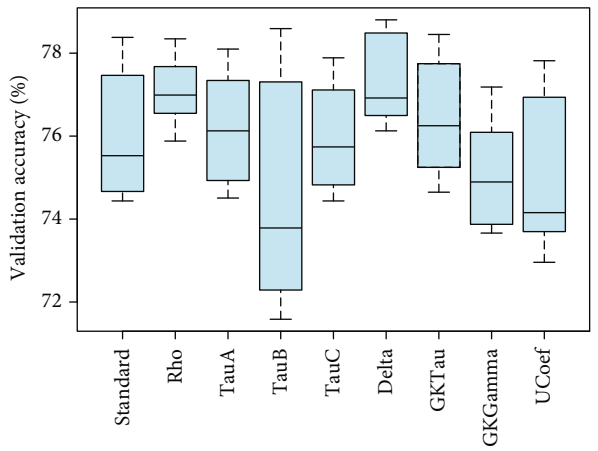

Figure 7: The validation accuracy of PLSR models based on rank correlation coefficients including Spearman's correlation coefficient (Rho), Kendall coefficient-*A* (tau-*A*), Kendall coefficient-*B* (tau-*B*), Stuart-Kendall (tau-*C*), Somers' delta (Delta), Goodman-Kruskal's tau (GKTau), Goodman-Kruskal's gamma (GKGamma), and Thiel's *U* coefficient (UCoef) models is presented.

The correlogram map measured strong correlation among 16 covariates while intermediate correlation among several other predictors is observed and shown in Figure 6. The existence of multicollinearity recommends the applicability of PLSR to deal ranked data with multicollinearity.

The frequency of ANC is classified into three ranks as inadequate, intermediate, and adequate. The ratio of 70 : 30 is used to randomly split data into training and testing sets, respectively. Initially, PLSR integrated with rank correlation coefficients as loading weights is executed. The Spearman's coefficient, Kendall'scoefficient-*A*, Kendall's coefficient-*B*, Stuart-Kendall's, Somers' delta, Goodman-Kruskal's tau, Goodman-Kruskal's gamma, and Thiel's *U* coefficient are used to modify loading weights. Then, three filter-based factor selection methods are performed on each of the nine PLSR models. Leave-one-out cross-validation by linear discriminant analysis is measured on predicted scores of all 27 models. Finally, the Monte Carlo simulation method is used with 10 iterations of repeated sampling for optimization of validation performance. The standard PLSR is compared with the PLSR integrated with Spearman's coefficient (PLSρ_s), PLSR integrated with Kendall's coefficient-*A* (PLSτ_A), PLSR integrated with Kendall's coefficient-*B* (PLSτ_B), PLSR integrated with the Stuart-Kendall (PLSτ_C), PLSR integrated with Somers' delta (PLS$_D$), PLSR integrated with Goodman-Kruskal's tau (PLSτ_{GK}), PLSR integrated with Goodman-Kruskal's gamma (PLS$_G$), and PLSR integrated with Thiel's *U* coefficient (PLS$_U$).

Figure 7 showed the comparison of validation performance of standard PLSR and eight proposed PLSR models integrated with correlation coefficients without considering any variable selection method. These results depicted that PLSρ_s and PLS$_D$ have optimum performance compared to standard PLSR and other proposed PLSR models for the observed data of ANC visits. The PLS τ_A and PLSτ_{GK} also have relatively higher accuracy than standard PLSR. In Figure 8, the loading weight factor selection method is incorporated with each PLSR model. The inclusion of the variable selection method enhanced the overall performance of standard and modified PLSR models. The results showed that PLSτ_A and PLSτ_B are more efficient in terms of optimization accuracy compared to standard and modified PLS models. A similar pattern of performance for PLSρ_s and PLSτ_C is observed compared to standard PLSR. Four other proposed PLSR models integrated with rank correlation coefficients showed slightly lower accuracy compared to standard PLSR.

Figure 9 established performance comparison of the PLSR model based on the RC factor selection method. The results demonstrated that compared to PLSR, the six proposed methods including PLSρ_s, PLSτ_A, PLSτ_B, PLSτ_C, PLS$_D$, and PLS$_U$ featured incremental performance after accounting RC selection method. Two other proposed methods PLSτ_{GK} and PLS$_G$ demonstrated approximately identical efficiency as standard PLSR. Standard and modified PLSR models embedded with the SMC factor selection method are compared in Figure 10 in terms of validation accuracy. The two proposed PLSR models including PLSρ_s

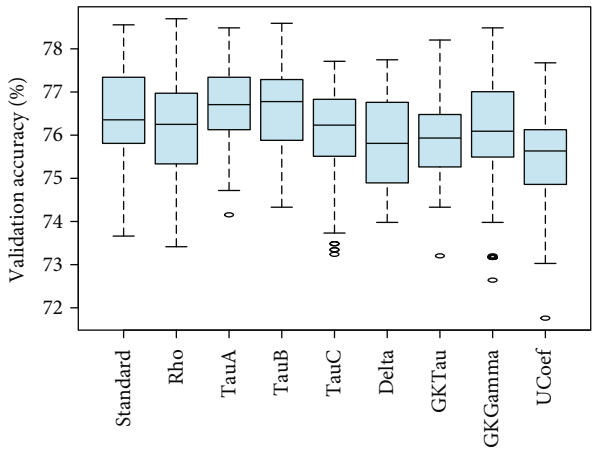

Figure 8: The validation accuracy of PLSR models based on rank correlation coefficients integrated with LW factor selection method is presented.

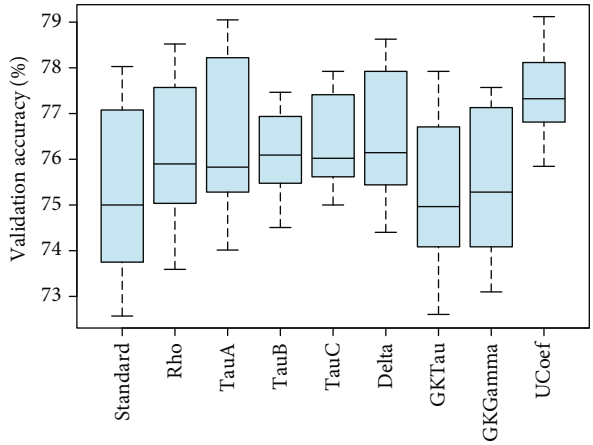

Figure 9: The validation accuracy of PLSR models based on rank correlation coefficients integrated with the RC factor selection method is presented.

and PLSτ_C evidenced higher accuracy than standard PLSR. The other four modified models including PLSτ_A, PLS$_D$, PLS$_G$, and PLS$_U$ measured analogous accuracy as PLSR.

Comparison based on validation accuracy supported that PLSρ_s is found to be the most appropriate proposed method to model the observed ranked data set of ANC. Figure 7 represented the optimal performance of PLSρ_s compared to all other models without considering any variable selection method. Integrated with RC factor selection methods, the proposed PLSρ_s showed higher efficiency compared to standard PLS visualized in Figure 9. Moreover, PLSρ_s established the highest optimization accuracy of nearly 78% among all other methods in 10 combined with the SMC factor selection method. Based on this evidence, PLSρ_s featured with the SMC method is finally picked for the selection of influential factors of ANC. For extraction of influential factors of ANC, PLSρ_s coupled with SMC is executed and estimates of 29 variables are presented in Table 1 with regression estimates.

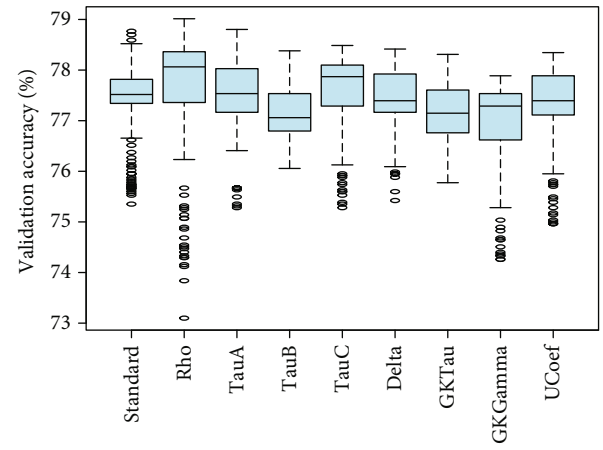

Figure 10: The validation accuracy of PLSR models based on rank correlation coefficients integrated with SMC factor selection method is presented.

4. Discussion

To examine the significant predictors associated with ANC, sample data obtained from PDHS (2017-2018) is used. The occurrence of multicollinearity pointed to the application of PLS being a popular substitute for the standard regression model. Data is randomly divided into testing and training sets. Eight PLS algorithms established on rank correlation coefficients are introduced to address particularly the ranked response and compared with the standard PLS model to prove the improved efficiency in model building. The proposed models include Spearman's coefficient (PLSρ_s), PLSR integrated with Kendall's coefficient-A (PLSτ_A), PLSR integrated with Kendall's coefficient-B (PLSτ_B), PLSR integrated with the Stuart-Kendall (PLSτ_C), PLSR integrated with Somers' delta (PLS$_D$), PLSR integrated with Goodman-Kruskal's tau (PLSτ_{GK}), PLSR integrated with Goodman-Kruskal's Gamma (PLS$_G$), and PLSR integrated with Thiel's U coefficient (PLS$_U$).

Furthermore, three variable selection methods are integrated with standard and modified PLS algorithms to estimate the accuracy to examine the variation in the performance of modified and standard PLS models with and without variable selection methods. The variable selection methods, namely, loading weights, regression coefficients, and significance multivariate correlation are considered here. The validation performance is computed for 10 iterations to examine the efficiency of nine PLS models integrated with variable selection methods.

Comparison based on validation performance supported that PLSρ_s is found to be the most appropriate proposed method to model the observed ranked data set of ANC. Figure 7 represented the optimal performance of PLSρ_s compared to all other models without considering any variable selection method. Integrated with RC factor selection methods, the proposed PLSρ_s showed higher efficiency compared to standard PLS visualized in Figure 9. Moreover, PLSρ_s established the highest optimization accuracy of nearly 78% among all other methods in 10 combined with

Table 1: Regression coefficient estimates of influential factors for PLSρ_s coupled with SMC.

Factor	Coefficient
Age of women	0.010
Type of residence	-0.036
Women's educational level	0.061
Source of drinking water	-0.036
Age of household head	0.023
Frequency of watching television	0.022
Wealth index	0.052
Total children ever born	0.048
Births in last five years	0.016
Number of living children	-0.037
Ever had a terminated pregnancy	-0.034
Visited health facility last 12 months	0.021
Previous birth a caesarean section	0.047
Getting medical help for self: getting permission to go	-0.030
Getting medical help for self: getting money needed for treatment	0.045
Getting medical help for self: distance to health facility	0.021
Heard of tuberculosis	-0.023
Husband's education level	0.040
Respondent's occupation	0.037
Husband's age	-0.017
Beating justified if wife neglects the children	-0.012
Beating justified if wife argues with husband	-0.049
Beating justified if wife refuses to have sex with husband	0.042
Sex of child	0.015
Number of pregnancy losses	0.035
Blood relationship with husband	-0.035
Had a say in choosing the husband	0.026
Ever heard of hepatitis B or C	-0.028
Receive any cash/kind benefit from Benazir Income Support Program	-0.024

the SMC factor selection method. Based on this evidence, PLSρ_s featured with the SMC method is finally picked for the selection of influential factors of ANC.

Regarding validation accuracy, very important and interesting facts are observed about the comparison of efficiency for ranked data. Primarily, PLSρ_s and PLS$_D$ have optimum performance compared to standard PLSR and other proposed models without considering any factor selection method. For the observed data set, the PLSτ_A and PLSτ_B combined with the LW variable selection method are found to be more efficient in terms of optimization accuracy compared to standard and modified PLS models. Integrated with RC method for variable selection, the PLSρ_s, PLSτ_A, PLSτ_B, PLSτ_C, PLS$_D$, and PLS$_U$ featured incremental performance compared to standard PLS. The PLSτ_{GK} and PLS$_G$ are found to exhibit approximately similar efficiency as standard PLSR. The PLSρ_s and PLSτ_C embedded with the SMC factor selection method evidenced optimum accuracy compared to standard PLS. Considering all validation comparisons, it is noticed that the modified models integrated with rank correlation coefficient exhibit higher efficiency for ranked data set of ANC compared to the standard PLS algorithm. The PLSρ_s coupled with SMC is suggested for modeling the ANC ranked data and 29 influential factors are observed to discriminate the ANC ranks. The proposed algorithms for rank response will facilitate researchers to address the regression models more efficiently even in the presence of multicollinearity in different fields of research. Since the rank response is specifically addressed rarely, the findings of this study offer new, potentially useful information for this ranked population. In the future, these algorithms may be integrated with other variable selection methods to observe the efficiency. Also, the proposed study can be extended for neutrosophic statistics [9]. The main limitation of this study is the small number of predictors as every possible factor was not available for the target population and also the interaction effects are not included.

5. Conclusion

Proposed PLS algorithms integrated with rank correlation coefficients are observed to be a better option with regard to model efficiency and variable selection of ranked

simulated and real data sets. This suggests that these rank measure-based PLS algorithms provide models with superior potential. The PLSρ_s coupled with SMC identified the significant predictors of ANC using the optimized model for the observed data. The modified PLS models have the ability to address multicollinear ranked data more effectively. Regarding the clinical importance of this study, the influential selected variables of ANC will help maximize the chances for a normal pregnancy by providing priority interventions, increasing coverage, and improving health quality.

Data Availability

Data is available at https://dhsprogram.com/data/.

Conflicts of Interest

The authors declare that they have no conflicts of interest.

Acknowledgments

The authors would like to acknowledge DHS (Demographic and Health Surveys) who made their data available for free.

References

[1] NIPS I, *Pakistan demographic and health survey 2017-18*, Islamabad, Pakistan, and Rockville, Maryland, USA: NIPS, ICF, 2019.

[2] Demographic P, *Health Survey 2012-13*, MA: National Institute of Population Studies and ICF International; 2013, Islamabad and Calverton, 2015, https://dhsprogram.com/data.

[3] Organization WH, *Standards for Maternal and Neonatal Care*, 2007.

[4] H. Budhwani, K. R. Hearld, and H. Harbison, "Individual and area level factors associated with prenatal, delivery, and postnatal care in Pakistan," *Maternal and child health journal.*, vol. 19, no. 10, pp. 2138–2146, 2015.

[5] J. W. Noh, K. Ym, L. J. Lee, N. Akram, F. Shahid, and Y. D. Kwon, "Factors associated with the use of antenatal care in Sindh province, Pakistan: a population-based study," *PLoS One*, vol. 14, no. 4, p. e0213987, 2019.

[6] M. Aslam, M. Sadiq, and T. Mehmood, "Assessment of maternal health services utilization in Pakistan: the role of sociodemographic characteristics," *Asian Biomedicine.*, vol. 14, no. 1, pp. 3–7, 2020.

[7] K. R. Bhowmik, S. Das, and M. A. Islam, "Modelling the number of antenatal care visits in Bangladesh to determine the risk factors for reduced antenatal care attendance," *PLoS One*, vol. 15, no. 1, article e0228215, 2020.

[8] S. T. Adedokun and S. Yaya, "Correlates of antenatal care utilization among women of reproductive age in sub-Saharan Africa: evidence from multinomial analysis of demographic and health surveys (2010-2018) from 31 countries," *Archives of Public Health.*, vol. 78, no. 1, pp. 1–10, 2020.

[9] R. A. K. Sherwani, H. Shakeel, W. B. Awan, M. Faheem, and M. Aslam, "Analysis of COVID-19 data using neutrosophic Kruskal Wallis H test," *BMC Medical Research Methodology.*, vol. 21, no. 1, pp. 1–7, 2021.

[10] G. S. Rao and M. Aslam, "Inspection plan for COVID-19 patients for Weibull distribution using repetitive sampling under indeterminacy," *BMC Medical Research Methodology.*, vol. 21, no. 1, p. 229, 2021.

[11] S. Arif, H. Khan, M. Aslam, and M. Farooq, "Factors influencing exclusive breastfeeding duration in Pakistan: a population-based cross-sectional study," *BMC Public Health*, vol. 21, no. 1, pp. 1–10, 2021.

[12] M. Azam, M. Aslam, J. Basharat, M. A. Mughal, M. S. Nadeem, and F. Anwar, "An empirical study on quality of life and related factors of Pakistani breast cancer survivors," *Scientific Reports*, vol. 11, no. 1, p. 24391, 2021.

[13] M. Aslam, G. S. Rao, M. Saleem, R. A. K. Sherwani, and C. H. Jun, "Monitoring mortality caused by COVID-19 using gamma-distributed variables based on generalized multiple dependent state sampling," *Computational and Mathematical Methods in Medicine.*, vol. 2021, pp. 1–17, 2021.

[14] M. Sadiq, T. Mehmood, and M. Aslam, "Identifying the factors associated with cesarean section modeled with categorical correlation coefficients in partial least squares," *PLoS One*, vol. 14, no. 7, article e0219427, 2019.

[15] S. Wold, M. Sjöström, and L. Eriksson, "PLS-regression: a basic tool of chemometrics," *Chemometrics and Intelligent Laboratory Systems*, vol. 58, no. 2, pp. 109–130, 2001.

[16] J. L. Myers, A. D. Well, and R. F. Lorch Jr., *Research Design and Statistical Analysis*, Routledge, 2013.

[17] M. G. Kendall, "A new measure of rank correlation," *Biometrika*, vol. 30, no. 1-2, pp. 81–93, 1938.

[18] A. Agresti, *Analysis of Ordinal Categorical Data*, vol. 656, John Wiley & Sons, 2010.

[19] K. J. Berry, J. E. Johnston, S. Zahran, and P. W. Mielke, "Stuart's tau measure of effect size for ordinal variables: some methodological considerations," *Behavior Research Methods.*, vol. 41, no. 4, pp. 1144–1148, 2009.

[20] R. H. Somers, "A new asymmetric measure of association for ordinal variables," *American sociological review.*, vol. 27, no. 6, pp. 799–811, 1962.

[21] L. A. Goodman and W. H. Kruskal, "Measures of association for cross classifications, IV: simplification of asymptotic variances," *Journal of the American Statistical Association.*, vol. 67, no. 338, pp. 415–421, 1972.

[22] W. H. Press, S. A. Teukolsky, W. T. Vetterling, and B. P. Flannery, *Numerical Recipes 3rd Edition: The Art of Scientific Computing*, Cambridge university press, 2007.

[23] T. Mehmood, M. Sadiq, and M. Aslam, "Filter-based factor selection methods in partial least squares regression," *IEEE Access.*, vol. 7, pp. 153499–153508, 2019.